Towards Dark Energy: Design, Development, and Preliminary Data from ACT

Michael D. Niemack

A dissertation presented to the faculty of Princeton University
in candidacy for the degree of Doctor of Philosophy

Recommended for acceptance by the Department of Physics
Advisor: Suzanne T. Staggs

April 2008

Abstract

Recent cosmological observations resulted in the surprising discovery that our universe is dominated by a dark energy, causing acceleration of the expansion of the universe. Understanding the dark energy (Λ) and the cosmic acceleration may require a revolution in our understanding of the laws of physics, and more precise data will be critical to this endeavor. The remainder of the universe is dominated by cold dark matter (CDM), while only $\sim$4% of the universe comprises baryonic matter.

To improve our understanding of dark energy and the ΛCDM model of our universe, we have developed a novel telescope and receiver technology to map the universe at millimeter wavelengths on arcminute angular scales. The Atacama Cosmology Telescope (ACT) and its receiver, the Millimeter Bolometer Array Camera (MBAC), are optimized to measure temperature anisotropies in the primordial cosmic microwave background radiation (CMB). On the smallest angular scales measured by ACT the anisotropies are dominated by secondary interactions of CMB photons, such as gravitational interactions and the Sunyaev-Zel'dovich (SZ) effects: the interaction of CMB photons with ionized gas in galaxy clusters.

We can use these measurements to probe dark energy in multiple ways. The CMB bispectrum quantifies the non-Gaussian nature of the secondary anisotropies and when combined with measurements from the Wilkinson Microwave Anisotropy Probe, will provide constraints on dark energy. By combining and cross-correlating measurements of the SZ effects with galaxy cluster redshifts, we can constrain the equation of state of dark energy and its evolution. In addition, by measuring the CMB on arcminute angular scales, we will probe the details of the ΛCDM cosmological model that describes our universe.

This dissertation begins with the development of the optical designs for ACT and MBAC that focus light onto the MBAC bolometer arrays. The kilo-pixel bolometer arrays are the largest ever used for CMB observations. The arrays utilize superconducting transition edge-sensor (TES) bolometers to measure changes in optical power, which are coupled to superconducting quantum interference devices (SQUIDs) for signal measurement and amplification. A model describing the functionality of the TES bolometers is presented in addition to a procedure developed to characterize all bolometers before assembling them into arrays. The capabilities and characterization of the time-domain SQUID multiplexing readout system and electronics are discussed, including the implications of magnetic sensitivity for the readout system and recently developed array characterization techniques. Measurements of the first fully-assembled detector array are presented, including: functionality, efficiency, detector time constants, and noise. Preliminary results from the first season of CMB observations are also discussed. A new approach for measuring photometric redshifts of galaxies using optical and ultraviolet observations is presented. These photometric redshifts will be cross-correlated with SZ cluster measurements from ACT to improve our understanding of dark energy. Finally, predictions are given for the sensitivity of the experiment from both one and two seasons of observations.

Acknowledgements

It never ceases to amaze me how the work of so many people has been successfully integrated into the beast described in this dissertation. The experiment would not have been possible without the critical developments and contributions of my collaborators at a number of institutions, including: NASA Goddard Space Flight Center, the National Institute of Standards and Technology, the University of Pennsylvania, the University of British Columbia, Cardiff University, and, of course, Princeton. Somehow, through the hard work and perseverance of many, we have managed to cobble together a massive instrument with incredible sensitivity that has measured the oldest light in the universe.

The years I have spent working on this project have made me incredibly grateful to have such an excellent advisor. Suzanne's guidance, support, dedication, and many insightful, protracted conversations inspired the majority of the work presented here. Actually, I feel as though I had three amazing advisors, because I was also lucky enough to work closely with and learn from the wisdom of both Joe and Lyman. They have been wonderful mentors, and I am dreading the day when I cannot simply walk a lap around the second floor of Jadwin Hall and find one of the three ready to talk about the puzzles of our experiment. Numerous other people have been integral to the development of the work I am presenting, so I have included at least partial acknowledgements at the end of each chapter to point out specific contributions that have been made. I am sure I have left people out, which I am sorry for, but it would take another book to simply list all the contributions from all the incredible people that have been involved in this project.

There are a number of people who have been critical in teaching me and supporting my work through graduate school. Paul Steinhardt, Uros Seljak, David Spergel, Raul Jimenez,

and Chris Hirata (among others) guided my learning about our strange and amazing universe. Marks Devlin and Halpern as well as Kent Irwin, Jay Chervenak, Harvey Moseley, Ed Wollack, and Randy Doriese taught me many things about our complex experiment. Norm Jarosik and Jeff Klein's incredible understanding of the way things work was always useful and often inspirational. Mike Peloso, Bill Dix, Glenn Atkinson, Lazslo Varga, Bert Harrop, Stan Chidzik, and Ted Lewis were among those who helped hone my abilities to design, machine, and build things, and then they built much of our experiment with incredible precision and functionality. Angela Glenn, Claude Champagne, Barbara Grunwerg, Mary Santay, Kathy Paterson, and John Washington were all awesome to work with and so helpful when I needed to actually get things done. I also thank Eric, Lyman, Maren, Dan, and Suzanne for spending the time to provide vital feedback on this lengthy document.

Princeton has really been an excellent place to go to graduate school. The distractions are so few and far between that it enables one to focus on ... work. Luckily for me, we have occasionally found some great distractions. I have especially fond memories (which sometimes include amazement that we all survived) of times with Jeff, Lewis, Glen, and Judy. Toby, Asad, Juan, "Dr. No", Dan, Eric, Adam, Ryan, Yue, Rolando, Madhuri, John, Lucas, Tom, Omelan, Krista, Beth, Elia, Bryce, and many short term students have made the last five years of working on this project far more interesting, fun, and successful. Excellent distractions of all sorts, from rock climbing to reunions hopping, have also been sought out and found with Micah, Sara, Phil, Denis, Ethan, Dave, Josh, Jed, Amber, Janice, and friends. At times, I have been guided through forays into the strange, but exciting, world of ecologists, and (among others) I have especially enjoyed talking over tasty beverages with Nathan, Jim, and Martin.[1] Despite the lack of distractions in Princeton, we have done pretty well, and I am really going to miss this place and all of the incredible people I have gotten to know here.

To my large and ever growing family: you guys are the best. Mom, Dad, Bruce, Ann, Elisa, Colleen, Tyler, and Kaylie, without your love and support I never would have made it here. I hope to see you all again soon.

[1] Not to mention all the excellent grub at Martin's place. They really have the free food thing figured out in EEB. On that note, I would also like to thank all the anonymous people who have joined the "leftovers for physicists program," which has fed so many starving researchers who could not bring themselves to walk further than the faculty lounge.

To my wonderful wife: Maren, you make me happy, keep me sane, inspire me, and give me something to look forward to every time I come home. I love you.

Contents

List of Figures

List of Tables

Chapter 1

Introduction

In the early 1920s Edwin Hubble used the 100-inch telescope at the Mount Wilson observatory to measured the optical spectra of variable stars in "spiral nebulae". Based on his measurements, he could predict the total luminosity of these stars, which allowed him to quantify the distance to them. He came to the startling conclusion that the "spiral nebulae" are in fact galaxies like our own and that they are separated from us by distances more vast than anyone had previously imagined. Even more surprising was his finding that all the distant galaxies are receding, and that the velocity of recession follows a simple relationship, which came to be known as Hubble's law:

$$v = H_0 d, \tag{1.1}$$

where v is the recessional velocity, d is the distance, and H_0 is Hubble's constant. This proportional relationship tells us that the universe is expanding. At intergalactic distances, everything in the universe that we can observe is moving away from everything else. If we were able to go back in time and thereby reverse this process, we would find the universe collapsing. Extrapolate far enough, and all the matter in the universe would collide generating an incredibly high temperature and density state. From these observations, the Big Bang theory was born.

When Einstein learned of Hubble's measurements, he realized that he had added unnecessary complication to his theory of General Relativity. He had previously assumed that the universe was static. General Relativity, however, indicates that a static universe is unstable, so Einstein added a cosmological constant to make the static solution viable. Hubble's measurements show that the universe is in fact dynamically evolving, which is consistent with General Relativity without the addition of a cosmological constant.

Decades later physicists were studying the Big Bang model. Based on an understanding of atomic and nuclear structure and binding energies, they hypothesized that at extremely early times, the universe was hot enough and dense enough to prevent protons and neutrons from fusing into atomic nuclei. As the universe expanded, the density decreased, and the mean photon energy dropped as the photon wavelengths were stretched by the expansion, both of which caused the universe to cool. The photons and subatomic particles were in relativistic thermal equilibrium until the temperature cooled to near the nuclear binding energies of the light elements ($\sim 10^6$ eV). At that point roughly a quarter of the protons and neutrons were bound in the form of helium, and almost all the rest were left as ionized Hydrogen [31]. Over the next ∼400,000 years the temperature dropped enough that the electrons began to combine with the nuclei. Because of the over-abundance of photons – there are $\sim 10^{10}$ photons for every baryon – the mean photon energy needed to fall significantly below the ionization energy of Hydrogen (to ∼1 eV) before the plasma-filled universe could become neutral. Since there were so few remaining ionized particles to interact with, the photons decoupled from the matter and began free-streaming in all directions. It was predicted that most of the photons released at this time of decoupling are still traveling through the universe today and that we should see this Cosmic Microwave Backround (CMB) radiation in every direction we look. The CMB radiation arriving at Earth today was emitted from the most distant part of the universe that can currently be measured, which effectively makes it the horizon of the known universe. The subsequent expansion of the universe has caused the temperature of the radiation to drop from the original ∼3,000 K to a few degrees Kelvin today.

1.1 Cosmic Microwave Background Radiation

In 1965, Penzias and Wilson were testing a mm-wave radiometer for Bell Labs on a telescope in Crawford Hill, NJ, and they found that when the instrument was pointed at the sky they measured an excess antennae temperature of $\sim$3.5 K. Their accidental discovery was the first detection of the Cosmic Microwave Background radiation. Since its discovery, the CMB has been characterized with remarkable precision. The Far-InfraRed Absolute Spectrophotometer (FIRAS) on the Cosmic Background Explorer (COBE) satellite measured the spectrum of the CMB radiation and found nearly perfect agreement between the measured spectrum and the Planck distribution for a thermal blackbody radiator at a temperature of $T_{CMB} = 2.725 \pm 0.001$ K [73] (Figure 1.1). The FIRAS data combined with measurements from ground-based, balloon-borne, and rocket instruments show that the CMB temperature is nearly constant over three orders of magnitude in radiation frequency. This incredible temperature isotropy indicates that at the time of decoupling the universe was in thermal equilibrium over distances greater than the horizon scale, or the distance that light could travel since the big bang. To explain this "horizon problem", theorists hypothesized that a period of exponential expansion, or inflation, occurred 10^{-35} seconds after the big bang, which separated regions that were previously in causal contact. Testing and understanding this inflationary paradigm is one of the primary goals of CMB experiments today [25].

The largest measured deviation of the CMB from isotropy is a dipole on the celestial sphere, which exists due to redshifting of CMB photons because of our velocity through the universe relative to the CMB rest frame. This dipole causes a temperature shift of roughly a part in 10^3 of T_{CMB}. After subtracting the dipole, T_{CMB} measured in all directions on the sky is uniform to almost a part in 10^5. The tiny fluctuations of the temperature about the mean are described as the CMB temperature anisotropies. The distance scales that these fluctuations occur at (measured as angular scales on the sky) contain a great deal of information about our universe. We parameterize the temperature anisotropies as ΔT and define

$$\Theta(\hat{\mathbf{n}}) \equiv \frac{\Delta T}{\langle T_{CMB} \rangle}, \tag{1.2}$$

where $\hat{\mathbf{n}}$ is the direction on the celestial sphere. The anisotropies can be studied as a function of angular scale by decomposing Θ in terms of spherical harmonics, Y_{lm}, on the sky

$$\Theta_{lm} = \int \Theta(\hat{\mathbf{n}}) Y^*_{lm}(\hat{\mathbf{n}}) d\Omega. \tag{1.3}$$

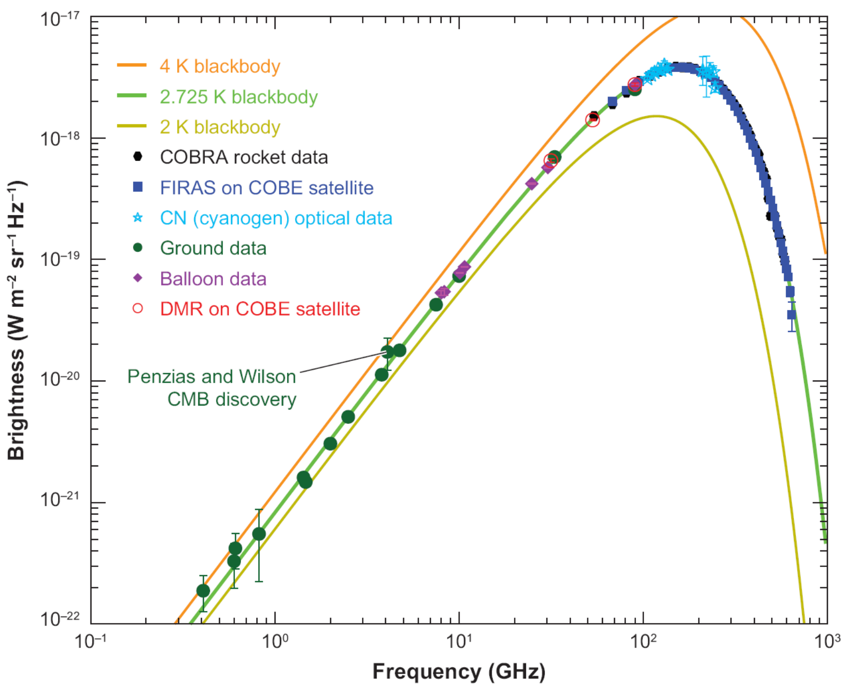

Figure 1.1: The CMB blackbody spectrum. The green line is the best fit blackbody spectrum with only one free parameter, $T_{CMB} = 2.725 \pm 0.001$ K, to all of the data points shown, which are from a number of different experiments as indicated in the legend [94]. The 4 GHz data point from Penzias and Wilson's original discovery is labeled. The orange and yellow lines show the spectra of blackbodies at 4 K and 2 K respectively. (Reprinted, with permission, from the Annual Review of Nuclear and Particle Science, Volume 57 ©2007 by Annual Reviews [94].)

The cosmological principle postulates that the universe is homogeneous and isotropic, indicating that there are no cosmologically preferred locations in the universe, and thus, the temperature fluctuations should have no preferred directionality. This principle guides us to explore the power spectrum of the fluctuations in terms of the multipole, l, while taking an ensemble average over the directional index, m. To do this, we define the angular power spectrum, C_l, as

$$\delta_{ll'}\delta_{mm'}C_l = \langle \Theta^*_{lm}\Theta_{l'm'} \rangle, \tag{1.4}$$

where the brackets indicate the average over m. The angular power spectrum of the temperature fluctuations is sensitive to a variety of fundamental parameters that describe our universe, which include: the age of the universe, the total energy density, the matter density, and the baryon density.

Three effects dominate the generation of primordial temperature fluctuations, or anisotropies, up to the time of decoupling [31, 87]. The first is the gravitational redshifting of CMB photons as they climb out of gravitational potential wells generated by super-horizon scale density fluctuations (the Sachs-Wolfe effect) [93]. This effect dominates on the largest angular scales ($l <\sim 90$) [85].

On sub-horizon length scales, the photon pressure combined with gravitational collapse of the photon-baryon plasma drives acoustic oscillations (compressions and rarefactions) of the plasma into overdense and underdense regions. As the horizon expands, the fundamental mode with wavelength equal to twice the size of the horizon begins to oscillate with a period related to the densities of the photons and baryons. At the time of decoupling, some of these oscillations are reaching their peak amplitudes, while others have returned to the mean density. The length scales with oscillations at their peak minima or maxima result in larger temperature anisotropies, and thus peaks in the CMB power spectrum, while those that have returned to the mean show up as troughs in the power spectrum. In particular, the first peak in the power spectrum is due to modes that have undergone a single compression at the time of decoupling, while the second peak is due to modes that went through both a compression and a rarefaction.[1] Because of the interaction between gravitational potential

[1]The third peak in the power spectrum is due to modes that have undergone a compression, a rarefaction, and a final compression, and the pattern continues.

wells formed by dark matter and the photon-baryon plasma, the amplitude of the first peak is largely determined by the total matter density in the universe, ρ_m. The rarefactions that cause the second peak, on the other hand, are affected by the inertia of the photon-baryon plasma, which is related to the baryon density, ρ_b. Thus, careful measurements of the first and second peak amplitudes in the CMB angular power spectrum allow us to constrain the matter densities in the universe.

On smaller scales ($l >\sim 900$), photon diffusion during decoupling wipes out the anisotropy signatures of the acoustic oscillations (Silk damping) [31]. The scale of this damping effect is determined by the period of time over which decoupling occurs (also described as the thickness of the surface of last scattering), because photon scattering during decoupling erases the anisotropies at or below the length scale of the scattering events.

These primary CMB anisotropies were first detected by the Differential Microwave Radiometer instrument on COBE (Figure 1.2). After this first detection, numerous groups worked to improve the anisotropy measurements using ground-based and balloon-borne instruments [111]. Critical questions they wanted to address included: what is the total energy density of the universe and does the density determine its evolution?

At that time many scientists assumed that gravity is the dominant interaction on the longest distance scales, which enables calculation of a critical energy density, ρ_c, above which the density of the universe, ρ_{tot}, is large enough that gravity would slow down and reverse the expansion that started with the big bang. In this scenario, the matter in the universe would eventually collapse in a "big crunch," as opposed to a universe with a density less than or equal to ρ_c which would expand forever, slowly getting colder and colder.[2] The total energy density of the universe thus determines the expansion history, and this history affects the angular scales at which we observe the CMB anisotropies on the sky. By measuring the dominant scale of the CMB anisotropies – the location of the first peak in the CMB power spectrum – we can determine the total density of the universe. As it turns out, gravity does not dominate our universe on the longest distance scales, which means that a measurement of the total density of the universe does not determine its evolution.

[2]These scenarios can be treated as projecting our $3+1$ dimensional space-time onto an additional dimension that defines the curvature of space-time. If $\rho_{tot} = \rho_c$, there is no curvature and space-time is Euclidean; however, if $\rho_{tot} < \rho_c$, the curvature is hyperbolic, or open, which would result in eternal expansion. Finally, if $\rho_{tot} > \rho_c$, the universe is closed and would be doomed to a "big crunch".

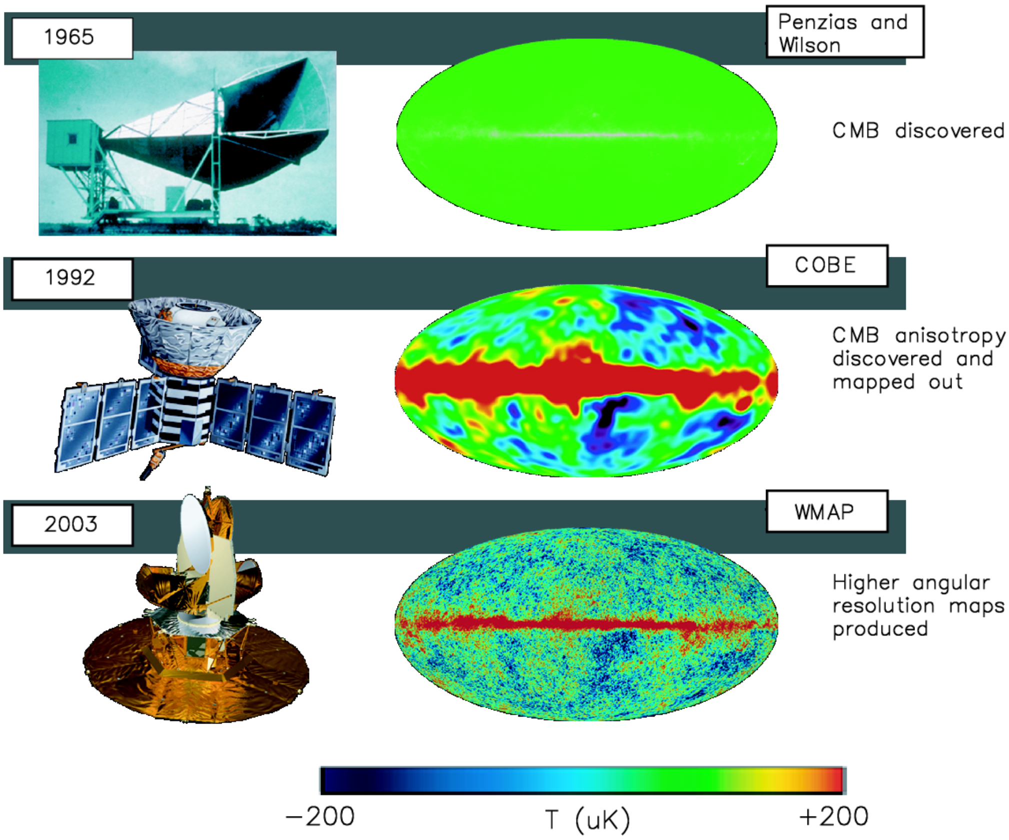

Figure 1.2: Maps of the CMB anisotropies. The maps are projections of the spherical sky and indicate the relative sensitivities and resolutions of the three instruments. *Top*: The original detection of the CMB by Penzias and Wilson using a horn antenna in Crawford Hill, New Jersey. (Note: Because it was ground-based, the horn antenna could not map the CMB across the entire sky, but the sensitivity of its measurement is plotted in this way for comparison with the all-sky measurements.) *Middle*: The Cosmic Background Explorer (COBE) detection of the CMB anisotropies. *Bottom*: The Wilkinson Microwave Anisotropy Probe (WMAP) measurements of the CMB anisotropies achieved an average resolution of $\sim 0.2°$. The color scale at the bottom is the same for all maps to emphasize the increases in sensitivity. (Figure courtesy of J. Lau [67] and the WMAP science team.)

1.2 Accelerating Expansion

At the same time cosmologists were beginning to probe the CMB anisotropies, other astrophysicists were developing new techniques to extend Hubble's measurements to larger distance scales. To do this, a new type of "standard candle" was needed. The Cepheid variable stars used by Hubble are good standard candles because there is a tight correlation between the (easily measured) period of the luminosity variability and the absolute luminosity of the star. The problem is that these stars are simply not bright enough to be observed in more distant galaxies. It was discovered that a certain type of supernova (Type 1a) can also be used as a standard candle [44]. These supernovae are the result of a carbon-oxygen white dwarf star accreting enough mass to bring it near the Chandresekar limit ($\sim$1.4 times the mass of the sun). The details of the resulting explosion are still being understood [74], but the total luminosity of these events consistently reaches $\sim 5 \times 10^9$ times the luminosity of the sun. By using wide field optical telescopes to detect the initial increase in flux from a supernova, then following up with deeper measurements to characterize the decaying light curve, scientists can estimate the distance to these events.

In the 1990s groups of astrophysicists set out to measure a large number of these supernova to characterize the evolution of the Hubble constant and thereby determine how our universe would end. To everyone's surprise, analysis of the data showed that the expansion of the universe was not decelerating as would be expected from gravity; instead the expansion of the universe is accelerating [88, 105].

In 2001, the Wilkinson Microwave Anisotropy Probe (WMAP) was launched to make detailed measurements of the CMB anisotropies on smaller angular scales than COBE. Over the next few years WMAP characterized the angular power spectrum in exquisite detail (Figure 1.3). The WMAP team found that the location of the first peak in the power spectrum indicates that the total energy density of the universe, ρ_{tot}, is consistent with the critical density; or using the conventional ratio expression, $\Omega_{tot} = \rho_{tot}/\rho_c = 1.02 \pm 0.02$. The relative peak heights of the power spectrum were best explained by a universe with a (similarly expressed) baryonic matter density of $\Omega_b = 0.044 \pm 0.004$, a total matter density

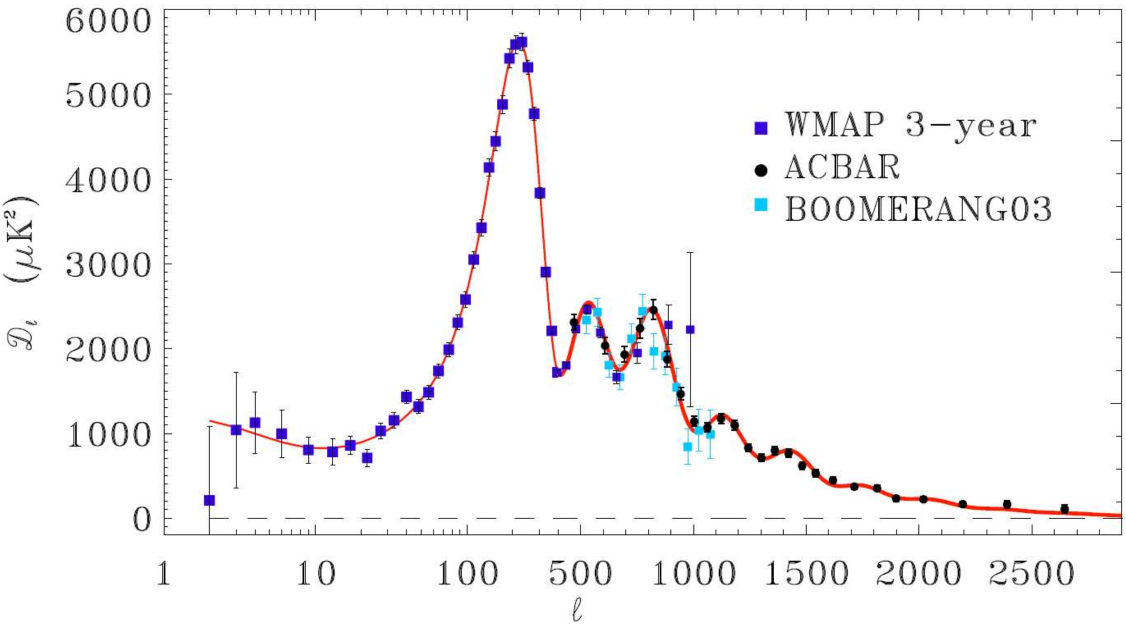

Figure 1.3: CMB temperature anisotropy angular power spectrum. The spherical harmonic multipole, l, is plotted versus the conventional $D_l \equiv l(l+1)C_l/2\pi$. The large angular scale (low multipole) WMAP data [98] (dark blue) as well as the intermediate scale Boomerang data [57] (light blue) and the recently released ACBAR results on small scales [90] are shown. The best fit theoretical model to the data is shown in red. (Figure courtesy of the ACBAR team [90].)

of $\Omega_m = 0.27 \pm 0.02$,[3] and the remaining almost three quarters of the universe in an unknown form of energy, Ω_Λ or "dark energy", that is responsible for the accelerating expansion[13, 98]. These data are consistent with the supernova results as well as a number of previous measurements [31], which found that cold dark matter (CDM) dominates the baryonic matter in the universe. After the release of these results, the ΛCDM model for our universe became the standard model of cosmology.

Based on the CMB and supernova observations, there are roughly three theoretical categories that could eventually explain the "dark energy". It could be a cosmological constant, mathematically equivalent – albeit with a different effect – to the constant that Einstein removed from his theory of General Relativity. Alternatively, it could be a new field, or quintessence, that acts on much larger distance scales than gravity. The difference

[3]CMB measurements of Ω_m are somewhat degenerate with the Hubble constant in equation (1.1) [85]. WMAP found $H_0 = 73 \pm 3$ km sec^{-1} Mpc^{-1}, which is consistent with measurements using other techniques [98].

between the cosmological constant and quintessence descriptions of dark energy can be quantified in terms of the equation of state: the relationship between the pressure, P_Λ, and the density, ρ_Λ, of the dark energy,

$$w = P_\Lambda/\rho_\Lambda. \tag{1.5}$$

Derivation of w from the Einstein equations indicates that accelerating expansion imposes an upper limit of $w < -1/3$ [31]. If w is measured to be between $-1 < w < -1/3$, then the dark energy can be described by some unknown particle or field within the standard model of cosmology. In this scenario, there is no reason to expect that w is constant over time, and testing for evolution of w is one of the primary objectives of current experiments. On the other hand, if w = -1 and is constant over time, then the dark energy is actually a cosmological constant. A cosmological constant is, in fact, predicted by many quantum field theories; however, the predicted values are of order 10^{100} times too large, and no resolution for this discrepancy has been found. The final possibility is that there is some fundamental flaw in the theoretical basis of General Relativity or the standard cosmological model. Discovering the fundamental cause of the accelerating expansion of the universe is one of the most compelling scientific pursuits of our time [26].

1.3 Probing Dark Energy

The accelerating expansion of the universe suggests two primary effects that can be probed to measure w and improve our understanding of dark energy. First, the accelerating expansion (clearly) affects the expansion history, or how distance scales change over time. This can be studied by probing the distances directly with recession velocity measurements or by measuring the evolution of the matter density. Second, the expansion rate of the universe affects how quickly overdensities can collapse into gravitational potential wells; thus, changes in the expansion rate will affect the growth of structure on the largest scales in the universe. Several approaches have been proposed to measure one or both of these effects, including: improved observations of Type 1a supernova, galaxy cluster counting measurements, weak gravitational lensing, and large scale characterization of baryon acoustic oscillations and how they evolved from the primordial CMB oscillations [26].

This dissertation describes a new experiment that will measure both the evolution of the matter density and the growth rate of structure to probe dark energy. In particular, we are mapping the CMB over a wide field ($\sim$1000 square degrees) on smaller angular scales ($\sim 1'$) and with better sensitivity than has previously been possible. At small angular scales (below $\sim 10'$) the CMB anisotropies are no longer dominated by the primordial fluctuations discussed in Section 1.1. Instead, the small-scale anisotropies are dominated by secondary interactions of the CMB photons with gravitational potential wells and ionized gas between the time of decoupling and today. Here I describe some of the secondary effects that are influenced by the properties of dark energy and measurements we will make to help understand these properties.

1.3.1 CMB Bispectrum

As the CMB photons travel through the universe after decoupling, they encounter density fluctuations. Like the initial gravitational redshifting of photons at the time of time of decoupling, redshifting occurs as photons climb out of potential wells and blueshifting occurs as they fall into wells. If a potential well grows while a photon is traversing the well, the net effect is redshifting of the photon. This effect is described for low-density fluctuations as the integrated Sachs-Wolfe (ISW) effect, and it was extended to include high-density regions (like galaxy clusters) by Rees and Sciama [89]. In addition, the potentials cause gravitational lensing of the anisotropies, which results in spatial (as opposed to spectral) distortions. These effects all induce non-Gaussian deviations from the primordial form. Assuming that the primordial anisotropies are Gaussian in nature (which is expected of acoustic oscillations [31]), these non-Gaussianities can be quantified in terms of the CMB bispectrum, $B_{l_1 l_2 l_3}$, which is defined (analogously to equation 1.4) as:

$$\binom{m_1 m_2 m_3}{l_1\ l_2\ l_3} B_{l_1 l_2 l_3} = \langle \Theta_{l_1}^{m_1} \Theta_{l_2}^{m_2} \Theta_{l_3}^{m_3} \rangle, \tag{1.6}$$

where $\binom{m_1 m_2 m_3}{l_1\ l_2\ l_3}$ is the Wigner three-J symbol [110]. Because the bispectrum is sensitive to the evolution of the gravitational potential, combining small-scale measurements of the CMB bispectrum with large-scale measurements from WMAP breaks a degeneracy between Ω_m and w, and thereby gives better constraints on the dark energy equation of state [110].

1.3.2 Sunyaev Zel'dovich Effects

After the time of decoupling, the universe remained neutral for more than $\sim 10^8$ years. During that time CMB photons redshifted to roughly 50 times their original wavelengths. Finally, the baryon density in some gravitational potential wells became high enough that thermal interactions could re-ionize the hydrogen gas. Since then, hot electrons in ionized hydrogen gas have interacted with and transferred energy to cold CMB photons. As the potential wells became deeper, galaxy clusters began to form and the temperature and density of the ionized gas within the clusters increased to the point where electron interactions with the CMB photons could cause significant changes in the photon spectrum. The results of these interactions were first calculated by Sunyeav and Zel'dovich (SZ).

Thermal SZ effect

The inverse Compton scattering[4] of CMB photons off of hot electrons ($> 10^6$ K) in intra-cluster gas is known as the thermal Sunyeav Zel'dovich (tSZ) effect [99]. Only $\sim 1\%$ of CMB photons that travel through a cluster are expected to be scattered through the tSZ effect, and since photon number is conserved in this interaction, the dominant result is a slight shift of the CMB blackbody spectrum to higher frequencies when the photons pass through a galaxy cluster (Figure 1.4).

A striking feature of the tSZ effect is its redshift independence. Unlike measurements of radiation emitted by clusters that suffer from $1/r^2$ dimming, where r is the distance to the source of the radiation, the tSZ effect is simply a spectral shift of already existing radiation. The amplitude of the effect is determined by the density and the temperature of the cluster gas, which (under certain assumptions) can be converted into a cluster mass [31].[5] These characteristics make measurement of the tSZ effect an excellent approach for detecting a relatively unbiased, mass-limited sample of galaxy clusters. By adding optical redshift measurements of these SZ selected clusters, we can count the number of clusters as a function of mass and redshift. This cluster counting technique allows us to probe dark

[4]In the rest frame of the electron this process is identical to Compton scattering, however, in the rest frame of the CMB, the net energy transfer is to the photon instead of the electron, hence the conventionally used "inverse."

[5]To improve the cluster mass estimates, we can also add, for example, optical lensing, velocity dispersion, or X-ray temperature data measured with other instruments.

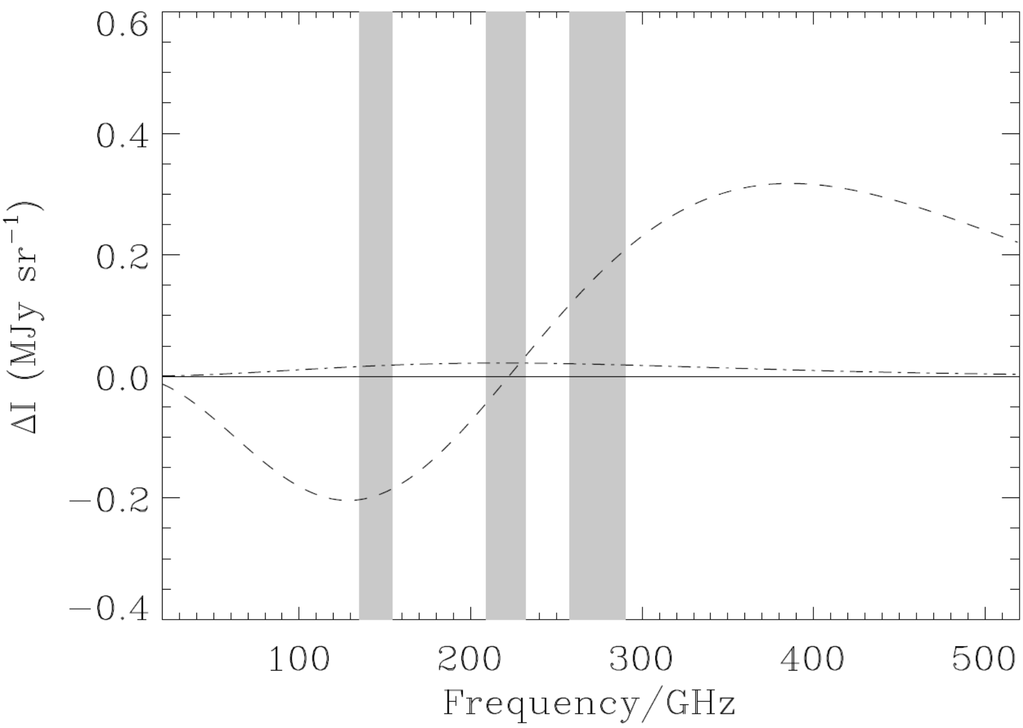

Figure 1.4: SZ effects on the CMB blackbody spectrum. The predicted change in intensity from the CMB blackbody spectrum (Figure 1.1) is plotted versus radiation frequency. The thermal SZ effect (dashed) has a clear frequency dependence, and the three ACT frequency bands (roughly the gray regions, actual bands are shown in Figure 2.4) bridge the null of the effect at ∼220 GHz. The kinetic SZ effect (dot dashed) has a much smaller amplitude and little frequency dependence across our bands, making it more difficult to detect and extract from the data. The curves are plotted for a cluster with a gas temperature of 10 keV and a peculiar velocity of -500 km/s [14]. (Figure courtesy of B. Benson [14].)

energy through both the expansion history, by measuring the evolution of the density within a volume element, and the growth of structure [26].

Kinetic SZ effect

In addition to the tSZ effect, if the cluster gas has a bulk velocity relative to the rest frame of the CMB, Thomson scattering will cause a Doppler induced shift in the effective temperature of the radiation (Figure 1.4). This kinetic SZ (kSZ) effect is typically an order of magnitude smaller than the tSZ effect. Because the kSZ effect depends on the peculiar velocity field, it is sensitive to large-scale density flows.[6] By cross-correlating kSZ measurements with cluster redshift information, we can probe the evolution of the gravitational potential, and thus, the equation of state of the dark energy and its evolution [16, 48].

1.4 The Atacama Cosmology Telescope Project

The Atacama Cosmology Telescope (ACT) is designed to map the CMB on degree to arcminute angular scales with a precision of a few microKelvin. This angular resolution range allows us to probe the transition from the scale of the primordial CMB anisotropies to the scales dominated by secondary effects. We will produce high resolution millimeter wavelength maps of the universe and extend the characterization of the angular power spectrum to multipoles approaching $l \approx 10,000$. These measurements will improve our understanding of the ΛCDM cosmological model, provide constraints on inflationary models of the early universe by measuring the scalar spectral index of the primordial fluctuations, n_s, probe light neutrino masses down to $m_\nu \approx 0.1$ eV, and map the mass distribution through tSZ and gravitational lensing measurements [61]. Measurements of the CMB bispectrum on these angular scales will also help to constrain the dark energy equation of state.

ACT will observe in three frequency bands (148, 215, 280 GHz) that bridge the null of the thermal Sunyaev-Zel'dovich effect to create a mass-limited catalog of tSZ selected clusters [96]. Having multiple frequency bands will also allow extraction of infrared point sources and other contaminants from the maps. In addition to measurements with ACT,

[6] Careful measurements of the SZ effects have been used to constrain bulk flows, but the kSZ effect has not yet been directly detected with high signal-to-noise [14].

the ACT Collaboration[7] has begun optical and ultraviolet observations to make redshift measurements of the tSZ selected clusters [78]. Combining these redshift data with the tSZ selected cluster sample and correlating them with kSZ signatures in the maps will allow multiple probes of the dark energy equation of state as described above.

In 2007, ACT was assembled at 5200 m on the Atacama plateau in northeastern Chile – one of the driest places on earth. A low moisture location is critical for this experiment, because water vapor in the atmosphere emits radiation in our frequency bands [71]. ACT has a six meter projected aperture primary mirror, allowing it to achieve arcminute scale resolution at our frequencies. The three detector arrays for ACT comprise 32×32 element superconducting transition-edge sensor (TES) bolometer arrays. Successful observations were made with the first of these arrays (148 GHz) during the 2007 season, making it the largest TES array ever to observe the sky. Analyses of the first season of observations are currently underway as we build and prepare to deploy arrays at all three frequencies for the 2008 observation season.

1.5 Overview

The focus of this thesis is the design, development and testing of ACT and its instrumentation, followed by preliminary results from the first season of observations. This work builds on previous theses, which describe the Column Camera (CCam) prototype receiver for ACT [3, 67] and the development of prototype detectors for the ACT receivers [67, 71]. We also present the results of a new approach for photometric redshift estimation using optical and ultraviolet observations, which will be combined and cross-correlated with data from ACT.

In Chapter 2 the optical design of ACT and its primary receiver, the Millimeter Bolometer Array Camera (MBAC) is described. Based on these designs, predictions for the throughput and resolution of the instrument are explored, which are followed by discussion of the optical design of the detector arrays.

[7] The ACT collaboration includes members at: Cardiff U., Columbia U., CUNY, Haverford College, INAOE, NASA/GSFC, NIST/Boulder, Princeton U., Rutgers U., U. British Columbia, U. Católica de Chile, U. KwaZulu-Natal, U. Massachusetts, U. Pennsylvania, U. Pittsburgh, and U. Toronto.

In Chapter 3 the TES bolometer technology used to measure power from the sky is presented, including: a theoretical model for the bolometers, an introduction to the multiplexed cryogenic electronics used to extract the optical signals measured by bolometers, the selection of the bolometer parameters, and detailed testing techniques that were implemented to characterize the bolometers and minimize the number of failures in the detector arrays.

In Chapter 4 the magnetic field sensitivity of the TES detectors and the superconducting quantum interference device (SQUID) readout components is explored. The room temperature readout electronics are also described, including: selection of some of the critical multiplexing parameters for the readout system and automated SQUID tuning and detector biasing procedures that were implemented during observations. Finally, new techniques for fast characterization of TES bolometer arrays during observations are presented.

In Chapter 5 we present the largest TES bolometer array yet used for astronomical observations. Detailed characterizations of the $\sim$900 working bolometers in the array are presented, and the failures that prevented $\sim$12% of the array from working are described. We compare detector time constant measurements acquired using different methods and show the results of preliminary receiver/detector efficiency and noise measurements made prior to deployment.

In Chapter 6 the successful deployment of MBAC, with the 148 GHz array, onto ACT for the 2007 season of observations is described. Preliminary data analysis from the observations is presented and compared to a model that combines the temporal and optical responses of the detectors. A preliminary efficiency analysis of the system using data from planet observations is also presented.

In Chapter 7 a new approach for calculation of photometric redshifts is presented and analyzed using ultraviolet data from the Galaxy Evolution Explorer combined with optical data from the Sloan Digital Sky Survey.

In Chapter 8 we conclude this body of work with a brief discussion of the results and a prediction of the sensitivity of the CMB observations with ACT for the 2007 and 2008 observation seasons.

Chapter 2

Optical Design

Meeting the ACT science goals requires a large increase in sensitivity over previous efforts: better than ten microkelvin rms uncertainty in map pixels of three square arcminutes over a hundred or more square degrees. Even with sensitive modern millimeter-wave detectors, large focal planes containing many hundreds of detectors, months of integration time, and careful control of systematics are all essential. This chapter begins with the development and analysis of the optical design (which are modified presentations of the ACT optical design paper [41]). The observation strategy is also discussed, including some of the engineering and observational implications. Using the optical design parameters, calculations are presented of the optical power expected at the arrays as well as of estimated point spread functions and the combined detector and point spread function resolution limit. We end with a discussion of the detector array optical design.

2.1 Telescope and camera overview

The fundamental requirement of the ACT and MBAC optics design is that the telescope and camera must reimage the sky onto three focal planes filled with detectors $\sim$1 mm in size, and that the image be near diffraction-limited. The design is subject to geometric limitations on the size and separation of the mirrors. Control of stray light is also of particular importance, since the ACT detectors are used without feedhorns. Spillover radiation from the ground around the telescope must be prevented from reaching the detectors, and reflections and

Warm Telescope Optics
• Clear aperture (off-axis optics) to minimize scattering and blockage.
• 6-meter primary mirror and 2-meter (maximum) secondary mirror diameters.
• Fast primary focus ($F \leq 1$) to keep the telescope compact.
• Large (FOV $\approx 1.0^\circ$ square) and fast ($F \approx 2.5$) diffraction-limited focal plane.
• Ground loading (due to spillover) much smaller than atmospheric loading.
• Space for structure and cryogenics between primary mirror and Gregorian focus.
• Entire telescope must scan five degrees in azimuth at 0.2 Hz.

Cold Reimaging Optics for MBAC
• Bandpasses 20–30 GHz wide, centered near 148, 215, and 280 GHz.
• Approximately $22' \times 22'$ square field of view in each band.
• Diffraction-limited resolution on three 34 mm by 39 mm arrays.
• Well-defined cold aperture stops to allow maximal illumination of the primary.
• Ghost images[1] due to reflections no brighter than the diffraction-limited sidelobes.

Table 2.1: Requirements and features of the ACT optics.

scattering within the optics must be minimized. These and other systems level requirements and features of our approach are summarized in Table 2.1.

ACT will make simultaneous observations at 148, 215, and 280 GHz to distinguish variations in the primordial CMB from secondary anisotropies such as SZ galaxy clusters and foreground emission from, for example, interstellar dust emission and extragalactic point sources [52]. ACT's receiver, the Millimeter Bolometer Array Camera (MBAC) will contain a 32×32 array of transition edge sensor (TES) bolometers [10, 72] at each of the three frequencies. At the time of writing, the first of these arrays has been built and successfully deployed for the first season of observations (Chapters 5 and 6). The arrays are cooled to 0.3 K by a closed-cycle helium-3 refrigeration system [29, 65]. Because the TES detectors are bolometric, the ACT optics must also have optical filters to define the bandpass for each camera. The filters are supplied by our collaborators, P. Ade and and C. Tucker at Cardiff University [4].

The ACT detectors are squares with 1.05 mm sides and are spaced on a 1.05 mm (horizontal) by 1.22 mm (vertical) grid. In terms of angle on the sky, the detectors at the lowest frequency band are spaced by roughly half a beamwidth apart, $1/2F\lambda$ spacing, and thus fully sample the field of view in a single pointing. This is advantageous for understanding detector and atmospheric noise in mapmaking [45]. All frequencies have between 1/2 to 1.1

$F\lambda$ spacing on the sky. The focal ratio is $F = f/D \approx 0.9$ for all arrays, where $f \approx 5.2\,\mathrm{m}$ is the effective focal length of the telescope and D is the illuminated diameter of the primary mirror. This gives a detector spacing of $\sim 44''$ (horizontal) and $\sim 51''$ (vertical) on the sky (Figure 6.2) – the asymmetry is dominated by the physical construction of the array (Section 5.3). This spacing is roughly half the beam size at 148 GHz and is similar to the expected beam size at 280 GHz. We considered using faster optics at the higher frequencies to achieve $1/2F\lambda$ spacing in all the arrays and to thus maximize mapping speed; however, faster optics would have lower detector coupling efficiency because of the high angles of incidence the arrays require. In addition, the design and data analysis are simplified by having an identical plate scale at all three frequencies.

2.2 Gregorian telescope optics

The two-reflector Atacama Cosmology Telescope was optimized to have the best possible average performance across a square-degree field of view by varying the mirror shapes, angles, and separation. This optimization procedure balances the various classical telescope aberrations for point images against each other. The design process for ACT used both analytic and numerical methods. Numerical methods alone might seem sufficient, because the end result of a global optimization is independent of the starting design. But the telescope parameter space is large and complicated, and we found it critical to enter the numerical stage with a good analytic design. We used the Code V optical design software [80] to optimize the telescope design and to analyze its performance.

Our initial analytic designs met the Mizuguchi-Dragone condition [33, 34, 75] to minimize astigmatism, following the implementation of Brown and Prata [18]. This condition also minimizes geometrical cross-polarization [101]. A comparison of Gregorian and Cassegrain solutions showed that in otherwise equivalent systems, the Gregorian offered more vertical clearance between the secondary focus and the rays traveling from the primary to the secondary mirror. The extra clearance leaves more space for our $\sim 1\,\mathrm{m}^3$ cryostat, so the Gregorian was chosen for ACT.

A simple Gregorian telescope satisfying the Mizuguchi-Dragone condition did not meet the diffraction limited field of view requirement but was taken as the starting point for the numerical stage. The system was optimized by minimizing the rms transverse ray aberration at field points across the focal plane.[2] Six design parameters were allowed to vary: the two conic constants, the tilt of the secondary axis relative to the primary axis, the secondary radius of curvature, and the location and tilt of the focal plane created by the two mirrors. The primary focal length was fixed at exactly 5 m to keep the telescope compact and thereby reduce the angular momentum of the system during scanning. The addition of aspheric polynomial corrections to the mirrors was also explored, but these terms only resulted in slight improvements in the image quality, which did not justify the additional manufacturing and characterization complication of those designs. We found that requiring the major axes (z-axis in Figure 2.2) of the primary and secondary mirror quadratic surfaces to be coaxial did not substantially degrade image quality, so we imposed this constraint to simplify manufacturing and alignment of the telescope.

Our final design approximates an ideal aplanatic Gregorian telescope (in that both our primary and secondary mirrors are ellipsoidal), which has no leading-order spherical aberration or coma in the focal plane [95, 46]. Through numerical optimization, we have improved the image quality of an ideal aplanatic Gregorian across a 1° square field of view by balancing the effects of spherical aberration, coma, and astigmatism. The image quality of the design was primarily quantified using Strehl ratios, or the ratio of the actual height of the point spread function over the ideal height from a diffraction limited mirror of the same diameter. Strehl ratios, S, were estimated by calculating σ, the rms optical path variation over a large bundle of rays, and taking $\ln S \approx -(2\pi\sigma)^2$ [17]. Over a 1.0° square field at the Gregorian focus, the Strehl ratio everywhere exceeds 0.9 at 280 GHz.

In the final ACT design the two mirrors are off-axis segments of ellipsoids. Figure 2.1 contains mechanical drawings, while Figure 2.2 presents a ray trace and shows the z and y axes. The parameters of each mirror are listed in Table 2.2. Both shapes can be described

[2]The transverse ray aberration minimization simply adjusts selected optical parameters to bring rays from a single position on the sky that are traced through different parts of the optical design to a single convergent point in the focal plane. This minimization is done by Code V for a user defined number of points (with optional weight adjustments) in the focal plane simultaneously.

Mirror	z_{vert} (m)	R (m)	K	y_0 (m)	a (m)	b (m)
Primary	0.0000	−10.0000	−0.940935	5.000	3.000	3.000
Secondary	−6.6625	2.4938	−0.322366	−1.488	1.020	0.905
Gregorian focus	−1.6758					

Table 2.2: Atacama Cosmology Telescope mirror shape parameters. The full shapes are given by Equation 2.1, where z_{vert} is the vertex position along the shared axis of symmetry between the mirrors, R is the radius of curvature at the vertex, K is the conic constant, and y_0, a, and b define the used apertures of the mirror surfaces projected into the xy plane. The Gregorian focus is the best-fit focal plane location for objects at infinity. The optimal Gregorian focal plane is slightly tilted around the x-axis.

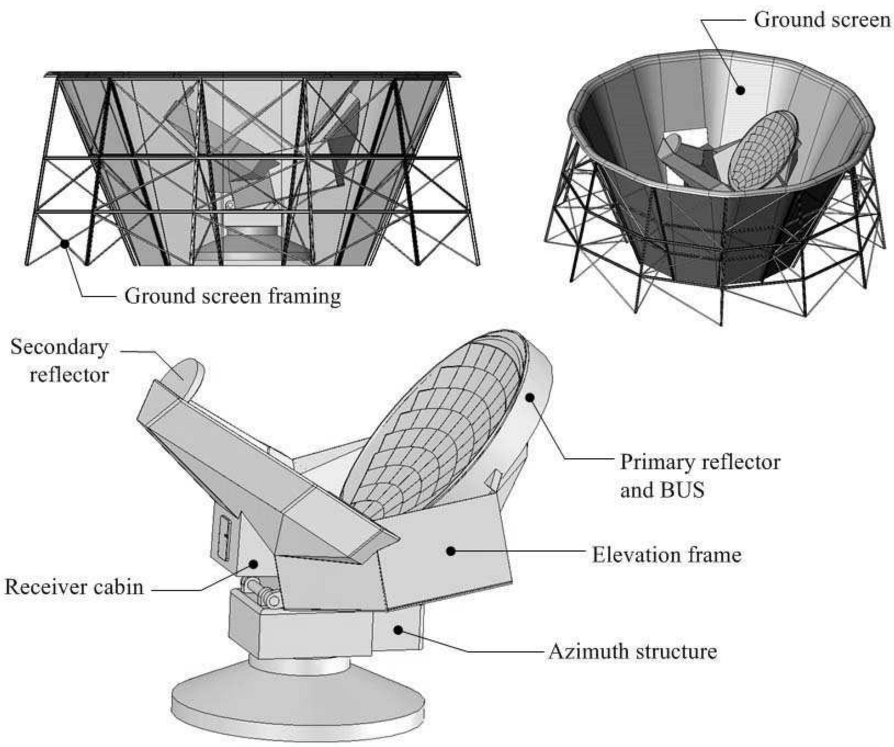

Figure 2.1: The ACT telescope. The mechanical design has a low profile; the surrounding ground screen shields the telescope from ground emission. The screen also acts as a weather shield (though it does channel wind to various parts of the interior). An additional ground screen (not shown) mounted on the telescope hides the secondary and half the primary from the vantage point of the lower diagram (shown in Figure 6.1). This inner ground screen is aluminum that is painted white to reduce solar heating. The primary mirror is $\sim$7 m in diameter including its surrounding guard ring. “BUS” refers to the mirror’s aluminum back-up structure. (Figures courtesy of AMEC Dynamic Structures.)

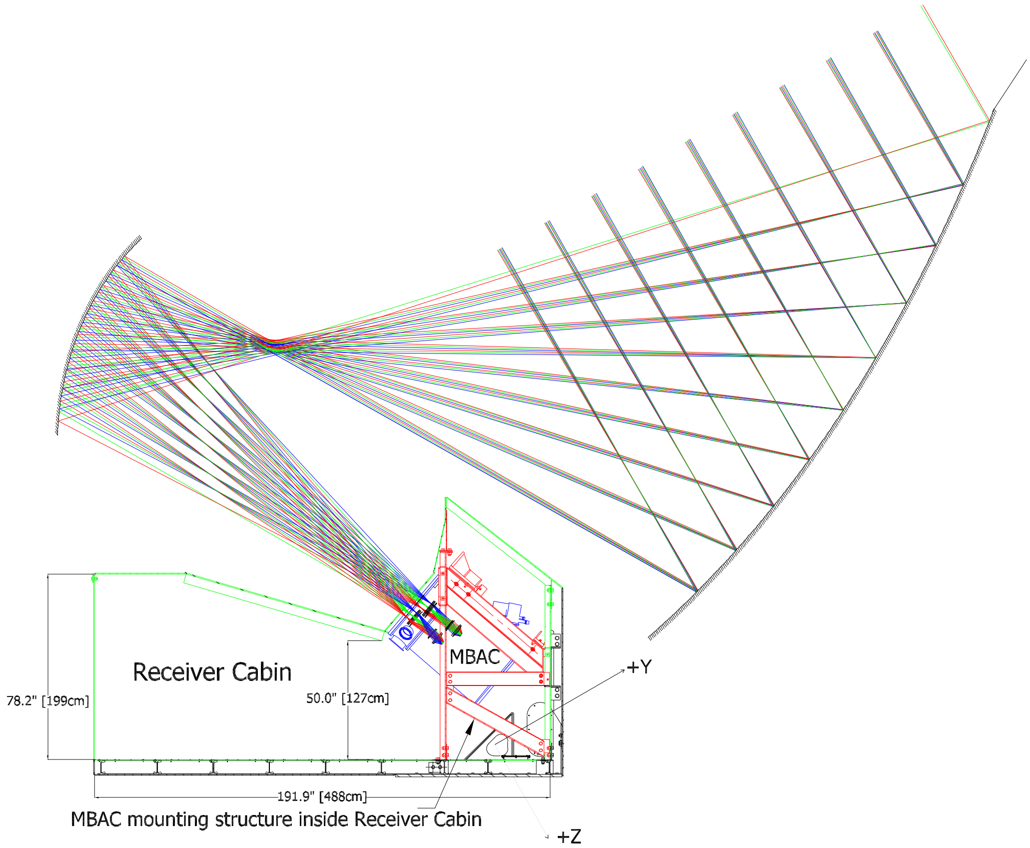

Figure 2.2: Rays traced through the telescope into the MBAC cryostat (color), which is mounted at the far right of the receiver cabin. The rays traced into each of the three cameras are grouped by position on the sky, so that high on the sky is blue, middle is green, and low on the sky is red. This order is maintained at the MBAC windows because it is the second image of the sky; however, each of the three cameras inverts the image one more time before illuminating the detectors (as discussed in Figure 2.5). The stowed position is shown, corresponding to an elevation of 60° (typical observations are acquired at an elevation of ∼50°). The rays are traced from the central, highest, and lowest fields in the 280 GHz camera (higher in the cryostat) and the 215 GHz camera. Both the 215 GHz camera and the 148 GHz camera (not shown) lie to the sides of the $x = 0$ midplane (Figure 2.3), relieving any apparent conflicts between filters and lenses from different cameras. The figure also shows the size and shape of the ACT receiver cabin, as well as the coordinate system of equation 2.1. Figure courtesy of D. Swetz and B. Thornton.

by

$$z(x,y) = z_{\mathrm{vert}} + \frac{(x^2+y^2)/R}{1+\sqrt{1-(1+K)(x^2+y^2)/R^2}}, \tag{2.1}$$

where z is along the shared axis of symmetry (see axes on Figure 2.2), z_{vert} is the vertex position (the primary vertex defines z=0), R is the radius of curvature at the vertex, the conic constant $K = -e^2$, and e is the ellipsoid eccentricity. (For a paraboloid, $K = -1$.) The usable region of each mirror is bounded by an elliptical perimeter. When projected into the xy plane, these boundaries are centered at $(x, y) = (0, y_0)$ and have semi-major and semi-minor axes of a and b in the x and y directions, respectively. The primary projection is circular, with $a = b$.

Diffraction at the cold aperture Lyot stop (in the cryogenic cameras) can lead to systematic errors, particularly if it loads the detectors with radiation emitted by ambient-temperature structures near the two mirrors. To minimize this spillover effect, each mirror is surrounded by a reflective aluminum "guard ring." The rings enlarge the mirror area beyond the geometric image of the aperture stop; they ensure that most radiation reaching the detectors comes from the cold sky, in spite of diffraction at the cold stop.

The ACT design also ensures that there is at least one meter of clearance between any ray approaching the secondary and the top of the Gregorian focal plane used by MBAC. The clearance allows room for a receiver cabin that will protect the cryostat and its supporting electronics from the harsh environment of the Atacama desert.

AMEC Dynamic Structures designed, modeled, and built the telescope's mechanical structure [7]. KUKA Robotics provided the motion control system [62]. The primary mirror and secondary surfaces consist of 71 and 11 aluminum panels, respectively. Forcier Machine Design [40] produced all of the panels. The panels were surveyed one at a time by a coordinate measuring machine and were found to have a typical rms deviation from their nominal shapes of only 2–3 μm. We measure the positions of all the panel surfaces relative to telescope fiducial points with a Faro laser tracking system [38]. Four manually adjustable screw-mounts on the back of each panel then permit precise repositioning. In November 2007, the secondary panels were aligned to 10 μm rms and the primary panels to 30 μm rms.

ACT's compact design allows placement of the MBAC cryogenics near the rotation axis to help maintain refrigerator stability, and it minimizes accelerations during azimuthal scanning of the secondary, which simplifies the mechanical design. The fast Gregorian focus ($F \approx 2.5$) keeps the vacuum window for the detector cryostat from being too large. Figure 2.2 shows the size and shape of the receiver cabin.

2.3 Cold reimaging optics in MBAC

Many possible architectures for the cold optics were studied, including all-reflecting designs, all-refracting designs, and hybrids of the two. We also compared designs of a single camera having dichroic filters to segregate the frequencies against a three-in-one camera design using a separate set of optics for each frequency. The final MBAC design uses only refractive optics instead of mirrors and employs the three-in-one approach for reasons described below.

2.3.1 MBAC architecture

Off-axis reimaging mirrors were studied by combining the equivalent paraboloid approximation [92] with the Mizuguchi-Dragone condition [18], then explored through numerical optimization. They were rejected because the twin demands of image quality and a wide field-of-view led to designs too large to fit in a cubic-meter cryostat. For off-axis mirrors, the compromises between image quality and access to a cold image of the primary were also unacceptable. On-axis mirrors violated the requirement of an unobstructed aperture.

Cardiff University has built dichroic beamsplitting filters as large as 15 cm diameter and metal mesh filters up to 30 cm diameter [4]. Dichroics reflect one band and therefore must be flat to $\sim\lambda/40 \approx 25\,\mu$m at 280 GHz. Our optical designs required dichroics larger than any so far produced, and in addition to the tradeoffs discussed below, we considered their production and mounting too great a risk.

We chose a camera architecture with a separate set of cold lenses for each frequency, eschewing both cold mirrors and dichroic beamsplitters. There are several advantages of this design: 1) anti-reflection coatings and capacitive mesh filters generally have higher

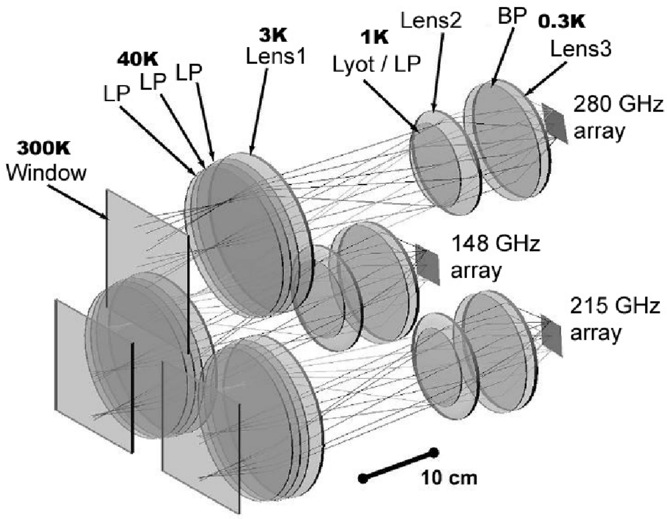

Figure 2.3: The cold MBAC reimaging optics. Each frequency has a similar set of lenses and filters. The 280 GHz silicon lenses are labeled Lens 1 to 3 (with Lens 1 closest to the window). Infrared-blocking and low-pass capacitive mesh filters are all labeled LP; the bandpass filter is labeled BP. A 300 K IR-blocking filter (not shown) is also integrated into the window assembly. The temperatures of the components decrease away from the window as indicated. The bandpass filter, Lens 3, and the array are held at 0.3 K.

transmission – and are easier to optimize – for narrower bands,[3] 2) the mechanical design is simpler, more compact, and easier to align, and 3) the three optical paths are modular and can be removed from the cryostat separately for maintenance or for deploying MBAC in stages. The disadvantage is that each combined optical path and detector array (henceforth camera[4]) observes a different area of sky. Maps made with separated cameras do not completely overlap, though ACT's observing plans mitigate the problem. ACT's scanning motion (Section 2.5) ensures that the 215 GHz and 148 GHz cameras observe most of the same sky region in a single scan, and rotation of the Earth moves fields on the sky from MBAC's lower-elevation cameras to the upper one at 280 GHz (or vice-versa) in less than 15 minutes.

[3]For our single bands $\Delta f/f \approx 0.15$, where f is the central frequency and Δf is the FWHM (Table 2.3, as opposed to $\Delta f/f \approx 0.7$ if all three bands had a common optical path

[4]The optical paths are henceforth referred to as cameras, despite the confusion that might arise between them and the entire Millimeter Bolometer Array Camera which comprises all three of the "cameras".

A triangular configuration was chosen for the three optical paths (Figure 2.3) because it packs the cameras as close as possible to the field center, where the Gregorian image quality is best (as measured by Strehl ratio). The close packing also maximizes the overlap of observations. The 280 GHz camera is centered on the telescope's plane of symmetry because it has the tightest diffraction requirements. The 215 GHz and 148 GHz cameras are placed symmetrically below it, allowing us to use a single design for the two lower-frequency lens sets. All the lenses within each camera are parallel and share one axis. The normals to the focal planes and the bolometer arrays are tilted by 8° or 5° from the common axis of the lenses in their respective cameras.

2.3.2 Camera components

Figure 2.3 shows the optics for all three MBAC "cameras". Separate vacuum windows are used for each camera frequency. The windows are made of ultra-high-molecular-weight polyethylene and have anti-reflection (AR) coatings appropriate to their respective wavelengths. Light entering a camera module passes through an ambient-temperature infrared blocking filter [106] (mounted just inside the vacuum window) and capacitive mesh filters cooled to 40 K (marked "LP" in Figure 2.3); these are infrared blocking filters and millimeter-wave low-pass filters. Together, these filters reduce blackbody loading on the colder stages and block out-of-band leaks in the bandpass filter (marked "BP"). Transmission measurements of the capacitive mesh filter designs selected for our bands are shown in Figure 2.4 and summarized in Table 2.3. A plano-convex silicon lens (Lens 1) creates an image of the primary mirror near lens 2. An assembly holding Lens 2 and two final low-pass filters at 1 K (despite there only being one in the Figure 2.3) contains a cold aperture stop (Lyot stop) at the image of the primary mirror. The last two plano-convex silicon lenses (Lenses 2 and 3) refocus the sky onto the array. The bandpass filter stands between these lenses where the beam is slow, so that band contaminating interference effects within the filters are minimized. Lens 1 is cooled to 3 K; Lens 2 and the associated filters are cooled to 1 K; Lens 3 and the bandpass filter are cooled to 0.3 K. The unobstructed circular aperture of each element is large enough so that the outermost ray that can strike any detector passes at least five wavelengths from the aperture's edge, with the intentional exception of the

Central Frequency (GHz)	148	215	280
FWHM (GHz)	22.6	21.6	29.8
Peak transmission	0.78	0.63	0.66
RJ Central Frequency (GHz)	149	216	281
RJ FWHM (GHz)	21.7	20.7	29.6

Table 2.3: Optical band summary using data from Cardiff University. The full-width half-maximum (FWHM) and peak transmission values from the total transmission curves in Figure 2.4 are given. The central frequency is defined here as the center of the FWHM range, and these values are used to name the three bands in the remainder of this document. The effective bandpass parameters for Rayleigh-Jeans (RJ) sources (Section 2.6) are also given by multiplying the transmission curves by the frequency squared and then solving for the RJ FWHM and central frequencies.

Lyot stop. The entire camera is contained in a light-tight tube with cold black walls to absorb stray light. The walls (including the flat regions of the Lyot stop) are blackened with a mixture of carbon lampblack and Stycast 2850 FT epoxy [35]. All walls between the bandpass filter and the array are held at the coldest available temperature, 0.3 K, because their emission reaches the detectors without filtering [45].

Silicon was chosen as the lens material because of its high thermal conductivity and high refractive index (n=3.416 at 4 K [86, 64]). Pure, high-resistivity silicon ($\rho > 5000\,\Omega{\cdot}\text{cm}$) is necessary to minimize absorption loss. Silicon of very low electrical conductivity and low millimeter-wave loss must be made by the float zone process rather than by the more common (and less expensive) Czochralski process. Float zone silicon is available in diameters up to 20 cm [97], restricting our clear aperture size to 19 cm due to mounting considerations. Alternative materials considered for the ACT lenses included high density polyethylene (HDPE), crystalline quartz, fused quartz, and sapphire. Quartz and sapphire are both more expensive to buy and more difficult to cut than silicon. Optical designs were made using HDPE as a backup option. However, the plastic designs have substantially poorer image quality, a result of making large deflections with a less refractive material. Also, the lower-index HDPE requires much thicker lenses and consequently higher absorption loss.

When using high refractive index materials, such as silicon, anti-reflective coatings are critical. We have developed a method for AR-coating silicon with quarter-wave layers of Cirlex (n=1.85) [66]. Test samples show reflectivities less than 0.5% and transmission

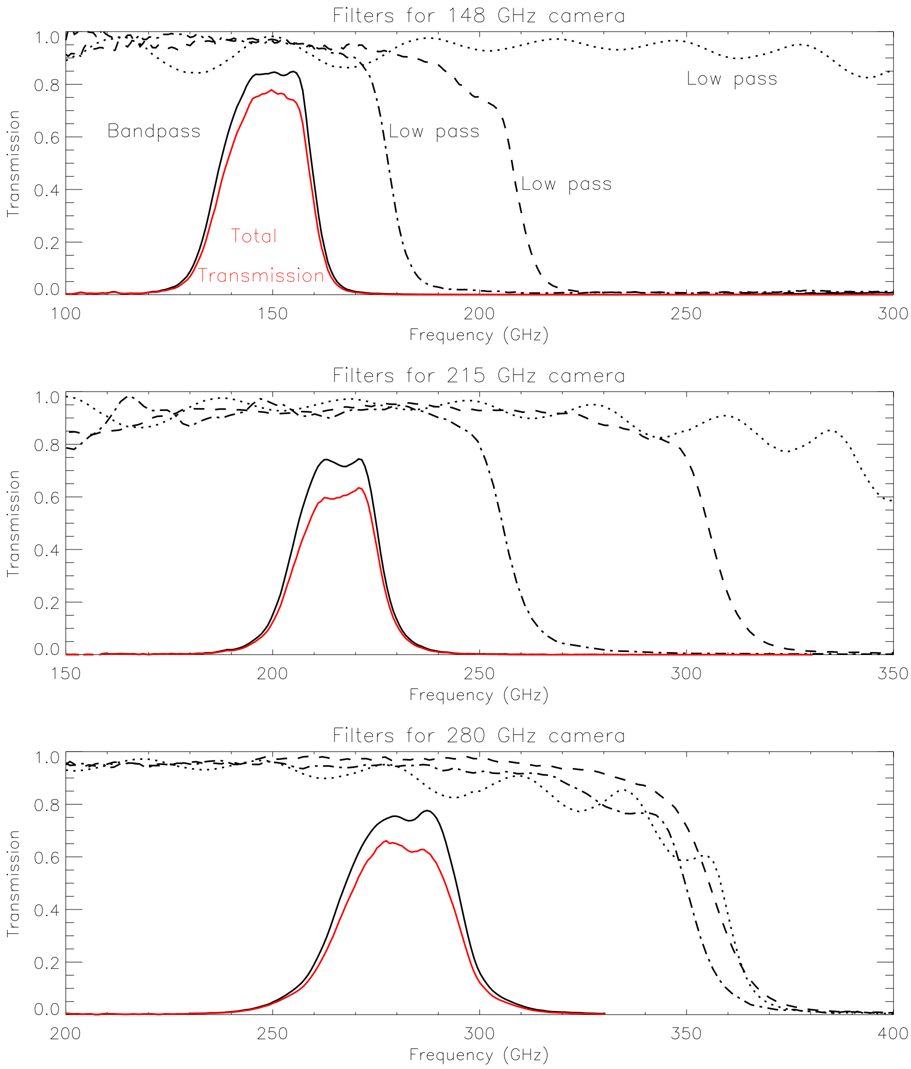

Figure 2.4: MBAC filter data from Cardiff University. Our collaborators at Cardiff U. acquired transmission data for the the low-pass and bandpass filter designs for MBAC (black) using a Fourier transform spectrometer. The combined transmission of the four filters on each plot is shown in red. Details of these total bandpasses are described in Table 2.3, and the total transmission curves are numerically integrated for loading predictions in Section 2.6.

exceeding 95% per sample. We expect that the three lenses in each camera will absorb a combined 15% - 20% of incident light, predominantly in the Cirlex coating (Table 2.4. Because of the corresponding emissivity in the lenses and their coatings, it is necessary to cool the lenses cryogenically, reducing the power they emit.

Plano-convex lenses are used so that only one face of each lens must be machined. The curved figures are surfaces of revolution of conic sections plus polynomial terms in r^4, r^6, r^8 and r^{10} to give maximal design freedom. As the lenses were diamond turned on a computer-controlled lathe, there was no cost penalty for adding axially symmetric terms to the lens shapes. The curved and flat surfaces of each lens were oriented so as to minimize the calculated amplitude of reflection-induced secondary ("ghost") images [41]. In particular, Lens 1 and Lens 2 have curved surfaces facing the dewar window, while the curved surface of Lens 3 faces the detector array.

2.3.3 Design procedure

The Gregorian telescope design was held fixed during the cold optics design process, while the lens shapes and positions were varied. The 280 GHz and 215 GHz cameras were optimized separately. Because the 148 GHz and 215 GHz cameras are placed symmetrically about the telescope's symmetry plane—and because there is no evidence for appreciable dispersion in silicon at millimeter wavelengths—the two design problems are mathematically equivalent; a single camera design was used for both.

The optimization method for the camera was similar to the method used to design the Gregorian telescope, but with additional constraints. Most importantly, we required a faithful image of the primary mirror in each camera at which to place a Lyot stop. This image quality was quantified by tracing rays from all field points through four points on the perimeter of the primary mirror. The rms scatter of such ray positions where they crossed the Lyot stop plane, projected onto the radial direction, was included in the merit function. Thus, an astigmatic image of the primary elongated tangent to the stop was not penalized, but a radial blurring was. This additional parameter measures the radial ray aberration at the aperture stop.

A second constraint was the effective focal length, which was fixed at 5.2 meters (to maintain our target $\sim 22'$ across each detector array) by checking the plate scale for points near the center of each sub-field. Finally, we found it necessary to require that the chief ray[5] from each field strike the focal plane at no greater than a 8° angle, which keeps the tilt of the detector plane small to maximize absorption of radiation in the detectors. This low-tilt requirement also produces an approximately telecentric image, meaning that the chief rays for all field points on the sky are approximately parallel at the focal plane. A telecentric image has the advantage that the plate scale does not depend to first order on the linear positioning of the detector array relative to the lenses.

The optimizer varied up to 27 parameters in each design: three lens positions along the optic axis, the position of the Lyot stop and its tilt, the detector position and tilt, and the lens shapes (parameters included curvature, conic constant, and four aspheric polynomial terms). We found that tilting the Lyot stop surface did not offer enough advantage to justify the added mechanical complication and thereafter did not allow it to tilt, reducing the number of parameters to 25. The center thickness of each lens was set by requiring the edge to be at least 2 mm thick for mechanical strength; the center thickness was not varied by the optimizer. We did not constrain the dimensions of the elliptical Lyot stop. Striking the right balance in the merit function between optimizing the image of the sky at the detector plane and the image of the primary at the Lyot stop was challenging. Our most successful approach to meeting both goals simultaneously was to make two optimizing passes. In the first pass, the Lyot stop image was given large weight. In the second, it was given zero weight, but all parameters that affect the stop image were fixed (including shape and placement of L1 and placement of the stop).

The MBAC cold optics design is somewhat unusual in its use of AR-coated silicon lenses at cryogenic temperatures. For this reason, we have a prototype 145 GHz receiver (CCam, the "column camera") with a cold optics design based on the same principles as MBAC. We tested CCam with both a 1.5 m telescope and more recently with ACT, and successfully used it to observe astronomical sources [3, 67, 77], giving us confidence in the soundness of the general design of MBAC.

[5]For each field point on the sky, the chief ray is the ray that reflects off the center of the primary mirror aperture.

2.4 Design evaluation

The full optical design was studied using both ray-tracing and physical optics. Many analyses were first developed for the Penn Array Receiver at the Green Bank Radio Telescope [30] and implemented for ACT by S. Dicker. We present some of the ray-tracing analysis here, while results of additional analyses including spillover, ghosting, and tolerancing can be found in the ACT optical design paper [41].

The median Strehl ratios across the fields in the final design are calculated to be 0.991, 0.980, and 0.983, at 148, 215, and 280 GHz, respectively (Figure 2.5). The lowest Strehls corresponding to any of the 225 field points tested in each camera are 0.971 (148 GHz), 0.939 (215 GHz), and 0.958 (280 GHz). These Strehl ratios establish that all points in the field of view will be diffraction-limited.

A small amount of field distortion results from reimaging such a large focal plane (Figure 2.6). One effect is anamorphic magnification, or horizontal image stretching: the plate scale in all cameras is $6.8'$ per cm for vertical separations, but for horizontal separations it is only $6.4'$ per cm in the 280 GHz camera and $6.6'$ per cm in the others. The other effect is a shearing of the image in the 148 and 215 GHz cameras; lines of constant elevation are twisted by approximately $1.4°$ with respect to horizontal rows of detectors. There is no appreciable rotation of lines of constant azimuth. These distortions will be taken into account in making CMB maps from the data, but at the predicted levels, they will not complicate our observations.

2.5 Observation Strategy

CMB experiments deliberately modulate their sensitivity to cosmic signals in order to reduce the impact of drifts in detector response, such as $1/f$ noise. Typical modulation methods involve using an optical chopping mirror or scanning the entire telescope in azimuth. In either case, the telescope beam moves rapidly back-and-forth on timescales faster than the $1/f$ knee of any low-frequency noise. We chose the scanning method, because it avoids the design complications and the complex scan-synchronous signals of a chopping flat, such as changing primary beam shape, ground pickup pattern, and mirror emission. Our nominal

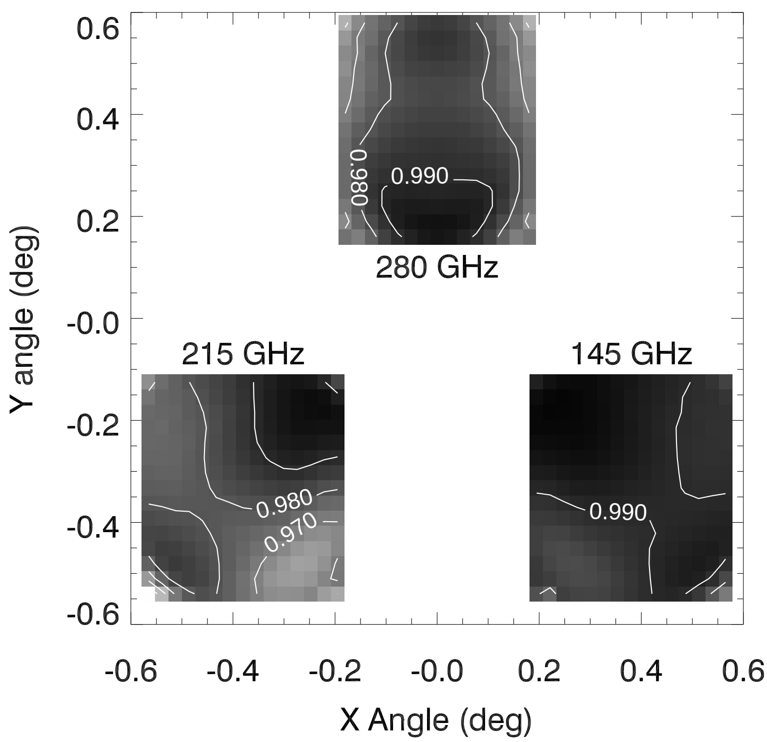

Figure 2.5: Strehl ratio at points in the three ACT fields, as a function of field angle on the sky. The rectangular aspect ratio of the detector array is primarily responsible for the departure from square fields, but anamorphic field distortion also contributes. The figure also indicates the relative spacing and size of the three fields. The median Strehl ratios are 0.983, 0.980, 0.991 for the 280, 215, and 148 GHz cameras. This figure is also a representation of a projection of the sky onto the MBAC dewar windows as viewed from the secondary. The orientation relative to the sky is discussed in Appendix A. (Figure courtesy of J. Fowler.)

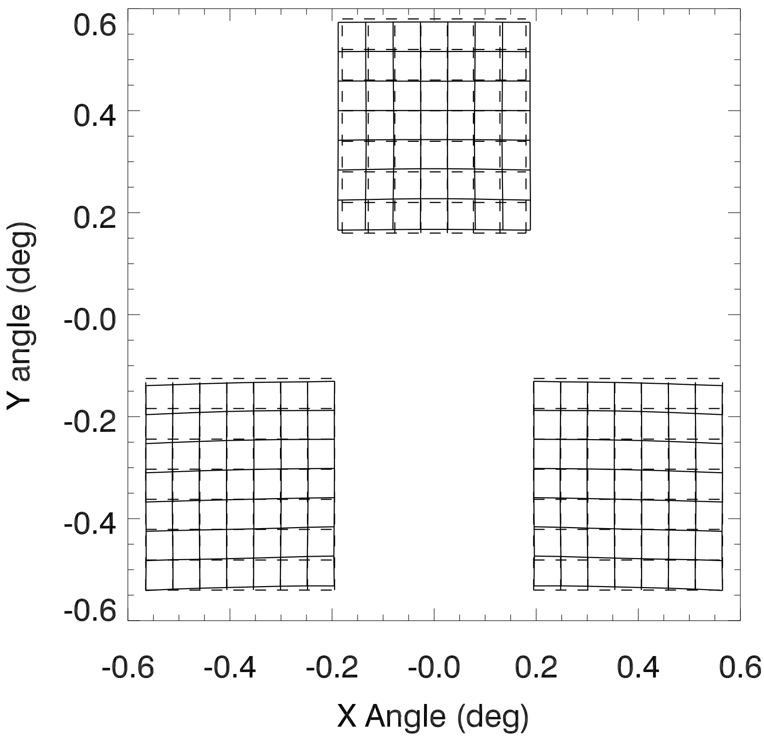

Figure 2.6: Field distortion for the ACT optical design. The dashed square boxes depict a notional rectangular grid of field points on the sky, without distortion; the solid lines indicate the image of the same grid after it is refocused at the detectors (assuming the nominal 5.20 m effective focal length). (Figure courtesy of J. Fowler.)

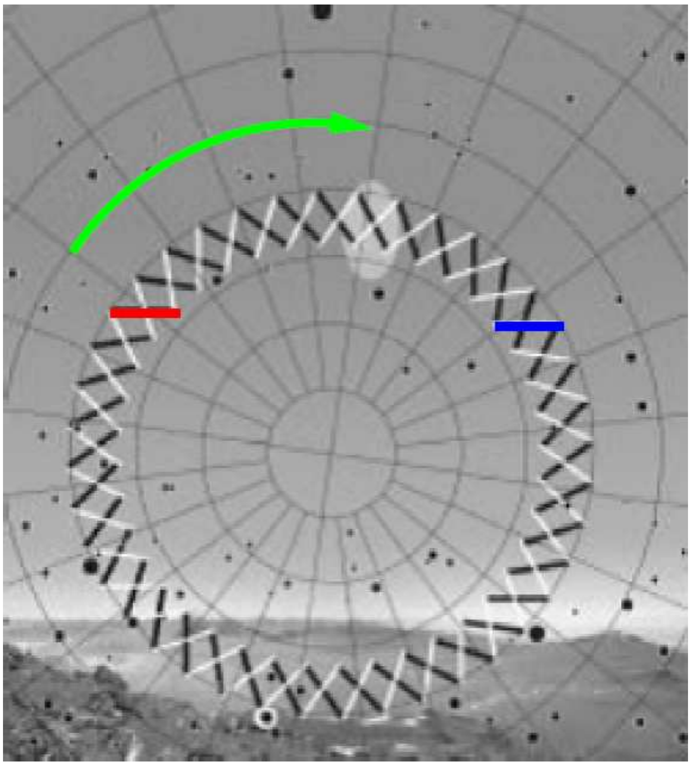

Figure 2.7: Azimuthal scanning strategy with cross-linking. Azimuthal scans are executed at a constant elevation both east and west of the south celestial pole (red and blue horizontal lines). The rotation of the sky (green arrow) causes this simple scanning strategy to map a continuous circular region. By scanning at a different azimuth and elevation from the south celestial pole, the east and west scans cross the region at different angles (dark and light lines). These cross-linked measurements are important for removing $1/f$ induced stripes in the resulting maps. (Figure courtesy of J. Klein and T. Marriage.)

observing mode is to scan the 50-ton telescope in azimuth over a few degree range repeating with a period of $\sim$5 seconds, while holding the elevation fixed (typically at $\sim 50°$). By observing in this mode at a constant declination both west and east of the south celestial pole, the observed regions can be cross-linked on the sky (Figure 2.7), which has been shown to be critical for removing $1/f$ induced stripes in sky maps by a number of experiments [13, 102, 115]. Observing at fixed elevation ensures that the large gradient in atmospheric emission enters each detector as a constant addition, not as an AC term synchronized with the signal. To maintain a constant speed for as much of the scan as possible, we aimed to limit the turn arounds to brief acceleration periods of 300 ms at either end of each scan.

The azimuthal scanning motion places considerable rigidity requirements on the telescope structure. Extensive effort has gone into ensuring the best possible performance for the scanning of the telescope, a difficult task given its size and weight ($\sim$50 tons). The telescope meets the scanning target of $\pm 2.5°$ at an angular speed of $2.0°$/s with a turn-around time of 300 ms [41].

2.6 Optical Performance Predictions

2.6.1 Optical loading

With bandpass data and solid angle calculations we can predict the change in power at the detectors from a thermal source, such as a liquid nitrogen load or the CMB. Comparing these predictions with the measured response of detectors allows computation of the efficiency of the bolometer absorption (Sections 5.3.2 and 6.4) as well as conversion of detector noise measurements into CMB temperature units (Section 5.5).

Here we calculate the load power from a uniform thermal source that fills the optical aperture. The conservation of throughput, or area times solid angle, $A\Omega$, in a lossless optical system indicates that the same optical power is predicted at the detectors whether a uniform source illuminates the primary mirror, the dewar window, or the detector array [95]. The throughput can be calculated at the detector array using the area of a single detector, $A = 1.10\ \mathrm{mm}^2$, and ray-tracing results to estimate the solid angle,

$$\Omega = \int_0^{2\pi} \int_0^{\theta_h} \sin(\theta)\cos(\theta)\ d\theta\ d\phi = \frac{\pi}{2}[1 - \cos(2\theta_h)], \tag{2.2}$$

where θ_h is the half-cone angle of illumination at the array (Table 2.4).[6] The cosine term in the integral is due to the planar nature of the aperture [95], which in this case is the detector area.

[6] Ray-tracing results indicate that there are variations in θ_h at the ± 5 - 10% level across each array, with the maximum θ_h near the center of each array. We plan to model and calibrate out these differences and any other variations between bolometers using point source measurements as discussed in Section 6.4.

The throughput calculation is combined with the Planck distribution,[7] which we write as the intensity density per unit frequency, $d\nu$,

$$I(\nu)d\nu = \frac{2h}{c^2}\frac{\nu^3}{e^{h\nu/kT}-1}\,d\nu, \tag{2.3}$$

where ν is the radiation frequency, T is the temperature of the thermal source in Kelvin, h is Planck's constant, c is the speed of light, and k is Boltzmann's constant [116]. To predict the total blackbody power on an individual detector as a function of temperature, $P_{bb}(T)$, the intensity density is numerically integrated over the bandpass data (Figure 2.4). The integration is done by summing each measurement frequency bin, i, multiplied by the transmission coefficient of the bandpass in that bin, η_{b_i}, and the width of the frequency bins, $\Delta\nu$; the sum is then multiplied by the optical efficiency coefficients, η_{opt} (Table 2.4), and the throughput,

$$P_{bb}(T) = A\ \Omega\ \eta_{opt}\sum_i \frac{2h}{c^2}\frac{\nu_i^3}{e^{h\nu_i/kT}-1}\ \eta_{b_i}\ \Delta\nu. \tag{2.4}$$

In Figure 2.8, we show P_{bb} for the three frequency bands over different temperature ranges. At large T the Rayleigh-Jeans equation is a good description of blackbody radiation, and P_{bb} is approximately proportional to T. As we approach the temperature of the CMB, $T = 2.73$ K, the Rayleigh-Jeans approximation breaks down, and the Planck distribution, equation (2.3), is required to predict P_{bb} (Figure 2.8). Since calibration measurements are typically made using point sources or loads in the Rayleigh-Jeans limit, we provide the predicted load from Rayleigh-Jeans sources and the conversion factor from Rayleigh-Jeans to CMB temperature units, $\delta T_{CMB}/\delta T_{RJ}$, in Table 2.4.

During observations, the precipitable water vapor (PWV) in the atmosphere will dominate the changes in loading on the detectors and affect the atmospheric opacity. The atmospheric emission can be modeled as a blackbody in each of our bands as described in the thesis of T. Marriage [71]. By fitting the conversions between zenith PWV and effective atmospheric blackbody temperature at an observation elevation of 45° [71], we predict the loading on the detectors as a function of zenith PWV (Figure 2.8). We will compare the

[7] A critical assumption for these predictions is that the source can be treated as a blackbody radiator at temperature T across the bandpass of each camera (Figure 2.4).

Frequency (GHz)	148	215	280
θ_h (deg)	33.6	33.6	33.3
Ω (sr)	0.96	0.96	0.95
η_{opt}	0.855	0.835	0.815
$\delta P_{bb}/\delta T_{RJ}$ (pW/K)	0.110	0.182	0.426
$\delta T_{CMB}/\delta T_{RJ}$	1.72	2.95	5.59
P_{opt} (pW)	0.3	0.6	1.5
P_{sky_0} (pW)	0.4	0.8	4.4
$\delta P_{bb}/\delta$PWV (pW/mm)	0.73	2.5	8.9

Table 2.4: Predicted optical loading parameters for the detector arrays (ignoring decreases caused by the detector absorption efficiency; see Figure 2.11). The half angle, θ_h is estimated from ray tracing results and varies across the arrays at the 5% – 10% level. The solid angle, Ω, is calculated from equation (2.2). A combined efficiency, η_{opt}, for the dewar window transmission (0.995 was assumed) and the six anti-reflection coatings on the silicon lenses (estimated by J. Fowler) is an input for the loading estimates. The predicted change in optical power incident on a bolometer from a Raleigh-Jeans source that fills the optical aperture, $\delta P_{bb}/\delta T_{RJ}$, is useful for efficiency calculations. The conversion between loading from sources at the temperature of the CMB versus in the Raleigh-Jeans temperature regime, $\delta T_{CMB}/\delta T_{RJ}$, allows us to estimate noise levels in CMB temperature units. The estimated background loading from emission of the optics, P_{opt}, is calculated using the analysis in the thesis of T. Marriage [71] combined with the solid angle estimates presented here. The background sky loading at PWV = 0 mm, P_{sky_0}, and the predicted change in optical power incident on a bolometer from atmospheric emission when observing at 45° elevation as a function of zenith PWV, $\delta P_{bb}/\delta$PWV, come from the fits in Figure 2.8.

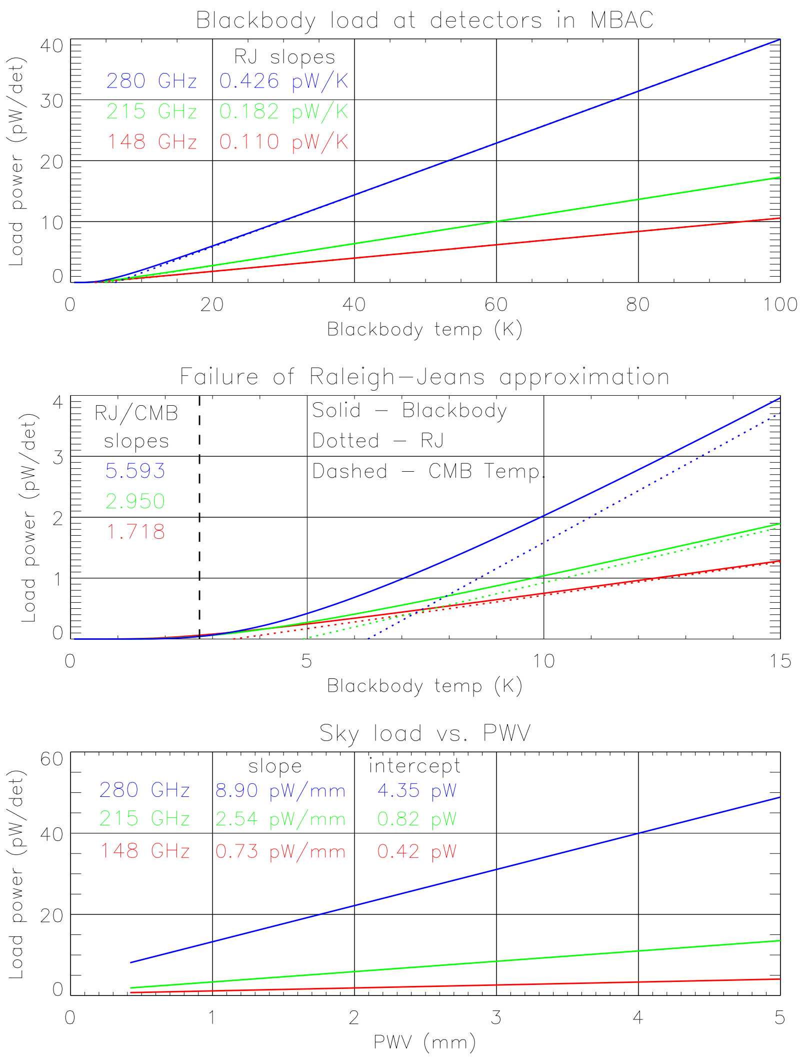

Figure 2.8: Predicted optical power incident on detectors in MBAC as a function of blackbody temperature and PWV. *Top*: The Raleigh-Jeans (RJ) approximation is good in all bands above ∼30 K. *Middle*: At lower temperatures the RJ approximation fails, but we can use the ratio of the RJ slope to the slope at the CMB temperature for conversion from calibrations that use RJ sources (such as planets) into CMB temperature units. *Bottom*: Predicted load on detectors from the atmosphere at an observation elevation of 45° as a function of zenith PWV, which is based on the atmospheric emission calculations in the thesis of T. Marriage [71]. These loading predictions combined with estimated loading from the optics (Table 2.4) [71] are used for selection of detector saturation powers (Section 3.3.3) and will be used for calibration of atmospheric opacity. Note: The load predictions are proportional to optical efficiency and are plotted for 100% detector efficiency.

detector performance to meteorological measurements of PWV, such as those measured by the ALMA collaboration's radiometers, and develop a model to account for changes in atmospheric opacity throughout the observation season. We also use these estimates combined with the background loading estimates from the optics (Table 2.4) to select target bolometer saturation powers as discussed in Section 3.3.3.

2.6.2 Preliminary beam model

Diffraction limits the resolution of the ACT optical design. Because of this and our prediction of nearly uniform illumination across the primary mirror [41], we can describe a beam model by averaging the point spread function (PSF) for a circular aperture across each of the bandpasses. The intensity of the PSF at a focal plane for a single wavelength, λ, can be written in terms of the first-order Bessel function, J_1,

$$I(r) = \frac{E\pi D^2}{4\lambda^2}\left(\frac{2J_1(\pi r)}{\pi r}\right)^2, \tag{2.5}$$

where E is the total energy incident on the circular aperture and r is the radius in the focal plane in units of $F\lambda$ [17]. $F = f/D$ is the focal ratio, or the effective focal length, $f \approx 5.2$ m, divided by the illuminated diameter of the primary mirror, $D \approx 5.8$ m. This can be integrated over the ACT bands, by summing the product of the PSF and the transmission coefficients of the bandpasses (dashed curves in Figure 2.9).

The detectors in the ACT arrays are squares with 1.05 mm sides, which ranges between 0.5 and 1.1 $F\lambda$ for the three frequencies. A first-order correction to the band-averaged PSF is to convolve the square detector geometry with the beam in each frequency band. Figure 2.9 shows the result of numerical convolutions from integrating the PSF over a square grid of points that represent the detector pixel, then repeating the integration as a function of radius from the PSF peak. The convolved models are representative of what is measured by detector pixels as the telescope scans across a point source, such as a planet. The model for the 148 GHz array is used to to explore the relative intensity across the array from a point source centered on a single detector in Figure 2.10. The logarithmic-scale plot shows how this PSF model spreads the illumination from a point source across most of the array. The linear-scale plot shows how the image of a point source is spread out across a

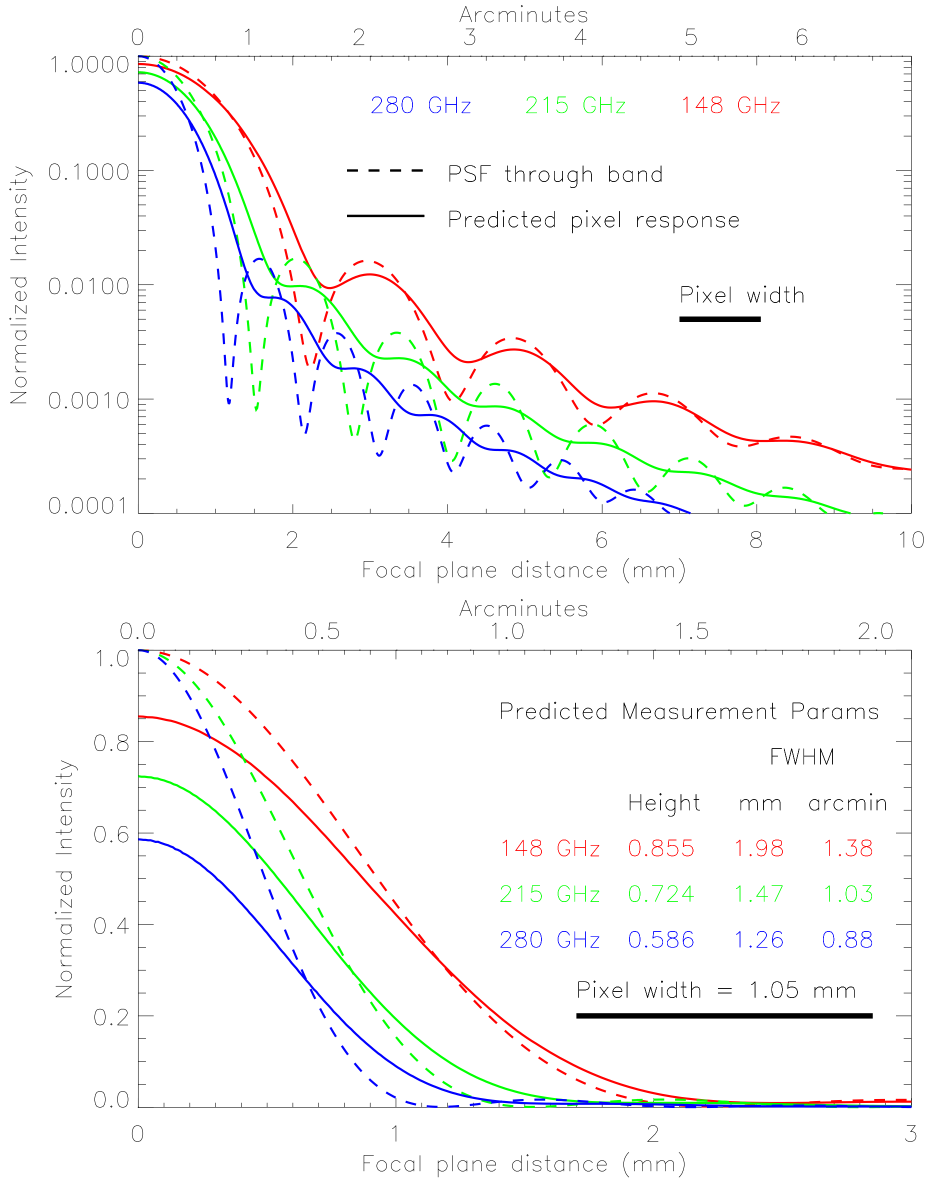

Figure 2.9: Normalized PSFs based on the bandpass centers and widths (dashed), then convolved with the square pixel to estimate the detector response to scanning across a point source (solid). The PSFs are plotted in terms of the distance from the peak on the focal plane (lower axis) as well as the angular distance on the sky (upper axis). *Top*: The logarithmic intensity of the convolved PSF clearly shows the smoothing caused by the detector size. *Bottom*: The linear intensity shows the decrease in peak height and widening of the FWHM from the detector size.

Frequency (GHz)	148	215	280
Coupling layer thickness (μm)	50	40	25
Distance to bolometers (μm)	110	55	45

Table 2.5: Silicon coupling layer thicknesses and target distance to bolometers [36].

3×3 detector area, indicating that the diffraction-limited response of the telescope is fully sampled in a single pointing.

In Chapter 6 this beam model is used to study the temporal response of detectors to point sources and compare the measured response to other measurements of the detector time constants. It is also used to explore the window function and estimate the optical efficiency of the detector array.

2.7 Detector Optical Design

Maximizing the efficiency of the bolometers is important for both increasing the ratio of signal to bolometer noise and minimizing reflections off the array that could otherwise cause "ghost" images [41]. Reflections are minimized by matching the impedance of the array to free space, and the efficiency is maximized through optimization of the bolometer absorber impedance. To optimize these impedances, multiple layers of silicon and ion-implanted absorber material are used. As radiation is focused onto the bolometer array, it first encounters a thin silicon coupling layer, then a vacuum gap and the bolometer ion-implanted absorber, followed by a silicon backbar, which is terminated with another ion-implanted absorber (Figure 5.6). The thickness of the silicon coupling layer and the distance between it and the bolometers were optimized for each frequency band (Table 2.5) [36]. Figure 2.11 shows the predicted efficiency of the bolometers in the 148 GHz array as a function of distance between the silicon coupling layer and the bolometers. With optimal alignment, the model predicts that reflections can be as low as a few percent and the efficiency as high as $\sim$75–80%. In Section 5.3 we present the design and procedure that were developed to control this critical distance for the 32 independent bolometer columns

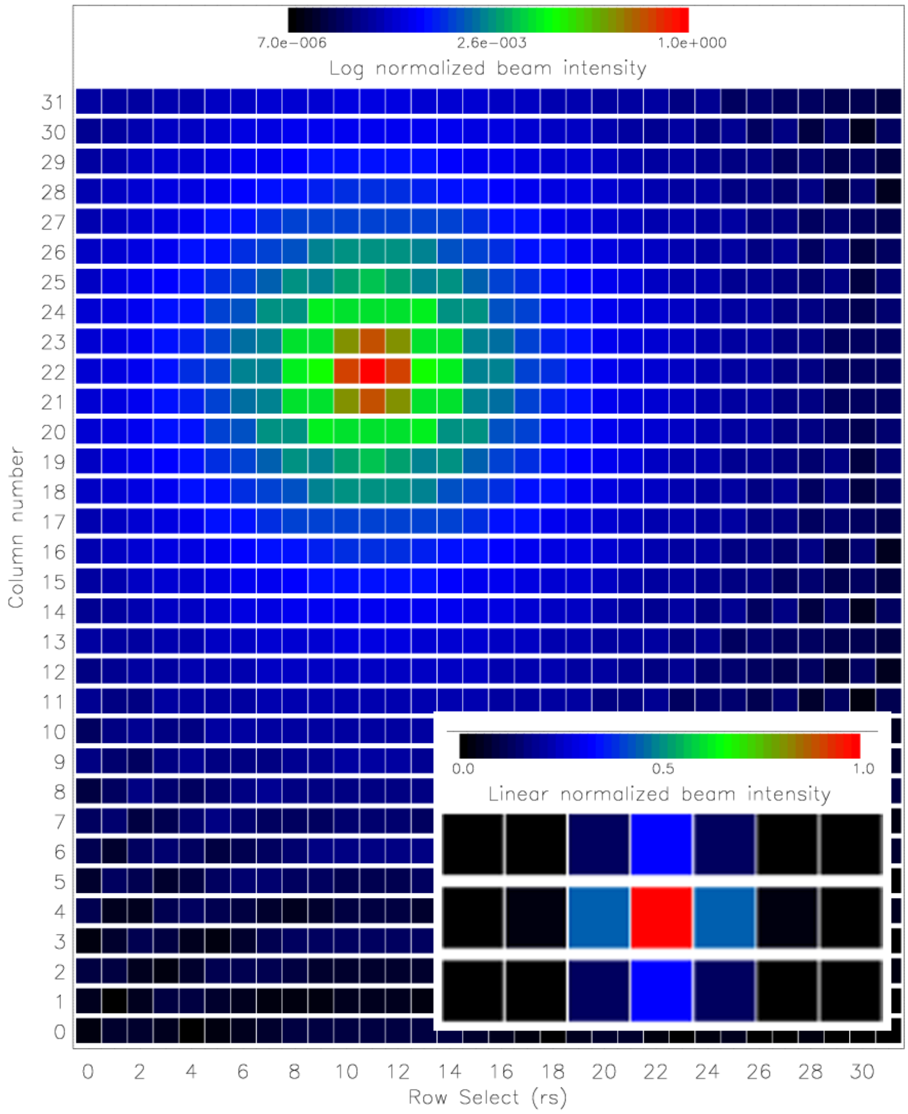

Figure 2.10: Normalized beam intensity on the 148 GHz detector array. The convolved beam model in Figure 2.9 is centered on row select 11, column number 22 and plotted as a function of position on the array in logarithmic units, and (*inset*) in linear units. This simple beam model is rotationally symmetric; however, the asymmetry between the spacing of the horizontal detector "columns" and the vertical detector "rows" causes the shape of the plotted beam to appear slightly asymmetric. The linear intensity plot (*inset*) shows how a 3×3 group of detectors simultaneously measure the diffraction-limited response to a point source. (Note: The orientation of this plot and all similar plots is as though we are looking through the back of the detector array out towards the sky as discussed in Appendix A.)

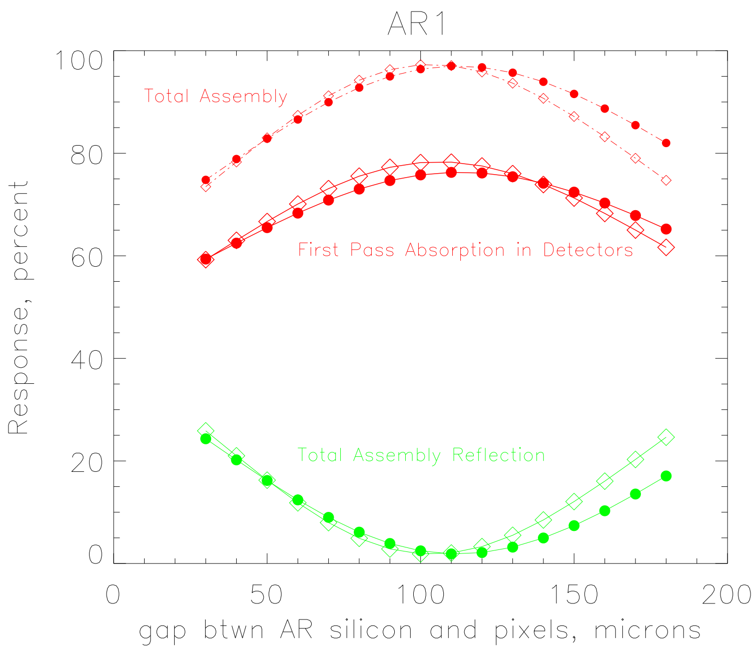

Figure 2.11: Predicted bolometer absorption versus distance to silicon coupling layer for the 148 GHz array. The predicted absorption and reflection are plotted for the two different polarizations (circles and diamonds) incident on the array. These calculations were done assuming infinite planes and an angle of incidence of 20°. (Figure courtesy of S. Staggs.)

as well as the results of efficiency measurements that test the optical design of the first detector array.

Acknowledgements

The design of the ACT telescope and a preliminary design for the MBAC receiver were realized through collaboration with numerous people, especially J. Fowler, A. Aboobaker, L. Page, S. Dicker, M. Devlin, and J. Klein. The design for ACT was finalized with many of the authors on the ACT optical design paper [41]. P. Mauskopf helped confirm that that we could not meet the MBAC design requirements using cold reflective optics. The final optical design for MBAC was optimized by J. Fowler with critical input from S. Dicker, D. Swetz, B. Thornton, and J. Klein. Most of the analysis of the final MBAC design was completed by S. Dicker and J. Fowler. A large number of collaborators are responsible for working with AMEC to ensure that the design was implemented properly, the telescope was delivered and installed in Chile, and for aligning the mirrors. The convolution of the PSF beam model with the square detectors was originally explored by D. Chuss and E. Wollack. The innovative detector optical design would not have been possible without inspired ideas from D. Chuss, H. Moseley, and E. Wollack. Implementation and optimization of the design were developed by L. Page and then S. Staggs with additional contributions from B. Besson, T. Essinger-Hileman, and J. Fowler.

Chapter 3

Detector Development and Characterization

The three MBAC cameras each comprise a 32×32 array of transition-edge sensor (TES) bolometers [68, 54], and are read out by time-domain multiplexing electronics [21, 91]. Here we describe a theoretical model for isothermal voltage-biased TES bolometers (closely following the discussion in Irwin and Hilton [54]) and introduce the multiplexed DC Superconducting Quantum Interference Device (SQUID) system used to measure the detectors. We also discuss the selection of detector parameters for the arrays and the screening and assembly of the components that make up a column of detectors, which is an extension of the discussion in the ACT first light paper [79]. Finally, we present the characterization procedure used to measure the properties of each of the 32 pixel columns of bolometers for the arrays, and the various failure modes that have been encountered and repaired. The data discussed in this chapter were acquired in the Column Camera (CCam) prototype instrument [3, 67] and the Super-Rapid Dip Probe (SRDP) testing dewars [71, 72, 79].

3.1 TES Bolometer Theory

During operation, the bolometers are biased onto their superconducting transition and remain there because of negative electrothermal feedback. When a positive CMB temperature fluctuation increases the photon loading, P, on the bolometer, its temperature increases,

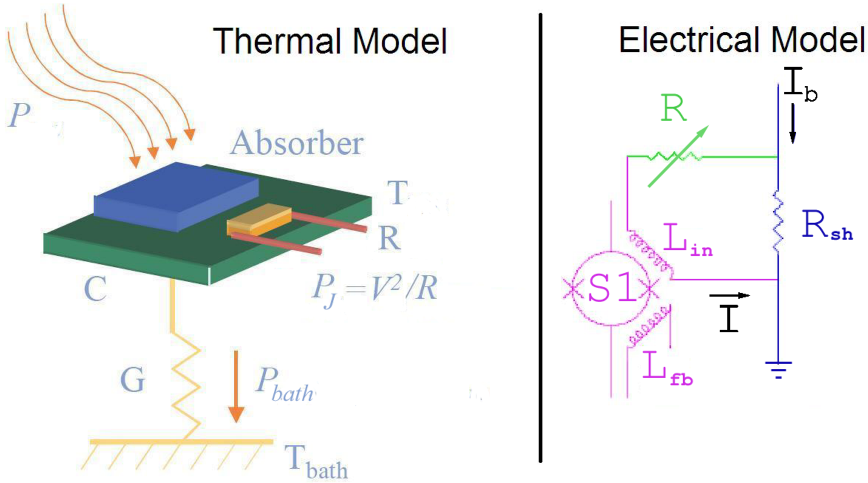

Figure 3.1: First order models of TES bolometers. *Left*: The thermal model for a TES bolometer. (Modified version of figure from D. Benford.) *Right*: The TES electrical model, including the stage 1 (S1) DC SQUID for measuring current through the TES. Each color in the electrical model represents a different microfabricated chip (Figure 3.4).

thereby raising the TES resistance. The detectors are approximately voltage biased, V, by applying a DC current bias, I_b, across the parallel combination of the TES resistance, R, and the shunt resistance, R_{sh}, where $R_{sh} \ll R$ (Figure 3.1), so that the Joule heating, $P_J = V^2/R$, decreases as R rises. This negative electrothermal feedback cancels the increase in photon power through a reduction in current [68, 54]. The change in current is the signal we measure using a DC SQUID [104]. Figure 3.1 provides schematics of the thermal and electrical operation of a TES bolometer.

The pop-up detector (PUD) bolometers [11] have weak thermal links, which also act as supporting legs, connecting them to the surrounding silicon cards. The legs' net thermal conductance, G (Figure 3.1), determines the power, P_{bath}, that is carried between the bolometer at temperature T and the thermal bath, T_{bath}. We can assume a power law dependence for the heat flow [54]

$$P_{bath} = K(T^n - T^n_{bath}). \tag{3.1}$$

The saturation power of the detectors, P_{sat}, is simply P_{bath} at the superconducting transition temperature, T_c,

$$P_{sat}(T_{bath}) = K(T_c^n - T_{bath}^n), \tag{3.2}$$

Since the superconducting TES transitions are narrow,[1] we also define the thermal conductance at T_c:

$$G \equiv dP_{bath}/dT|_{T_c} = nKT_c^{n-1}, \tag{3.3}$$

where n and K are constants that are fit to bolometer measurements [71]. If G or P_{sat} are too low the detectors will saturate and be useless, and if G and T_c are too high thermal noise will dominate the detector signals, decreasing sensitivity to the CMB. By modeling the predicted sky loading at our observing site (Section 2.6) and carefully minimizing the loading from the optical components, we can estimate the P_{sat}'s that will be required for each frequency band. Because of variations in the optical loading from the sky, the optimal saturation power will in fact vary from night to night. In Section 3.3.3 we discuss the approach that was used to optimize the saturation power for observations.

Our observation strategy (Section 2.5) guides us to understand the bolometer response on a range of time scales. We can explore the temporal response by solving the coupled thermal and electrical differential equations:

$$C\frac{dT}{dt} = -P_{bath} + P_J + P, \tag{3.4}$$

where C is the bolometer heat capacity, and

$$L\frac{dI}{dt} = V - IR_{sh} - IR(T, I), \tag{3.5}$$

where L is the total inductance in the loop (which includes L_{in} in Figure 3.1), V is the Thevenin equivalent voltage, $V = I_b R_{sh}$, I is the electrical current through the TES, and $R(T, I)$ is the TES resistance, described explicitly as a function of both its temperature and current [54].[2] We could also include parasitic (series) resistance in the TES loop, R_{par}, in these equations by simply substituting $R_L = R_{sh} + R_{par}$ for R_{sh}, however we have found $R_{par} \ll R_{sh}$ for our detector columns [71], so we ignore R_{par}.

[1] The transition widths, ΔT_c, are typically smaller than $T_c/100$.

[2] Since the TES is a superconductor, its temperature T (and thus R) is also a function of magnetic field [104]. The TES and SQUID responses to magnetic fields are explored in Section 4.1

To solve the coupled equations (3.4) and (3.5), we assume the small signal limit and expand the variables about their DC levels (denoted with subscript '0') to linear order in δT, δI, and δV. We can use G to expand about the heat flow to the bath

$$P_{bath} \approx P_{bath_0} + G\delta T = P_{J_0} + P_0 + G\delta T, \tag{3.6}$$

where $\delta T \equiv T - T_0$. The TES resistance can be similarly expanded

$$R(T,I) \approx R_0 + \left.\frac{\delta R}{\delta T}\right|_{I_0} \delta T + \left.\frac{\delta R}{\delta I}\right|_{T_0} \delta I, \tag{3.7}$$

where $\delta I \equiv I - I_0$. It is common practice with superconductors to express $\delta R/\delta T$ in terms of the unitless logarithmic sensitivity,

$$\alpha_I \equiv \left.\frac{\delta \mathrm{ln} R}{\delta \mathrm{ln} T}\right|_{I_0} = \left.\frac{T_0}{R_0}\frac{\delta R}{\delta T}\right|_{I_0}, \tag{3.8}$$

and we can do the same thing with $\delta R/\delta I$,[3]

$$\beta_I \equiv \left.\frac{\delta \mathrm{ln} R}{\delta \mathrm{ln} I}\right|_{T_0} = \left.\frac{I_0}{R_0}\frac{\delta R}{\delta I}\right|_{T_0}, \tag{3.9}$$

so that the TES resistance, can be expressed as

$$R(T,I) \approx R_0 + \alpha_I \frac{R_0}{T_0}\delta T + \beta_I \frac{R_0}{I_0}\delta I. \tag{3.10}$$

This leads to a straightforward expansion of the first order Joule power,

$$P_J = I^2 R \approx P_{J_0} + 2I_0 R_0 \delta I + \alpha_I \frac{P_{J_0}}{T_0}\delta T + \beta_I \frac{P_{J_0}}{I_0}\delta I. \tag{3.11}$$

We substitute the natural thermal time constant,

$$\tau \equiv C/G, \tag{3.12}$$

the negative electrothermal feedback loop gain (as defined by Irwin and Hilton [54]),

$$\mathscr{L}_I \equiv P_{J_0}\alpha_I/GT_0, \tag{3.13}$$

and equations (3.6), (3.10), and (3.11) into equations (3.4) and (3.5). The DC terms cancel, and we are left with

$$\frac{d\delta I}{dt} = -\frac{R_{sh} + R_0(1+\beta_I)}{L}\delta I - \frac{\mathscr{L}_I G}{I_0 L}\delta T + \frac{\delta V}{L} \tag{3.14}$$

[3]For typical TES bolometers, α_I is of order 100, while β_I is of order 1. Analysis results for these parameters from a single bolometer are presented in Table 3.2.

and

$$\frac{d\delta T}{dt} = \frac{I_0 R_0 (2+\beta_I)}{C}\delta I - \frac{1-\mathscr{L}_I}{\tau}\delta T + \frac{\delta P}{C}. \tag{3.15}$$

With constant bias ($\delta V = 0$) and in the limit where $\mathscr{L}_I \to 0$ as it would for a device with a small α_I (like a normal resistor) or low P_{J_0}, we can integrate (3.14) to find the electrical time constant,

$$\tau_{el} = \frac{L}{R_{sh} + R_0(1+\beta_I)}. \tag{3.16}$$

Continuing with the solution by Irwin and Hilton [54], we write equations (3.14) and (3.15) in matrix form

$$\frac{d}{dt}\begin{pmatrix} \delta I \\ \delta T \end{pmatrix} = -\begin{pmatrix} \dfrac{1}{\tau_{el}} & \dfrac{\mathscr{L}_I G}{I_0 L} \\ -\dfrac{I_0 R_0(2+\beta_I)}{C} & \dfrac{1-\mathscr{L}_I}{\tau} \end{pmatrix}\begin{pmatrix} \delta I \\ \delta T \end{pmatrix} + \begin{pmatrix} \dfrac{\delta V}{L} \\ \dfrac{\delta P}{C} \end{pmatrix}. \tag{3.17}$$

Following the change of variables approach used by Lindeman [70], we find the homogeneous form of equation (3.17) by setting δV and δP to zero and diagonalizing the matrix using its eigenvectors, $\vec{v}_\pm$. This decouples the first order differential equations, which can then be integrated to find the full homogeneous solution:

$$\begin{pmatrix} \delta I \\ \delta T \end{pmatrix} = A_+ e^{-\lambda_+ t}\vec{v}_+ + A_- e^{-\lambda_- t}\vec{v}_-. \tag{3.18}$$

Here the coefficients, $A_\pm$, are unitless constants and two time constants, $\tau_\pm$, are defined as the inverse of the matrix eigenvalues:

$$\frac{1}{\tau_\pm} \equiv \lambda_\pm = \frac{1}{2\tau_{el}} + \frac{1-\mathscr{L}_I}{2\tau} \pm \frac{1}{2}\sqrt{\left(\frac{1}{\tau_{el}} - \frac{1-\mathscr{L}_I}{\tau}\right)^2 - 4\frac{R_0}{L}\frac{\mathscr{L}_I(2+\beta_I)}{\tau}}, \tag{3.19}$$

and the eigenvectors are found to be

$$\vec{v}_\pm = \begin{pmatrix} \dfrac{1-\mathscr{L}_I-\lambda_\pm\tau}{2+\beta_I}\dfrac{G}{I_0 R_0} \\ 1 \end{pmatrix}. \tag{3.20}$$

Before we add perturbations to this solution, we can explore the meaning of the eigenvalues in equation (3.19). In the low inductance limit where $\tau_{el} \ll \tau$, we find that $\tau_+ \ll \tau_-$, and simplification of equation (3.19) leads to the solutions

$$\tau_+ \longrightarrow \tau_{el} \tag{3.21}$$

and

$$\tau_- \longrightarrow \tau_{eff} = \tau \frac{1 + \beta_I + R_{sh}/R_0}{1 + \beta_I + R_{sh}/R_0 + (1 - R_{sh}/R_0)\mathscr{L}_I}, \tag{3.22}$$

indicating that τ_+ generally describes the electrical time constant, while τ_- describes the thermal response.[4] As the inductance increases, these time constants approach each other and can interact in potentially devastating ways, such as driving the bolometer into unstable electro-thermal oscillations (Section 3.3.4).

Now, we can add a perturbation to this solution in the form of a small time varying change in power absorbed by the bolometer, $\delta P = Re(\delta P_0 e^{i\omega t})$, to study the spectral response to changes in power measured from the sky. We insert this perturbation into equation (3.17) and follow the solution of Irwin and Hilton [54] to find the power to current responsivity for the detectors,

$$s_I(\omega) = -\frac{1}{I_0 R_0}\left(\frac{L}{\tau_{el} R_0 \mathscr{L}_I} + \left(1 - \frac{R_{sh}}{R_0}\right) + i\omega \frac{L\tau}{R_0 \mathscr{L}_I}\left(\frac{1 - \mathscr{L}_I}{\tau} + \frac{1}{\tau_{el}}\right) - \frac{\omega^2 \tau}{\mathscr{L}_I}\frac{L}{R_0}\right)^{-1}. \tag{3.23}$$

Because the TES bolometers are voltage biased and have strong electrothermal feedback, the first term in the denominator of the DC responsivity ($\omega \to 0$) is small compared to the second term,[5] allowing us to approximate the DC responsivity by

$$s_I(\omega = 0) \approx -\frac{1}{I_0(R_0 - R_{sh})}. \tag{3.24}$$

This estimate of the responsivity is used to calibrate the low frequency detector noise equivalent power (NEP, Table 5.2). It is also used for optical efficiency calibrations and later we combine it with measurements of noise and the detector time constants to assess the NEP and responsivity as a function of frequency.

[4] Note that $\tau_{eff} \approx \tau/\mathscr{L}_I$ for $\mathscr{L}_I \gg 1 + \beta_I$ and $R_{sh}/R_0 \ll 1$, which indicates that negative electrothermal feedback speeds up the bolometer response by a factor of $\sim 1/\mathscr{L}_I$.

[5] The first term in the denominator is $\frac{L}{\tau_{el} R_0 \mathscr{L}_I} = \frac{(R_{sh} + R_0(1 + \beta_I))GT_0}{R_0 P_{J_0} \alpha_I}$. Using parameters in Table 3.2, we find that this term is less than 0.04 throughout the transition, while the second term is ≈ 1 until the TES is very low on the transition (where $R_0 \approx R_{sh}$) and no longer in a voltage biased state. Using parameters measured from a prototype bolometer [71], we similarly find that the first term is less than 0.06 throughout the transition.

3.2 SQUID Readout and Multiplexing

To realize the benefits of negative electrothermal feedback, the TES bolometers must be voltage biased, which means that fluctuations in sky power are manifest as changes in bolometer currents. To measure these currents, each TES is connected in series to an inductor, which is coupled to a DC superconducting quantum interference device (SQUID, Figure 3.1). The SQUIDs convert the changing magnetic flux, ϕ, from the inductors into a voltage response [104]:

$$V = (R/2)\{I^2 - [2I_c cos(\pi\phi/\phi_0)]^2\}^{1/2}, \qquad (3.25)$$

where R is the resistance of the Josephson junctions, I is the SQUID bias current, I_c is the Josephson junction critical current, and ϕ_0 is a magnetic flux quantum[6] (Figure 3.2). This conversion of current responses into flux for readout by a SQUID has become a standard for making low noise, low temperature current measurements.

The SQUIDs are inherently nonlinear devices. The bias voltage oscillates between two limiting curves with the change of a single magnetic flux quanta inside the loop between the two Josephson junctions (Figure 3.2). The SQUIDs are kept in the linear regime (where $V \propto I$) through the use of external feedback electronics, which use a Proportional, Integral (PI) response loop to tune the feedback flux response until it cancels the signal input from the TES. The difference between the output of the SQUID and a target locking point is considered the error, and in the limit of zero error, the feedback contains all the information in the signal. Because of this canceling feedback, the PI loop response becomes our measured signal, while the output of the SQUIDs is representative of the error in the PI calculation. When operated independently, each of these SQUIDs would require a minimum of four wires,[7] so a 32×32 array would require 4096 readout wires, not including the TES biasing lines.

Multiplexing of the SQUID electronics dramatically reduces the number of connections between room temperature data acquisition electronics and cold detectors. We have implemented a NIST-designed and fabricated time-domain multiplexing (TDM) system, which

[6] $\phi_0 \equiv h/2e = 2.07 \times 10^{-15}$ Wb $= 2.07 \times 10^{-7}$ G-cm^2, where h is Planck's constant and e is the electron charge [104].

[7] Two wires are used to both apply the SQUID bias current and allow measurement of the SQUID voltage response. The other pair of wires is used to apply flux feedback to keep the SQUIDs in the linear regime [21]

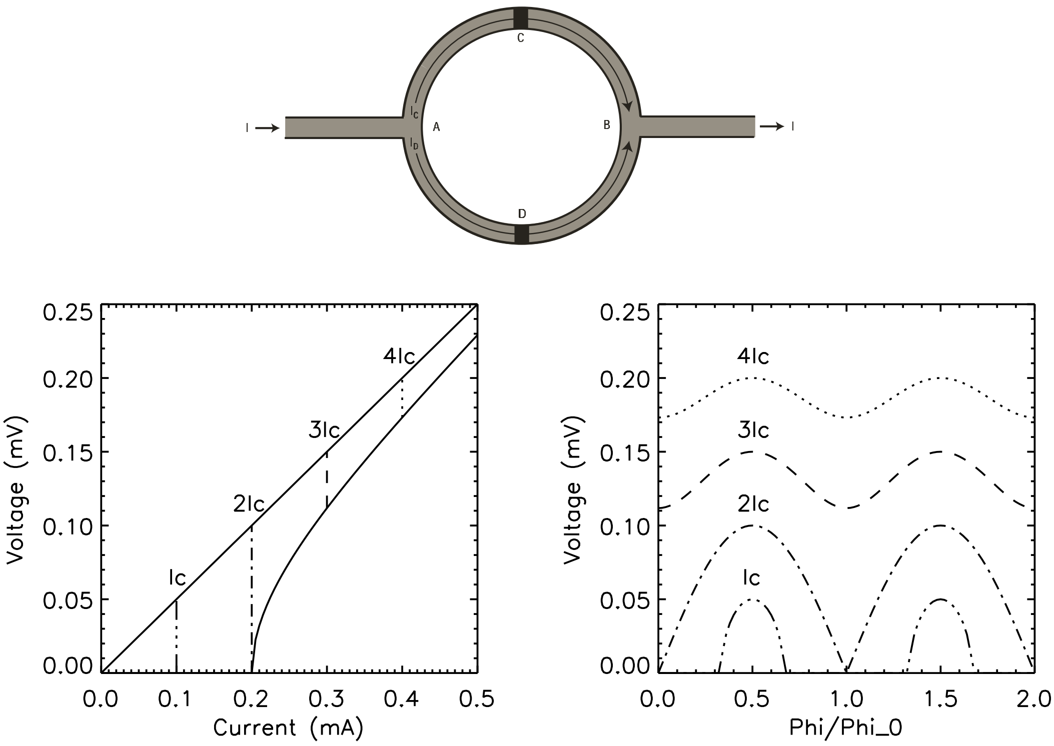

Figure 3.2: DC SQUID description. *Top*: The blackened areas represent the two Josephson junctions (drawn as 'X' in circuit diagrams like in Figures 3.1 and 3.3). *Left*: Current versus voltage for a DC SQUID from equation (3.25). These plots are for Josephson junctions with $R = 1\ \Omega$ and $I_c = 100\ \mu$A, which are roughly the values of our stage 1 SQUIDs (Figure 3.1). The top and bottom lines indicate the magnetic flux limits of the DC SQUID response. A change of one flux quanta inside the SQUID loop results in an oscillation between the two limits as shown for the constant bias currents I_c, $2I_c$, $3I_c$, and $4I_c$ by the dotted and dashed lines. *Right*: The SQUID voltage response as a function of ϕ/ϕ_0 for the aforementioned bias currents. The maximum V–ϕ amplitude is achieved at a bias current of $I = 2I_c$. Above this value, the V–ϕ curves appear more sinusoidal, but have a smaller peak-to-peak amplitude. Magnetic flux feedback is used to keep the SQUID response in the linear regime along the steepest part of the V–ϕ response. In our system we do not apply perfect current biases to the all the SQUIDs, so the SQUID responses move through diagonal cuts in the voltage vs. current graph instead of the vertical cuts plotted here. Also note that the SQUID Josephson junctions have a minimum critical current to turn on, which is ignored in equation 3.25, and means that the actually zero current point on the plot at the left is below zero on the x-axis.

acquires data from each of the 32 rows of TESs in series, reducing the wire count from 4096 to 384 lines (Figure 3.3). Wire count reduction is important for multiple reasons, including space constraints (the entire TES detection surface in a camera is 34mm x 39mm) and limiting thermal conduction into the cryogenic system. Our closed cycle refrigerators [67] have limited cooling power; if the thermal load is too great, the fridges will not be able to cool to below the TES critical temperature. A decrease in heat load on the refrigerators also increases the amount of time between cycling the fridges, which can ultimately increase our observation time.

The multiplexing system consists of three cold stages of SQUIDs connected to warm electronics (Section 4.2). The first stage (S1) is coupled to a TES through an inductor, L_{in}, in series with the TES (Figure 3.1). Each S1 SQUID is biased in parallel with an inductor, L_{SQ1}, and bias resistor that is similar in resistance to the S1 Josephson junctions. Another inductor, one of 33 in series on a column, is coupled to L_{SQ1} in each S1 SQUID loop, connecting the entire column of 33 SQUIDs[8] through a transformer loop to a single second stage (S2) SQUID on the same multiplexing chip (Figures 3.3 and 3.4). Putting the L_{SQ1} in parallel with the SQUID (rather than in series) maintains more uniformity when choosing the optimal S2 SQUID feedback for each column. This is true because there is no change in flux through the S2 SQUID until a given S1 SQUID's Josephson junctions are driven above their minimum critical current. It also means that the biasing of the S1 SQUIDs is somewhere between voltage and current biasing (unlike the V–ϕ curves shown in Figure 3.2), so that changes in flux result in significant changes in current through both the S1 SQUID and its bias resistor. In fact, (as indicated above) we measure the change in current through the bias resistor, not through the S1 SQUID. The S2 SQUIDs, on the other hand, are strongly voltage biased by biasing them in parallel with a 0.1 Ω resistor,[9] which is much smaller than the S2 Josephson junction resistance [28]. Both the S2 and the 33 S1 SQUIDs are on a common silicon chip that is maintained near 0.3K during operation.

The output/biasing lines for the S2 SQUIDs are connected between the 0.3 K and 4 K cryogenic stages to a series of inductors on the series array (SA) chip, which is operated at

[8]There are 32 SQUIDs connected to detectors in each column as well as a 33^{rd} dark SQUID which may be used for background subtraction.

[9]Despite the voltage biasing of the S2 SQUIDs and the mixed biasing of the S1 SQUIDs, we follow the convention of referring to all measured SQUID responses to sweeping ϕ as V–ϕ curves

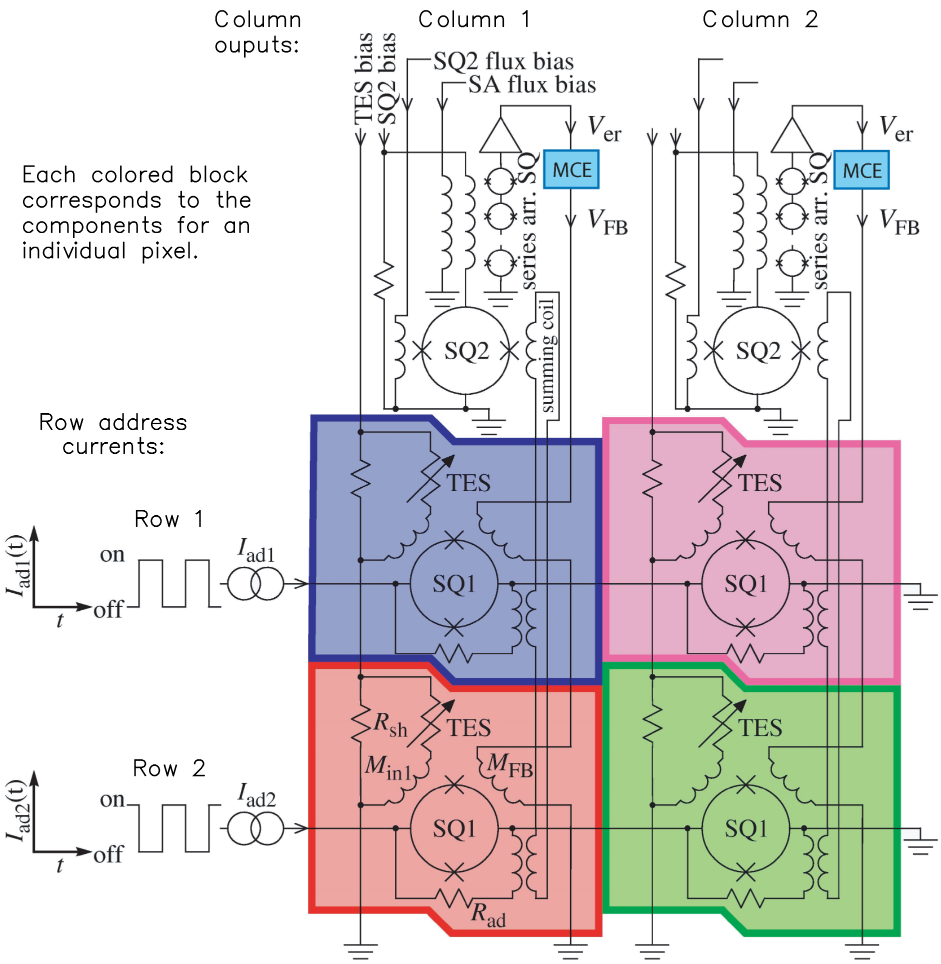

Figure 3.3: Two column multiplexing readout schematic. The large decrease in readout wiring from multiplexing is due in part to addressing rows of SQUIDs in series as depicted here in a two column by two row array. (Figure courtesy of R. Doriese.)

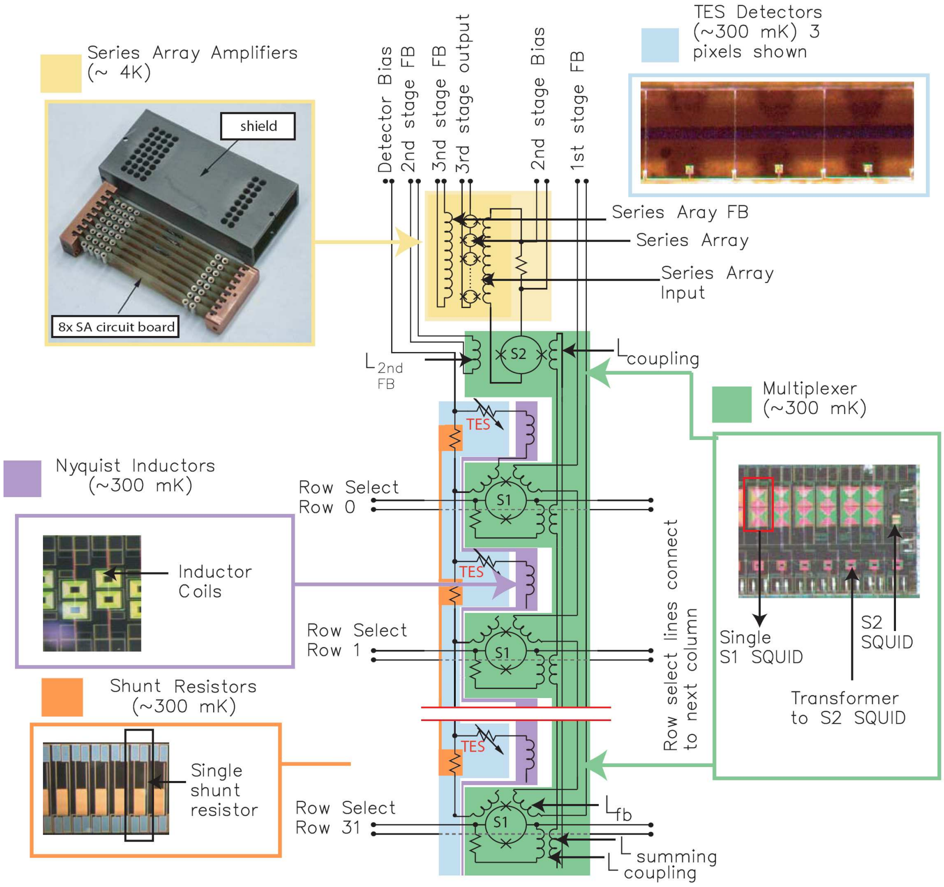

Figure 3.4: Single column detector readout schematic with photos of the components fabricated by GSFC (TES detectors and shunt chips) and NIST (series arrays, multiplexer chips, and Nyquist inductor chips). All of the components shown here are operated at 0.3 K, except for the series array modules, which are operated near 4 K because of the large amount of power that they dissipate. The series array photo in the upper left depicts 8 circuit boards, which each hold a series array for a different detector column and the magnetic shielding box (made of a layer of high permeability material which covers an additional layer of superconducting niobium) that houses the 8 series arrays. (Figure courtesy of J. Lau and D. Benford.)

the 4 K stage. A series array chip consists of a series of 100 amplifying SQUIDs, which are all coupled to inductors in series with the S2 SQUID, enabling them to measure the change in current through the S2 SQUID. The voltage biasing of the S2 SQUIDs is important, because it allows direct measurement of the changes in S2 current by the SA SQUIDs. It is critical to maintain low resistance and inductance in the wiring between the S2 and SA SQUIDs to maximize the response of the SA SQUIDs to changes in S2 current and minimize low-pass filter effects that can reduce the bandwidth of the readout system. To achieve this, we use a superconducting niobium-titanium alloy for the wires and connect multiple twisted pairs in parallel to minimize the inductance. The design of these cables is presented in Appendix B.

The SA SQUIDs are current biased, which enables usage of a standard room temperature voltage preamplifier for measurement of each chip. The preamplifier passes the amplified output to the digital feedback (DFB) electronics for the PI loop calculation. The PI response is sent to the S1 Feedback inductor with the result that all three stages of SQUIDs are kept in the optimal/linear regime on the V–ϕ curves. As described earlier, the feedback output by the DFB electronics becomes our signal, which is a measure the change in power on the TES. The error voltage, or SA output, can also be recorded for studying the performance of the PI loop.

In addition to the decrease in wiring from coupling all 33 S1 SQUIDs per column into a single S2 SQUID, the other major reduction comes from biasing each row of 33 SQUIDs, one from each of 32 separate columns, in series (Figure 3.3). This requires that the SQUID critical currents in a given row be similar across 32 mux chips, since the same current will be applied to all of them.

Time-domain multiplexing is implemented by turning on a single row of S1 SQUIDs with a boxcar applied to their common current bias, or address, line (Figures 3.3 and 3.5). When this boxcar is turned on, the SQUIDs in that row are responsive to changes in the detector current, and when the boxcar is turned off, the SQUIDs exhibit no response to the detector current. One frame of data, f, is acquired from all detectors by turning on and measuring the output from a row of SQUIDs then turning it off and successively repeating that process for all rows in the array. After one row of SQUIDs is turned on, the system waits for the transients to settle (Section 4.2.1) before reading out the change in detector current as a change in the SA outputs, $x_{f,n}$, for all detectors in that row, where n is the row number. The PI feedback response, $y_{f,n}$, is calculated as

$$y_{f+1,n} = P_{user} x_{f,n} + I_{user} \sum_{i=0}^{f-1} x_{i,n}, \tag{3.26}$$

where P_{user} and I_{user} are the predetermined PI values [91] (Section 4.2.3). During frame f, the PI response that was calculated during the previous frame, $y_{f-1,n}$, is applied. After samples are acquired, the S1 SQUID bias and feedback are turned off for row n and on for row $n+1$. This continues with incrementing steps through the array until all rows have been measured and the frame, f, is completed (Figure 3.5), then the next frame, $f+1$, begins.

In Section 4.2 the different types of room temperature digital feedback electronics (the NIST developed DFB electronics and the Multi-Channel Electronics (MCE) developed at the University of British Columbia, which are used for observations) are described and differentiated. In addition, the techniques used for determining the multiplexing rate and PI value selection are presented, and other details and capabilities of the multiplexing electronics are discussed.

3.3 Parameter Selection for the ACT arrays

Three critical bolometer properties determine the functionality and sensitivity of the detector arrays during observations: the saturation power, the noise level, and the time constant. The saturation power, P_{sat}, determines whether the detectors can function without saturating during observations. The noise level impacts the ratio of photon noise to detector noise and affects the final sensitivity of the sky maps. The time constant, $\tau = (2\pi f_{3dB})^{-1}$, determines whether the detector response will low-pass filter small angular scales on the sky as the telescope scans (Section 2.5). The selection of detector parameters for the arrays has been a gradual process of optimizing these properties. It has been motivated by a combination of theoretical calculations, measurements, and fabrication recipe success. Here we describe some of the calculations and measurements that led us to the selected parameters for the arrays.

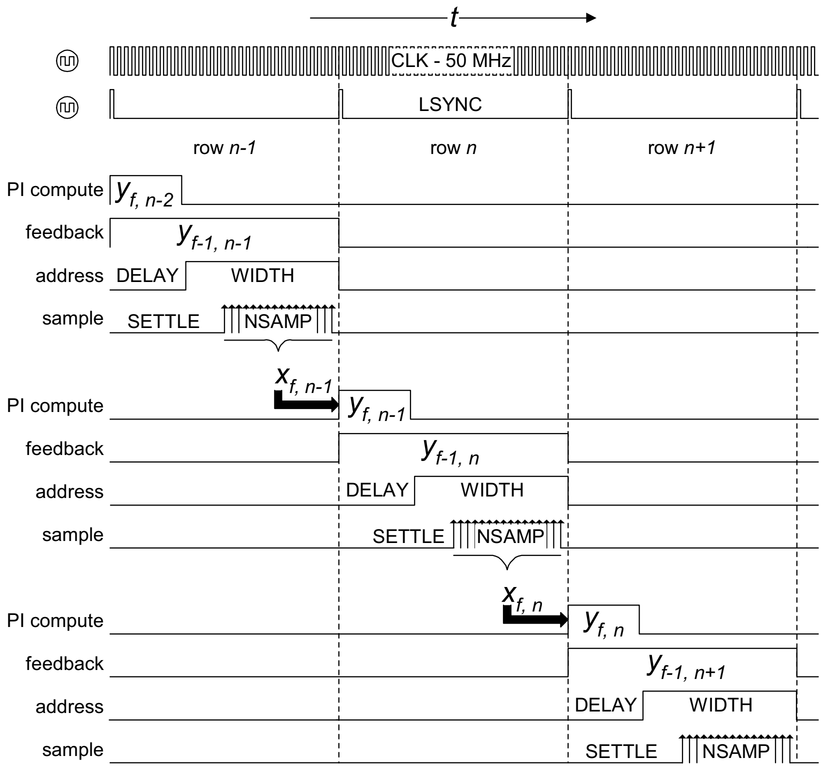

Figure 3.5: Multiplexing timing diagram for the NIST digital feedback (DFB) electronics, showing the PI loop timing for rows of S1 SQUIDs [91]. (The timing diagram for the Multi-Channel Electronics is similar with slightly different variable definitions [37].) Measurements of three rows in a single column are represented. A 50 MHz clock is used to synchronize the commands. The row period is determined by LSYNC, or the number clock cycles between turning on successive rows. For ACT we use the equivalent of LSYNC=100, or 500 kHz row switching, and since there are 33 rows, this results in 15.2 kHz sampling of the entire array (Section 4.2.1). At the beginning of each row period: the PI response based on measurements from the previous row is computed, then it is stored until it is applied during the following frame; the S1 feedback for the current row is turned on and applied for the entire row period; there is a waiting period, DELAY, before the current row addressing line is turned on for a duration of WIDTH clock cycles; there is a settling time between turning on the S1 SQUIDs and acquiring data, SETTLE - DELAY, which gives time for transients to settle; finally, a number of samples, NSAMP, of the SA output are acquired during successive clock cycles and summed into $x_{f,n}$ for the next PI loop calculation. (Figure courtesy of C. Reintsema.)

3.3.1 Multiplexing considerations

Time-domain SQUID multiplexing (TDM) is a powerful tool for reading out large TES arrays; however, it has one main drawback: the limited sampling rate of TDM means that high frequency noise is aliased back into the signal band. There are two fundamental sources of high frequency noise, which are detector noise and SQUID readout noise. Intrinsic detector noise can extend to high frequencies, so we filter it with a Nyquist inductor, L_{Ny}, to reduce the amplitude of the aliasing (Section 3.3.4). The SQUID readout system is required to have high bandwidth to enable TDM, so the low-pass filter solution is not appropriate. Non-multiplexed SQUID noise, N_{SQ}, on NIST multiplexer chips has been measured to be $N_{SQ} = 0.5\ \mu\phi_o/\mathrm{Hz}^{1/2}$ [28]. We determine that aliasing resulting from multiplexing at our planned frame rate, $f_{samp} = 15.2$ kHz (Section 4.2.1), increases the SQUID noise level by a factor of ~7 to $N_{SQ} \approx 3.5\ \mu\phi_o/\mathrm{Hz}^{1/2}$, which can be converted into detector current using the SQUID input mutual inductance of $M_{in}^{-1} = 7.5\ \mu\mathrm{A}/\phi_0$ (Section 3.5.1) giving 26 pA/Hz$^{1/2}$ (Figure 3.6). We can compare this to the detector thermal fluctuation noise, NEP_{th}, which is expected to be the primary contributor to the detector noise and to dominate over the sky noise for the 148 GHz array. Using estimates of the detector thermal conductivity, $G(T_c) \approx 100$ pW/K [72], and the transition temperature, $T_c \approx 0.5$ K, we find

$$(NEP_{th})^{1/2} = \sqrt{4k_B T_c^2 G F_{link}} \approx 3.7 \times 10^{-17}\ \mathrm{W/Hz^{1/2}}, \tag{3.27}$$

where k_B is Boltzmann's constant, and F_{link} is a dimensionless constant near unity[10] that depends on phonon reflection effects at the bolometer boundaries [54]. Combining this with our responsivity estimate, equation (3.24), allows estimation of the phonon-induced low frequency current noise from thermal fluctuations,

$$(NEC_{th})^{1/2} \approx \frac{(NEP_{th})^{1/2}}{I_0(R_0 - R_{sh})} = \frac{(NEP_{th})^{1/2}}{(P_0/R_0)^{1/2}(R_0 - R_{sh})}. \tag{3.28}$$

With a rough estimate of the detector bias power, $P_0 \approx 10$ pW (Section 3.3.3), we can see that a low detector resistance is required to ensure that the detector current noise will dominate the aliased SQUID noise level. This drove selection of a low TES normal resistance, $R_n \approx 30$ mΩ, so that on the transition, where $R_0 \approx 10$ mΩ and

[10] We assume $F_{link} = 1$ for these calculations.

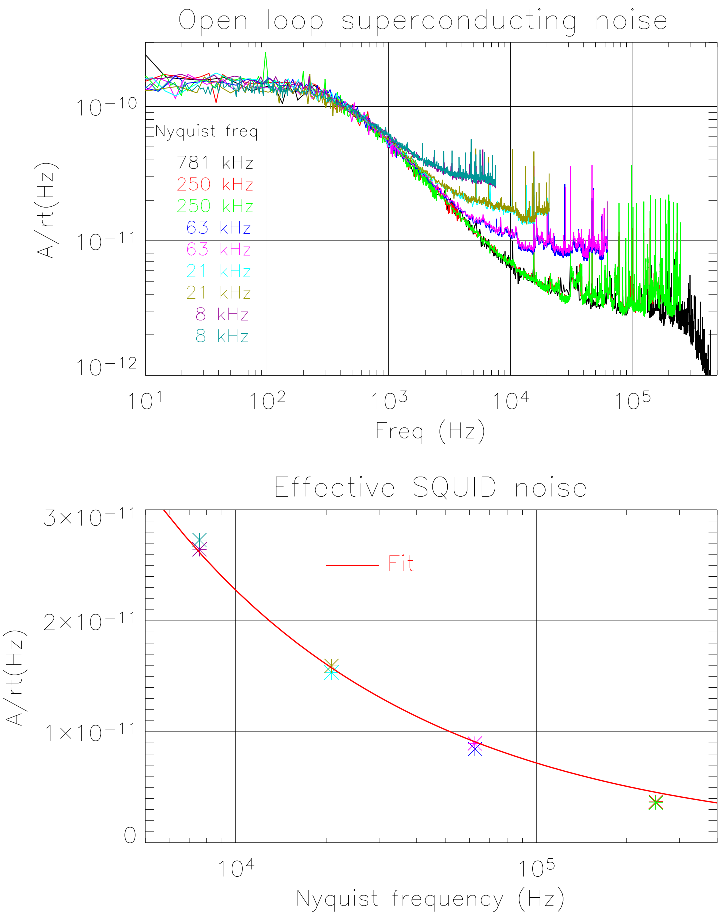

Figure 3.6: SQUID noise aliasing at different multiplexing rates. *Top*: Open loop Johnson noise data were acquired with the detectors superconducting and fit as described in Section 3.5.2 (Figure 3.15) at rates between $f_{samp} = 2f_{Ny} = 15$ kHz - 1.6 MHz to extract the effective SQUID noise level. As the sampling rate is decreased, aliasing causes the effective SQUID noise amplitude to increase. *Bottom*: The effective SQUID noise levels extracted from the data above are fit to $N_{eff}^2 = N_{SQ}^2 f_{SQ}/f_{Ny}$, where N_{SQ} is the SQUID white noise level, f_{SQ} is the cutoff frequency of the SQUID noise, f_{Ny} is the Nyquist frequency, and N_{eff} is the effective SQUID noise at the sampling frequency. The form of this fit assumes that the maximum SQUID noise frequency, $f_{SQ} \gg f_{Ny}$. This assumption is probably not valid for the $f_{Ny} = 250$ kHz data, which may explain why these data fall below the line of the fit. The displayed fit has $f_{SQ} \approx 400$ kHz and $N_{SQ} \approx 3.6$ pA/Hz$^{1/2}$ $= 0.6$ $\mu\phi_0$/Hz$^{1/2}$, which appears reasonable based on the roll-off frequency of the $f_{Ny} = 781$ kHz data (black) in the top plot. Note: the high frequency noise spikes observed in these data are not typical and are believed to be due to poor grounding of the DFB electronics during the acquisition.

$I_0 = (P_0/R_0)^(1/2) \approx 3 \times 10^{-5}$ A, $(NEC_{th})^{1/2} \approx 1.2 \times 10^{-10}$ A/Hz$^{1/2}$. The aliased SQUID noise is ∼5 times smaller than this underestimate of the total detector noise level and since they add in quadrature, it only increases the total noise by ∼2%.

The shunt resistance value was selected to be $R_{sh} \approx 0.7$ m$\Omega \approx R_n/40$ to keep the TESs nearly voltage-biased throughout much of the transition. This resistance is still large enough that only a small amount of Joule heating is generated in the 1024 shunt resistors, $P_{sh} = 1024 \times (I_0 R_0)^2/R_{sh} \approx 10^{-7}$ W, which only increases the 0.3 K stage bath temperature by ∼0.2 mK and has a negligible impact on the ^{3}He sorption fridge hold time [67].

3.3.2 Time constants

Our observation strategy is to scan the entire telescope in azimuth ∼5° peak-to-peak (Section 2.5). The angular velocity of this scan imposes a lower limit on the detector f_{3dB} to minimize suppression of the response to small angular scales, or high frequencies [77]. Because of the complexity of the model used to explain our bolometer response (Section 3.5.5) [71], optical measurements were required to characterize the bolometer time constants. In-band optical time constant measurements were made using the 8 × 32 prototype array of bolometers in the Column Camera (CCam) receiver [67]. The measurements were made by chopping a source over a range of frequencies (4 Hz - 200 Hz) to measure the relative magnitude of the filtering by the detectors over the range of scales that are sampled on the sky (Section 6.2).

The chopper wheel alternately exposed the detectors to a 300 K Ecosorb source and a reflective plate, through a small aperture near a focus of the CCam dewar. A 9% transmissive neutral density filter was in the dewar optical path at ∼4 K to prevent saturation of the bolometers. Different data files were acquired for each frequency, and analyzed by Fourier transforming the time streams, integrating over the fundamental peak of the response to the chopper, and subtracting the background power spectral density (PSD). The bolometer f_{3dB} is calculated from a single-pole fit to the frequency response (Figure 5.13). Load curves (Section 3.5.3) acquired before and after each series of measurements confirmed system stability and provided detector parameters (R_0 and P_{J_0}) at the numerous bias points studied.

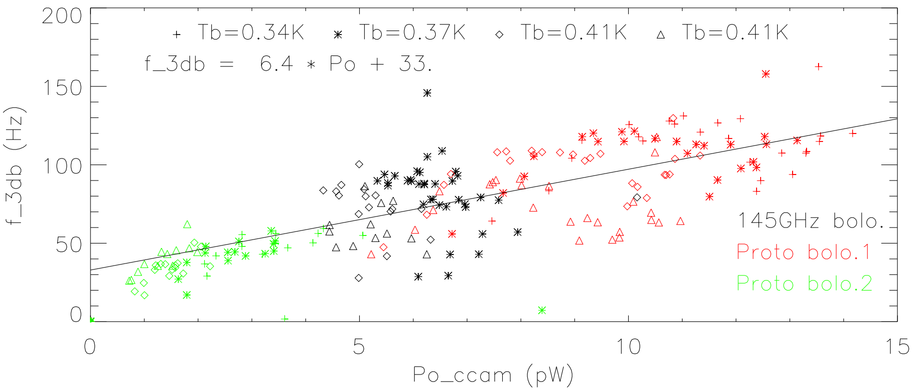

Figure 3.7: Time constants of prototype bolometers in the 8 × 32 array. Three different types of bolometers measured at three bath temperatures near $R_0 \approx R_n/2$ follow the trend $f_{3dB} \approx (6.4\ \mathrm{Hz/pW})\ P_{J_0} + 33$ Hz. The 8 × 32 array column numbers presented here are 4 (red), 6 (black), and 7 (green).

Assuming an isothermal TES bolometer model in the low inductance limit, we can rewrite equation (3.22) as

$$\frac{1}{2\pi\tau_{eff}} = f_{3dB} = \frac{G}{2\pi C}\left(1 + \frac{(1 - R_{sh}/R_0)\alpha_I}{(1 + \beta_I + R_{sh}/R_0)GT_0} P_{J_0}\right). \tag{3.29}$$

The low-inductance limit is an acceptable approximation, despite our use of Nyquist inductors (Section 3.3.4), because the L/R electrical time constant is roughly an order of magnitude smaller than the optical time constants. As seen in equation (3.29), with other parameters held constant, f_{3dB} contains a term proportional to P_{J_o}. Measurements of two columns of prototype detectors and one column of detectors for the first array follow the trend $f_{3dB} \approx (6.4\ \mathrm{Hz/pW})\ P_{J_0} + 33$ Hz (Figure 3.7). The bolometers have roughly constant f_{3dB} between 25% - 75% of R_n (Figure 3.8), indicating that changes in the parameters α_I and β_I throughout this range do not have a strong impact on f_{3dB}. These measurements were made at elevated bath temperatures and loading in CCam; however, by combining the fit to the data in Figure 3.7 with G measurements, we can estimate f_{3dB} under observing conditions and use it to guide parameter selection for the arrays (Table 3.1).

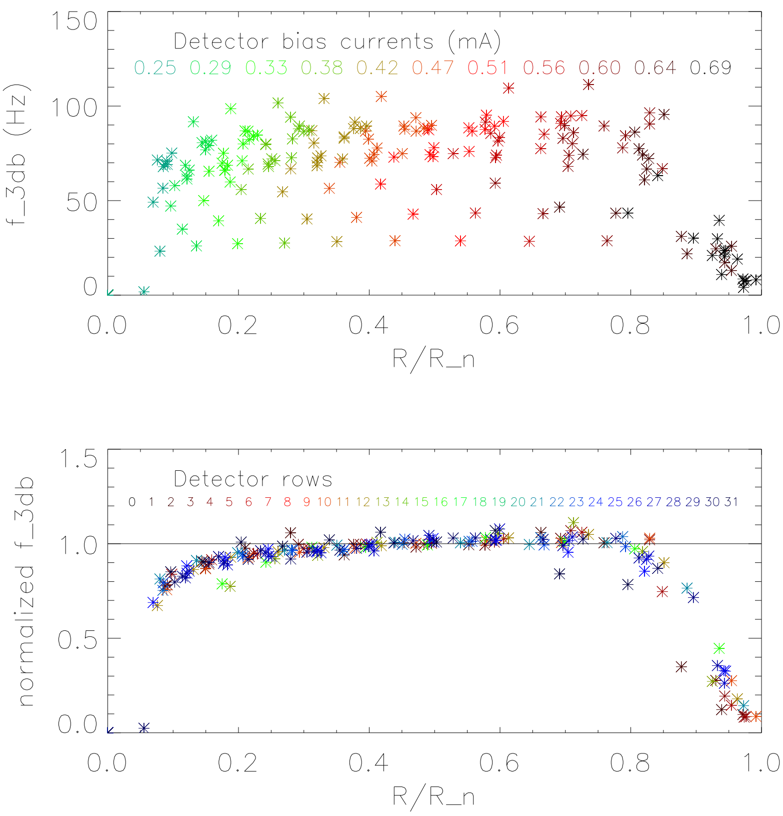

Figure 3.8: Time constants as a function of resistance ratio, R/R_n. These data were acquired from column number 6 in the 8 $\times$ 32 prototype array, which was in the same fabrication group as the 145 GHz array bolometers. *Top*: A large amount of scatter is observed in the f_{3dB} values for the detectors in this column. *Bottom*: After normalizing all f_{3dB} measurements for each individual detector using the mean of its measurements between $0.3 - 0.7\ R_n$, we see that the change in the $f_{3dB}(R/R_n)$ is fairly consistent for all detectors in the column. The f_{3dB} only changes by $\sim$10% between $0.25 - 0.75\ R_n$, which gives a rough guideline for future data cuts. We note that prototype bolometers from different fabrication groups (other columns in the 8 $\times$ 32 prototype array) do not have this level of consistency on all measured bolometers.

3.3.3 Saturation power

Optical loading predictions for the Atacama Plateau during the observation season are presented in Section 2.6. These put lower limits on the acceptable saturation powers, P_{sat}, for the three arrays. Consideration of the measured scatter in the prototype detector parameters, desire to bias the entire kilopixel detector array with only a few detector bias lines, and the results of time constant measurements (Section 3.3.2) drove selection of P_{sat} values substantially higher than these limits. In particular, P_{sat}s for the three arrays were targeted that would maintain nearly the same product of angular resolution element on the sky and f_{3dB}, because this should result in the telescope scan velocity impacting beam measurements in all three bands roughly equally. This was done by using the empirical fit to the time constant data, $f_{3dB} \approx$ (6.4 Hz/pW) P_{J_0} + 33 Hz (Figure 3.7), to select the target P_0 for each array, then adding the predicted load to arrive at the target P_{sat}.

In addition to its dependence on the bath temperature, P_{sat} depends on the TES transition temperature, $T_c \approx T_0$, and the thermal conductivity, G, of the weak link to the bath, equation (3.2). Measurements of the T_c, G, and P_{sat} were made on bolometers with a variety of different leg widths (Figure 3.9) to determine their dependence on fabrication recipes [72]. This information allowed us to select leg widths and target T_c's to achieve the desired saturation powers and time constants (Table 3.1).

3.3.4 Nyquist inductance

TES bolometers have at least two interacting time constants, as indicated by equation (3.19). In the low inductance limit, the electrical time constant is much faster than the thermal time constant, and they can be approximated as in equations (3.21) and (3.22). From equation (3.19) we see that there should exist critically damped solutions for L which will cancel the terms in the square root, causing $\tau_+ = \tau_-$. These solutions are

$$L_{crit\pm} = \frac{R_0 \tau}{(\mathscr{L}_I - 1)^2}\left[\mathscr{L}_I\left(3 + \beta_I - \frac{R_{sh}}{R_0}\right) + 1 + \beta_I + \frac{R_{sh}}{R_0} \pm 2\sqrt{\mathscr{L}_I(2+\beta_I)\left(\mathscr{L}_I - \mathscr{L}_I\frac{R_{sh}}{R_0} + 1 + \beta_I + \frac{R_{sh}}{R_0}\right)}\right]. \tag{3.30}$$

In the range $L_{crit-} < L < L_{crit+}$, the response of the TES is underdamped, which can result in unstable oscillations. Outside of this range the response is overdamped. The

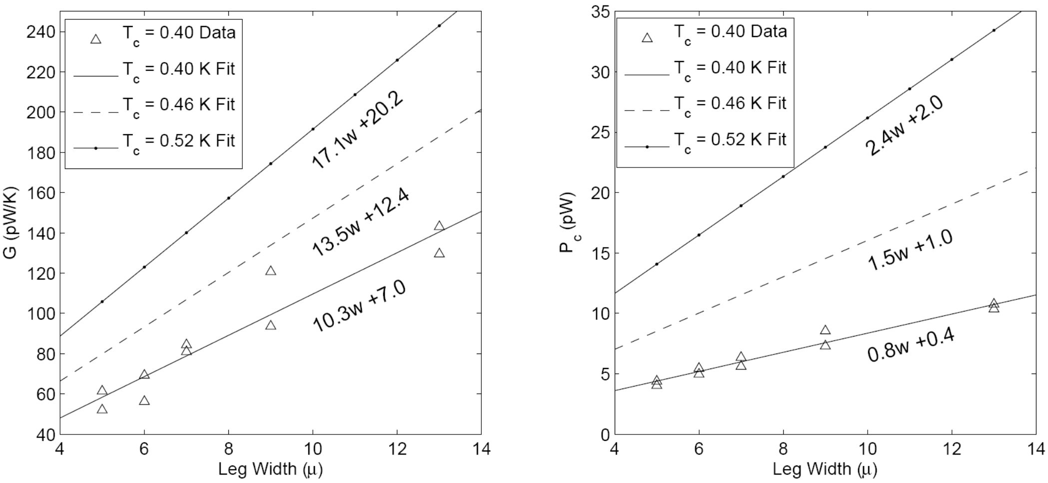

Figure 3.9: Thermal conductivity, $G = nKT_c^{n-1}$, and saturation power, P_{sat}, measurements and predictions as a function of bolometer leg width in μm. The data presented above (triangles) are the result of fitting equation (3.2) to load curves (Section 3.5.3) acquired at multiple bath temperatures on detectors with $T_c \approx 0.4$ K. Since there is significant degeneracy between n and K, a roughly fit value of $n \approx 3$ was held constant, and then K was effectively fit as a function of bolometer leg width (solid line) to calculate G and P_{sat} for the different designs. The fit was extrapolated to the plotted values of $T_c = 0.46$ K and 0.52 K (dashed and solid with dots lines respectively) using equation (3.2) [71]. These measurements were made on prototype devices with leg thicknesses of 1.4 μm. (Figure courtesy of T. Marriage [71].)

Frequency Band (GHz)	148	225	280
Sky resolution (arcmin)	1.4	1.0	0.9
Optical load (pW)	1	3	10
Leg width (μm)	5	7	9
Leg thickness (μm)	1.1	1.4	1.4
Target T_c (mK)	510	520	540
Target G (pW/K)	90	130	180
Target P_{sat}(0.3 K) (pW)	10	18	27
Estimated P_{J_0} (pW)	9	15	17
Estimated f_{3dB} (Hz)	90	130	140

Table 3.1: T_c and leg width selection to achieve target saturation powers. For the 145 GHz array, the bolometers were fabricated using 1.1 μm thick Si, instead of the 1.4 μm thick silicon used for the prototype devices, making the thermal conductivity different from the predictions in Figure 3.9. For the 1.1 μm devices we use $n \approx 4$ for the calculations as opposed to the 1.4 μm devices that were found to have $n \approx 3$ (Figure 3.9), but we note that significant degeneracy exists between n and K in data from both types of bolometers. To calculate P_{sat} and P_{J_0}, $T_{bath} = 0.3$ K is assumed. (In 2007 MBAC observed with $T_{bath} \approx 0.29$ K.) The parameters for the higher frequencies are roughly adjusted to maintain the product of the f_{3dB} and the sky resolution. The sky resolution is taken as the FWHM of the convolved beam profiles in Figure 2.9. The optical loads are estimated from Table 2.4 assuming 70% detector efficiency and PWV = 1 mm.

most practical region to operate voltage-biased TESs is in the lower overdamped regime where $L \leq L_{crit-}$ because at small L the electrical time constant does not limit the thermal response [54].

Since time-domain multiplexing is being used to read out the detectors, there is limited sampling bandwidth. To minimize aliasing of out of band noise into the signal band, the inductance in the TES circuits is increased, thereby rolling off the high frequency TES noise. We can reduce the aliasing by increasing the effective time constant, τ_+, above our Nyquist sampling period, τ_{Ny},

$$\tau_+ > \tau_{Ny} = \frac{1}{2\pi f_{Ny}} = 21\ \mu\text{s}, \tag{3.31}$$

where $f_{Ny} = f_{samp}/2 \approx 7.6$ kHz. We use this to estimate the minimum inductance, L_{min}, by inserting equation (3.16) into (3.19), substituting τ_{Ny} for τ_+ and solving for L,

$$L_{min} = \frac{R_{sh} + R_0(1+\beta_I) - \frac{\tau_{Ny}}{\tau}(\mathscr{L}_I(R_0 - R_{sh}) + R_{sh} + R_0(1+\beta_I))}{\frac{1}{\tau_{Ny}} - \frac{1-\mathscr{L}_I}{\tau}}. \tag{3.32}$$

These solutions give us a working range $L_{min} \leq L \leq L_{crit-}$, which can be solved for with knowledge of the TES parameters. Using the parameters for a prototype bolometer fit by R. Dünner and T. Marriage [71], and ignoring the isolated heat capacities, we find a large potential range for L of 0.35 μH $\leq L \leq$ 2.0 μH. With bolometers that follow the isothermal model presented here, it is ideal to use a circuit inductance near L_{crit-}, however, due to the complexity of the three block bolometer model (Figure 3.18) and the degeneracy of parameters fit to that model, the inductance for the arrays was selected experimentally. This range was explored using a NIST multi-L chip with values between $L = 0.1 - 1.4$ μH (Figure 3.10). The noise on each prototype bolometer was measured at multiple bias points before and after adding the inductor (Figure 3.11). The noise level after aliasing, $N_a(f)$ where f is a frequency $\leq f_{Nyq}$, was estimated before and after adding the inductor by measuring the power spectral density (PSD, measured in in A^2/Hz), $N_m(f)$, out to 100 kHz and folding it about f_{Nyq}:

$$N_a(f) = N_m(f) + \sum_{j=1}^{k}[N_m(2jf_{Nyq} - f) + N_m(2jf_{Nyq} + f)]. \tag{3.33}$$

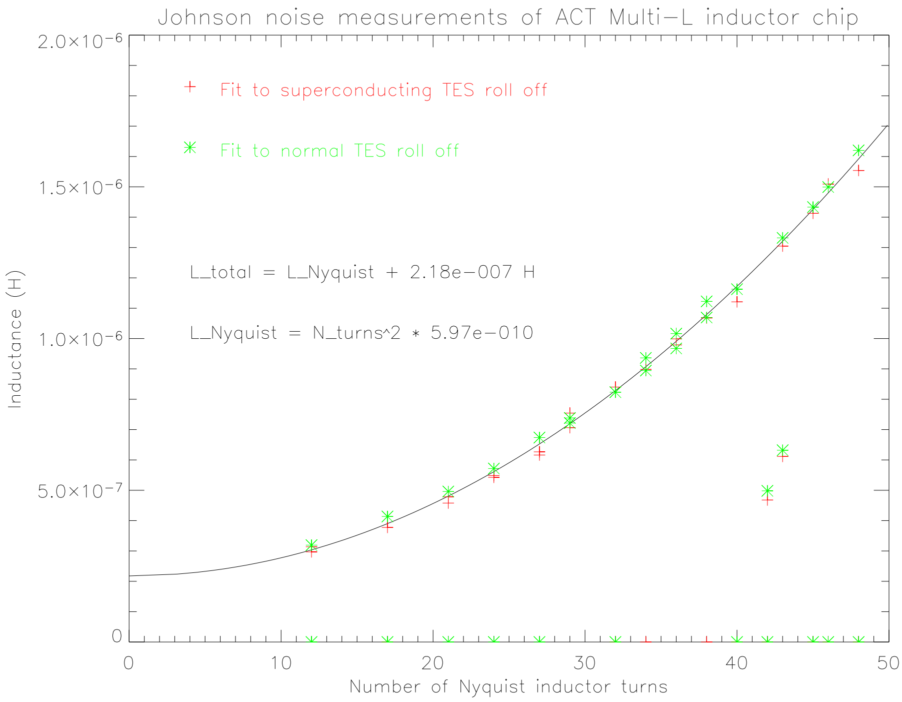

Figure 3.10: NIST multi-L Nyquist chip inductances were measured by fitting Johnson noise spectra with the TESs both normal and superconducting as discussed in Section 3.5.2. The intercept in this plot arises because these data were acquired using a prototype Mux05c multiplexing chip on the column, which combined with the other wiring in the TES loop has an inductance of ~220 nH. Measurements of the Mux06a chips being used for the arrays indicate that they have a reduced inductance of ~50 nH. The outlying measurements for inductors with 42 and 43 turns were found to be due to shorts on the Nyquist chip, by measuring lower than expected warm resistances through those inductors.

We sum over $i = 0 \rightarrow k$ folds, where k is an integer that meets the condition: $N_m(2kf_{Nyq} + f) \ll N_a(f)$ for k and integers greater than k.

To select the optimal inductance, we found the maximum decrease of in-band aliased noise that occurred after introducing the inductor. Above the optimal inductance, detectors tend to either have an increase in low-frequency noise or be driven into oscillations (Figure 3.12). Due to the scatter in our detector properties, we chose to use 34-turn inductors ($L \approx 0.69$ μH). These appear to have near optimal inductance on the measured column (Figure 3.12) but are a conservative choice for use with the Mux06a chips, which have 0.17 μH less input inductance than the tested Mux05c chips, resulting in a total circuit

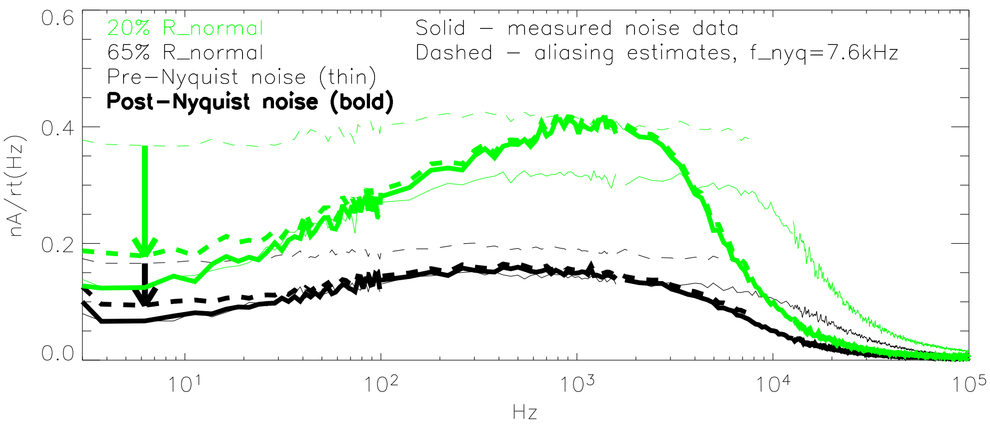

Figure 3.11: Noise aliasing comparison with Nyquist inductors. Noise measurements (solid) and aliasing estimates calculated from equation (3.33) (dashed) pre-Nyquist inductors (thin lines) vs. post-Nyquist inductors (bold lines) at 0.2 R_n (green - the top four curves) and 0.65 R_n (black). Thick vertical arrows near 6 Hz indicate the estimated reduction of in-band aliasing by adding the Nyquist inductor into the TES loop. If the Nyquist inductors had not been added, the aliased noise levels would have been at the levels of the thin dashed lines, but since the inductors were added, the aliased noise was reduced to the levels of the thick dashed lines. These aliasing estimates were summed to $k = 4$, or 38 kHz.

inductance of $\sim$0.74 μH for the first array, or $\sim$20% below optimal according to this estimate. Due to shorts on the Nyquist chip, like the two in figure 3.10, the median inductance is somewhat lower than the targeted inductance (Table 5.2).

This approach has been successful in that only 13 detectors were found to oscillate in the first kilopixel array. It is possible that a more optimal solution could be found with a higher inductance; however, this would require careful consideration of bias points and whether the decrease in aliased noise on some detectors outweighs the loss of additional detectors to oscillations. A similar regime can be explored by reducing the detector % R_n, which reduces the frequency of the L/R roll-off and can also drive detectors into an unstable state (Figure 3.12). Preliminary results from the first season of observations (Chapter 6) indicate that we can bias the first array of detectors relatively low on the transition (a median bias of $R_0/R_n = 0.3$ and potentially even lower) without causing noticeable detector oscillations.

3.4 Detector Column Design

Our bolometer arrays are highly modular [72, 67], which enables us to screen and choose the best components for each 32 pixel column at multiple stages during the array development process. Each column module is comprised of 5 primary components: a TES bolometer chip, a chip of shunt resistors to voltage bias the TESs, a Nyquist inductor chip to band-limit the TES response, a SQUID multiplexing chip, and a silicon circuit board with Al wiring to which all the other components are mounted (Figure 3.13) [71]. The PUD bolometers [11] as well as the shunt resistor chips are fabricated at NASA Goddard's Detector Development Laboratory. The multiplexing chips and Nyquist inductor chips are fabricated at NIST, Boulder. The two-layer silicon circuit boards are fabricated at Princeton, where components are tested and built into arrays.

3.4.1 Component Screening

Prior to assembly into array columns, some of the individual components of the columns are screened for failures and to select the best components for installation into the array.

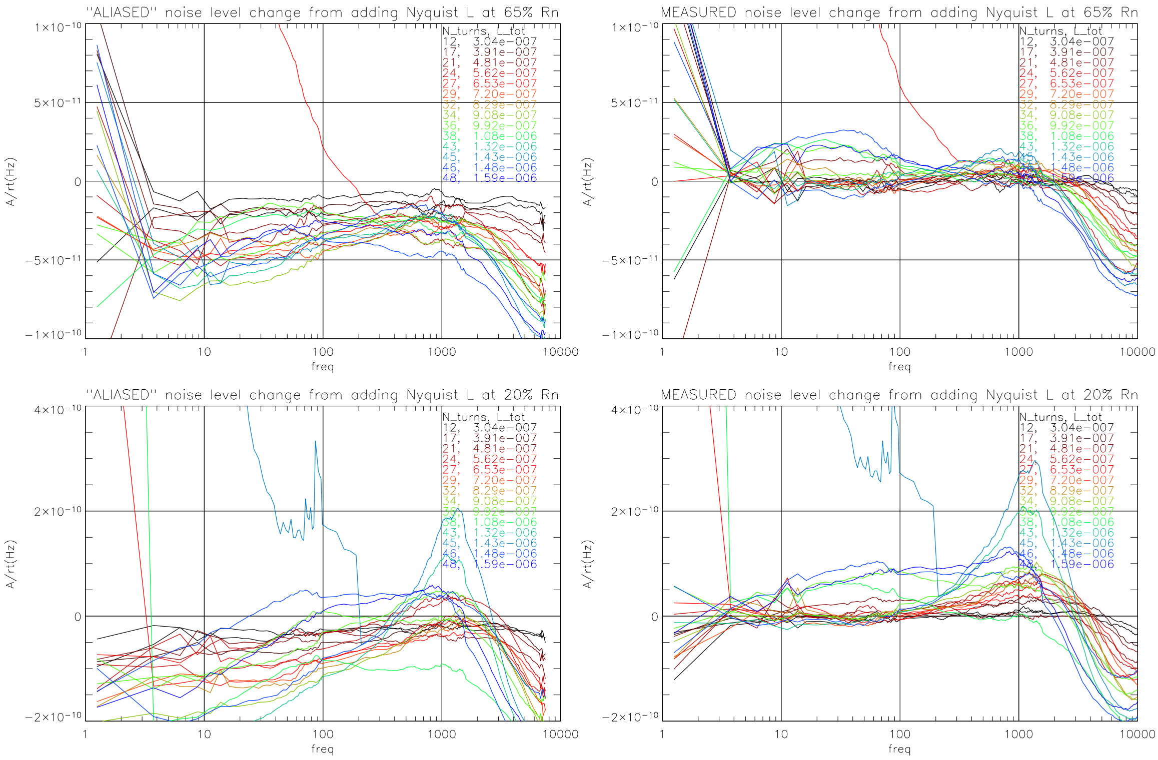

Figure 3.12: Change in aliased noise from adding Nyquist inductors. *Top:* Data from 65% R_n. *Bottom:* Data from 20% R_n. *Left:* The difference between the estimated aliased noise levels, equation (3.33), with the Nyquist inductor minus without the Nyquist inductor. At 65% R_n (top left) the noise level is improved for all inductor values and is minimized below 100 Hz by the 34-turn inductor $L_{tot} \approx 0.9$ μH. There are no significant resonances observed (except possibly the red detector with strange 1/f). At 20% R_n (bottom left) the resonances near 1 kHz increase substantially with the size of the inductance when $L_{tot} > 1$ μH. The 34-turn inductor again has the lowest noise of any detector without a strong resonance. *Right:* The case of no aliasing is studied using the difference between the measured noise levels with the Nyquist inductor minus without the Nyquist inductor. On these plots, we observe that the noise level appears to be consistent with no significant in-band increase until $L_{tot} > 0.9$ μH, which also points to the 34-turn inductor being optimal. Out of the 20 measurements, only one lower inductance detector displays an exception to this trend.

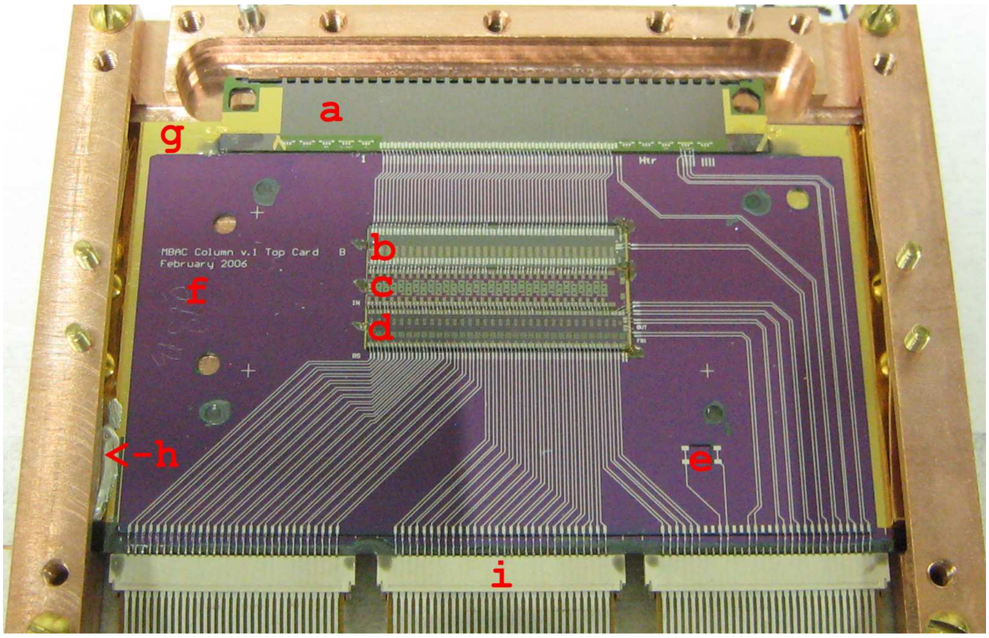

Figure 3.13: Detector column in a SRDP testing mount. Each detector column comprises the following components: (a) folded detector chip (the bolometer absorption surface is facing towards the top of the photo and cannot be seen from this angle); (b) shunt resistor chip (near the middle of the chip wirebonds have been removed from a problematic detector to prevent bias current from flowing through the detector or SQUID input coil as described in Table 3.5.6); (c) Nyquist inductor chip; (d) SQUID multiplexing chip; (e) Ruthenium oxide (ROx) thermistor location, except no ROx was installed on this column; (f) silicon top card with Aluminum wiring; (g) silicon bottom card with gold layer that is used to heat sink all the components including through gold wirebonds to the detector chip; (h) heat sinking wire soldered onto the gold layer on the bottom card, the wire can be seen exiting the mount near the lower left corner; (i) zero-insertion force (ZIF) connectors and the flexible circuitry that connects each column to a detector backplane (Appendix B).

Shunt resistor chips

The shunt resistors are characterized in a liquid ^{4}He dip probe in groups of eight chips. They are tested through a four-lead measurement of the sum resistance of the 32 bias resistors on each chip. The measurements are made at a variety of different driving currents to check for resistance variability with bias current. During this process we also confirm that the critical current of the shunt is > 5 mA, roughly ten times the typical bias current for the detectors.

SQUID multiplexing chips

The SQUID multiplexing (mux) chips are also tested in groups of eight in the ^{4}He dip probe; however, much more detailed screening is required than for the shunt chips, because of the complexity of the components. For each mux chip the SQUID critical currents, I_cs, are measured on all 33 stage 1 (S1) SQUIDs. It is important that we have minimal scatter in the S1 I_cs, since each row of 32 S1 SQUIDs (on 32 different columns/mux chips) will be biased in series (Figure 3.3).

We also probe for unwanted shorts between all accessible combinations of lines on the mux chips. This is critical, because in the past we have observed different combinations of shorts between the S1 and S2 SQUID feedbacks, S1 and S2 SQUID biases, and S1 SQUID inputs. These shorts are thought to be due to poor formation of the oxide layer between wires crossing over each other, or due to excess metal deposition during fabrication [32]. Shorts like these can prevent entire columns or portions of columns from functioning, or at a minimum, they can prevent proper tuning of the SQUIDs in the array. The latter occurred on three columns in the CCam 8×32 prototype array. All three of the columns had shorts between the stage 2 SQUID feedback (S2 FB) line and another of the lines listed above. By removing connector pins from the Multi-Channel Electronics instrument backplane that linked the S2 FB to the system ground, we were still able to use some of the detectors on these columns, however, the SQUID tuning could not be made reliable, because there was always a random uncontrolled flux offset in the S2 SQUID. The result was that more than half of the detectors on those three columns were often prevented from achieving a stable lock. This is even worse than having fewer functional detectors, because the poorly locked ones sometimes result in the PI loop sweeping the S1 feedback as it searches for a good lock point, which couples into the signals on other detectors in the same column. Most failures like these can be easily observed by measuring room temperature resistances between all combinations of lines. Detailed continuity checks to search for these failures were implemented after discovering the failures in the prototype array.

Si cards

Another major electrical failure mode was caused by slight misalignments of the silicon cards during laser dicing. When the laser dicer cuts through the Aluminum traces on the silicon card, it makes an electrical connection through the silicon oxide layer, and appears to dope the bulk silicon in such a way that electrical connections can form between many of the cut Aluminum traces. Sometimes the charge carriers for these shorts do not freeze out of the conduction band upon cooling the column to 0.3 K, leaving electrical connections between the shorted lines. Any columns that are known to have laser diced traces are deemed unacceptable for the array.

Detectors

After fabrication at GSFC, each detector chip is carefully inspected for defects before being transported to Princeton, where another inspection occurs. Each pixel is examined for problems like broken legs, incomplete etching or over-etching. The wiring for every pixel is studied to find shorts caused by excess metal deposition and open circuits. Chips that pass these inspections with two or fewer failures are mechanically folded by: laser dicing through the supporting structure at the ends of the column, inserting an absorbing silicon backbar behind the pixels, and folding and epoxying the frame, as described by J. Lau [67].

3.4.2 Column assembly and pre-screening

The successfully screened mux, shunt, and folded TES bolometer chips are assembled into column modules on silicon cards with an unscreened Nyquist chip (Figure 3.13). These five components are varnished together (using Lakeshore [63] varnish, VGE-7031) for the first round of cryogenic testing to facilitate removal if major problems are discovered or created during column testing. After successful testing, the detector chips are carefully aligned (Section 5.3.1) and epoxied into place (using 3M [1] Scotch-Weld Epoxy Adhesive 2216 B/A Gray) in preparation for installation into the array.

Numerous mechanical failure modes have caused partial to total column failures. In addition to those, a large variety of electrical failure modes have been encountered. Resistance measurements at room and cryogenic temperatures between all potentially shorted combinations of lines have been implemented to detect these. Some of them can be detected during warm probing and 4 K mux chip characterization measurements, like the mux chip shorts between the S2 FB and S1 FB discussed above. Others (such as shorts between the S1 bias and S1 input lines) require the entire column to be assembled because nothing is connected to the S1 input lines during the 4 K dip probe testing. Once a column passes all of the resistance checks, it is ready to begin the detector column characterization process.

3.5 Detector Column Characterization

Each column of 32 bolometers is subject to a series of tests prior to insertion into an array. These tests are conducted in two Super-Rapid Dip Probe (SRDP) dewars [72] developed by N. Jarosik, which can cool from room temperature to 0.3 K in a few hours. The SRDPs use analog electronics for the flux-lock loop calculation, which have low noise and allow characterization of the detector response to frequencies above the electrical band limit of the detector circuit (Figures 3.11 and 3.18). The tests performed on every detector include: measurements of the SQUID V–ϕ curves, TES T_c, Johnson noise spectra with the TES superconducting, load curves, and multiple noise measurements on the transition. Based on these measurements, columns for the final array have typically had $> 90\%$ pixel yield. The few bad pixels on each column are caused by a variety of different failure modes (Table 3.3), including: mechanically broken pixels, unresponsive or open stage 1 SQUIDs, electrical shorts on the TES or the mux chip, and oscillating detectors at certain biases (Figure 3.19).

3.5.1 SQUID response

SQUID V–ϕ curves are the first data acquired on each column to confirm the functionality of the S1 SQUID for each bolometer and to tune up the SQUIDs in preparation for other measurements. In addition to testing the SQUID functionality, the continuity through the TES loop is tested by sweeping the detector bias with the detectors superconducting (Figure 3.14). So long as the detector loop is superconducting and the shunt resistor is not, all the current goes through the detector and is measured by the SQUID. By comparing the S1 FB current, I_{fb}, per ϕ_0, and the detector bias current, I_b, per ϕ_0, we are able to check the mutual inductance ratio of the SQUIDs,

$$M_{rat} \equiv \frac{M_{in}}{M_{fb}} = \frac{I_{fb}/\phi_0}{I_b/\phi_0}, \tag{3.34}$$

where M_{in} is the mutual inductance between the SQUID and the input coil and M_{fb} is for the feedback coil. Direct measurements of M_{in} are made by sweeping current through the dark SQUID input. The combination of the dark SQUID and detector bias line measurements shows that there is negligible parasitic resistance in the TES loop. For the generation of mux chips used in the first array (Mux06a design), $M_{fb}^{-1} = 64$ μA$/\phi_0$ and $M_{in}^{-1} = 7.5$ μA$/\phi_0 \rightarrow M_{rat} = 8.5$.

3.5.2 Johnson noise

Noise measurements are made while the TESs are superconducting to extract the shunt resistance, R_{sh}, for each detector. Thermal fluctuation noise in R_{sh} and any parasitic resistance, R_p, in the TES loop generates a white Johnson noise spectrum, which depends on the load resistance $R_L = R_{sh} + R_p$. Since the SQUID readout system measures current, the Johnson noise level, $I_{J_{noise}}$, increases as the resistance goes down [51],

$$I^2_{J_{noise}} = \frac{4k_bTB}{R_L}, \tag{3.35}$$

where k_b is Boltzmann's constant, T is the temperature of the resistor, and B is the measurement bandwidth. The white Johnson noise is rolled off by the one-pole L/R filter in the TES loop, so that at high frequencies the noise level is dominated primarily by SQUID noise. We measure the Johnson noise between 0 Hz - 100 kHz (Figure 3.15), so that we can

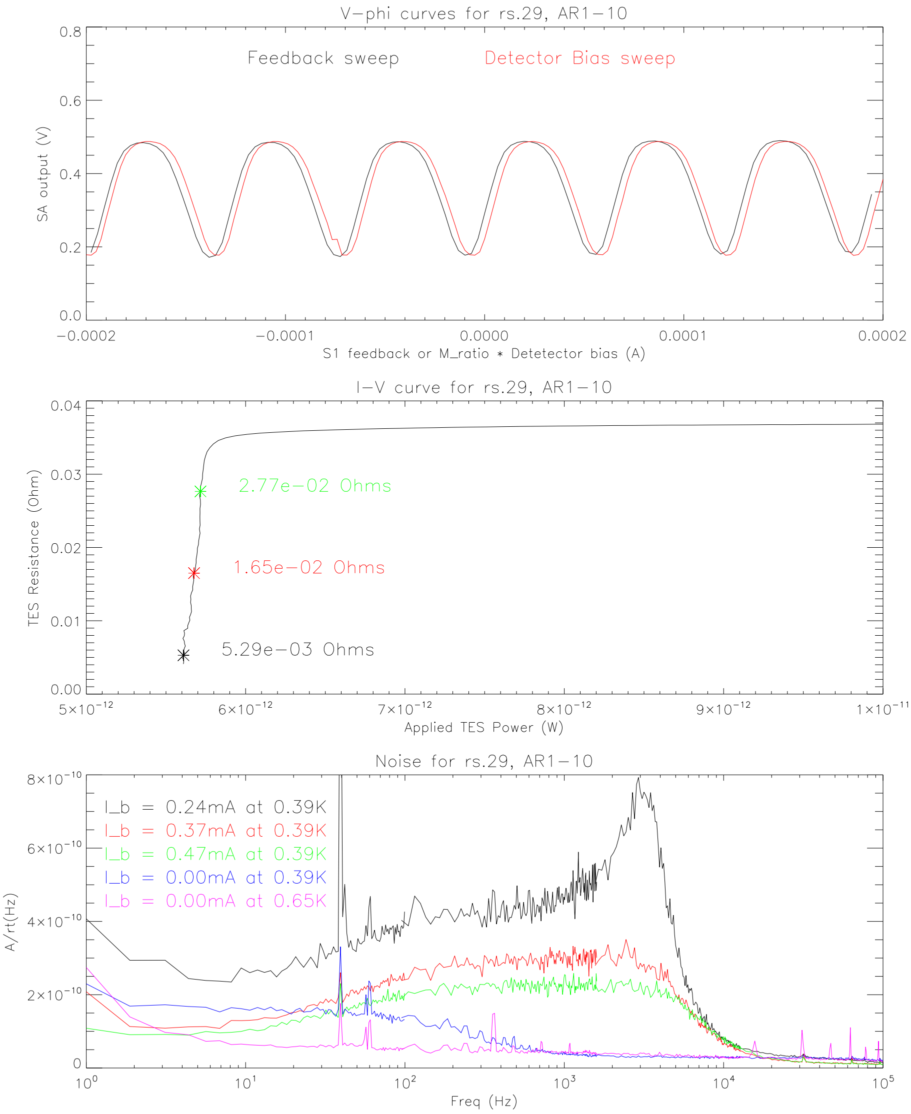

Figure 3.14: SRDP data from a single detector. These plots are generated for every detector and examined to characterize the functionality of each detector. *Top:* V–ϕ curves acquired by sweeping the S1 SQUID feedback as well as the TES detector bias with the TES superconducting. The arbitrary DC offset between the curves is due to the different conditions under which the curves were acquired. *Middle:* Load curve acquired at a bath temperature of 0.39K. *Bottom:* Noise acquired at different biases that correspond to the bias points on the load curve as well as Johnson noise measurements with the TES superconducting (blue) and normal (pink). The rise in the black noise curve near $\sim$3 kHz occurs low on the transition as a result of the decreasing L/R filter frequency (Section 3.3.4).

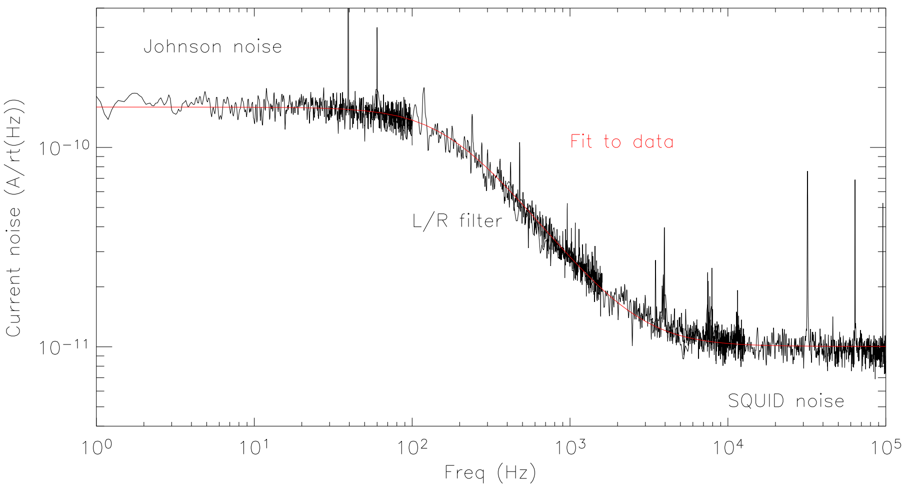

Figure 3.15: Johnson noise data from the SRDP while the detectors are superconducting allow us to fit the load resistance, R_L, the total inductance, L, and the background noise level, $I_{bk_{noise}}$. The spikes in the data were removed before fitting. The roll-off is due to the L/R_L response of the TES loop. The best fit is shown in red.

fit all three of these features to extract R_L, the total loop inductance, $L \approx L_{Ny} + L_{in}$, and the background white noise level, $I_{bk_{noise}}$, using

$$I^2_{noise} = \frac{I^2_{J_{noise}}}{1 + (\omega L/R_L)^2} + I^2_{bk_{noise}}. \tag{3.36}$$

The V–ϕ and load curves show that $R_p << R_{sh}$, so we assume $R_L = R_{sh}$ from the fits. This was expected, since all components in the TES loop (even the aluminum wire bonds) are superconductors except the shunt resistors.

3.5.3 Load curves

Detector load curves are acquired to measure R_n, select bias points for noise measurements, and characterize the superconducting transition. Because of the biasing configuration, the detector response to changes in bias current, I_b, is strongly hysteretic. Starting from $I_b = 0$, as I_b increases all of the current goes through the superconducting TES. This continues until the TES critical current is reached at which point the TES is suddenly driven normal. Critical currents have been measured as high as 5 mA, which corresponds to $\sim$2 nW of power through the normal TES or roughly 200 times the saturation power of the bolometer.

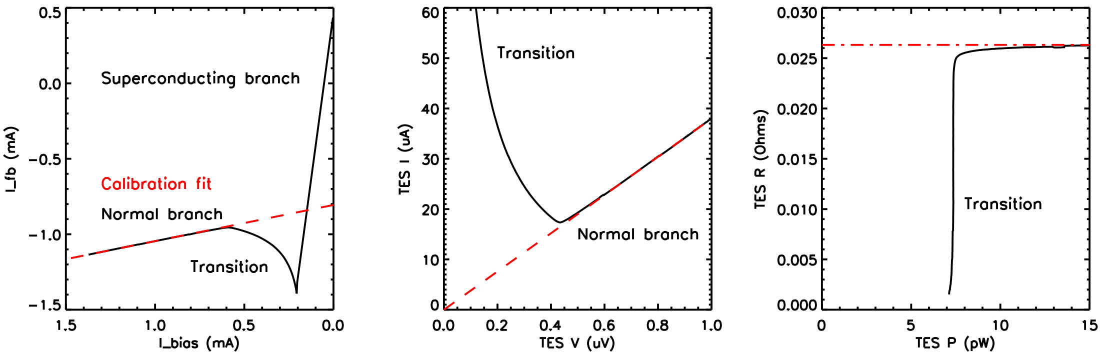

Figure 3.16: Load curve calibration. *Left:* Raw load curve data I_b versus I_{fb}, equation (3.34) which shows the arbitrary DC offset that is calibrated out by fitting the normal branch of the curve. *Middle:* Calibrated TES data in the I–V plane. *Right:* Calibrated TES data in the R–P plane. The bias power is nearly constant through most of the superconducting transition because these bolometers have narrow transitions, $\Delta T_c \approx 2$ mK, compared to the difference $T_c - T_{bath} \approx 200$ mK.

Once the detector is normal, the majority of the current flows through the shunt resistor. By decreasing the bias current through a normal detector we can simultaneously measure the current and voltage response, which is known as an I–V or load curve. As the bias current is decreased the measured TES current response remains nearly linear until the bias power, $P_J = I^2R$, drops below $P_{sat} - P$, where P is the optical power, and the bolometer enters the strong negative electrothermal feedback regime. The TES current is measured throughout this regime by SQUIDs, which have unknown DC offsets. These current offsets can be calibrated by measuring the normal branch of the load curve and assuming the TES resistance is constant in this regime (Figure 3.16). After calibration, the detector parameters throughout the load curve can be calculated since R_{sh} and I_b are known and I comes directly from the SQUID measurements and equation (3.34),

$$V = R_{sh}(I_b - I) - R_pI. \tag{3.37}$$

Since $R_p \ll R_{sh}$, we can ignore it here as well.

The calibrated load curve data allow us to select a good detector bias current to drive the majority of the detectors on the column onto the transition. For column noise characterization, the median currents to drive the detectors on the column to 0.2, 0.5, and 0.8 R_n

are selected. The load curves also provide estimates of the detector responsivity throughout the transition, equation (3.24), which are used to calibrate optical signals and noise.

3.5.4 Critical temperatures

Superconducting critical temperatures, T_c, are measured for each bolometer. These measurements are made by increasing the bath temperature to near the critical temperature and sweeping the detector bias over a small range ($\pm 3\ \mu$A) at a variety of different temperatures near T_c. When the detector is above T_c the feedback amplitude is a factor of $R_{sh}/(R_{sh}+R_n)$ smaller than when the detector is superconducting. Even these small currents will drive detectors near T_c normal at the higher biases. By making measurements at temperatures with a few mK steps between them, we can derive fairly accurate T_c for all pixels in a short period of time. This method has been confirmed by Johnson noise measurements of the T_c with zero bias current.

3.5.5 Noise and impedance

Using the detector bias currents selected from the load curves, noise data are acquired from all detectors near 0.2, 0.5, and 0.8 R_n (Figure 3.14). These data are critical for verifying the functionality of the detectors, because some detectors are unstable when biased onto the transition and exhibit electrothermal oscillations that can couple into neighboring pixels (Figure 3.19).

The detector noise does not fit the predictions of the isothermal model for TES bolometers presented in Section 3.1 [54], because there is an excess of noise in the mid-frequency range (Figures 3.14 and 3.18). Similar excess noise has been observed and explored by other research groups [43, 49, 107], and discrepancies from the isothermal model are also found in complex impedance measurements of the bolometers.

R. Dünner and T. Marriage have led an effort to model data from these bolometers as a three element system with isolated heat capacities (Figure 3.17) [43, 71]. They found that the noise and impedance data can be explained well by a model in which the TES and absorber heat capacities are thermally isolated and connected to the bath through the bolometer silicon (Figure 3.18). This seems plausible since these bolometers have a small

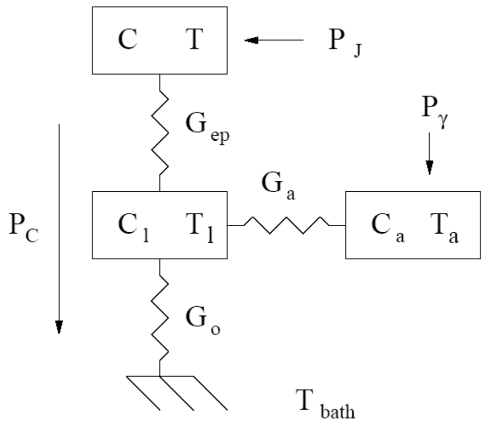

Figure 3.17: The three block detector model developed by R. Dünner and T. Marriage. The TES (top) and the ion-implanted absorber (middle right) are treated as though they are thermally isolated from the bulk silicon (middle left) by the thermal conductivities G_{ep} and G_a. The Joule power, P_J, and the photon power, P_γ, are generated in the isolated TES and absorber respectively. The bulk silicon is heat sunk to the bath through the weakly conducting bolometer legs, which have thermal conductivity G_0 as defined in equation (3.3). This model is fit to data in Figure 3.18 (Figure courtesy of T. Marriage [71].)

TES (50 μm $\times$ 50 μm for the prototype bolometers and 80 μm $\times$ 80 μm for the current design), a thin absorber layer ($\sim$0.06 μm), and a relatively large (1.05 mm $\times$ 1.05 mm $\times$ 1.1 μm) bulk Si.

The model has been helpful in providing a physical description for the bolometer behavior; however, there are a large number of free parameters in the fits [71] which can result in degenerate solutions. Because of these degeneracies, we have used the model for guidance but have attempted to optimize the bolometer parameters empirically, such as the Nyquist inductance discussed in Section 3.3.4. In Table 3.2 we show the isothermal model parameters for one of the 145 GHz array bolometers which were obtained from a fit to the more complex model using R. Dünner's code. These parameters are used for some of the estimates presented in this chapter.

3.5.6 Detector failure modes and remediations

There are a variety of different ways that individual detectors can fail in an otherwise working column (Table 3.3). These are diagnosed through a combination of the screening

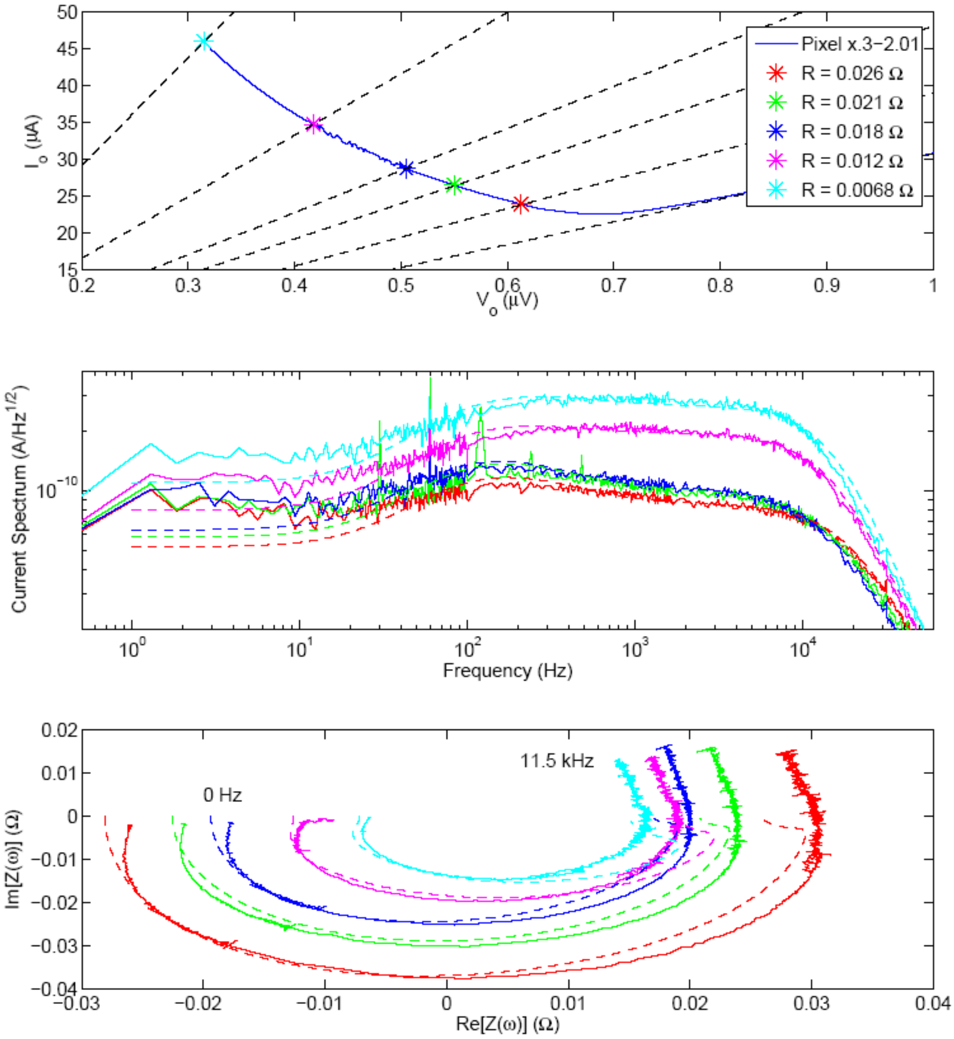

Figure 3.18: Detector noise and complex impedance data with fits to the three block detector model (Figure 3.17). The model developed by R. Dünner and T. Marriage was used to simultaneously fit the noise and complex impedance data acquired from bolometers. Load curve (top, where dashed lines are lines of constant resistance), noise (middle), and complex impedance (bottom) data (solid) at different bias points (colors) that was fit to the three block model (dashed). Note that an isothermal bolometer model does not predict the rise in current noise level between roughly 100 Hz – 1 kHz [54]. (Figure courtesy of T. Marriage [71].)

R_0/R_N	0.79	0.47	0.16
Inputs			
I_0 (μA)	18	23	39
V_0 (μV)	0.39	0.30	0.17
R_0 (mΩ)	22	13	4.4
Fit Results			
T_0 (K)	0.494	0.494	0.494
α_I	220	330	640
β_I	0.13	0.38	2.3
C_{tot} (pJ/K)	14	14	14

Table 3.2: Bolometer parameters from fits to noise and complex impedance data. The top group of parameters are measured from a load curve, and the bottom group are the isothermal model terms fit by R. Dünner's code, where C_{tot} is the sum of the heat capacities fit to all three isolated blocks in the model (Figure 3.17). Additional inputs to the fitting code include the following parameters: $R_{sh} = 0.83$ mΩ, $R_n = 28$ mΩ, $L = 0.99$ μH, $T_b = 0.397$ K, $n = 4.5$, and $K = 260$ pW/K^n, where n and K are defined in equation (3.2) and result in $G = 99$ pW/K. The parameters in the table were fit to a detector (8x32-17, rs.07) by J. Appel using code developed by R. Dünner, and the inputs to the fitting code were calculated by Y. Zhao.

methods described in Sections 3.4.1 and 3.4.2 and the data acquired from each detector (Section 3.5). It is critical that these failure modes are carefully tracked and accounted for because some of them (such as open S1 bias lines, shorts on the mux chip, or oscillating detectors) have the potential to be devastating to the array. Table 3.3 shows how each type of failure is remediated before inserting the detector columns into an array.

By recognizing, tracking, and repairing the failure modes presented here, we have prevented all of these problems from arising in the 145 GHz array, and achieved almost 90% pixel functionality in the array (Chapter 5).

Acknowledgements

The combination of pop-up detector TES bolometers read out by a time-domain SQUID multiplexing system was primarily conceived by H. Moseley of GSFC and K. Irwin of NIST. The detector model in this chapter is a partial summary of the model presented by Irwin and Hilton [54]. The SQUID multiplexing work was greatly aided by discussions with T. Marriage and training sessions with R. Doriese and the NIST team. Z. Kermish and J.

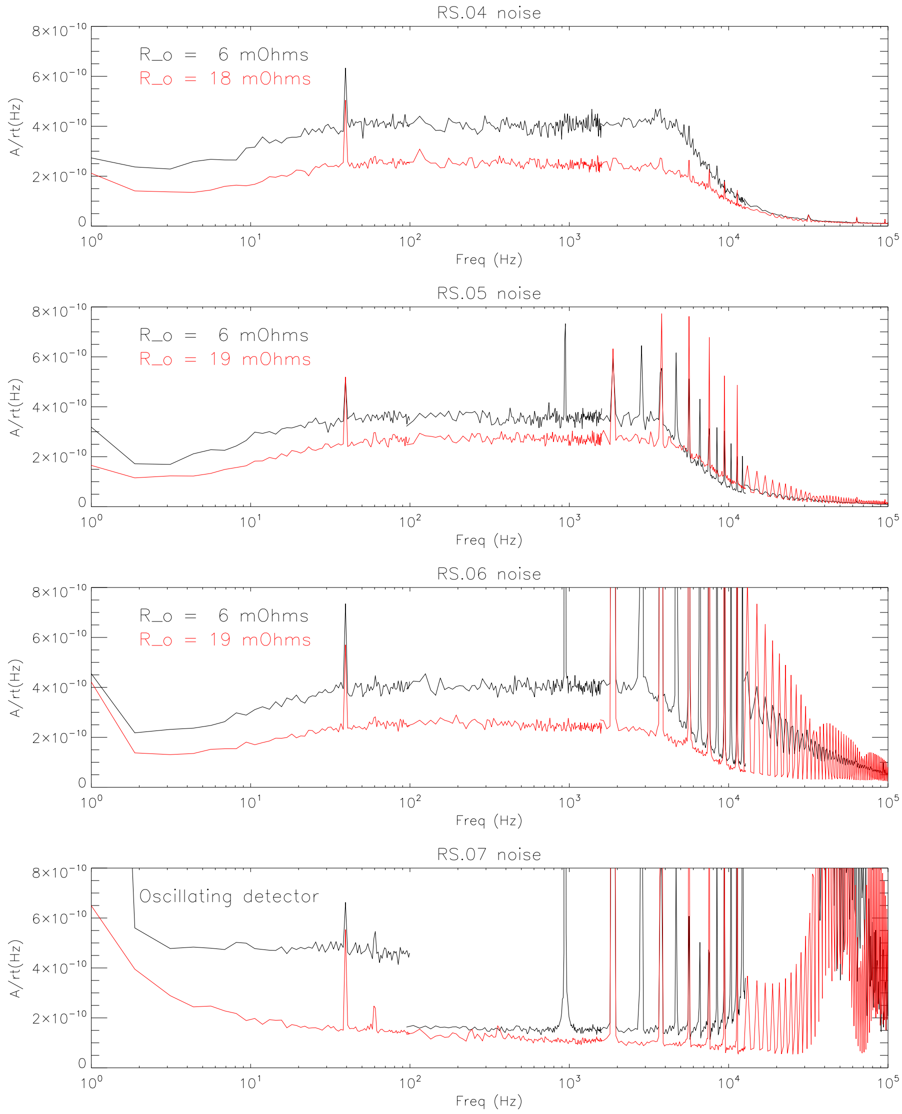

Figure 3.19: Noise during electrothermal oscillations. When biased onto the transition, some bolometers are driven into unstable electrothermal oscillations, such as row 7, or RS.07, in the bottom plot. These oscillations couple into neighboring detectors with a decreasing amplitude as a function of distance, as shown in RS.06 and RS.05. In this instance, the coupling drops to near the detector noise level three bolometers from the source, as shown in the top plot of RS.04. These appear to be electrothermal oscillations because the oscillation frequency varies with the detector resistance. It is important to remediate this failure mode because the oscillations that couple into neighboring detectors may be aliased into our signal band during observations.

• Mechanical bolometer failure. → Remove any remaining pieces of the bolometer to prevent damage to others.
• Electrically open TES-loop on silicon board, shunt, mux, Nyquist, or detector chip. → No remediation required.
• Detector that remains superconducting after applying a bias current of ~5 mA. → Remove wirebonds for that detector from shunt chip to prevent excess current through S1 SQUID input.
• Oscillating or unstable detector. → Remove wirebonds for that detector from shunt chip to prevent biasing of the detector, because the noise could couple into neighboring detectors (Figure 3.19)
• Short between S1 bias or input and another line on the mux chip. → Disconnect wirebonds from the shorted S1 bias or input line to isolate the short and add repair wirebonds as necessary.
• Electrically open S1 SQUID bias line on silicon board or mux chip. → Short across Al traces on silicon board to prevent open circuit on an entire row.
• Unresponsive S1 SQUID with an electrically continuous bias line. → No remediation required, but a shorting bond across S1 bias line is added for safety.

Table 3.3: Detector failure modes and remediations.

Burwell did the very first testing of mux chips at Princeton. The mux chip testing and shunt screening was primarily run by R. Fisher who worked with A. Dahlen to automate the mux testing and was aided by K. Martocci, L. Sun, S. Denny, and S. Iyer. T. Marriage and the NIST team were especially helpful in understanding the functionality of the NIST digital feedback electronics. The detector column parameter selection was a gradual process with input from numerous members of the ACT collaboration primarily at GSFC, NIST, and Princeton. The column design and prototyping were worked out by N. Jarosik, T. Marriage, J. Lau, and S. Marriage. Column production was primarily done by O. Stryzak, L. Parker, B. Harrop, T. Essinger-Hileman, K. Martocci, L. Sun, and J. Ling. The dip probes were designed and made functional for detailed detector characterization by N. Jarosik with help from T. Marriage, A. Hincks, and R. Dünner. Automation of the column testing done in collaboration with Y. Zhao. Recent column data was analyzed primarily by Y. Zhao, me, and S. Staggs. Column testing was carried out primarily by Y. Zhao with help from me, J. Appel, T. Essinger-Hileman, and A. Sederberg.

Chapter 4

Array Readout, Magnetic Field Sensitivity, and Characterization Techniques

The SQUID readout system is designed to have a high signal-to-noise response to the small magnetic fields generated by currents in the TES loop (Section 3.2). This also makes the readout prone to contamination from external magnetic fields. In addition, superconducting materials (such as the molybdenum in the TES) have an inherent sensitivity to magnetic fields [104]. Potential sources of contaminating fields include the low frequency modulation of the Earth's field as the telescope scans during observations (Section 2.5) as well as higher frequency changes in the motor currents used to drive the telescope. These varying magnetic fields can contaminate our observations and adversely affect data acquisition with the room temperature array readout electronics.

In this Chapter we explore the sensitivity of the TES and SQUID response to magnetic fields, then discuss the capabilities of the room temperature readout electronics and the optimization of detector array measurements. We describe the automated SQUID tuning procedure developed to correct for field-induced SQUID offsets as well as automated load curve acquisition and detector bias selection for the array. We finish with a discussion of a fast approach to array characterization that has been implemented in the Multi-Channel

Electronics system and allows full-array characterization of sky power, detector responsivities, and detector time constants on time scales as short as a few seconds.

4.1 Magnetic Sensitivity

4.1.1 Detector sensitivity

A detector's response to applied fields is due to a reduction in T_c of the TES as well as a broadening of the superconducting transition width as the field increases. A change in T_c of the TES changes the saturation power (Equation 3.2), and thus, the current going through the bolometer. The change in T_c was explored in both the SRDP and CCam by installing wire coils inside the magnetic shielding layers. The location of the coils was selected to orient the field perpendicular to the plane of the bolometers and minimize the field gradient across the column of detectors, while also minimizing the component of the field along the most sensitive axis of the SQUIDs.

Noise measurements were made at different bath temperatures to determine the TES T_c in constant magnetic fields. When the TES warms through the superconducting transition, the resistance in the TES loop increases from $R_{sh} \approx 0.7$ mΩ to $R_{sh} + R_n \approx 32$ mΩ, which causes a large reduction in the Johnson current noise (Equation 3.35). The SRDP measurements (Figure 4.1) were made using a spectrum analyzer to measure the noise level. These are more accurate T_c measurements than those described in section 3.5.4, because no bias current is applied, and the measurements are made at a constant resistance (of $\sim R_n/2$) by adjusting the temperature servo in 0.2 mK increments to maintain a constant Johnson noise level. The low level and stability of background loading in the SRDP are also critical for the accuracy of these measurements. Measurements of multiple detectors were made in CCam while multiplexing and slowly sweeping the bath temperature with similar results, however, optical loading drifts in CCam make the measurement more difficult and prone to error.

The measurements indicate that $T_c \approx T_{c_0} - wB^2$, where $w \approx 43$ mK/G^2 (Figure 4.1). This can be used to estimate the signal from a change in the magnetic field at the detectors during observations. Using Equation 3.3 we can convert this to a change in saturation

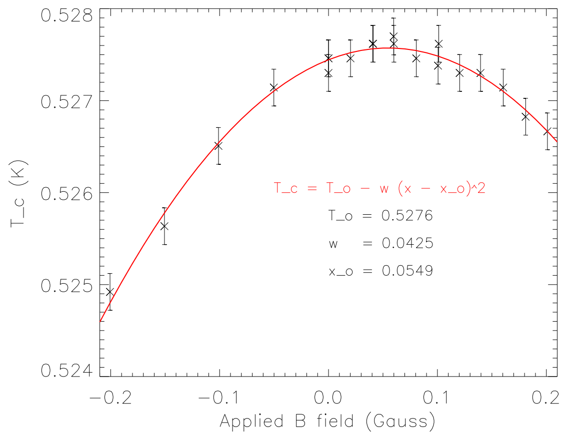

Figure 4.1: TES T_c versus magnetic field. These measurements were made on a bolometer in the SRDP. The maximum $T_c = T_{c0}$ was found to occur at an applied field of $x_0 \approx 55$ mG, which is an indication of a background field in the SRDP that is not excluded by the shielding. Ignoring this background, the general result from the fit is $T_c \approx T_{c0} - B^2 * 43$ mK/G^2.

power, or equivalently bias power under constant loading conditions, P_{J_0}, with estimates of $n \approx 4$, $K \approx 150$ pW/K^n, and $T_c \approx 0.5$ K for these detectors. A bias voltage estimate, $V_0 \approx 0.3$ μV, allows conversion into a change in detector bias current, and we find

$$\frac{\delta I_0}{\delta B} \approx \frac{\delta I_0}{\delta P_{J_0}} \frac{\delta P_{J_0}}{\delta T_c} \frac{\delta T_c}{\delta B} \approx \frac{nKT_c^{n-1}(-2wB)}{V_0} \tag{4.1}$$

Changes in T_c increase as we move away from zero field, so we estimate the response near $B_{DC} \approx 0.05$ G, or $\sim 1/10$ the Earth's field, which is roughly the DC field amplitude measured in the SRDP (Figure 4.1) and is larger than we expect to have inside the MBAC magnetic shielding:

$$\frac{\delta I_0(0.05 \text{ G})}{\delta B} \approx 1 \ \mu\text{A/G} \tag{4.2}$$

In Section 4.1.2 this is compared to a SQUID sensitivity estimate.

The detector noise and complex impedance were also studied as a function of applied field in the SRDP. Qualitatively similar results were found to those described in the Ullom et al. paper from NIST [107], including a large reduction in the amplitude of the excess noise in the mid-frequency range (Section 3.5.5) with an applied field and a widening of the superconducting transition width. In addition, large changes were measured in the frequency at which the real component of the complex impedance goes to zero; however, when similar tests were done in CCam, optical measurements of the detector time constants (Section 3.3.2) did not show a strong dependence on applied field.

4.1.2 SQUID sensitivity

The most sensitive component in the SQUID multiplexing system to changes in external magnetic fields is expected to be the superconducting transformer loop that inductively sums the 33 S1 SQUIDs into the S2 SQUID on each column (Figures 3.4 and 4.3). The SQUIDs themselves are also exquisitely sensitive to fields; however, they have effective collection areas ($A_{S1} \approx 2.5{*}10^{-9}$ m^2 and $A_{S2} \approx 1.4{*}10^{-9}$ m^2) that are smaller than the collection area of the 33 summing coils in the transformer loop ($A_{sc} \approx 7.6{*}10^{-7}$ m^2) [55].[1] There is a factor of ~110 gain due to mutual inductances between the SQUIDs and the summing coils, which brings these numbers closer together, but the summing coils still dominate the magnetic pickup. The summing coils comprise a relatively large superconducting loop, which acts like a perfect diamagnet in small fields (Lenz's law), canceling changes in magnetic flux through the loop with compensating superconducting currents. These changes in current have an analogous effect to changing DC offsets in the S2 SQUID feedback.

The mux chip sensitivity to applied fields was measured in CCam as well as in the 4K liquid ^{4}He dip probe used for screening mux chips. The most carefully calibrated measurements were made in parallel with magnetic shielding tests in CCam by driving an external AC field with a large coil and simultaneously measuring the response inside the dewar with a smaller coil and the S2 SQUID on a mux chip. These measurements were calibrated with warm measurements of the pickup between the two coils after removing the magnetic shielding. The combination of these measurements allows us to extract the mean field attenuation by the magnetic shielding across the CCam focal plane, and thus estimate the local field at the mux chip while measuring the mux chip response (Figure 4.2). With only the S2 SQUID turned on, we found that the sensitivity was $\delta \mathrm{S2}_{\phi_0}/\delta B \approx 300{\pm}100\ \phi_0/\mathrm{G}$. This sensitivity was measured to be nearly constant at different field amplitudes (attenuated fields between ~0.5 mG and ~50 mG) and over a range of oscillation frequencies (between 0.05 Hz – 0.5 Hz), which includes the nominal ACT scan frequency of ~0.2 Hz. Because of

[1] These calculated effective collection areas are for the Mux05c design and are considerably larger than is expected for the gradiometric Mux06a design (Figure 4.3) [55].

the consistency of the results at the lowest frequencies, we believe that this estimate holds at oscillation frequencies below the measured range (Figure 4.2).

These measurements were made with a 50 μm thick strip of superconducting Nb foil underneath the mux chip for additional shielding, and the effect of this additional shielding has not yet been removed. It is standard practice, however, to mount the mux chips on Nb foil on all our detector columns, so the combined response of the mux chip plus Nb foil presented here is the most interesting quantity for this comparison. The effect of the Nb foil can be estimated, however, using the magnetic flux quantum to convert the SQUID sensitivity into an effective SQUID collection area of $\sim 6 * 10^{-9}$ m^2. Comparing this to the sum of the predicted summing coils collection area over the gain plus the S2 SQUID collection area, the Nb appears to be attenuating the field by roughly a factor of two-thirds.

The NIST team has recently developed a novel mux chip design (Mux06a) to minimize the magnetic pickup. The measurements and effective areas above all refer to a previous design (Mux05c). A number of changes were made between the two designs of chips to reduce the coupling to external magnetic fields; the greatest reduction is a result of converting the S1 and S2 SQUID coupling coils and the transformer loop summing coils into gradiometric configurations (Figure 4.3). Because of excess magnetic pickup in the CCam prototype [77, 3], the Mux06a design was selected for use in the ACT detector arrays.

Magnetic sensitivity measurements were made of both Mux05c and Mux06a mux chips simultaneously in the 4 K ^{4}He dip probe. With only the S2 SQUID turned on, we found that the coupling of external fields into the Mux06a chips was $\sim$9 times smaller than the Mux05c chips, or from the conversion above $\delta \mathrm{S2}_{\phi_0}/\delta B \approx 33\ \phi_0/\mathrm{G}$, justifying the use of the Mux06a design for the ACT arrays.

The mux chip sensitivity estimate can be combined with V–ϕ measurements to convert into a predicted signal response, or effective change in detector current, $\delta I_{0_{eff}}$, as a function of the magnetic field inside the shielding,

$$\frac{\delta I_{0_{eff}}}{\delta B} \approx \frac{\delta I_{0_{eff}}}{\delta I_{fb}} \frac{\delta I_{fb}}{\delta \mathrm{D}_{fb}} \frac{\delta \mathrm{D}_{fb}}{\delta \mathrm{D}_{S2_{fb}}} \frac{\mathrm{D}_{S2_{fb}}}{\mathrm{S2}_{\phi_0}} \frac{\delta \mathrm{S2}_{\phi_0}}{\delta B}, \tag{4.3}$$

where $\delta I_{0_{eff}}/\delta I_{fb} = 1/8.5$ is the mutual inductance ratio from equation (3.34), $\delta I_{fb}/\delta \mathrm{D}_{fb} = 1\ \mathrm{V}/(2^{14}\ \mathrm{DAC} * 7106\ \Omega) = 8.59$ nA/DAC is the conversion between S1 FB current and the

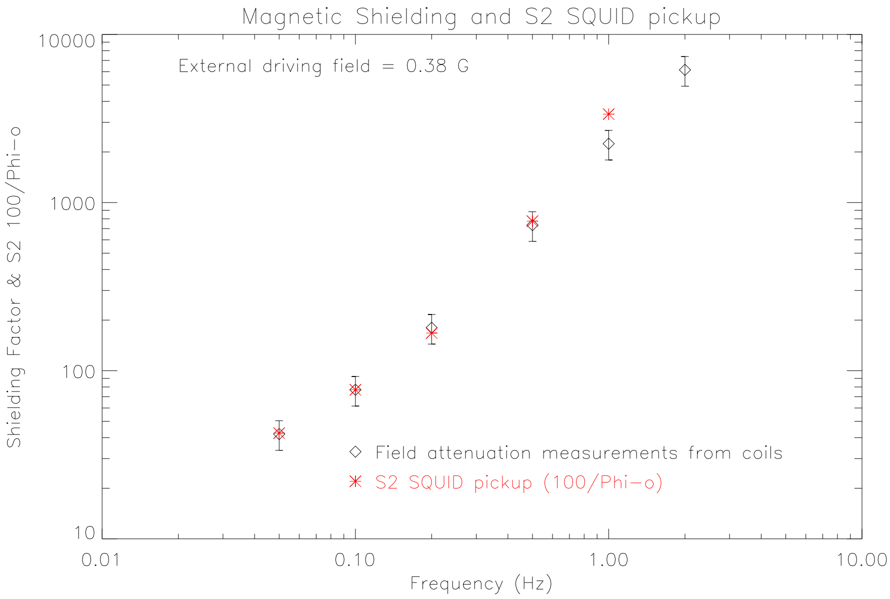

Figure 4.2: Magnetic Shielding and S2 SQUID pickup in CCam. The attenuation of the CCam Cryoperm shielding was found to have a strong dependence on the field oscillation frequency. This unexpected result was confirmed using both measurements on an S2 SQUID (red) and with a coil inside the shielding (black) and has not yet been quantitatively explained [77]. Despite the unexplained frequency response, the relative scale of the two measurements allows us to calculate the S2 field sensitivity, $\delta \mathrm{S2}_{\phi_0}/\delta B \approx 300 \pm 100\ \phi_0/\mathrm{G}$, which was measured to be nearly constant at different field amplitudes (attenuated fields between ~0.5 mG and ~50 mG) and over a range of oscillation frequencies (between 0.05 Hz – 0.5 Hz). In the figure, we see that this estimate fails near and above ~1 Hz, where the red points no longer fall within the black error bars, but the consistency at lower frequencies makes it appear as though this relationship holds for slower oscillations. Measurements versus frequency were also made in the 4 K dip probe (which has a continuous Cryoperm shield with a better aspect ratio), where there was negligible change in the attenuation over a similar frequency range. The problems with the CCam shielding design originated with the requirement that the dewar fit inside the WMAP mirror structure, which which made the use of long continuous shields impossible [3].

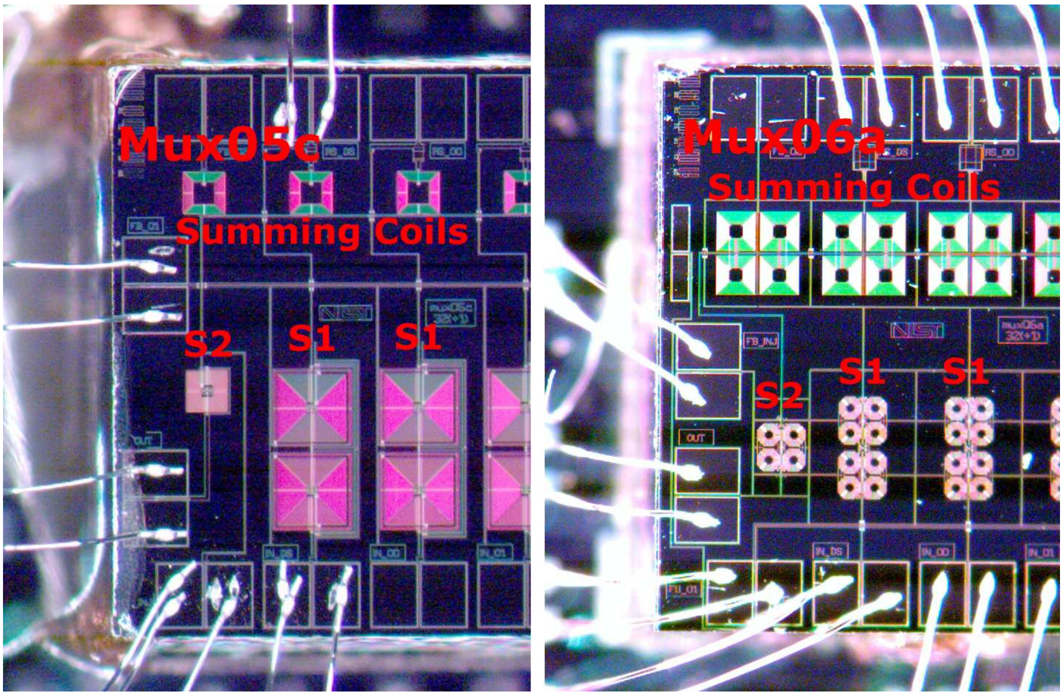

Figure 4.3: Comparison of mux chip designs. *Left*: The older Mux05c design is non-gradiometric, meaning that it is sensitive to DC changes in magnetic field as opposed to being sensitive to gradients in the field. *Right*: The new Mux06a design, which is used in the ACT arrays, has gradiometric winding of the summing coils and coupling coils for S1 and S2 SQUIDs. The coil wiring is not resolved in these photographs, but the coils themselves are the square (as well as circular on the right) objects in the photos. The S1 SQUIDs have dummy coils (and dummy SQUIDs) above the real coils to minimize crosstalk with neighboring SQUIDs and pickup of external fields. The S1 SQUID Josephson junctions are located at the center of the square coils on the left and in between the four circular coils on the right. Beyond this limited knowledge, the details of the wiring are proprietary NIST designs. Measurements of the relative pickup of the S2 SQUID and summing coils made in a 4 K ^{4}He dip probe indicate that the Mux06a chips are $\sim$9 times less sensitive to an external varying field than the Mux05c chips.

digital to analog converter (DAC) units[2] (Figure 4.11),$\delta \mathrm{D}_{fb}/\delta \mathrm{D}_{S2_{fb}} \approx 2$ $\mathrm{DAC}_{S1fb}/\mathrm{DAC}_{S2fb}$ is the slope of the S1 V–ϕ curve extracted from Step 5 of the auto-tuning procedure (Figure 4.10), and $\mathrm{D}_{S2_{fb}}/\mathrm{S2}_{\phi_0} \approx 4100$ $\mathrm{DAC}_{S2fb}/\phi_0$ is the period of the S2 V–ϕ curve extracted from Step 4 of the auto-tuning procedure (Figure 4.9). The product of all these values for a Mux06a chip is

$$\frac{\delta I_{0_{eff}}}{\delta B} \approx \; 270 \; \mu\mathrm{A/G}, \tag{4.4}$$

which is ∼270 times larger than the estimated detector response to field fluctuations around $B = 0.05$ G (Equation 4.2).

There is expected to be less magnetic shielding attenuation along the axis of the optics tube (the direction the detectors are sensitive to) than perpendicular to the optics tube (including the primary direction of SQUID sensitivity). In single cylinders, we have measured the difference between attenuation in these directions to be as large as a factor of 5–10. It seems unlikely that the attenuation difference in MBAC will be as large as a factor of 270; however, there are three concentric cylinders in the MBAC shielding, and one would expect these attenuation effects to be multiplicative. Thus, the MBAC shielding needs to be characterized (including the amplitude of any residual DC field along the optical axis) to determine whether detectors could contribute significantly to the magnetic pickup during observations.

When estimating the predicted sensitivity of SQUIDs to applied fields (Equation 4.3), all of the variables should remain constant within a column of detectors except one. The conversion between the S1 FB and S2 FB, $\delta \mathrm{D}_{fb}/\delta \mathrm{D}_{S2_{fb}}$, is the slope of the V–ϕ plots in Figure 4.10. This slope depends on the amplitude of the S1 V–ϕ curve, which is roughly proportional to the S1 critical current (Equation 3.25). The V–ϕ curve slopes for eight different columns are shown in Figure 4.10 and vary by almost 40% (at the selected cross-hairs). When SQUIDs within the same column have variable S2 FB offsets (Figure 4.7) or multi-valued lock-points (Figure 4.11), the selected lock-points will move throughout the S1 V–ϕ range, which is equivalent to changing the location of the cross-hairs in Figure 4.10.

[2]Note that the digital to analog (DAC) converter units plotted on the x-axis of Figure 4.11 are the unfiltered units applied by the S1 FB DAC. The anti-aliasing filter has a gain of 1216, so the conversion for filtered data would be $\delta I_{fb}/\delta \mathrm{D}_{filtered}$ 7.06 pA/$\mathrm{DAC}_{filtered}$.

This could easily change $\delta D_{fb}/\delta D_{S2_{fb}}$, and thus the magnetic pickup on different rows of SQUIDs within the same column by a factor of two.

The problem of variable magnetic pickup on the S2 SQUID within a column will be minimized by the next generation of Multi-Channel Electronics by multiplexing the S2 FB line, so that every SQUID is biased optimally. Further reduction of this effect is possible by minimizing the variability of the S1 SQUID critical currents. These solutions will greatly facilitate magnetic pickup removal during analysis, because the pickup should be strongly dominated by common-mode signal within each column. Until then, more creative approaches will be required for magnetic pickup removal from the detector time streams.

4.2 Readout Electronics

Two systems have been used for multiplexed data acquisition: the NIST digital feedback (DFB) electronics [91] and UBC's Multi-Channel Electronics (MCE) [37]. Both systems utilize a 50 MHz master clock which drives and synchronizes the multiplexing events. Common capabilities between the systems include: addressing the rows of SQUIDs by applying square waves to each successive S1 addressing line; applying DC bias values to the SA and S2 SQUIDs to tune them appropriately; synchronized digital sampling of the SA outputs after each row turns on; synchronized PI response calculation and application to the S1 FB lines based on SA output, or error, measurements from the previous frame (Figure 3.5). In addition, the NIST electronics can store every frame of data acquired onto a computer (through $n + 3$ fiber optic cables, where n is the number of columns) and one can easily connect any input or output to an oscilloscope or signal analyzer for realtime data viewing. The MCE was designed to be part of a facility instrument for SCUBA-2 [50], and does not have those specific capabilities, but it has numerous others that make it superior for field use, as described below.

4.2.1 Rate selection

The time-domain multiplexing (TDM) rate is limited by the required settling time of the SA output after turning on a row of S1 SQUIDs (Figure 4.4). It is important to drive this rate as high as the system is capable of to reduce aliasing of high frequency SQUID noise into the signal band (Figure 3.6). The rate was selected using the NIST electronics, which enable viewing of the real-time data on an oscilloscope at faster data rates than either TDM electronics system is capable of storing (Figure 4.4).

The settling time after turning on an S1 SQUID row was measured for multiple rows to be ~1.7 μs (Figure 4.4). A slightly longer settling time of 1.8 μs was selected, which is immediately followed by acquisition of 10 data samples at 20 ns intervals, resulting in a total row length of 2 μs. The data sampling rate, or frame rate, is defined by the row length and the number of multiplexed rows to be $f_{samp} = (2\ \mu\text{s/row} * 33\ \text{rows})^{-1} = 15.15$ kHz.

4.2.2 Multi-Channel Electronics

The MCE was designed specifically to control the NIST TDM system in an instrument for which the operator may have no knowledge of SQUIDs or TDM operation [37]. It is fully remote controllable, and has been regularly tested from thousands of miles away. Multiple MCEs reading out different arrays can be synchronized using an external "sync box" with a 25 MHz clock. On ACT, this sync box also sends serial numbers to the housekeeping data acquisition system, which are critical for combining the detector data with encoder measurements of the telescope position and other housekeeping data. The MCE has a built-in time-domain filter, so that the data can be read out at a reasonable rate without aliasing high-frequency noise into the signal band [37]. This allows all data from an array to be transmitted through a single fiber optic and recorded at rate of ~400 Hz, which is sufficiently higher than our signal band to prevent loss of information (as opposed to the NIST electronics from which the data must be recorded at the frame rate, ~15 kHz).

A recent addition to the MCE capabilities is the ability to apply uniform triangle waves or square waves on almost any bias line in the system. We use this feature to quickly characterize the state and performance of the detector array (Section 4.3). The MCE is also capable of reporting data from a subset of the array at data rates up to the chosen frame rate. This has been useful for characterizing aliasing and detector noise for comparison with the SRDP measurements as well as studying the PI loop response and the anti-aliasing filter.

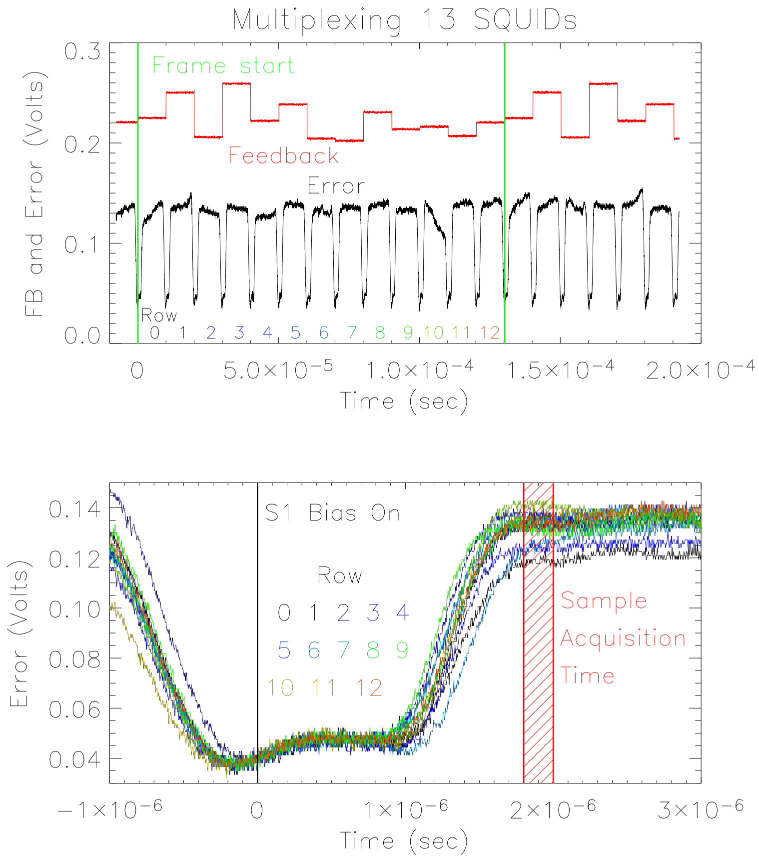

Figure 4.4: Multiplexing data and rate selection. *Top*: Multiplexing one column of 13 SQUIDs with a slower than normal row length of 10 μs or 500 clock cycles using the NIST electronics in CCam. This equates to a frame rate of 3 kHz when multiplexing 33 rows of SQUIDs. At the beginning of each data frame (green lines) row 0 is turned on and the appropriate S1 feedback value (red) is applied, causing the error, or SA output, (black) to ramp up to the lock-point. Recall that the error measurement is used to calculate the feedback response for the following frame. The row addressing and feedback then step through the other multiplexed rows (Figure 3.5) with a similar error response on each. The cause of the ramping of the error on 10^{-5} s time scales is not well understood, but it is a small effect at the faster time scale of our measurements shown below. *Bottom*: The error data for each row has been offset by the row number * 10 μs, so that the time the S1 SQUID bias turns on is at zero seconds. The settling time before acquiring data should be at least as long as the SA response requires to settle to a relatively constant value. The selected interval for data acquisition in MBAC is marked in red (resulting in a row length of 2 μs or 100 clock cycles). During this time 10 samples of the error value are acquired and summed at 20 ns intervals, then the S1 SQUID bias would be turned off and the next row turned on (unlike in the top plot where each row is left on five times longer). The inverse product of the row length and the number of rows gives the data frame rate, $f_{samp} = (2\ \mu\text{s/row} * 33\ \text{rows})^{-1} = 15.15$ kHz.

An enormous amount of hardware, firmware, and software has been developed at UBC, within the SCUBA-2 collaboration [50], and to a lesser extent at Princeton, to realize the capabilities of the MCE. In the remainder of this chapter we describe some details of the optimization and use of the MCE, including: the selection of the PI loop parameters for the first season of observations, the automated tuning of the thousands of SQUIDs in the TDM system, the automated detector bias selection for observations, and the bias-step measurement technique for fast characterization of detector time constants, responsivities, and optical loading.

4.2.3 PI loop parameter selection

The PI loop parameters determine the ability of the MCE to track changes in the detector signal (Section 3.2 and Figures 3.3 and 3.5). Setting them to zero completely turns off the feedback response,[3] and setting them too high drives the PI loop into oscillations (Figure 4.5) that can couple into neighboring detectors on the same column, increasing their noise levels. In between these two limits, the PI parameters must not be so low that they limit the PI response bandwidth and act as a low-pass filter on the data. Since the sampling frequency, ∼15 kHz, is so much higher than the data acquisition frequency, ∼400 Hz, there is some flexibility in the PI parameters, which facilitates the selection.

We have found that we can fully compensate for the changes in detector current using only an integral term (I-term). One advantage of using only an I-term is the simplification of the PI loop response, so that its only effect on the data should be low-pass filtering. If the I-term is selected properly, this filtering will only occur above the signal band and have a negligible impact on our measurements.

To probe the MCE I-term space in MBAC, data were acquired in an unfiltered data mode that allowed us to measure both the applied feedback and SA output, or error, simultaneously. The standard deviation of both of these measurements was extracted for a range of different I-terms (Figure 4.6). When the I-term was set too high, PI oscillations

[3]The PI parameters are set to zero for detectors with non-functional or noisy SQUIDs. This prevents ramping of the S1 FB line on those detectors, which otherwise couples into the signals of other detectors in the same column. When the SQUID auto-tuning process fails or there is substantial drift in the SQUID parameters, the SQUIDs can come unlocked, resulting in similar ramping of the S1 FB and the introduction of noise on other detectors in the same column.

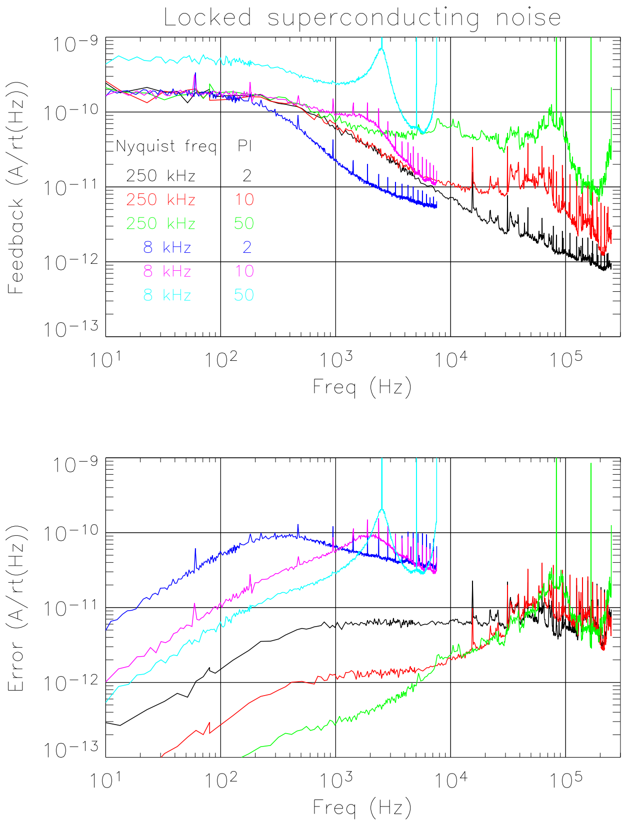

Figure 4.5: The PI loop parameter space was explored using the NIST electronics on a superconducting detector. P and I values were each set to 2, 10, and 50, and data were acquired at two rates, $f_{samp}/2 = f_{Ny} = 250$ kHz and the nominal ACT rate, $f_{Ny} = 15.2/2$ kHz $= 7.6$ kHz. *Top*: The PI loop feedback response changes from acting like a low-pass filter ($f_{Ny} = 7.6$ kHz, P = I = 2, blue) to oscillating at frequencies near the sampling rate as the PI values are increased (magenta). At $f_{Ny} = 7.6$ kHz, P = I = 50 (cyan), these oscillations result in a huge increase in noise in the signal band. Similar effects are observed at higher frequencies in the 250 kHz data. *Bottom*: The residual error noise associated with the feedback data above. As the PI values are increased, the bandwidth of the feedback increases and higher frequency information is extracted from the error, causing the drop in low frequency noise level as a function of PI parameters. High frequency error noise increases as the PI values are driven too high, which eventually results in a large increase in the error standard deviation (Figure 4.6). Note: the high frequency noise spikes observed in these data are not typical and are believed to be due to poor grounding of the DFB electronics during the acquisition.

caused a sudden increase in the measured standard deviation. The selected I-term was chosen to be roughly a factor of two below the value that drove the PI loop into high frequency oscillations (Figure 4.6).

4.2.4 Automated SQUID tuning

Tuning of the SQUIDs for our detector arrays is a critical process that has the potential to prevent large numbers of detectors from functioning if done improperly. An auto-tuning procedure has been developed for the MCE that requires a number of default SQUID parameters as inputs, and then automatically optimizes the variable tuning parameters for observations.

The constant input parameters for the auto-tuning include: the SA, S2, and S1 SQUID biases, and for each column an S1 SQUID row is defined that is used for the S2 feedback selection during the auto-tuning. The SA SQUID bias levels were selected by maximizing the amplitude of the SA V–ϕ response. The auto-tuning procedure is capable of selecting these biases as well, however, we chose to keep the SA biases fixed in the field to minimize the variable parameters between observations on different nights.[4] The S2 and S1 SQUID biases were set between ∼1.5 - 2 times the maximum SQUID critical currents because this reduces the amplitude of the V–ϕ curves (Figure 3.2). The smaller amplitude reduces the probability of any single S2 or S1 V–ϕ coupling through the non-linear regime of the SA or S2 V–ϕ respectively, and resulting in a multi-valued lock-point (Figure 4.11). The S1 SQUID row used for S2 feedback selection was chosen for each column by running Step 5 of the tuning procedure (below) to find the optimal S2 feedback for every S1 SQUID. The row with the median optimal S2 feedback within each column was selected as the tuning row for use in Step 5 of all future auto-tunings (Figure 4.7).

The variable parameters during a full auto-tuning are the SA and S2 SQUID feedback (FB) values and the digital offsets, or lock-points, in terms of error digital-to-analog converter units for each individual detector. These parameters are adjusted every night, because changing magnetic field values can change the optimal SA and S2 FB, and these

[4]The main variable that can cause changes in the optimal SA bias values is the SA, or ∼4 K stage, temperature. Drifts have been observed in this temperature during the 2007 season of observations, but they are not large enough to require selection of new bias currents.

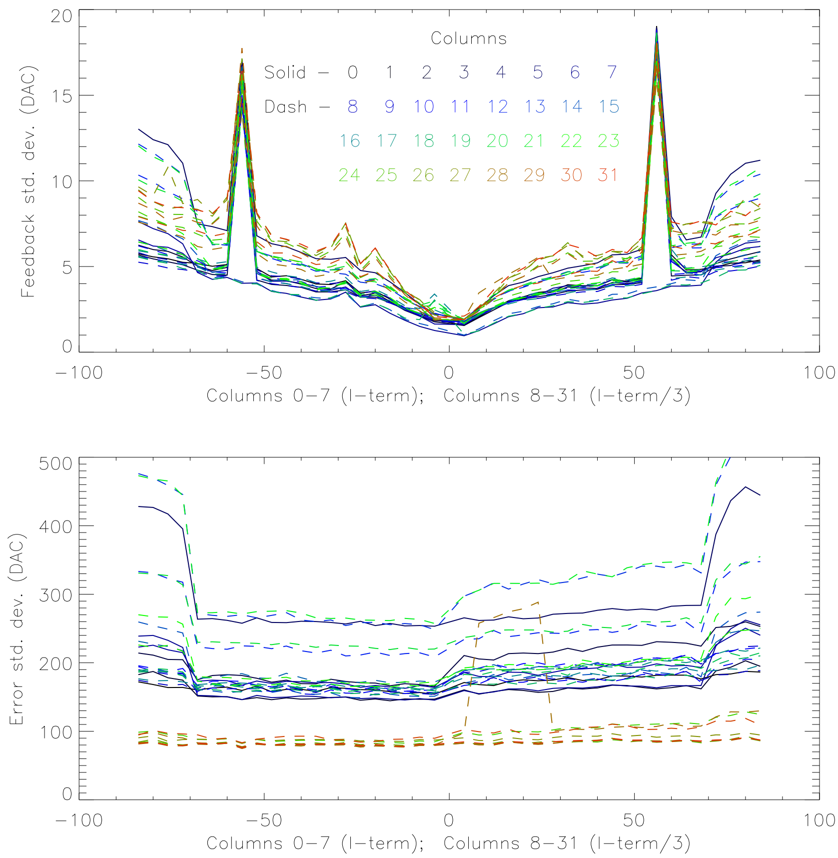

Figure 4.6: PI loop parameter selection. Unfiltered MCE data were acquired with the TESs superconducting at 400 Hz with a range of different I-terms. Positive I-term values lock on the negative SQUID slope and vice versa. The standard deviation of the feedback (*top*) and error (*bottom*) of a row was extracted and plotted versus I-term for all columns. (Note: The large spikes at I-term = ± 56 are due to DC level jumps in the feedback. It has not been confirmed whether these are related to the specific I-term selection, or if it was chance that the jumps occurred at both ± 56.) As the I-term magnitude increases, the feedback bandwidth increases (Figure 4.5), which drives up the variance of the feedback signal. Because of the large amount of high frequency noise aliasing into the unfiltered error signal, there is little noticeable change in its standard deviation until the I-term magnitude reaches ∼70 at which point the PI loop is driven into oscillations. These oscillations generally contaminate both the feedback and error signals. Based on these measurements, I-term = -40 and -120 were selected for columns 0-7 and 8-31 respectively (x-axis scale is I-term and I-term/3 respectively). The factor of three difference between the values compensates for the factor of three lower mutual inductance on the series array SQUID inputs for columns 8-31.

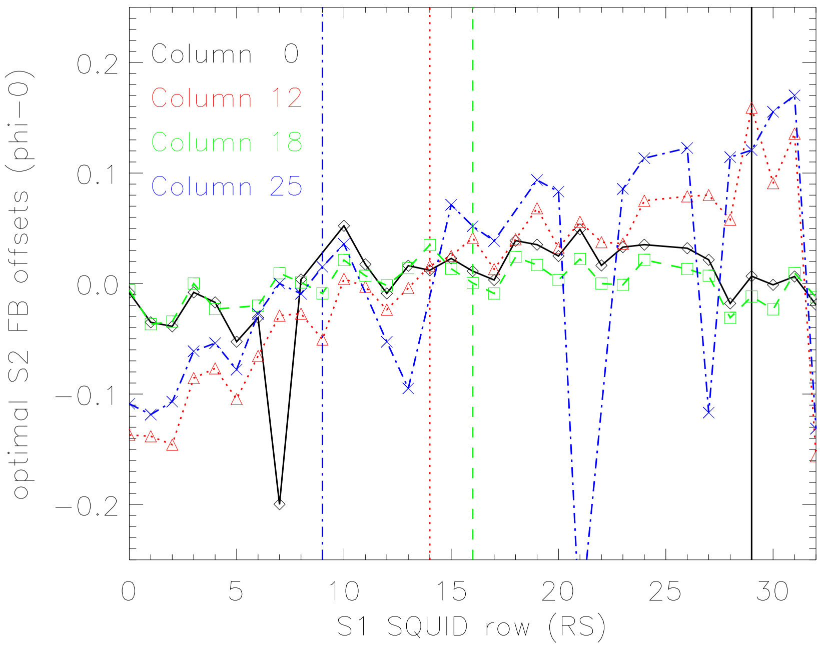

Figure 4.7: Mean-subtracted optimal S2 feedback values versus row number of four columns in MBAC. The optimal S2 feedback was measured for each SQUID by running Step 5 of the auto-tuning procedure on each row separately. The optimal value is generally proportional to the S1 SQUID critical current, I_c, and since some mux chips have I_c trends across the column, there are proportional trends in the optimal feedback (Columns 12 and 25). The median SQUID row in each column (*vertical lines*) is one of the input parameters for future automated SQUID tunings. Taking into account the S1 V–ϕ amplitude and S2 asymmetry, we find that S1 SQUIDs approaching $\pm\phi_0/4$ are likely to sweep through zero slope regions in the S2 V–ϕ curve, reducing the amplitude of the S1 V–ϕ response and increasing the likelihood of having a multi-valued lock-point (Figure 4.11). Because of the asymmetry of the S2 V–ϕ curves – we lock to the flatter slopes in Figure 4.9 – SQUIDs that lie off of this plot (such as column 25, row 21) will sweep through the steep S2 V–ϕ slope and have a substantially different PI response, and thus a different bandwidth, than those on the flatter S2 slope [56]. To solve these problems, the next generation of MCE will have the capability to multiplex the S2 feedback. This will enable optimal S2 feedback selection for every detector by using the plotted offsets as inputs for the new auto-tuning procedure and adjusting these relative to the offset measured for an individual row.

as well as drifts in the 4K stage temperature can cause changes in the lock-point offsets. The following procedure has been developed to select these parameters and maximize the number of responsive SQUIDs when the detectors are biased onto the transition.

1. **SA initialization:** Confirm that the SA and S2 SQUID bias currents are turned on, so that they have warmed the 4K stage to its nominal operating temperature. This prevents future warming of the 4K stage, which would cause the SA I_c's to change and thus drift in the lock-points. The same bias currents were used for the SA and S2 SQUIDs for the entire first season of observations.

2. **Detector initialization:** Drive detectors normal, then bias them near the planned bias point. Large changes in the detector bias current cause shifts in magnetic pickup by the S2 SQUID, which changes the optimal S2 FB, so it is important to tune the SQUIDs with similar detector biasing parameters to those used for successive measurements.

3. **Measure SA V–ϕ curves:** Sweep the SA FB to determine a rough voltage offset for each SA (Figure 4.8). This voltage offset is used as the lock-point for S2 and S1 software servos in Steps 4 and 5. In addition to confirming the response of the SA, the determination of appropriate offsets during this step is critical for acquiring accurate S2 and S1 V–ϕ curves. These offsets are later reset to individually optimized values for each detector in Step 6.

4. **Select the SA FB:** Sweep S2 FB while using a software servo on the SA FB line to keep the SA in the linear regime. The extracted S2 V–ϕ curve is used to select the SA FB value for each column (Figure 4.9).

5. **Select the S2 FB:** Sweep S1 FB while using a software servo on the S2 FB line to keep the S2 in the linear regime while measuring the V–ϕ of the median S1 SQUID for each column (Figure 4.7). The extracted S1 V–ϕ curve is used to select the S2 FB value for each column (Figure 4.10).

6. **Select lock-points:** Sweep S1 FB while recording the SA output to measure the combined V–ϕ curves of all SQUIDs. Search for the largest SA output amplitude

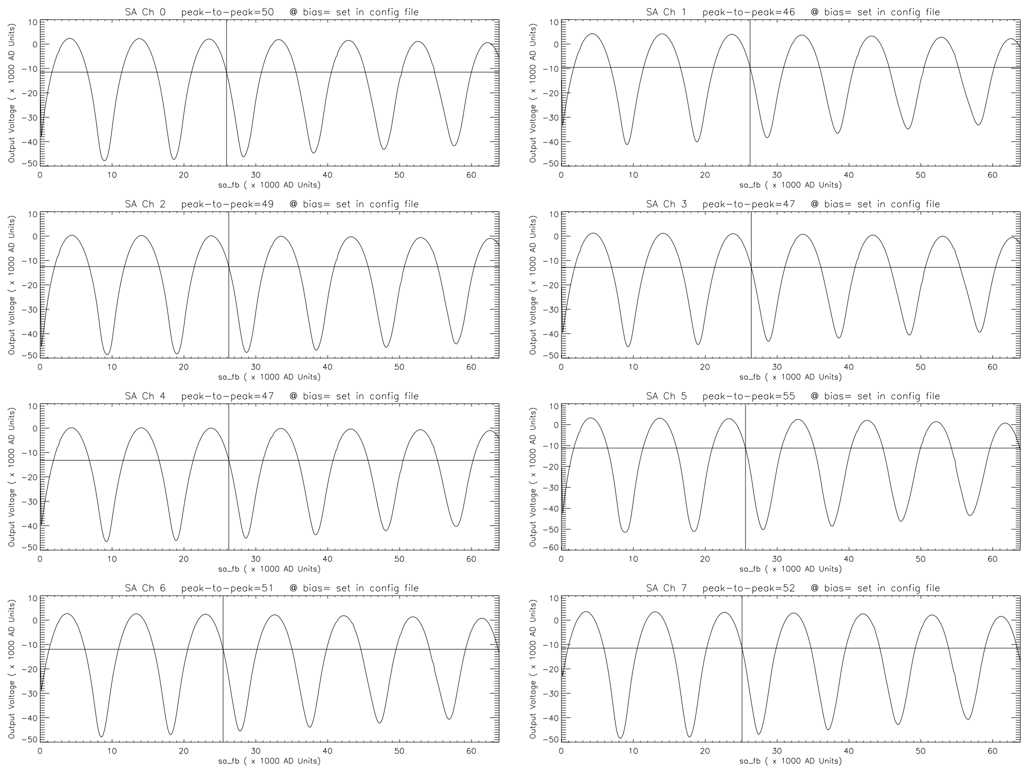

Figure 4.8: Series array V–ϕ curves for eight columns acquired during Step 3 of the auto-tuning procedure. These curves were acquired by simply ramping the SA FB line and measuring the output of the SAs. The cross-hairs show the vertical offsets used for the software servo loop in Steps 4 and 5 as well as the starting SA FB value for Step 4. The selected offset is between the V–ϕ maxima and minima to maximize the dynamic range in ϕ of the SA response, which is why it is higher than the mean value.

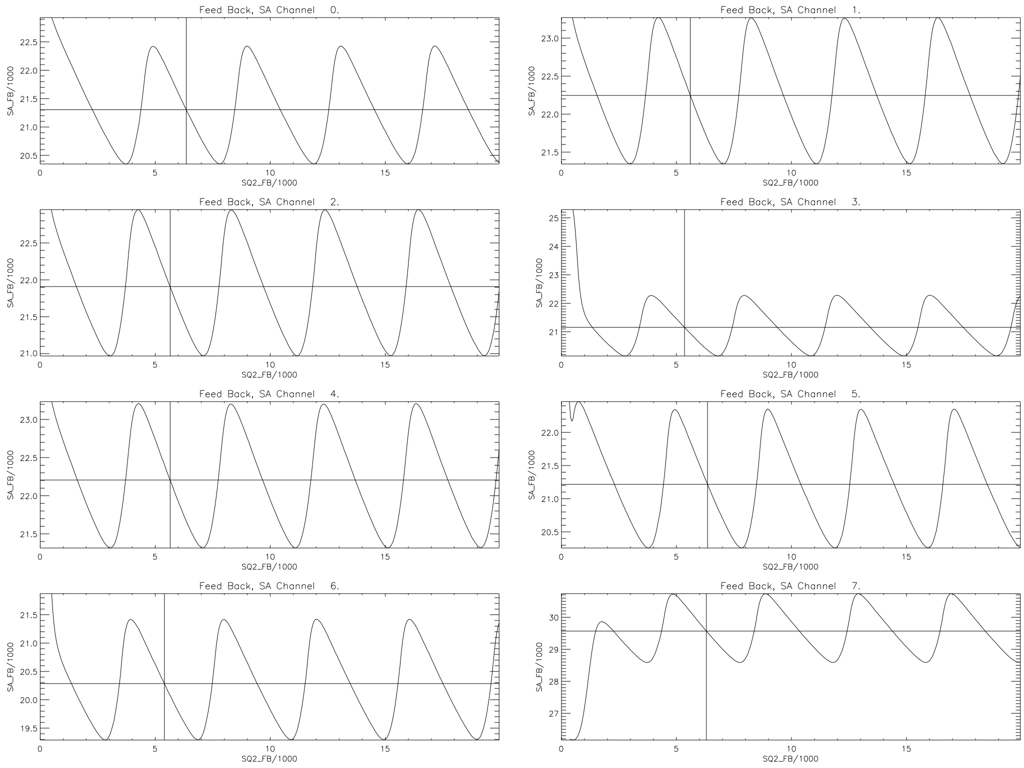

Figure 4.9: S2 SQUID servo V–ϕ curves for eight columns acquired during Step 4 of the auto-tuning procedure. These V–ϕ curves were acquired using a software P-term flux lock loop, which applies feedback onto the SA FB to compensate for the changes in output as a result of ramping the S2 SQUID FB. They are used to determine the optimal SA FB value for each column. The servo response is especially visible immediately after it is turned on at the left end of the plots, where it is still searching for a good lock point. The plots clearly show the asymmetry of the S2 V–ϕ curves. The V–ϕ curves are made asymmetric [42] to linearize the SQUID response and provide a large dynamic range with minimal variations in bandwidth [56]. The cross-hairs show the selected SA feedback value for each column (horizontal lines) as well as the initial S2 feedback value for Step 5.

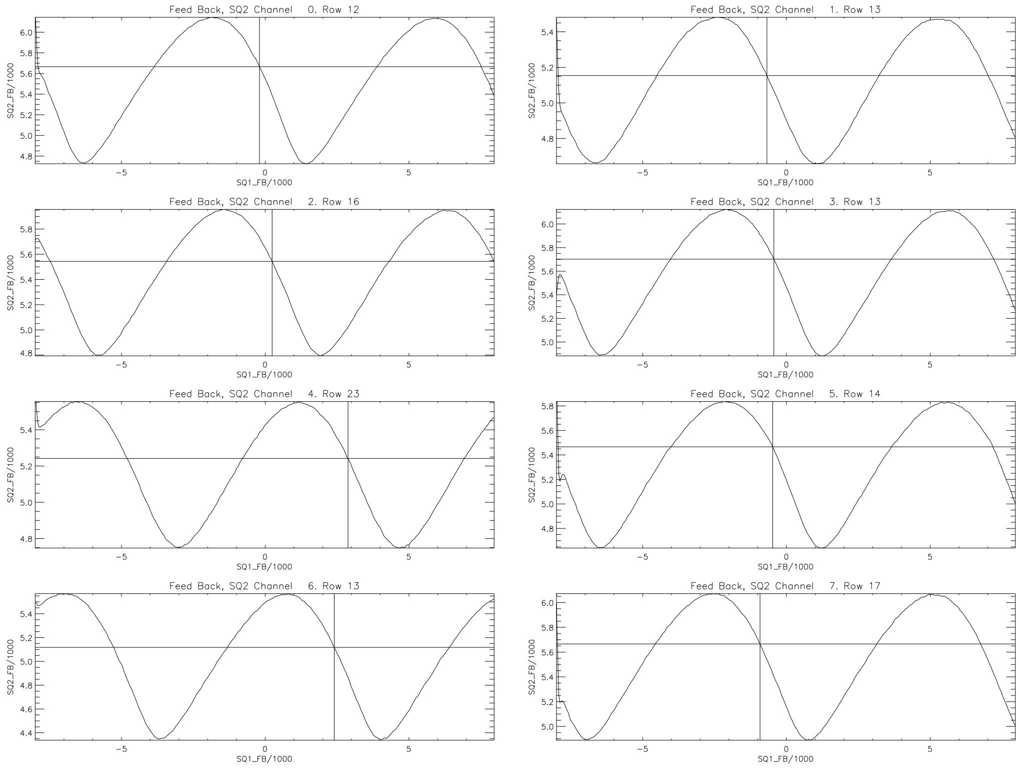

Figure 4.10: S1 SQUID servo V–ϕ curves for eight columns acquired during Step 5 of the auto-tuning procedure. These V–ϕ curves were acquired in a similar method to those in Figure 4.9, except that the S2 FB line was used to lock while ramping the S1 FB. The row plotted is different for each column and is the median optimal S2 FB row for each column as described in Figure 4.7. The horizontal line shows the selected S2 FB for each column.

between zero slope points in each SQUID V–ϕ and apply an offset for every SQUID to lock at the center of that region (Figure 4.11).

7. **Measure final V–ϕ curves:** Repeat the previous measurement (Step 6) to confirm that lock-points were properly selected and extract useful parameters from the V–ϕ curves. Useful parameters to extract include: the combined V–ϕ amplitude, slope at the lock-point, range between zero slope regions around the lock-point, and whether the V–ϕ has multiple locking slopes within one ϕ_0 (Figure 4.11).

8. **Confirm locking:** Turn on the S1 SQUID digital feedback to lock the SQUIDs and acquire a short time stream while measuring the FB and SA output, or error. The data are examined to estimate which detectors are properly locked by looking for detectors with mean error that is non-zero and comparing these to the detectors with the PI loop turned off, which have zero FB.

Shorter versions of the auto-tuning procedure have also been implemented (Table 4.1). These shorter versions were designed to correct for specific environmental shifts that might occur during observations. The full tuning described above is referred to as Mode 0. One of the shorter versions (Mode 1) re-optimizes the S2 feedback selection for each column. This corrects for changing DC magnetic field levels picked up by the S2 SQUID and any hysteretic response of the S2 SQUID to time varying fields, such as those generated by scanning through the Earth's field. The fastest version (Mode 2) simply measures the V–ϕ curves in the current tuning state and selects a new lock point for each S1 SQUID. Mode 2 has been the most often used tuning procedure during observations because of drifts in the 4K stage temperature, which changes the SA I_c and thus the vertical offset of the V–ϕ curves.

4.2.5 Automated detector bias selection

The detector bias currents are selected at the beginning of every night of observations to maximize the number of detectors on the transition. A load curve is acquired on all bolometers in the array and analyzed using the procedure described in Section 3.5.3 to calculate the detector bias current that drives each bolometer to $0.3R_n$ (or another predefined percentage

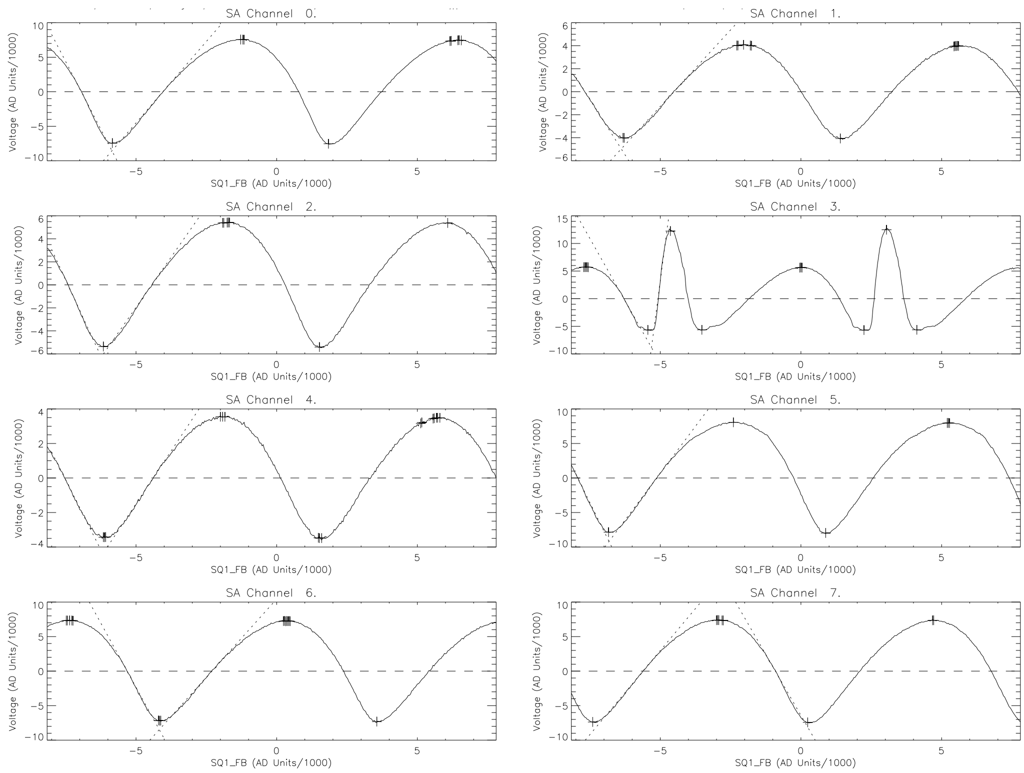

Figure 4.11: S1 SQUID raw V–ϕ curves for row 09 of eight columns acquired during Step 7 of the auto-tuning procedure. These V–ϕ curves were acquired after all the tuning parameters were set by simply ramping the S1 FB line and measuring the output. The horizontal dashed line near the center of each V–ϕ indicates the locking point. The dotted diagonal lines are fits to the positive and negative V_ϕ slopes at the locking point. The second plot down on the right, is an example of a SQUID with a poorly tuned S2 FB value (Figure 4.7). Because of the bad S2 FB value, it has a multi-valued lock point with different V–ϕ slopes of the same sign. This causes problems for the PI loop because the different slopes have different optimal PI parameters. Since the majority of the SQUIDs in the array are on the flatter slope, the PI parameters are chosen to work there. When the feedback locks on the steeper slope, the same PI values can cause large oscillations.

Auto-tuning description	Mode	Steps	Time (min)
Full tuning	0	1 - 8	4.5
S2 feedback and lock-points	1	5 - 8	2.9
Lock-point adjustment	2	6 - 8	1.5

Table 4.1: SQUID auto-tuning modes. At the beginning of each night of observations, a full tuning is run (Mode 0). Large telescope motions through the Earth's field could cause hysteretic magnetic offsets in the S2 feedback, in which case we would want to run auto-tunings in mode 1, however, these have not been observed to have a large impact on the tuning parameters during a single night, so this mode has not been used since early in the 2007 season. Mode 2 simply adjusts the lock-points by measuring V–ϕ curves and choosing a new digital offset for each S1 SQUID. These offset adjustments correct for variations in the 4K stage bath temperature that change the SA I_c, and can also improve the tuning after minor shifts in S2 feedback. Mode 2 auto-tunings are typically run a few times a night after major telescope moves. The estimated execution times quoted here are for the software versions used during the 2007 season, and are expected to drop by roughly a factor of two by the 2008 season.

of R_n). The median current on each bias line is selected, and the detector bias current is set to that value. After the bias current is known, the detector parameters at that bias (including: s_I, P_{J_0}, V_0, and R_0/R_n) are extracted from all the analyzed load curves and stored with subsequently acquired data files for future analysis. This approach often results in as many as ∼98% of the working detectors in the first array being biased between $0.15 - 0.75R_n$, which is considered a good regime for observations. Detector biasing during observations is explored in more detail in Section 6.2.1.

4.3 Fast Array Characterization Techniques

Applying a small amplitude square wave on the detector bias line (bias-step) provides measurements of both the DC and AC response of all the detectors in the array in a fast and consistent way. Over the last two years, we have worked closely with the MCE firmware development team to integrate and test the detector bias-step capability and have used it extensively during the 2007 observation season. The amplitude of the detector response allows extraction of the TES resistance, R_0, and Joule power, P_{J_0}, which can be used to study changes in responsivity and sky loading, respectively. The decay time of the detector response allows estimation of the detector time constant.

4.3.1 Optical loading and atmosphere

Knowledge of the atmospheric temperature and opacity is important for calibration of all observations. They can be monitored by measuring changes in total optical loading, P, over time, as well as by executing sky dips in which the atmospheric power is measured as a function of elevation. An efficient way of doing this is by measuring the change in detector current as a function of the change in bias current, $\delta I/\delta I_b$, to extract P_{J_0}, which is proportional to P.

We assume that the saturation power is constant near the bias point, [5] and express the constant bias power being measured as $P_{J_0} = I^2 R$, where I and R are the current through and resistance of the TES. The voltage across the TES is

$$V = R_{sh}(I_b - I) = IR, \tag{4.5}$$

where I_b is the applied detector bias current and R_{sh} is the constant shunt resistance for each detector. Combining these equations and completing the square allows us to solve for

$$I = I_b/2 \pm \sqrt{I_b^2/4 - P_{J_0}/R_{sh}}. \tag{4.6}$$

The derivative of this,

$$\frac{\delta I}{\delta I_b} = \frac{1}{2} \pm \frac{I_b/4}{\sqrt{I_b^2/4 - P_{J_0}/R_{sh}}}, \tag{4.7}$$

puts all variables into measured or known quantities, allowing us to solve for the bias power,

$$P_{J_0} = I_b^2 R_{sh} \frac{(\delta I/\delta I_b)^2 - \delta I/\delta I_b}{(1 - 2\delta I/\delta I_b)^2}. \tag{4.8}$$

To complete our understanding of the detector state, we can also calculate R_0 in terms of the bias-step response by solving equation (4.5) for I and taking the derivative

$$\frac{\delta I}{\delta I_b} = \frac{1}{1 + R_0/R_{sh}}, \tag{4.9}$$

which becomes

$$R_0 = R_{sh}\left(\frac{1}{\delta I/\delta I_b} - 1\right). \tag{4.10}$$

[5] The width of the superconducting transition has been measured to be ~2 mK. Using equation 3.2 with $T_c = 0.51$ K, $T_{bath} = 0.3$ K, and $n = 4$, we find that the saturation power, and thus bias power, will vary by less than 2% across the transition as a result of this width. The bias step peak-to-peak amplitude used during the first season of observations was ~6 μA, and this change in bias current only changes the TES resistance by ~3% above $R_0/R_n \approx 0.3$, and by ~6% at $R_0/R_n = 0.1$. Thus, the approximation that the saturation power remains constant throughout the small amplitude bias-step measurements is good.

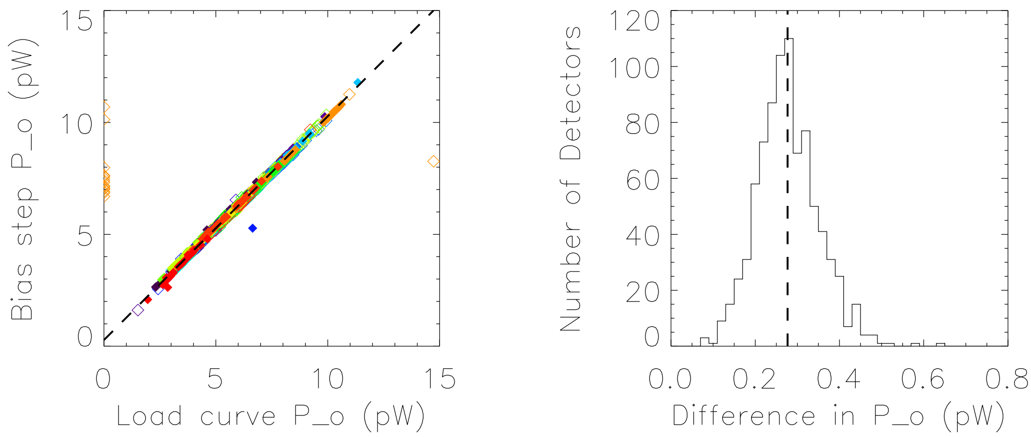

Figure 4.12: *Left*: Comparison of bias powers calculated using bias-step versus load curve data. *Right*: The mean difference between the calculated values is ∼0.28 pW, which is most likely due to changes in optical loading during the many hours that passed between the acquisition of the load curve and the bias-step data. The standard deviation of the residuals is ∼0.09 pW if we ignore the group of ∼25 detectors on column 14 that often have bad load curves (orange diamonds). Because of the detectors that failed the load curve acquisition, good P_{J_0} values were successfully calculated for ∼4% more detectors using the bias-step method.

Using this method to calculate P_{J_0} gives values consistent with load curve measurements with little scatter (Figure 4.12). Because of failures in SQUID locking during load curve acquisition, good P_{J_0} measurements were made on ∼4% more detectors using the bias-step method than from the load curve. These points and the capability to calculate R_0 indicate that using the bias-step technique to select detector bias currents for observations may be more efficient and more accurate than using load curves (Section 4.2.5). Analysis of bias-step data does not give the the value of R_n for each detector, which is used to select the bias points, however, the R_n values could be easily stored in a look-up table for use with bias-step analysis. To completely replace load curve acquisitions with bias-step data during future observations, we must confirm that making bias-step measurements at a small number of detector bias values provides sufficient information to accurately select a good bias point for observations.

4.3.2 Responsivity

Understanding the detector responsivity is critical for data calibration. With a perfect voltage bias across the TES and ΔT_c across the transition negligible compared to $T_c - T_{bath}$, the DC responsivity would be perfectly stable until saturation. Those are reasonable first-order approximations throughout much of the operation range, but a more accurate understanding is required. Combining equation (4.5) with the DC part of equation (3.4) and the Joule heating of the TES,

$$P_J = I^2 R = R_{sh}(I_b I - I^2) = P_{bath} - P, \tag{4.11}$$

provides a simple approach to calculating the DC responsivity in terms of the TES current,[6] I_0, or resistance, R_0,

$$s_I = \frac{dI}{dP} = -[R_{sh}(I_b - 2I_0)]^{-1} = -\left[I_b R_{sh}\left(\frac{1}{R_0/R_{sh}+1} - \frac{1}{2}\right)\right]^{-1}. \tag{4.12}$$

The form of this equation indicates that the percentage variability in the responsivity as a function of optical loading only depends only on the ratio R_0/R_{sh} (Figure 4.13, lower plots and legend). Inserting the value of R_0 from equation (4.10) into equation (4.12) allows us to estimate the responsivity of each detector, and thus characterize drifts in the responsivity, with high signal to noise from bias-step measurements.

To explore the effect of changes in T_c across the transition on the responsivity, we use data from a load curve to estimate the real power going to the bath, $P_{bath}(R)$. An estimate of the background loading on the detector when the load curve was acquired, P_{bg}, allows us to write $P_{bath}(R) = P_0(R) + P_{bg}$, where $P_0(R)$ is the measured load curve (Figure 4.13). The TES resistance as a function of optical loading, $R(P)$, can be calculated by combining equations (4.5) and (4.11),

$$R(P) = \frac{R_{sh}(2(P_{bath} - P) - I_b^2 R_{sh} - I_b R_{sh}^{1/2}(I_b^2 R_{sh} + 4(P - P_{bath}))^{1/2})}{2(P - P_{bath})}. \tag{4.13}$$

Since $P_{bath}(R)$ is nearly constant throughout the transition (Figure 4.13), we can accurately solve for $R(P)$ with only two iterations. $R(P)$ is then inserted into equation (4.12) to attempt to calculate a more accurate responsivity. Figure 4.13 shows that the load curve

[6] This DC approach gives the same result as the approximation to the AC responsivity in equation (3.24).

correction to the change in responsivity is negligible, which justifies ignoring ΔT_c across the transition and using equation (4.12) to calculate the responsivity.

4.3.3 Detector time constants

The bias-step approach to measuring bolometer time constants probes a different physical phenomena than optical measurements (Section 5.4). Instead of measuring the response to optical power absorbed by the ion-implanted absorber at numerous frequencies, it measures the response to a sudden DC shift in the applied bias voltage across the TES. Using the isothermal TES bolometer model, we solve for the AC response of the bolometer, then compare this model to measurements of the response.

In Section 3.1, we followed the change of variables approach used by Lindeman [70] and the notation of Irwin and Hilton [54] to arrive at a description for the TES power to current responsivity. Here we stray from that analysis by perturbing the system summarized by equations (3.17), (3.18), (3.19) and (3.20) with a small step in Thevenin equivalent voltage, $\delta V(t \geq 0) = \Delta V_0$,

$$\begin{pmatrix} \delta I \\ \delta T \end{pmatrix} = A_+ e^{-\lambda_+ t} \vec{v}_+ + A_- e^{-\lambda_- t} \vec{v}_- + \begin{pmatrix} \Delta V_0 / L \\ 0 \end{pmatrix}. \tag{4.14}$$

We solve for the constant prefactors, $A_\pm$, when $t = 0$ and $\delta I = \delta T = 0$, and find

$$A_\pm = \pm \frac{\Delta V_0}{L} \frac{1}{\tau(1/\tau_+ - 1/\tau_-)} \frac{I_0 R_0 (2 + \beta_I)}{G}. \tag{4.15}$$

Substituting 3.19, 3.20, and 4.15 into 4.14, we find the change in TES current for $t > 0$,

$$\delta I(t) = \frac{\Delta V_0}{L} \left(\frac{1}{\tau_+} - \frac{1}{\tau_-} \right)^{-1} \left[\left(\frac{1}{\tau_I} - \frac{1}{\tau_+} \right) e^{-t/\tau_+} - \left(\frac{1}{\tau_I} - \frac{1}{\tau_-} \right) e^{-t/\tau_-} \right] + \frac{\Delta V_0}{L}, \tag{4.16}$$

where $\tau_I \equiv \tau/(1 - \mathscr{L}_I)$. Figure 4.14 displays this solution with the three time constants adjusted to be within a factor of 20 of each other to clearly show the form of the response.

High sampling rate measurements of detector responses to bias-steps have been made and fit to test whether this model describes the detector response (Figure 4.15). The model clearly provides the correct qualitative description of the response; however, there appears to be at least one additional time constant in the bolometers that is not included in equation (4.16). This is not surprising considering that isolated heat capacities were required to fit

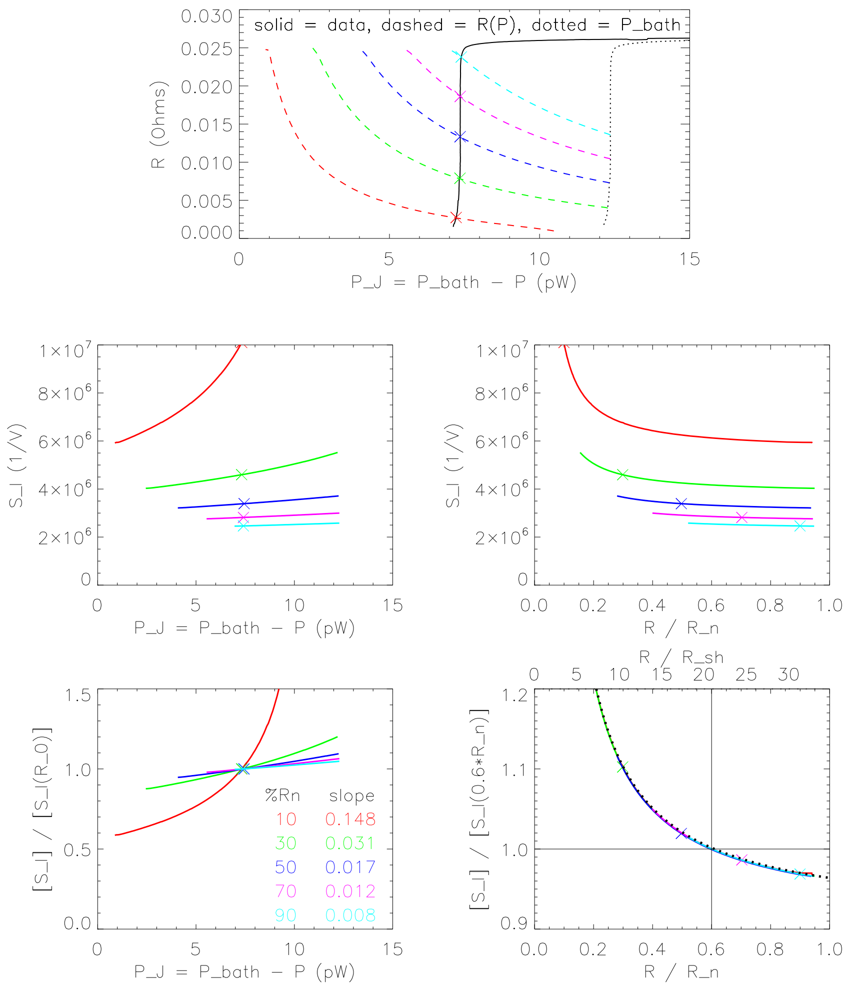

Figure 4.13: DC responsivity stability analysis. *Top*: The acquired load curve (solid) plus a constant, $P_{bg} = 5$ pW, is used to estimate the power carried to the bath, P_{bath} (dotted), and thus the resistance as a function of optical loading, $R(P)$. $R(P)$ is plotted starting from bias points (crosses) on the acquired load curve at 0.1, 0.3, 0.5, 0.7, and 0.9 times the normal resistance, R_n. *Upper Left*: The responsivity, s_I equation (4.12), is plotted versus $P_J = P_{bath} - P$ for each of the curves in the top plot. *Lower Left*: The responsivity is normalized to the responsivity at the bias point, $s_I/s_I(R_0)$. The slope of the percentage change in responsivity per pW at R_0 is shown in the legend. The responsivity obviously has less variability at higher bias points on the transition. *Upper Right*: s_I versus normalized resistance, R/R_n. *Lower Right*: The responsivity is normalized to its value at $R/R_n = 0.6$, and we see that all the curves match in these units. Equation (4.12) is also plotted versus R/R_{sh} (dotted line and top axis) with a similar normalization. The negligible errors between equation (4.12) and the calculation based on the load curve (colors) justify ignoring the change in T_c across the transition and using the simplified description of equation (4.12) to explore changes in responsivity.

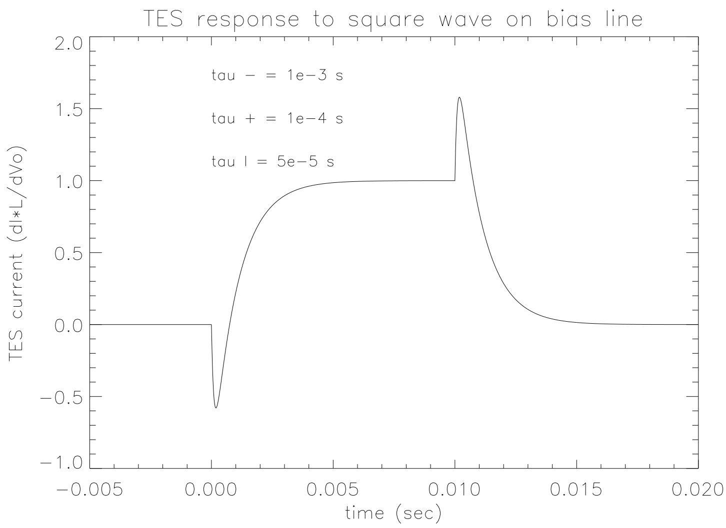

Figure 4.14: Model of detector bias-step response to a square wave perturbation on the TES bias voltage line. The parameters have been adjusted here to make the electrical rise time, τ_+, more visible. Qualitatively, at time $= 0$ a sudden decrease in I_b causes an sudden decrease in V, which becomes a decrease in the measured I limited by the L/R response of the TES loop, or τ_+. Because the detectors are nearly voltage biased and P_{J_0} can be treated as constant throughout the bias-step amplitude, as the system approaches thermal equilibrium the decrease in $V = \sqrt{P_{J_0} R}$ must be compensated by a larger percentage decrease in R, which causes a net increase in $I = V/R$, limited by τ_-.

Model	Time range fit	τ_-	τ_+	τ_I
Bias-Step	0 - 5×10^{-2} s	7.2×10^{-4} s	1.8×10^{-5} s	1.3×10^{-5} s
Bias-Step	5×10^{-4} - 5×10^{-2} s	6.0×10^{-3} s	8.6×10^{-4} s	3.1×10^{-3} s
Exponential	5×10^{-4} - 5×10^{-2} s	1.2×10^{-3} s	NA	NA
Exponential	2.5×10^{-3} - 5×10^{-2} s	1.4×10^{-3} s	NA	NA

Table 4.2: Bias-step fitting results.

the noise and impedance data (Figure 3.18). For observations we are primarily concerned with the thermal response of the bolometers, and since the electrical response time is more than an order of magnitude smaller, we can take the approximation to equation (4.16) that the response is described by a single exponential. In Figure 4.15 we fit both the full bias-step function as well as a single exponential to the bias-step response. We also explore cutting early data from the fit to both remove the electrical response data from the single exponential fit and test the robustness of the fits.

The time constant results from fitting equation (4.16) versus a single exponential are presented in Table 4.2. Not surprisingly, the only fit that comes close to describing the electrical response, τ_+, is the bias-step model fit to the entire data set, and the best fit is achieved by cutting the electrical response data before 0.5 ms and fitting the full bias-step model to the rest of the data. The latter approach effectively allows fitting of an additional time constant, which may be indicative of the isolated heat capacities in the bolometer, however, we do not have an analytic justification for doing this. Unlike the large variability between the results of the two bias-step model fits, the time constants from the two exponential fits differ by only ∼20%. This is especially encouraging considering that the planned data reporting period from the MCE is ∼2.5 ms, which is the length of time that was cut from the beginning of the later exponential fit. These variations are also a justification for fitting a relationship between optical time constant measurements and bias-step time constant measurements as is done in Section 5.4.

Acknowledgements

The relative magnetic sensitivity measurements between the Mux05c and Mux06a chips were made by R. Fisher, T. Essinger-Hileman, and L. Sun. Previous magnetic shielding

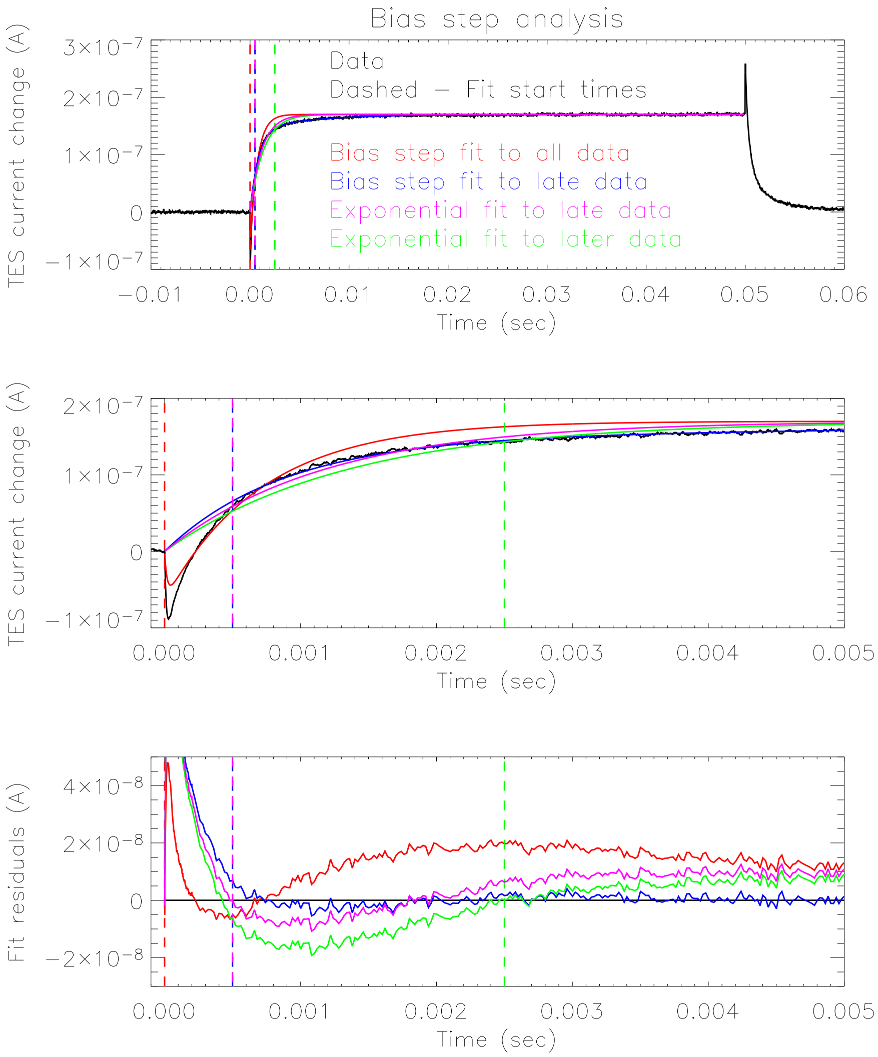

Figure 4.15: Measured and fit detector bias-step response to a square wave perturbation on the TES bias current line. *Top*: Measured detector response (black) with four different attempts to fit the data (color). As described in the legend, two different models were fit to the data: the bias-step model (red and blue) in equation (4.16) and a single exponential (pink and green). Different amounts of early data were cut when fitting the different models (vertical dashed lines, with colors matching the legend). The fit parameters and results are in Table 4.2. *Middle*: An expanded view of the data and fits, focusing on the initial electrical response through the TES. As expected, the only model that comes close to fitting this appropriately is the full bias-step model fit to all of the data. The error in the fit is believed to be due to distributed heat capacities in the bolometers, which result in additional internal bolometer time constants not accounted for in the isothermal model (Figures 3.17 and 3.18). *Bottom*: Residual errors between the measured data and the four different fits.

measurements were aided by J. Reidel, C. Ritter, and B. Dixon. Measurements with the NIST DFB electronics were greatly aided by discussions and collaboration with R. Doriese, T. Marriage, and others at NIST and Princeton. The PI term selection was informed by numerous discussions and firmware revisions with the MCE team at UBC and E. Switzer who modeled and simulated the PI loop. The automated SQUID tuning procedure was primarily implemented by E. Battistelli and many other MCE team members were critical to its development. The bias-step capability was added to the MCE to help characterize time constants by B. Burger and the MCE team. Discussions with K. Irwin and T. Marriage were especially helpful in understanding the bias-step model. J. Appel has analyzed the bias-step data from the first detector array to compare with load curves (Figure 4.12), explore atmospheric loading, and for comparison with the optical measurements in Section 5.4.

Chapter 5

The First Detector Array

The MBAC detector arrays are the largest arrays of PUD bolometers ever developed, and in 2007 the 148 GHz array (Figure 5.1) was the largest TES bolometer array ever fielded. These are the first free-space close-packed bolometer arrays developed for CMB observations. In this chapter we discuss the functionality of the 148 GHz array before and after assembly, including statistics from the SRDP measurements (Section 3.5) and repairs made prior to deployment. We also present the design of the array structures that maintain the critical alignment between the silicon coupling window and the bolometers, followed by studies of the alignment and optical efficiency measurements to characterize the improvements from adding the coupling window. In Section 5.4 the results of optical time constant measurements on $\sim$60% of the array are used to calibrate time constant measurements from the entire array using the bias-step method (Section 4.3). Finally, we compare bolometer noise measurements from the SRDP with measurements in MBAC and use the predicted loading calculations from Chapter 2 to estimate the noise in CMB temperature units.

5.1 Pre-Assembly Detector Statistics

Detailed measurements of all detector columns and components were made in the SRDP prior to assembly of the array (Section 3.5). Here we discuss the results of some of these measurements and their implications for the array.

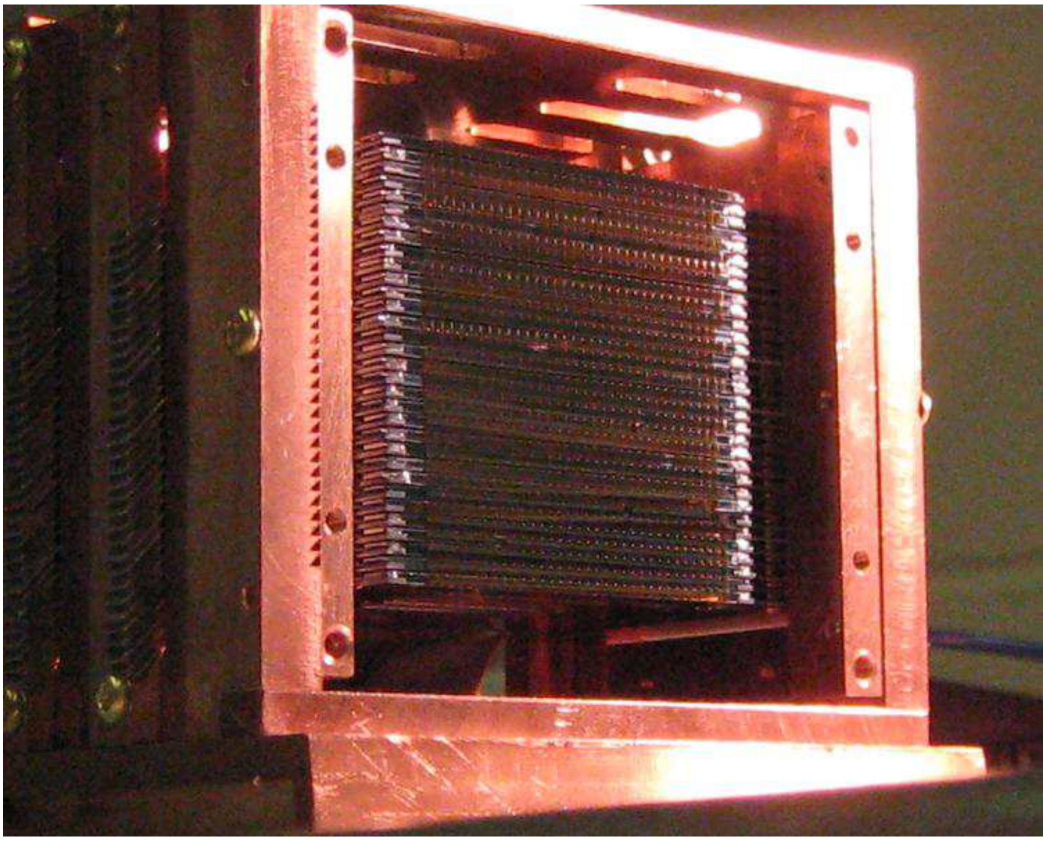

Figure 5.1: The 148 GHz array. The silicon coupling layer is removed in this photo, so we can see the 32 columns of folded TES bolometers. Each horizontal column has 32 pixels (or rows), and they are stacked on top of one another within the copper array structure to build the array. Each column also has an unused mechanical pixel (far right of array), which was often broken during the folding process. The numbering of the bolometers starts in the lower right corner at row select 00, column 00, with the columns incrementing up to 31 in the upper right corner. This is compared with the orientation on the sky in Appendix A.

Failure mode	# detectors
SQUID failure	10
Mechanical bolometer failure	10
Open TES circuit	22
Superconducting TES loop	26
Oscillating detector	13
Total failed detectors	81
Percentage failed detectors	7.9%

Table 5.1: Detector failures observed before and during SRDP testing. The details of these failure modes and remedy procedures are described in Section 3.5.6 and Table 3.3. (Note: a few of these pixels had more than one failure mode, but each pixel is only counted once in this table.) To achieve this low ~8% failure rate on the 32 columns in the array, 41 potential detector chips were tested. Of the nine extra detector chips: three had catastrophic mechanical failures, one had shorts on the silicon card due to laser dicing through the bond pads, two went through a different fabrication process (CVC) and were excluded because of low saturation powers (column 31 is the only CVC chip in the array), and the remaining three were on spare columns that were considered for use in the array. Throughout the SRDP testing process, various failures caused a number column components to be moved between silicon cards or require retesting for another reason, so that in total ~70 column tests were run in the SRDPs to develop the first detector array.

5.1.1 Pixel failures

Of all 1024 detectors in the array, the screening processes described in Chapter 3 – and great care when handling the detector columns – kept the number of failures down to only 81 detectors, or eight percent of the array, prior to assembly. The causes of the failures were widely distributed (Table 5.1), and all critical problems (Section 3.5.6) were remedied.

5.1.2 Pixel parameters

As described in Section 3.5, parameters measured for all functional detectors included: superconducting transition temperature, T_c, normal resistance, R_n, (Figure 5.2), shunt resistance, R_{sh}, bias power at fixed operating temperature of 380 mK, P_{J_0}, bias current to reach 50% of R_n, $I_b(R_n/2)$, and noise at multiple bias points on the transition. The average values and standard deviations of these measurements are presented in Table 5.2.

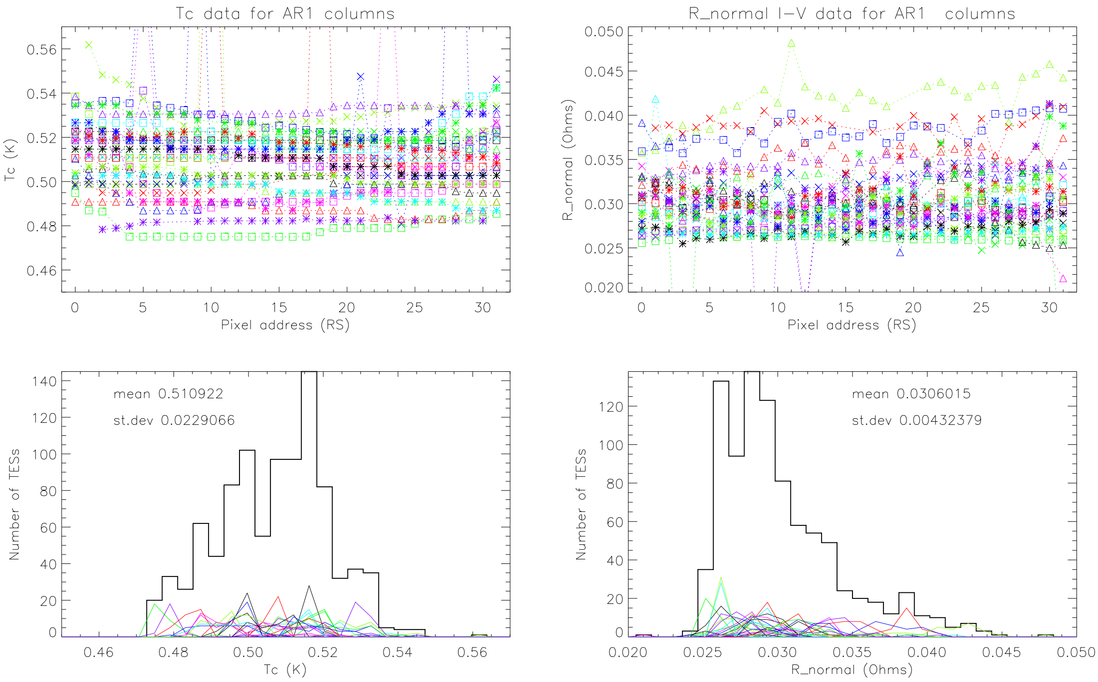

Figure 5.2: *Left*: Superconducting transition temperatures, T_c – *Right*: Normal resistances, R_n, for the 148 GHz array. The upper plots are the data as a function of row number, where each color-symbol combination is a different column of detectors. The lower plots are histograms of the data.

Detectors	T_c	R_n	P_{J_0}	Noise at 10 Hz
Average	0.511 K	31 mΩ	6.8 pW	5.8×10^{-17} W/Hz$^{1/2}$
Median	0.511 K	30 mΩ	6.5 pW	5.6×10^{-17} W/Hz$^{1/2}$
Std. Dev.	0.023 K	4 mΩ	1.6 pW	1.9×10^{-17} W/Hz$^{1/2}$
Components	R_{sh}	L_{Ny}	$I_b(R_n/2)$	Background noise
Average	0.77 mΩ	0.70 μH	0.45 mA	11 pA/Hz$^{1/2}$
Median	0.76 mΩ	0.72 μH	0.45 mA	10 pA/Hz$^{1/2}$
Std. Dev.	0.13 mΩ	0.13 μH	0.07 mA	7 pA/Hz$^{1/2}$

Table 5.2: Dark measurement results from the detector columns in the 148 GHz array. These measurements were acquired at $T_b \approx 0.38$ K, which is why the bias power, P_{J_0} is somewhat lower than discussed in Section 3.3.3. The background noise level was meant to be a measure of the SQUID noise level, however, during measurements of the first array, there was a significant noise contribution from the analog feedback electronics, making it difficult to extract the SQUID noise level. Extreme variations in this background noise level also occasionally added uncertainty to the R_{sh} measurements from Johnson noise.

5.1.3 SQUID noise

The SQUID noise measurement in Johnson noise data sets (Section 3.5.2) permits study of the noise under different SQUID tuning conditions. Since both the S2 and S1 SQUIDs have asymmetric $V-\phi$ curves (Figures 4.9 and 4.10), there are four distinct slope combinations for tuning the SQUIDs, all of which could result in different SQUID noise levels. The SQUID noise is over an order of magnitude smaller than the detector noise. However, its bandwidth is so high that after aliasing, it has the potential to substantially raise our system noise level (Section 3.3.1). Comparison of the SQUID noise and the slope of the SQUID $V-\phi$ curve near the locking point indicates a trend towards higher noise with lower SQUID slopes (Figure 5.3). The details of the SQUID tuning cannot be extracted from the data shown in Figure 5.3, such as whether the SQUIDs were locked on the steep S2 slope and the shallow S1 slope or vice-versa. There were difficulties with the SQUID noise measurements, however, due to the installation of a noisy op amp in the SRDP electronics, which contributed to the background noise level that we interpret as SQUID noise. Current studies using electronics with lower background noise and recording the SQUID slopes should determine whether aliased SQUID noise contributes significantly to the in-band noise level during observations.

5.2 Array functionality

Preliminary cryogenic testing of the array in MBAC indicated that 84% of the array was functional (as opposed to 92% during SRDP measurements), and there was a low critical current problem somewhere on the detector bias line that caused heating of the array. Here we describe the failures and the repairs that were made to bring the array yield up to 88% and solve the heating problem. We then discuss some of the details of the array heat sinking.

5.2.1 Details of the 148 GHz array

The detector biasing lines for the array were split up into three groups to improve our ability to bias detectors near the optimal bias and prevent the possibility that a single electrical

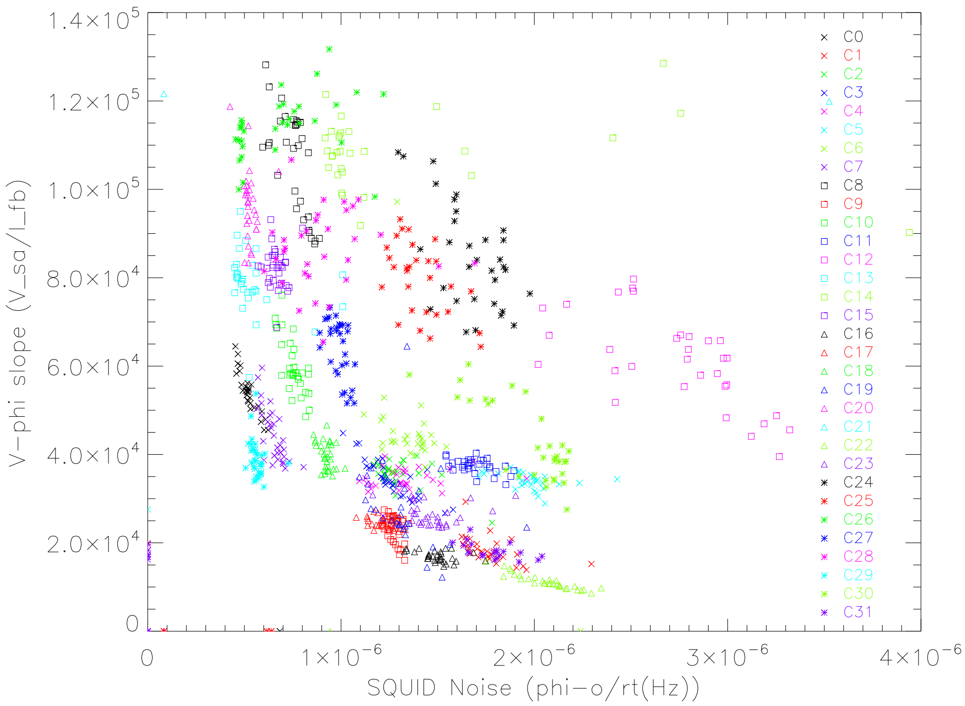

Figure 5.3: SQUID noise versus $V - \phi$ slope measurements made in the SRDP on all columns in the first array indicate a trend towards increasing SQUID noise when locking to shallower $V - \phi$ slopes. The slopes are measured in terms of the (somewhat arbitrary) amplified series array SQUID voltage response, V_{sa}, divided by the stage 1 SQUID feedback current, I_{fb}, which is the same as the slopes shown in Figure 4.11 (except that the previous slopes are plotted in terms of digital-to-analog converter units). One possible contributor to this increase is excess noise in the room temperature amplifier chain. If the SQUID $\phi_0/\mathrm{Hz}^{1/2}$ noise were to stay constant throughout the $V-\phi$ curve, then the SQUID current noise would drop as the slope decreases, causing other sources of noise to increase the effective noise level in $\phi_0/\mathrm{Hz}^{1/2}$. Studies are underway to characterize the SQUID noise on different S2 and S1 slopes using less noisy electronics. Each different color and symbol combination is data from a different column in the array, as described in the legend.

failure could cause the entire array to fail.[1] The three groups originally comprised columns 00-15, columns 16-30, and column 31, which was isolated because it is a different type of detector with a substantially lower saturation power and bias current. All of these bias lines were functional, except that a critical current problem (described below) on the bias line for columns 16-30 caused substantial warming of the 0.3 K stage. This drove us to make a number of measurements with the bias line for those detectors turned off.

The two failures that caused the majority of the 8% drop in yield between single column and array measurements were: 1) initially row 25 failed and 2) a failure on column 22 prevented all of its detectors from functioning properly. The row 25 failure was later diagnosed as a single bad solder joint at a zero-insertion force (ZIF) connector and was repaired prior to deployment. The column failure appeared to be due to a low critical current, I_c, failure on the column 16-30 detector bias line at column 22. The I_c was found to be $\sim$2 mA. After driving the detector bias line above this current (which was required to drive the detectors normal), then reducing it to $\sim$0.5 mA to bias the detectors onto the transition, the self-heating through the low-I_c region prevented it from returning to a superconducting state and warmed the detector array by $\sim$60 mK. Observations indicating that column 22 caused the heating include: the SQUIDs on column 22 responded to sweeping the detector current at low detector biases below I_c, but after going above I_c, there was no SQUID response; load curves acquired with columns 16-30 turned on show a reduction in detector bias power near column 22 row 30 (Figure 5.4), as if there were power being radiated from a hot region on column 22. Before deploying the camera, column 22 was removed from the detector bias circuit using jumpers on the detector backplane.

Measurements of the array after deployment confirmed that the repairs worked. Row 25 is fully functional and the heating problem was solved by removing column 22. The drop in functional pixel yield from 92% in the SRDP to 88% in the field is primarily due to the loss of column 22 (Figure 5.4). For comparison, the 256 detector prototype array dropped in functional pixel yield from $\sim$80% in the SRDP to $\sim$45% in the array. Considering that a single failure of one of the numerous critical electrical connections on the 300 mK stage – 4736 wirebonds, 5000 ZIF connections, and 3088 solder joints – would cause between 32 -

[1] The current MCE design only includes three low noise lines suited for detector biasing, or the array would have been divided into more groups for detector biasing.

Figure 5.4: Bias powers on the 148 GHz array before and after repairs. *Left*: The drop in power of all detectors near column 22 row 30 (region in red circle) is an indication of the radiating normal region on column 22 (thin red horizontal stripe). Row 25 (thin red vertical stripe) initially failed due to a bad solder joint but was repaired before deployment. *Right*: After removing column 22 from the biasing circuit, the heating problem was repaired and the excess radiation load near column 22 row 30 disappeared. (The trend of slightly decreasing powers on a number of columns in that region was expected based on the SRDP measurements.) Column 22 itself continues to be non-functional since it was removed from the detector biasing circuit (thin red horizontal stripe). The 124 black detectors on this plot are the ~12% of the array that was non-functional during the first season of observations. The single detector with a '+' sign has a bias power above the range of the color scale.

512 detectors to fail, a decrease of only ∼40 detectors during the array assembly process is clearly a success.[2]

5.2.2 Heat sinking

Heat sinking of the silicon cards in the array is critical, or the columns will warm up, and the elevated operating temperature will reduce the saturation power of the bolometers. The primary heat sinking for each column was accomplished by soldering copper wires onto a gold heat-sinking layer on the structural (bottom) silicon card as depicted in Figure 3.13. The shunt resistor, multiplexing, Nyquist, and detector chips are all mounted on top of this gold layer to maximize their thermal conduction to the bath [67]. The loose ends of the copper wires are bundled together in groups of eight, and bolted to the copper detector slab (Figure 5.5), which has a strong thermal link to the ^{3}He fridge [100].

Upon deployment, the array was indeed found to have a strong thermal link to the ^{3}He fridge. Biasing the entire array onto the transition near $0.4R_n$ only warmed the silicon card thermometers[3] by ∼0.3 mK and the ^{3}He bath temperature by < 0.1 mK. Even driving ∼1 mA through the shunt resistors when acquiring the normal branch of detector load curves only caused an increase of ∼6 mK at the silicon cards. Minimizing this increase is important for acquiring accurate load curves, because changes in bath temperature as a function of bias will change the saturation power, equation (3.2), and can confuse interpretation of the load curves. Since the temperature changes by less than 3 mK while the detectors are on the transition, a conservative estimate of the change in saturation power along the transition from temperature drift during load curve acquisition is ∼0.6%.

In addition to the heat sinking of the individual columns, all of the control wiring going to the 0.3K stage must be low thermal conductivity. Superconducting wiring is used for all of these lines. Multiple heat sinking ground planes were designed into the 4K and 0.3K circuit boards to ensure that both ends of the cables are at the same temperature as the respective

[2]The 88% array functionality should only make our required integration time $\sim(0.88)^{-1/2} = 1.07$ times longer than having a complete 1024 pixel array, or ∼1.02 times longer than if we had the 92% functionality found during SRDP testing.

[3]Three of the columns had Ruthenium Oxide (ROx) thermometers installed on the silicon cards (Figure 3.13, and all three showed the same response to biasing the detector array within measurement error.

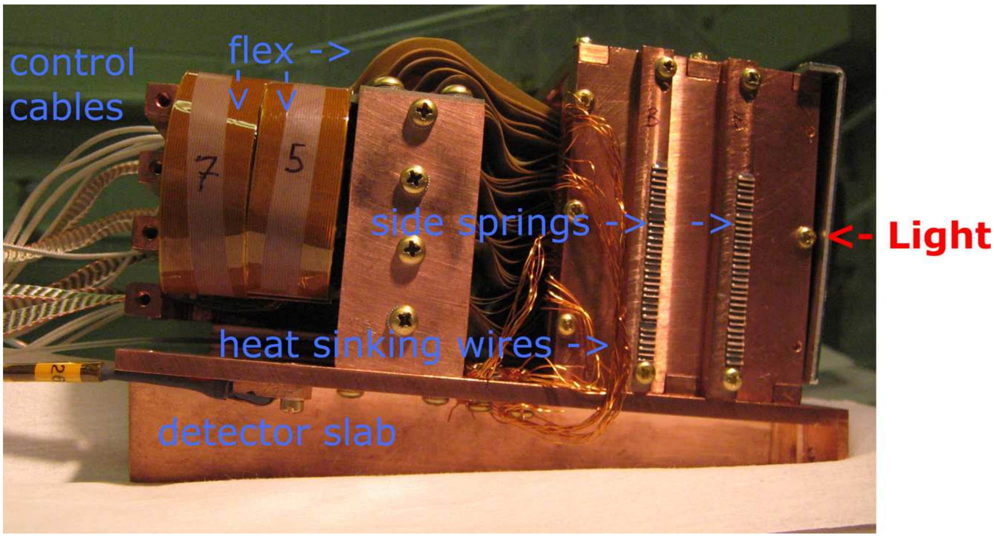

Figure 5.5: Heat sinking in the 148 GHz array. This side view of the array shows the copper heat sinking wires coming out of the back of the array, which were each soldered onto a gold heat sinking plane on one of the 32 columns (Figure 3.13). These wires are bolted down onto the detector slab in groups of 8 to improve the thermal connection between the columns and the bath. Also visible are the side springs that apply pressure to hold each of the 32 columns in place (Figure 5.6). Another type of spring is used to apply forward pressure on each of the columns to maintain the critical alignment to the silicon coupling layer as depicted in Figure 5.6. The aluminum cover at the right is protecting the array and is removed prior to installation in MBAC. The detector slab that the array is mounted to provides the tilt relative to the lenses and filters in the optical path as discussed in Section 2.3.3. Part of the superconducting control cables that connect the 0.3 K and 4 K readout electronics are shown at the left as well as the flexible circuity (flex) that connects each column to a detector backplane and connects the row addressing lines between backplanes. Some details of these cables are discussed in Appendix B.

stages. Minimizing the thermal load is also important because there will be roughly three times the load next season when the 215 GHz and 280 GHz arrays are installed.

5.3 Bolometer Alignment and Efficiency Measurements

5.3.1 Alignment

The alignment of the bolometers relative to the silicon coupling window is critical to maximize photon absorption, or efficiency (Section 2.7) [36]. Building off the prototype array design [67], we have developed and tested a new method to achieve the critical tolerances between the 32 manually assembled bolometer columns and the coupling window (Figures 5.6 and 5.7). The target alignment tolerance for the new method is ± 20 μm for the second and third arrays (Figure 5.7). It was discovered that the edges of the detector chips, which are formed during a chemical deep-etching process [71], have variable positions relative to the bolometer positions at the ± 25 μm level. This is greater than the entire target error budget for the alignment, without including errors in machining or the alignment process. The metallic features, however, do have constant position offsets relative to the bolometer positions with ± 5 μm errors. The new technique utilizes some of these metallic layers on the detector chip for the alignment. Using a column vacuum manifold [67], metallization near the edges of the detector chips is aligned to calibrated laser dicer marks on the manifold, while the manifold position is held constant relative to the front silicon card edges. This is similar to how the "stop blocks" in the array holder are used align the silicon cards relative to the silicon window as shown in Figure 5.6. The largest remaining error in the alignment is due to tilting of the detectors during the folding process (described in detail by J. Lau [67]), which occurs when an offset is introduced between the two thick silicon portions of the detector chip (purple in Figure 5.6; a vertical offset between the purple regions in the figure would result in tilting of the bolometers). Figure 5.8 shows these errors, which were measured to be as large as $^{+55}_{-75}$ μm on the worst of columns 00 through 07 in the first array. For the second and third arrays, the folding alignment issues have also been solved, and preliminary measurements indicate that we should achieve the alignment target of ± 20 μm.

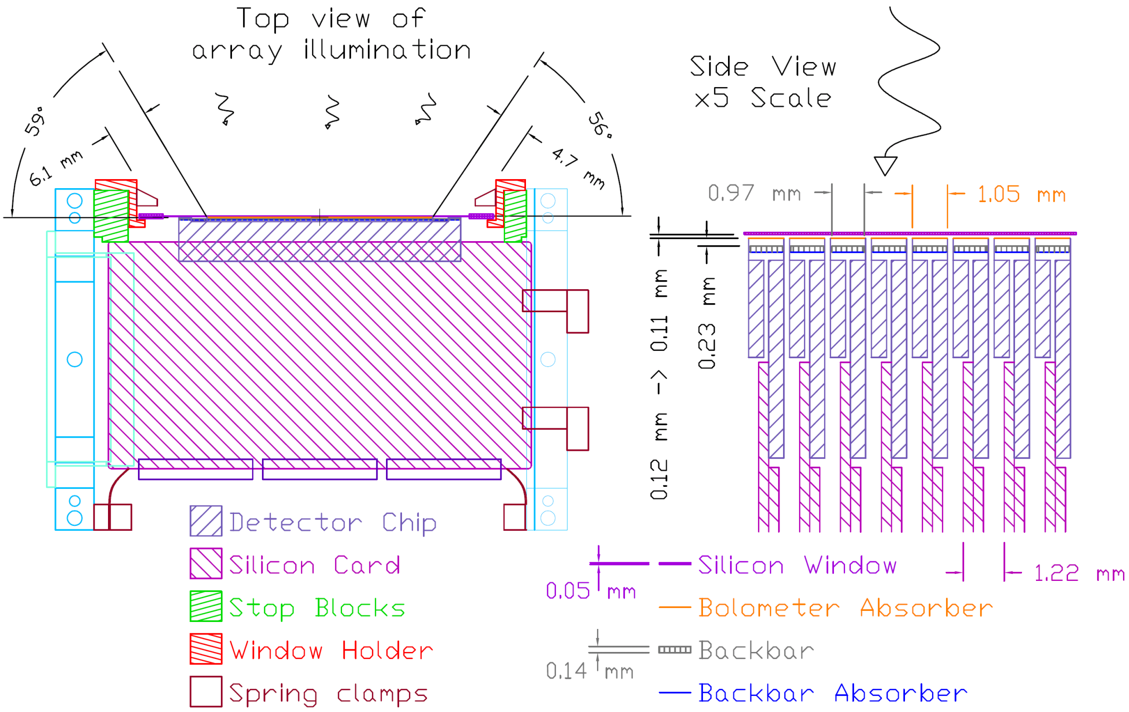

Figure 5.6: Array schematic of critical alignment components and detector geometry. The most critical alignment for maximizing the efficiency is the 0.12 mm gap between the bolometer absorber and the silicon window, which becomes 0.11 mm at 0.3 K because of differential thermal contraction between the copper and silicon structures. (This dimension as well as the non-critical alignment between the bolometer and backbar of ∼0.23 mm is shown in black at the right.) The critical alignment is defined for each column by the relative positions of seven different parts of the array assembly as well as the folding alignment of the detector chip. At the left, the most extreme rays from the optical design are shown striking the outside edges of the row 00 and 31 detectors. At the right (where the array is rotated to a side view and the scale is five times larger) we show some of the critical dimensions of the detector optical design as well as the width of the backbars (grey, 0.97 mm), the width of the bolometers (orange, 1.05 mm), and the spacing between neighboring columns (magenta, 1.22 mm). With the exception of the silicon coupling window thickness and its distance to the bolometer absorber (Table 2.5), we plan to maintain all the measurements presented here for the 215 GHz and 280 GHz arrays.

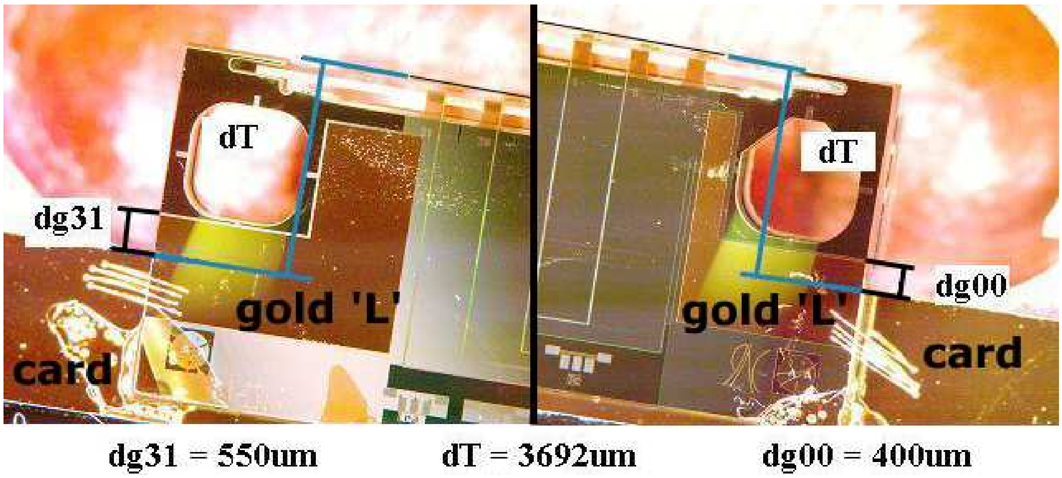

Figure 5.7: Detector column alignment technique for positioning the detector chips accurately relative to the silicon card edge. The row 31 (*left*) and row 00 (*right*) ends of a column of detectors mounted onto a silicon card are shown. (These are zoomed views of a column like the one depicted in Figure 3.13.) The goal for aligning the detector chips is to have constant distance between the silicon card edge and the bolometer absorbers (whose edges have been darkened for emphasis in the photo). This distance is shown as dT = 3692 μm (blue dimensions) on the photographs. To achieve this, the column is placed in a vacuum manifold [67] (not shown) and the top edges of the gold 'L' shapes on the detector chip are aligned to calibrated marks made by a laser dicer on the manifold. The calibrated marks are spaced by dg31 = 550 μm and dg00 = 400 μm (black dimensions) from the edge of the silicon card, so that the bolometer absorbers are held parallel to the silicon card edge. Note that gold wirebonds are connected between the gold on the silicon card and the detector chip to improve heat sinking.

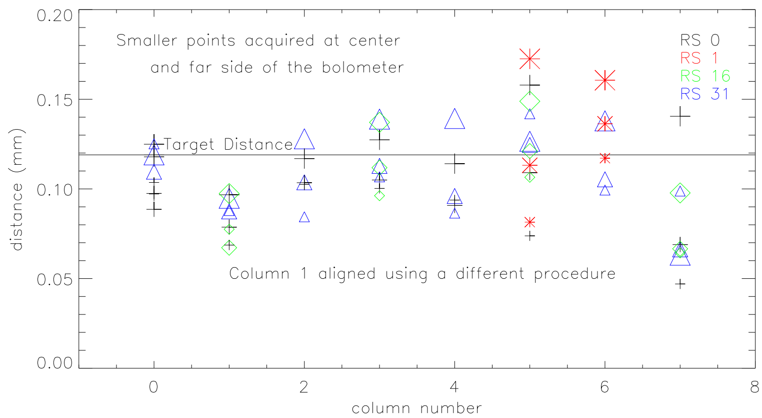

Figure 5.8: Alignment measurements of eight columns in the first array. The distance between the silicon coupling layer and the bolometers is plotted versus the column number. Each color represents measurements made of a different detector row (RS). The largest data points are from measurements made near the TESs, medium points were made near the middle of the bolometer, and small points near the far side of the bolometer. The spread in the black crosses on column 7 clearly indicates how badly the folding misalignment can skew the position of individual pixels relative to the coupling layer. Because of differential thermal contraction during cooling, the target distance of 0.12 mm is 0.01 mm longer than the optimal distance shown in Figure 2.11.

The array was assembled in two stages. The first eight columns were installed and measured in MBAC to confirm that all of the major problems encountered in the prototype array [67] were solved by the new screening techniques presented in Sections 3.4 and 3.5. After the MBAC tests were complete, a microscope with xyz measurement capability and $\sim$5 μm resolution along the z-axis was borrowed from R. Austin to measure the alignment of pixels on the eight columns relative to a silicon frame that represented the location of the silicon coupling layer.[4] Height measurements were made at three positions on two to four pixels on every column (Figure 5.8) as well as at 23 positions on the surrounding frame. During analysis a plane was fit to the frame measurements, which was treated as the coupling layer height, and the plotted distance measurements were calculated by subtracting the measured height from the height of the coupling layer plane at the x-y coordinates of the measurement. Line fits to the three calculated distances on each bolometer were used to estimate pixel tilt around the column axis and height at the bolometer center (ignoring bowing of the pixels, which is expected to be more pronounced on the future arrays that will have wider bolometer legs); then, these values were fit across each column to estimate the height and tilt of every bolometer (Figure 5.9).

5.3.2 Efficiency measurements

Liquid Nitrogen (LN_2) load measurements were made with MBAC to measure the change in efficiency from adding the silicon coupling layer as well as attempt to measure the absolute efficiency of the bolometers. A styrofoam container filled with LN_2 and Ecosorb was swept across the MBAC optical path near the focus at the dewar window. A $\sim$2% neutral density filter (NDF) was installed in MBAC to prevent saturation of the bolometers with the dewar window open to the laboratory. The measurements were made before and after adding the silicon coupling layer to make a robust measurement of the change in efficiency (Figure 5.10). The amplitude of the bolometer response was calculated using DC responsivity estimates,

[4]Because of the danger associated with having the fragile array exposed (especially while moving a relatively large and massive microscope lens around near the bolometers), no more measurements were made after additional columns were installed in the array.

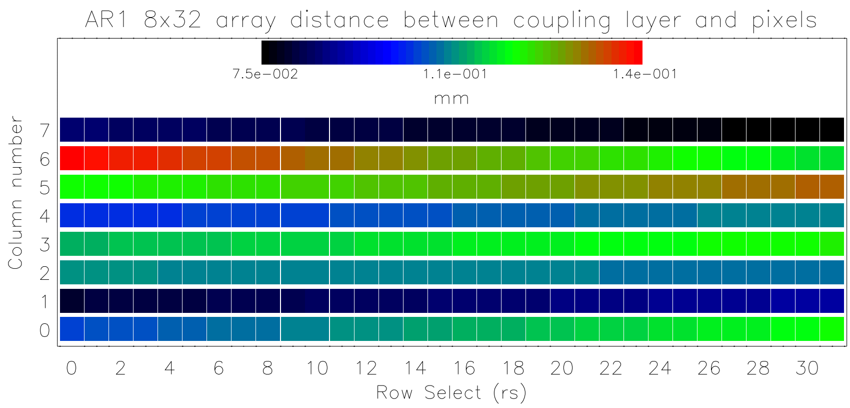

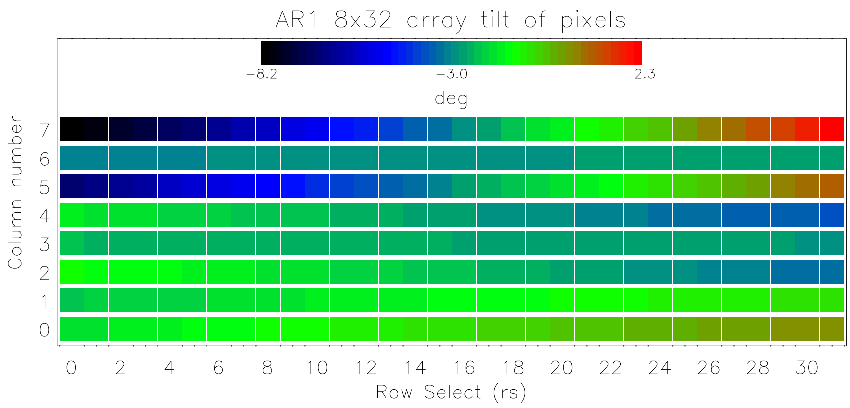

Figure 5.9: Alignment height and tilt of eight columns in the first array. The height and tilt are estimated for each column using fits to the measurements acquired on a few pixels within each column (Figure 5.8). These height and tilt variations affect the bolometer interaction with the silicon coupling layer and are used to fit the model described in Figure 5.11.

equation (3.24), from load curve data. Installing the silicon coupling layer improved the efficiency of the eight tested columns by a median ratio of $\sim$1.55.[5]

The efficiency improvement ratio measurements (Figure 5.10) were combined with the bolometer height and tilt estimates (Figure 5.9) to explore an efficiency model. The improvement ratio data, z, were fit to $z = z_0 - w_x(x - x_0)^2 - w_y y^2$, where x is the distance from the silicon coupling layer (mm), and y is the tilt of the bolometer (degrees).[6] The form of the fit is motivated by the approximately parabolic shape of the predictions as a function of distance in Figure 2.11 and because the tilt angles result in changes in distance that go as $\sin(y)$, which is approximately y for the small angles measured. The fit was done using a four dimensional matrix search of the maximum efficiency increase, z_0, the optimal alignment position, x_0, and parabolic widths for the distance, w_x, and the tilt, w_y. The minimum variance solution is $z_0 = 1.60$, $x_0 = 0.117$ mm, $w_x = 112$ mm^{-2}, and $w_y = 0.00345$ deg^{-2}, which is shown as the contours in Figure 5.11. Because the distance measurements were made at 300 K, differential thermal contraction causes x_0 to become $\sim$0.107 mm when cooled to 0.3 K, which is consistent with the optimal distance predicted in Figure 2.11.

The column with the greatest efficiency improvement is column 00, which has bolometers with improvement ratios as high as 1.72, while the column with the least improvement is column 07 with all measurements below 1.4 (Figure 5.3.2). It is also interesting to note that the column 00 values are all above the fit model, while the column 07 values are all below the fit model (see residuals in Figure 5.11). This may be a coincidence, although, it may also be an indication that the coupling layer improves the efficiency of columns at the edge of the array (like column 00) more than columns in the middle of the array. This is particularly relevant for column 07, since during the first test without the coupling layer it was at the edge of the eight column array, then columns 08 – 31 were installed before the second test, which packed column 07 between neighboring columns and may have caused a reduction in its efficiency. To examine this hypothesis, the analysis presented in Figure 5.11 was repeated using only columns 01 – 06. The minimum variance fit to only these six

[5] Analysis by L. Parker comparing the signal to noise improvement from adding the silicon coupling produced similar results.

[6] Rows 00 and 31 (on all eight columns) were excluded from the fit because of the consistently lower efficiency improvement ratio on these bolometers shown in Figure 5.10.

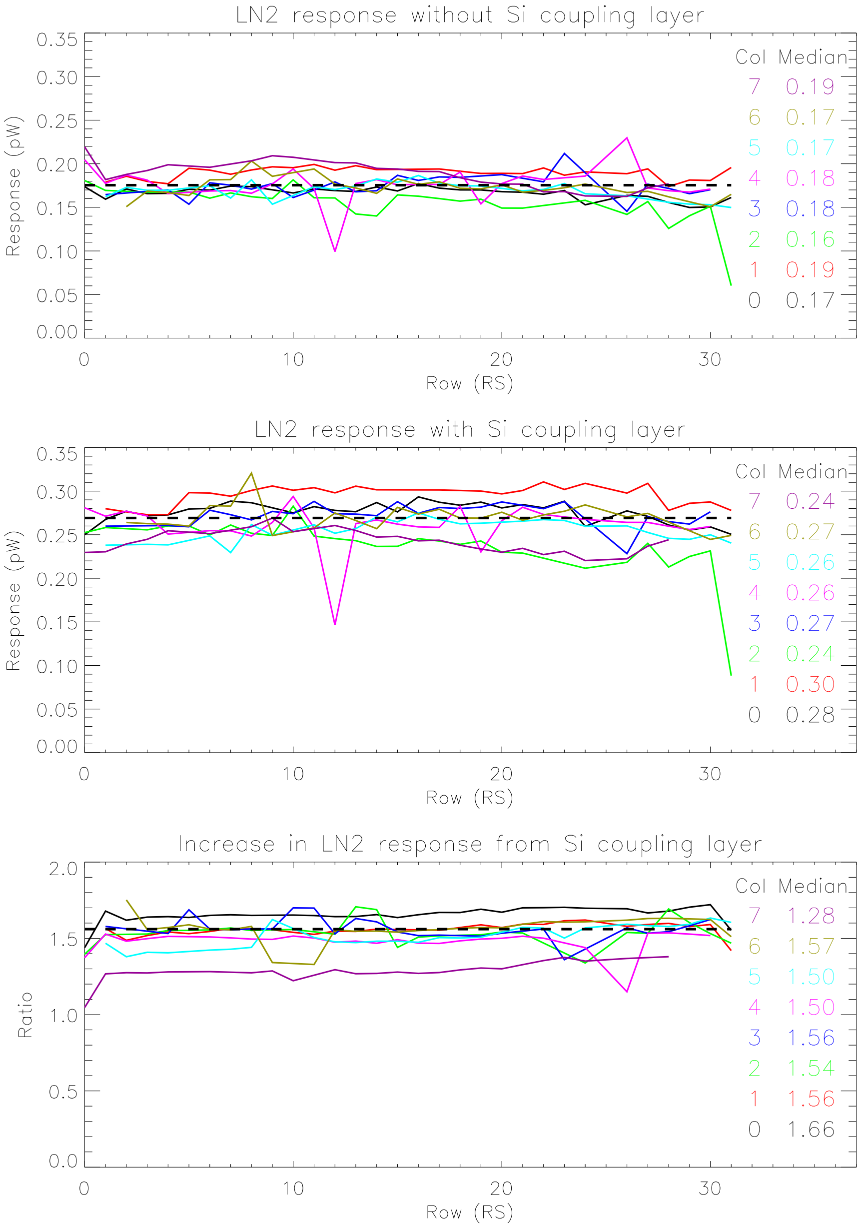

Figure 5.10: Liquid Nitrogen load measurements for columns 00 through 07 of the first array before (*Top*) and after (*Middle*) installing the silicon coupling layer, which were converted into power using load curve data and equation (3.24). The ratio of the two measurements (*Bottom*) shows the improvement in efficiency of the detectors from adding the silicon coupling layer. Dashed lines are plotted at the median value for each group of measurements. The improvement ratio is combined with the height and tilt measurements (Figure 5.9) to fit the model in Figure 5.11.

columns is $z_0 = 1.55$, $x_0 = 0.102$ mm, $w_x = 52.8$ mm^{-2}, and $w_y = 0.00161$ deg^{-2}. The fit to only these six columns has an average variance of the fit residuals of 0.0049 as opposed to the fit for all eight columns, which has an average variance of 0.0069. This and the decreased efficiency ratio of bolometers in rows 00 and 31 seem to indicate that the silicon coupling layer has a different effect on bolometers at the edge of the array than bolometers with neighbors on all sides. Thus, the fit to only columns 01 – 06 seems more appropriate for comparison with the model predictions than the fit results for all eight columns.

The infinite plane analysis used to calculate the optimal distance to the silicon coupling layer predicts that the efficiency improvement could be as large as a factor of two.[7] In addition to the efficiency improvement, adding the silicon coupling layer is expected reduce reflections off the array (and thus "ghost" images [41]) from ~50% without the coupling layer to less than a few percent as shown in Figure 2.11. Unlike the silicon coupling layer, however, the bolometer array only fills ~86% of the planar space in the row direction, and the absorbing back-bars in each column only fill ~80% of this space (Figure 5.6), so it is not surprising that the infinite plane approximation over-predicts the efficiency increase.

In addition to calculating the efficiency increase from adding the silicon coupling layer, we can also use these data to estimate the absolute efficiency of the bolometers. The difference in blackbody temperature between the LN_2 load and room temperature radiation is estimated to be 290 K − 80 K = 210 K. Because the LN_2 load fills the solid angle viewed by the detectors, we can simply multiply the temperature difference by the Raleigh-Jeans slope for the 148 GHz band from Table 2.4 and the 2% transmission of the NDF[8] to predict the change in loading at the detectors, $\Delta P \approx 0.46$ pW. Comparing this prediction to the LN_2 measurements without the silicon coupling layer, we find $\Delta P_{J_0} \approx 0.18 \pm 0.03$ pW (Figure 5.10), or $39 \pm 7\%$ efficiency, which is near the predicted absorption for these bolometers without the coupling layer. After adding the coupling layer, $\Delta P_{J_0} \approx 0.27 \pm 0.05$ pW, or $58 \pm 10\%$ efficiency. Column 00, which is the best aligned, has a number of bolometers with estimated efficiencies $> 60\%$ (Figure 5.10).

[7] The theoretical increase in efficiency from ~40% without the silicon coupling layer to ~80% with the silicon coupling layer was calculated by S. Staggs as well as T. Essinger-Hileman.

[8] The 2% NDF transmission value was obtained from an email from C. Tucker at Cardiff University.

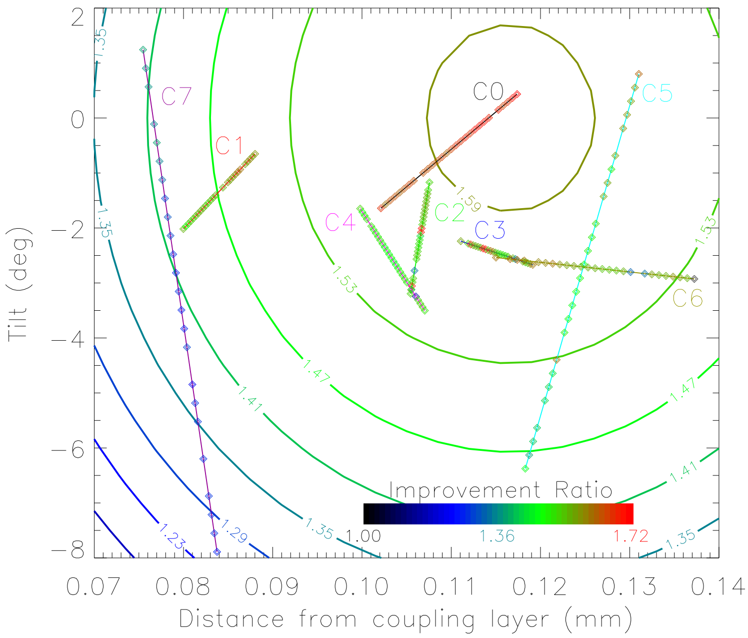

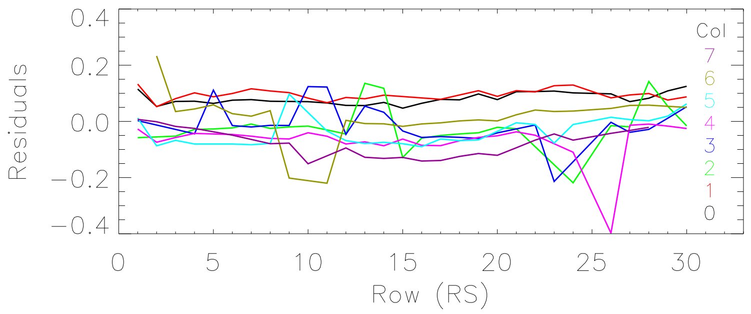

Figure 5.11: Fit to the silicon coupling layer improvement ratio data as a function of detector distance and tilt. *Top*: The data from the bottom of Figure 5.10 were fit to $z = z_0 - w_x(x - x_0)^2 - w_y y^2$, where z is the improvement ratio, x is the distance from the silicon coupling layer (mm), and y is the tilt of the bolometer (degrees) (Figure 5.9). The other four variables were found by minimizing the total variance between the model and the data using an iterative matrix search. The lowest variance solution was found to be $z_0 = 1.60$, $x_0 = 0.117$ mm, $w_x = 112$ mm^{-2}, and $w_y = 0.00345$ deg^{-2}. The fit w_x and x_0 appear consistent with expectations from the model (Figure 2.11), because thermal contraction will move the coupling layer 0.01 mm closer to the array after cooling $\rightarrow x_0(0.3\ \mathrm{K}) \approx 107\ \mu$m. *Bottom*: Residual improvement ratio differences between the data points and the fit model.

Uncertainties in the efficiency measurements include the effective blackbody temperatures of the LN_2 loads and the laboratory as well as the efficiency of the NDF and the responsivities calculated from the load curves.[9] Each of these uncertainties are estimated to be between $\pm 10\% - 20\%$ about the assumed values (or roughly $\pm 25\%$ summed in quadrature), and errors in these values change the absolute efficiency estimates proportionally; however, the relative efficiency estimates and model shown in Figure 5.11 are primarily sensitive to changes in the relative temperature of the lab and LN_2 load between the two tests, which are estimated to be $\pm 5\%$, and random load curve failures. Another potential source of error is the impedance of the ion-implanted bolometer absorber. This impedance is a critical input for the model in Figure 2.11, and it is being measured on witness samples from the first array by our collaborators at GSFC to check whether the values used in the model are accurate. In Section 6.4 we compare the absolute efficiency estimates to analysis of measurements of a planet during observations.

5.4 Detector Time Constants

The detector time constants are critical parameters for our measurements, because if they are too slow, they will filter the sky signal at small angular scales (Section 2.5). Multiple approaches were attempted to determine the detector time constants prior to fielding the instrument including: measurements of complex impedance, optical response to a square wave, detector bias-step response, and response to a chopped source at a variety of different frequencies. The chopped source is the most appropriate, because as the telescope scans across the sky, signals will illuminate the detectors at different frequencies in the signal measurement band (< 200 Hz) depending on their angular size, so this method effectively allows us to probe the detector response to different angular scales.

The problem with optical chopper measurements is that they are too complex and time consuming to conduct during observations. Acquisition of one set of measurements

[9] Load curve responsivities errors can be caused by random failures in fitting the normal branch of the load curve (Section 3.5.3) or systematic errors caused by the shunt resistance values (measured in the SRDP, Section 3.5.2). The former can cause random scatter between the different measurements, while the latter primarily causes load curve calculations to be systematically wrong by a constant factor; although, a higher order effect caused by shunt resistance errors occurs when measurements acquired at different detector resistances, R_0 are compared, equation (3.24).

takes a few hours to achieve sufficient signal to noise for accurate fits. It also requires a moving chopper wheel in front of the MBAC window, which must be removed again for sky observations. A far more practical method for characterizing time constants in the field is the detector bias-step technique, which has been recently integrated into the MCE (Section 4.3), and can be made with high signal to noise across the entire array in under a minute. These two approaches are described and compared here.

5.4.1 Optical measurements

Optical chopper wheel measurements were made at the beginning of the first season of observations in series with detector bias-step measurements. Detector bias-step acquisitions were then repeated five to ten times per night during the remainder of the observation season. Data were acquired with the MCE digital filter turned off to prevent confusion between the filter and detector response. The chopper wheel was locked at a frequency between 4 Hz - 200 Hz, then 40 seconds of data were acquired. This was repeated 43 times at 30 different frequencies (in approximately random order), so that some frequencies were regularly repeated to monitor the stability of the measurements. Unlike the measurements of the prototype array described in Section 3.3.2, these measurements were made on the telescope, so that the chopper wheel presented a reflecting surface to the detectors, then moved past to reveal small apertures open to the night sky (Figure 5.12). It is important to position the chopper wheel close to the apertures used for the measurements to be sure that the radiation reflected by the wheel into the dewar is primarily cold radiation thermalized inside the dewar and not ∼300 K radiation from outside, which will saturate the bolometers. The dewar window where the chopper was located is near a focus, so that only ∼60% of the array was illuminated sufficiently for the measurements (Figure 5.12). The area under the chopper frequency peak in the power spectrum of the 40 second data segments is integrated, then the nearby white noise background level is subtracted. A one-pole filter response model,

$$I_{pk} = \frac{I_{DC}}{\sqrt{1 + (f/f_{3dB})^2}}, \tag{5.1}$$

is fit to the integrated peak amplitudes, I_{pk} (in units of A/Hz$^{1/2}$), as a function of frequency, f, to calculate the bolometer f_{3dB} values (Figure 5.13). The f_{3dB} results for the array –

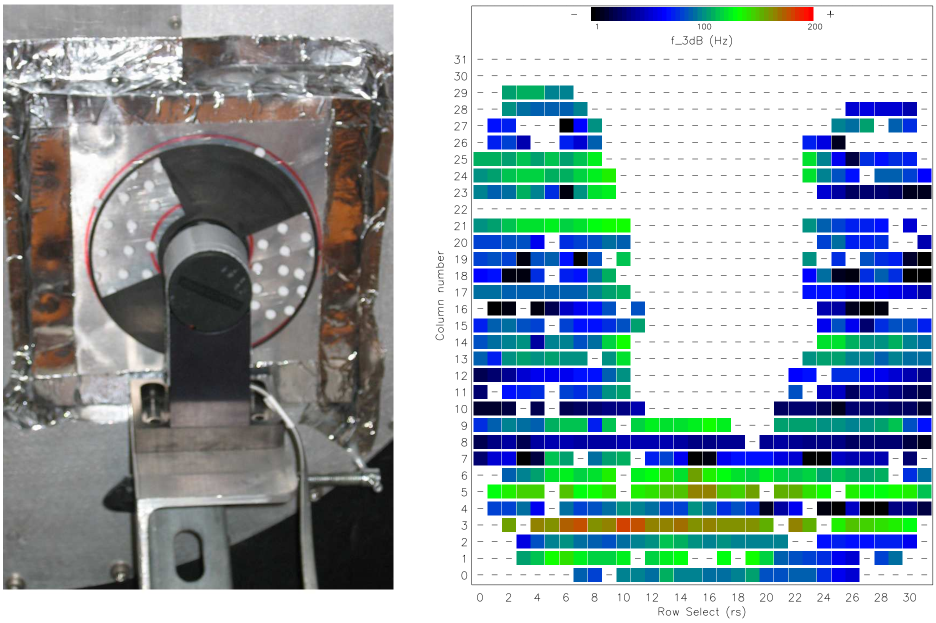

Figure 5.12: Optical time constant measurements of the first array. *Left*: Photograph of the chopper wheel set up in front of the MBAC 148 GHz camera window for time constant measurements. Small holes were drilled in the window cover, so that as the chopper wheel spins the detectors alternately see a reflecting metal blade and the sky. *Right*: Time constant measurements that passed the response amplitude cut described in the text. The 'U' shape of the bolometers on the array that passed the cuts is the inverted shape of the chopper wheel (and its support structure) and is due to it being near a focus. The fit data for row 4, columns 2 - 8 is shown in Figure 5.13. The median detector bias point during this data acquisition was $R_0/R_n = 0.4$, and the detector bias powers were measured to be similar to values measured on clear nights while observing the sky.

after cutting bolometers with DC response amplitudes, I_{DC}, less than 4×10^{-7} A/Hz$^{1/2}$ – are shown in Figure 5.12.

Using information from load curves acquired before and after the chopper measurements, the f_{3dB} was studied as a function of R_0/R_n and P_{J_0} (Figure 5.14). There appears to be some f_{3dB} dependence on P_0 in the array, but there is a great deal more scatter than was observed in three prototype columns (Figure 3.7). The large scatter in the time constants across the array makes it critical that we assess them during observations, because they will vary with P_{J_0} as the atmospheric loading level changes from night to night. A

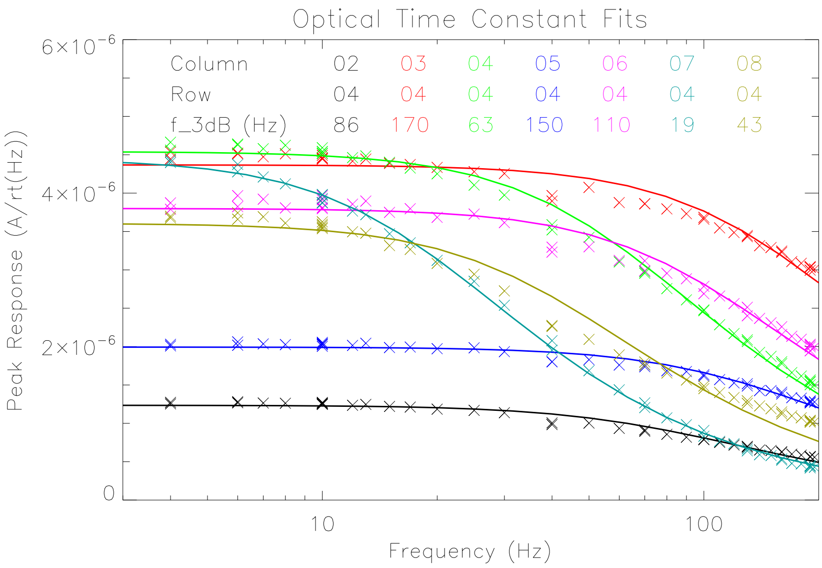

Figure 5.13: Detector time constant fits to optical chopper data. A sample of detectors from row 04 are plotted and have fitted f_{3dB} values between 19 Hz - 170 Hz. The simple one-pole filter model (lines) appears to be a good description of the measured bolometer response (Xs) for most bolometers. All data points lie within ±10% of the corresponding one-pole filter model value for all bolometers except column 02 and column 08, which lie within ±15% and ±30% respectively.

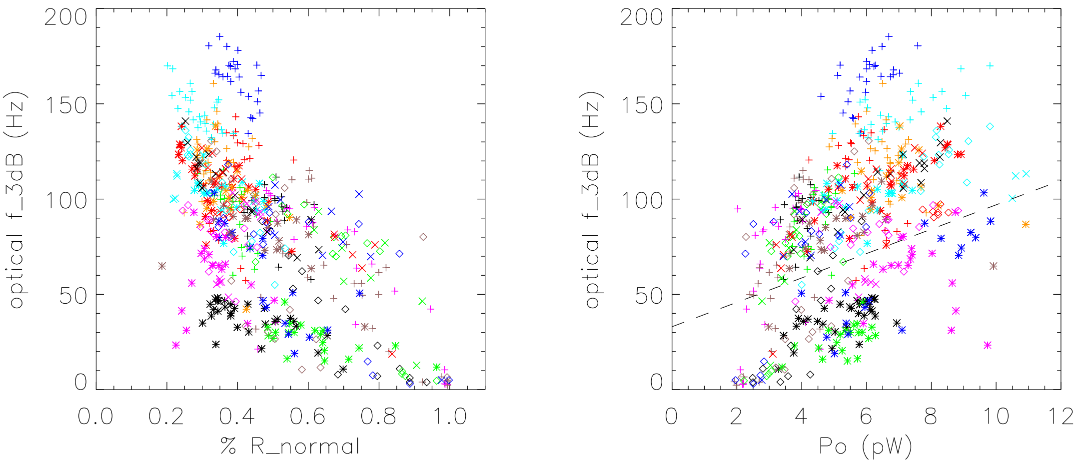

Figure 5.14: Time constants versus detector resistance ratio, R_0/R_n (*Left*), and bias power, P_{J_0} (*Right*), for the ~60% of the array for which this data exists (Figure 5.12). There is a large amount of scatter in the distribution of time constants across the array. The linear function fit to the prototype bolometer data in Figure 3.7 is also plotted (dashed) for reference. Each column of detectors in the array has a different color-symbol combination. Many of the slowest detectors are at high R_0/R_n, and these were found to have faster time constants when the target bias point was lowered as described in Section 6.2.

histogram of the distribution of time constants is shown in Figure 5.15. Measurements are planned to explore whether individual bolometers in this array have the same consistency of time constants as a function of R_0/R_n as the prototype column presented in Figure 3.8; preliminary indications are yes from comparing the time constant distributions at different bias points in Section 6.2.

5.4.2 Bias-step measurements

As described in Section 4.3.3, we have developed a method for quickly characterizing the detector time constants using a square-wave step on the detector bias line (bias-step). The decay of the bolometer current response after a sudden DC increase in voltage bias is fit with an exponential function to extract the time constant. Bias-step measurements were acquired before and after the chopper measurements described in the previous section. The results of the two techniques are compared in Figure 5.15.

We find that the bias-step time constant measurements need to be scaled by a constant factor of ~1.78 to match the chopper results. This factor is not particularly surprising given the variability in the results of different fitting techniques discussed in Section 4.3.3. This indicates that if the bias-step fitting technique or data acquisition method are ever changed, a new calibration between bias-step and optical chopper measurements is required. After removing the constant factor, the errors between the two measurement techniques appear Gaussian with a full-width half-maximum (FWHM) of ~22 Hz (Figure 5.15). Since only ~60% of the array was measured during the chopper test, we use the scaled bias-step measurements to estimate the distribution of time constants for the entire array (Figure 5.15). The complete distribution closely tracks the subset of bolometers with optical chopper measurements.

5.5 Noise comparison

Prior to deployment to Chile, detector noise measurements were made in both the SRDP (Section 3.5.5) and in MBAC with the dewar window covered by a metal plate. Here we compare those measurements to each other and to an estimate of the theoretical noise

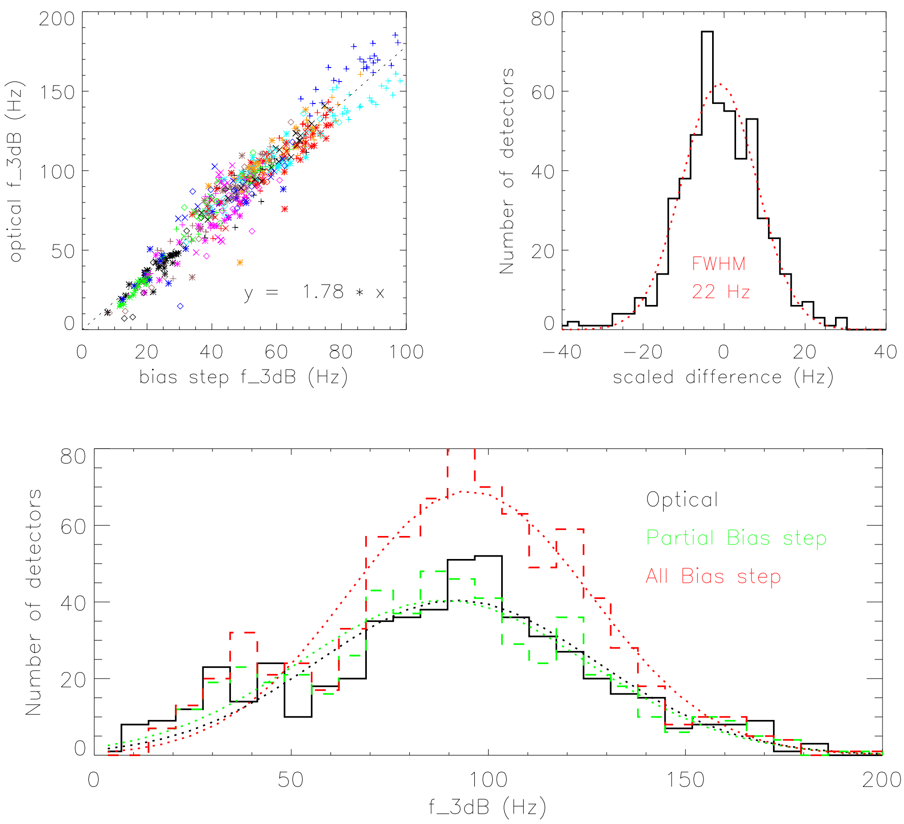

Figure 5.15: *Upper Left*: Comparison of optical chopper and bias-step measurements of time constants indicates that we can approximate the chopper f_{3dB} by scaling the bias-step f_{3dB} by a factor of ∼1.78. *Upper Right*: The residual difference between the chopper f_{3dB} measurements and the scaled bias-step measurements has a Gaussian form with FWHM of ∼22 Hz. *Bottom*: Histograms of the chopper measurements (black) the scaled bias-step measurements of the same detectors (green) and the scaled bias-step measurements for the entire array (red). Gaussian fits to the chopper measurements and the bias-step measurements of the same detectors (dotted) indicate that they peak at 92 Hz and 89 Hz with FWHM of 83 Hz and 85 Hz respectively. The distribution of bias step measurements for the entire array peaks at 95 Hz with FWHM of 73 Hz. Because of an excess of slow bolometers near 25 Hz, however, the Gaussian functions do not accurately describe the distribution of time constants. (The bias-step analysis was done by J. Appel.)

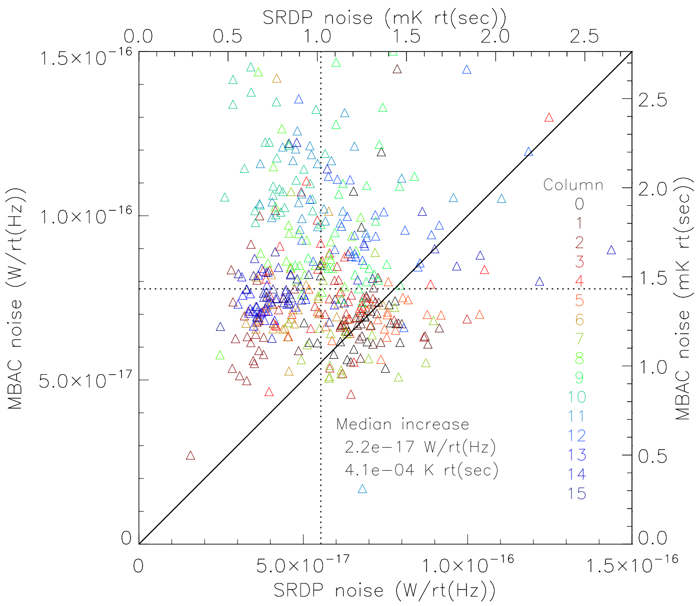

Figure 5.16: Comparison of measured detector noise levels in the SRDP and MBAC prior to deployment. The noise levels were extracted from Fourier transforms near 10 Hz and calibrated into W/Hz$^{1/2}$ (lower and left axes) using load curve data, then estimated in mK sec$^{1/2}$ (upper and right axes) as described in the text. The median values (dotted) of the two sets of measurements are compared to assess the increase in noise in MBAC. The median increase in noise in MBAC was $\sim$2.2 $\times 10^{-17}$ W/Hz$^{1/2}$, or $\sim$0.41 mK sec$^{1/2}$. Significant work has been done since these measurements to reduce the noise in MBAC, and studies are underway to quantify the success of these attempts. Note: Because of the heating problem when biasing half of the array during preliminary testing in MBAC (Section 5.2.1), these comparisons are only made on 16 of the columns. (Noise analysis was done with Y. Zhao.)

limit. Low-frequency data from both sets of measurements are converted from A/Hz$^{1/2}$ into W/Hz$^{1/2}$ using the DC responsivity, equation (3.24), calculated from load curve data, and then these are converted into CMB temperature units.

The median 10 Hz noise level measured in the SRDP was 5.5×10^{-17} W/Hz$^{1/2}$. The largest contributor to this noise level in the isothermal TES model is expected to be thermal fluctuation noise (TFN) from phonon interactions between the bolometer and the bath. Inserting the T_c from Table 5.2 and the median measured $G \approx 80$ pW/K (and assuming $F_{link} = 1$) into equation (3.27), we find the median theoretical limit of the TFN for these bolometers is $(NEP_{th})^{1/2} \approx 3.4 \times 10^{-17}$ W/Hz$^{1/2}$. Some of our bolometers are at or below this value, but the median bolometer in-band noise is $\sim$60% higher (Figure 5.5). This excess noise is believed to be primarily due to the isolation of heat capacities by weak thermal links within the bolometers, as described in Section 3.5.5.

After array assembly and installation in MBAC, the same bolometers were measured while multiplexing to have a median 10 Hz noise level of 7.8×10^{-17} W/Hz$^{1/2}$. This 40% increase in noise is larger than expected, and significant work was done before observations in Chile to reduce this, including: optimization of the SQUID tuning and MCE parameter selection, grounding of guard wires on the SA SQUID readout lines, isolation of the system from RF sources, and numerous other steps. Studies are underway to understand whether these steps have brought the MBAC noise level closer to that measured in the SRDP. Possible sources of noise that have not been fully ruled out include: excess noise (such as that in Figure 3.11 or the SQUID noise in Figure 5.3) that is aliased into the signal band, unexplored multiplexing artifacts, radio-frequency interference (RFI), or an optical loading leak from a 4 K or 40 K blackbody in MBAC. More detailed characterizations of any remaining differences in noise levels are planned prior to the 2008 observation season.

These noise levels are estimated in CMB temperature units using the calculations of $\delta P_{bb}/\delta T_{RJ}$ and $\delta T_{CMB}/\delta T_{RJ}$ from Section 2.6 as well as a 60% efficiency estimate (based on Sections 5.3.2 and 6.4). After these conversions, the SRDP noise level becomes $\sim$1.0 mK sec$^{1/2}$ and MBAC $\sim$1.4 mK sec$^{1/2}$ with respect to the CMB. Recent progress has been made in characterizing multiplexing artifacts and apparent RFI pickup that could be contributing to the noise level increase in MBAC; however, even with this elevated noise level, with $\sim$850 bolometers observing the sky, we predict that ACT with MBAC will characterize the CMB at small angular scales substantially more accurately than has been done before (Chapter 8).

Acknowledgements

The majority of the people involved in the design and building of ACT, MBAC, and the detector arrays have been directly or indirectly involved in the work described in this chapter. Here are a few of the key people that made possible some of the specific work described. The details of the array and heat sinking design were developed primarily by N. Jarosik, T. Marriage, J. Lau, and L. Page and are discussed in the thesis of J. Lau [67]. The new

techniques for aligning the columns relative to the silicon coupling layer built off techniques developed by J. Lau, and they – as well as the detector folding alignment – were fine tuned by L. Parker for the next two arrays. The array alignment measurements were made possible by the help of R. Austin, J. Puchalla, and P. Galajda and the use of their microscopes. K. Martocci and L. Parker were critically involved in the final physical assembly of the array, and in addition to all of the people above, it could not have been completed without the help of O. Stryzak, T. Essinger-Hileman, J. Appel, Y. Zhao, R. Fisher, and B. Harrop among others. The integration of the array with MBAC also involved a number of those people and the University of Pennsylvania team, including: B. Thornton, D. Swetz, M. Kaul, J. Klein, and M. Devlin. Of course, none of this would have happened without the incredible machinists in the Princeton machine shops, especially B. Dix, G. Atkinson, L. Varga, and M. Peloso. D. Swetz, J. Klein, and E. Switzer were instrumental in the testing of the array at U. Penn, as was the MCE team, especially E. Battistelli, M. Amiri, and M. Hasselfield, who ran many tests remotely and B. Burger who came to U. Penn to further the development of the MCE. The bias-step analysis and comparison with optical measurements and noise analysis were done with J. Appel and Y. Zhao.

Chapter 6

Preliminary Results from ACT Observations

First light with MBAC on ACT was achieved on October 22, 2007, when Venus was observed with the 145 GHz detector array. With almost nine hundred functioning bolometers, this was the largest millimeter-wave detector array ever to observe the night sky. Observations continued into December 2007 until a gear box on one of the telescope motors failed on December 16. Systematic tests and data acquisition with MBAC continued until it was shipped back to the University of Pennsylvania to prepare it for three band observations during the 2008 season. An intense effort is currently underway to analyze the data acquired during the 2007 season. In this chapter we present preliminary results from the 2007 season, including: performance of the optical design, detector time constant comparisons with point source observations, estimated beam window functions, detector biasing analysis with data cut analysis, and optical efficiency results. Complete maps, cluster catalogs, and cosmological analysis will be presented in future publications.

6.1 Optical Performance

Point source observations indicate that the optical design is performing as predicted. Numerous measurements of Mars were made on all working detectors in the array by scanning in azimuth as Mars moved through the field. In Figure 6.2 we show the relative peak loca-

Figure 6.1: ACT and MBAC deployment. *Left*: ACT before the external ground screen was completed. The view of the primary and secondary mirrors is blocked by the inner ground screen, which moves with the telescope. The receiver cabin provides access to the MBAC instrument and mirror surfaces. The cabin doors are ∼1.8 m tall for scale. *Right*: Preparing for deployment of the MBAC receiver onto ACT. The external ground screen now blocks the view of the entire telescope.

tions of Mars from a single ten minute observation (found from two-dimensional Gaussian fits) for all detectors in the array that passed preliminary data cuts. The measured plate scale and field distortion are consistent with the predictions presented in Chapter 2.

6.2 Detector Time Constants from Planet Observations

The detector time constants act as low-pass filters on the sky signal during scanning of the telescope (Section 5.4). The response of the detectors to scanning across a point source can be simulated using the beam model presented in Section 2.6.2. A typical azimuthal scanning velocity ($\omega_{az} = 1^\circ$/s) and observation elevation ($\theta_{el} = 50^\circ$) are used to apply a causal unidirectional low-pass filter to the beam model for a range of different detector f_{3dB} values (Figure 6.3). Near the peak of the time constant distribution ($f_{3dB} \approx 90$ Hz), the simulation predicts that the detector time constant shifts the peak of the point source response by $\sim 4''$ in the direction of the scan. Because these shifts occur in opposite directions for left-going versus right-going scans, this becomes an $\sim 8''$ difference in fits to the peak response between the two directions. Slower detectors obviously cause larger shifts,

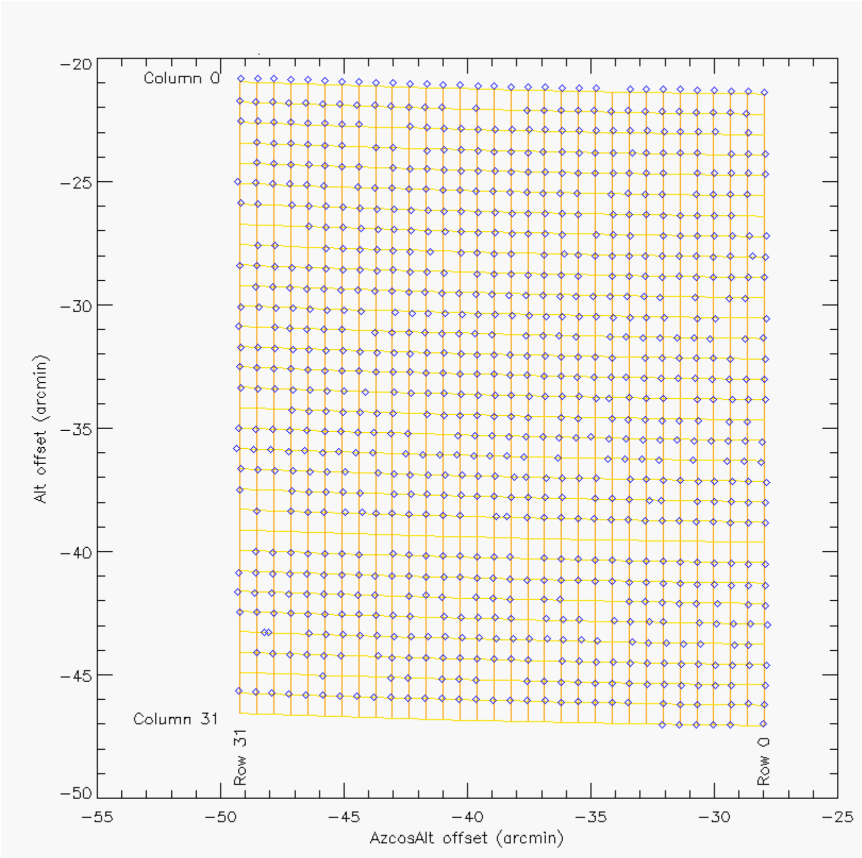

Figure 6.2: Point source measurements and field distortion from a single ten minute scanning observation of Mars. The grid is a fit to the peak locations with a parabolic tilt in the vertical direction to account for field distortion (Figure 2.6). Small offsets of each detector column were allowed during assembly of the array, which is why many of the horizontal detector columns have horizontal DC shifts relative to the grid. From this single ten minute observation, the responses of 850 detectors in the array survive preliminary data cuts, measure Mars, and are plotted here. (Figure courtesy of J. Fowler.)

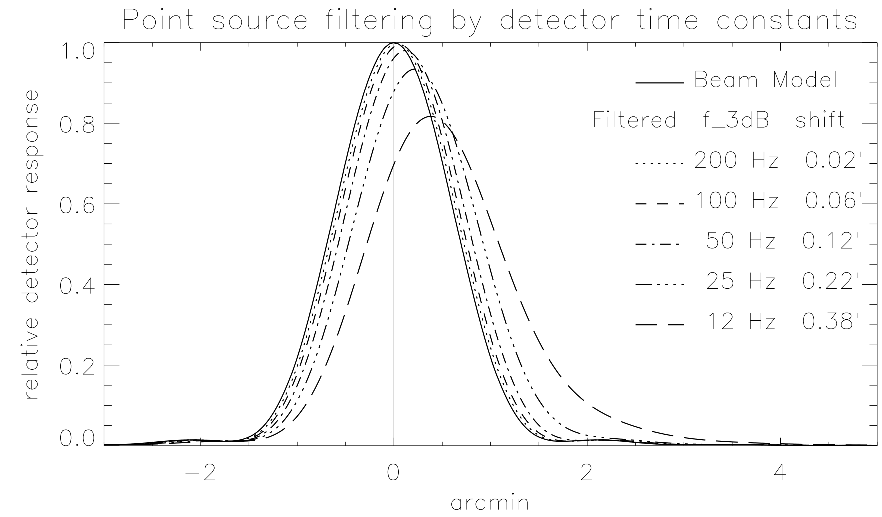

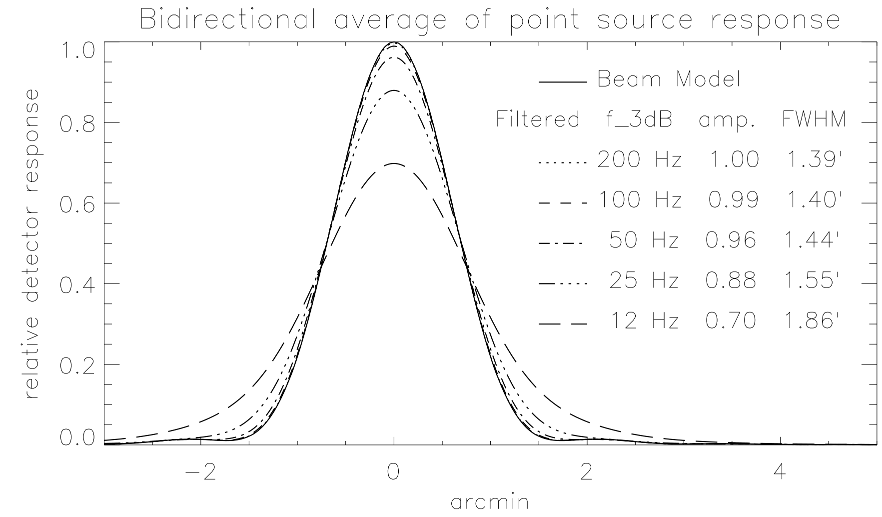

Figure 6.3: Predicted detector time constant effect on point source measurements using the PSF model from Section 2.6.2. *Top*: Assuming the nominal CMB scan parameters during the 2007 season ($\omega_{az} = 1°/\mathrm{s}$ and $\theta_{el} = 50°$, or $\omega_{sky} = 0.64°/\mathrm{s}$), the predicted response of detectors with five different time constants are shown. The legend shows the f_{3dB} as well as the shift in the position of the peak along the direction of the scan. *Bottom*: If we ignore the time constants and simply average the bidirectional response from left-going and right-going scans, they cause significant changes in the peak amplitude and FWHM as shown in the legend.

so that a 12 Hz detector is expected to have a relative shift of $\sim 46''$ between the two scan directions. These shifts are straightforward to measure from point source observations by separately fitting two-dimensional Gaussians to the left-going and right-going scan data. The detector time constants also reduce the amplitude of and broaden the response, which should be accounted for when using the response amplitude for calibration and potentially deconvolved to prevent widening of the beams, or smearing of the small scale signals across the sky (Figure 6.3).

The effects of the detector time constants on beam measurements can be parameterized in terms of the ratio of f_{3dB} and the scanning velocity across the sky, ω_{sky}. To explore these effects in greater generality, we define the angular time constant

$$f_s \equiv \frac{f_{3dB}}{\omega_{sky}} = \frac{f_{3dB}}{\omega_{az} cos(\theta_{el})}. \tag{6.1}$$

Figure 6.4 shows the predicted unidirectional shift, relative peak height, and effective FWHM as a function of f_s. These unidirectional shift predictions are used in reverse to convert the offsets measured in point source observations into time constants. In Figure 6.5 the time constants extracted from preliminary fits to an observation of Mars are compared to optical chopper measurements (Section 5.4) and bias-step measurements (which are renormalized as described in Section 5.4.2). There are strong correlations between the time constants measured on the majority of the detectors despite the significant differences in these measurement approaches and the different conditions at the times the measurements were acquired – chopper measurements were acquired 44 days prior to the others. This indicates that the one-pole filter model is a reasonable approximation for the detector response in the signal band (0 Hz - 200 Hz). There are two significant groups of outliers when comparing the Mars results to the chopper measurements. The first group has large errors in the point source azimuth position fits and are therefore removed from the analysis. We are still working to understand the details of the causes of the large fit errors. The second group of outliers was biased at $R_0/R_n > 0.75$ during the chopper time constant measurements; however, a different detector biasing target was used during the Mars measurements, which brought these detectors to lower R_0/R_n as discussed in Section 6.2.1.

There also appear to be a group of detectors that have significantly faster point source f_{3dB} measurements than chopper or bias-step measurements. These fast detectors are the

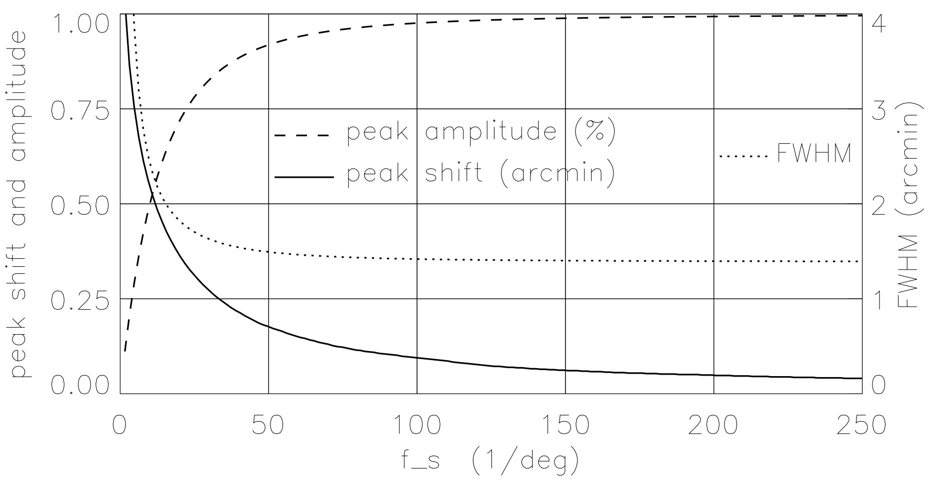

Figure 6.4: Simulated time constant effects on point source measurements. The changes in three measures of the PSF are plotted as a function of $f_s = f_{3dB}/\omega_{sky}$. *Left axis*: The unidirectional shift in the peak centroid (solid - scale is arcminutes) is used to calculate detector f_{3dB} values in Figure 6.5. The bidirectional average of the relative peak amplitude (dashed - scale is percentage) is used to apply a correction to the efficiency estimate in Figure 6.10. *Right axis*: The bidirectional average FWHM (dotted) is used to compare the window functions of the PSF model to Gaussian models with the same FWHM in Figure 6.8.

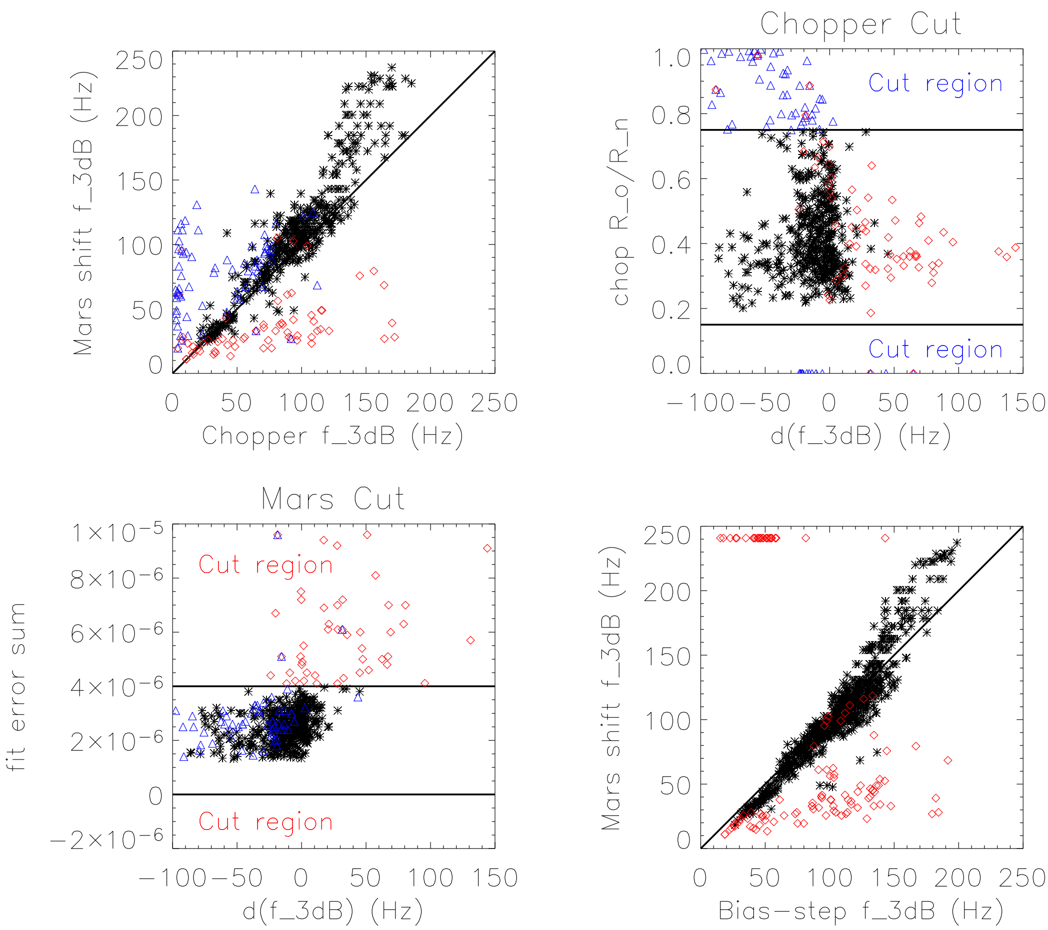

Figure 6.5: Time constant comparison between point source, optical chopper and bias-step measurements. *Upper left*: Comparing the optical chopper versus point source f_{3dB}. This comparison shows a strong correlation between the point source and chopper response. Blue and red points respectively show data cut on the resistance ratio during chopper data acquisition, R_0/R_n, (*upper right*) as well as the sum of the errors in the left-going and right-going azimuthal point source fits (*lower left*), which remove the data points with the largest deviations, $\mathrm{d}(f_{3dB}) = f_{3dB}(\mathrm{chopper}) - f_{3dB}(\mathrm{Mars})$. *Lower right*: Comparing bias-step f_{3dB} (after application of the 1.78 correction factor, Section 5.4.2) versus point source f_{3dB} acquired on the same night of observations. The strong relationship between these nightly measurements indicates that we have multiple good probes of the detector time constants every night of observations. The red points with Mars shift $f_{3dB} \approx 240$ Hz are not the chopper plot because these detectors are not in the ∼60% of the array measured by the chopper. Measurement distributions are shown in Figure 6.6. (The Mars data was fit by B. Reid and the bias-step data was analyzed by J. Appel.)

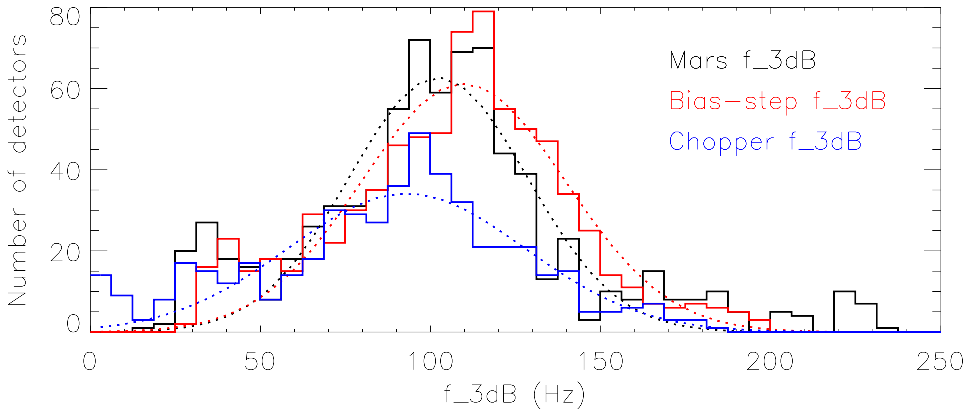

Figure 6.6: Distribution of time constants from point source (black), optical chopper (blue) and bias-step measurements (red). The f_{3dB} are only shown for detectors that survived the Mars error cut (Figure 6.5). The peak f_{3dB} of Gaussian fits to these distributions (dotted) clearly show that the Mars and bias-step distributions are faster. The cluster of slow detectors below $f_{3dB} \approx 25$ Hz in the chopper measurements are also shifted to higher frequencies. An explanation for the differences in the distributions is discussed in Section 6.2.1.

least worrisome, because they are fast enough that the time constants will have little effect on the analysis. The point source measurements were also compared to bias-step measurements (multiplied by the the normalization factor of 1.78 from Section 5.4.2) from the same night. There is an even stronger correlation between these measurements, and almost all outliers can be removed by cutting beam fits with large or negative errors.

An encouraging result of this study is that many of the detectors with slow optical chopper measurements at the beginning of the season appear to have increased f_{3dB} from the point source measurements. Gaussian fits to the time constant distributions (Figure 6.6) peak at 93 Hz for the chopper measurements, 110 Hz for the bias-step measurements, and 102 Hz for the Mars measurements. More importantly, the majority of the detectors below ∼25 Hz in the chopper distribution are shifted to higher frequencies in the other distributions. We note that there are ∼100 working detectors ignored in this analysis, which fail the Mars error cuts. The cause of the increase in f_{3dB} is explored in Section 6.2.1.

The ACT analysis team is currently studying the costs and benefits of using the results of (planet and bias-step) time constant measurements to deconvolve the time constants from the detector time streams as opposed to simply removing the slowest bolometers from the analysis prior to making maps of the sky.

6.2.1 Detector Biasing and Data Cuts

The cuts made on the chopper time constants in Figure 6.5 are an indication of a strong relationship between R_0/R_n and f_{3dB} in these bolometers. At the beginning of the 2007 observation season – and during the optical chopper measurements – the detector bias currents were selected so that the median detector would be biased at $0.4R_n$. With this bias target, 66 otherwise working bolometers were found to have $R_0/R_n > 0.75$ from load curve analysis, compared to 791 with $R_0/R_n < 0.75$ (Figure 6.7). Shortly after the chopper measurements, the median detector bias point was dropped to $0.3R_n$ and left there for the remainder of the season. Lowering the target bias point brought all detectors into the $R_0/R_n < 0.75$ regime, which substantially increased the time constants of many of the 66 bolometers that were not previously in this regime (Figure 6.6).[1] This is a clear indication that $0.3R_n$ is a superior detector bias target for this array.

A lower cut limit of $R_0/R_n > 0.15$ has also been suggested based on previous characterization of the detector time constants across the transition (Figure 3.8). After lowering the detector bias target, no detectors in the array were measured to be below this limit (Figure 6.7), with the exception of 27 detectors that failed the load curve acquisition. The cause of the load curve failures is not well understood but is believed to be related to S1 SQUID feedback locking failures when sweeping through a large range of detector bias currents. There is, however, an alternative method of accurately measuring R_0/R_n using the bias-step amplitude analysis described in Section 4.3.1. Based on these results we have two suggestions for future data analysis: 1) Use bias-step measurements to calculate R_0/R_n during each night of observations; 2) Cut detectors outside of the range $0.15 < R_0/R_n < 0.75$.

[1] We have confirmed that despite significantly higher PWV on the night of the chopper acquisition, the limited illumination of the array by the sky (Figure 5.12) caused the detector bias powers to be similar to those during the Mars acquisition.

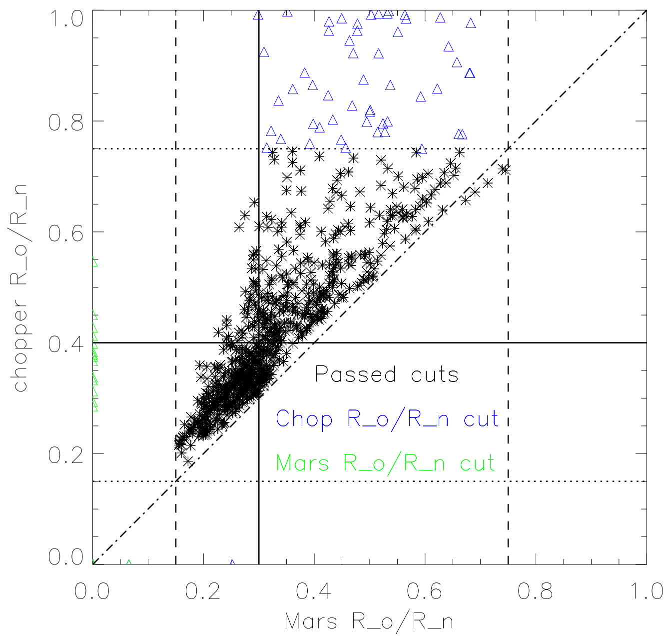

Figure 6.7: Detector biasing and data cuts. During the chopper measurements, the target bias point was $0.4R_n$, and soon after it was dropped to $0.3R_n$ (solid lines). The higher bias point resulted in 66 detectors (blue points) falling outside of the suggested cut range of $0.15 < R_0/R_n < 0.75$ (horizontal dotted lines). Reducing the bias point to $0.3R_n$ brought all of these detectors within the suggested cut range for the Mars acquisition (vertical dashed lines). The points along the $x = 0$ and $y = 0$ axes are detectors that failed the load curve acquisition and an indication that we should instead use bias-step analysis to measure R_0/R_n for making cuts during data analysis.

6.3 Time Constant Effects on Beam Window Functions

Now that the implications for the detector time constants on point sources are established, we can explore how untreated detector time constants affect measurements on larger scales. Using an average of the predicted left-going and right-going scan response (Figure 6.3), we can Legendre transform the beam into spherical harmonics on the sky and explore the window function in terms of the multipole moment, l. To simplify this preliminary analysis, the beam is treated as though it were azimuthally symmetric – despite the asymmetry of the scanning measurements – which allows the transform to be expressed as

$$b_l = 2\pi \int b^S(\theta) P_l(cos\theta) d(cos\theta)/\Omega_b, \tag{6.2}$$

where $b^S(\theta)$ is the beam model as a function of angular radius, θ, on the sky, P_l is a Legendre polynomial, and Ω_b is the total beam solid angle, which normalizes the function [84]. The window function is $w_l = b_l^2$. The bidirectional-averaged beam models (for different f_{3dB}) in Figure 6.3 are integrated numerically out to $\sim 12'$ (which is $\sim$98% of the PSF encircled energy) to arrive at the window functions in Figure 6.8. The FWHM values from the beam models are used to compare the models to the limit of Gaussian beams, for which equation (6.2) can be integrated analytically [84],

$$b_l = e^{-l(l+1)\sigma_b^2/2}, \tag{6.3}$$

where $\sigma_b = \text{FWHM}/(8\ \ln(2))^{1/2}$. Gaussian beams are also integrated numerically to test the precision of the analysis (Figure 6.8).

The reduction in the window function amplitude for slow detectors above $l \approx 1000$ is a clear indication that we should either deconvolve the detector time constants from the time streams or cut detectors with $f_s < \sim 50\ (^\circ)^{-1}$ from the map-making and power spectrum analysis. Based on the preliminary analysis of Mars f_{3dB} results, only $\sim$30 detectors that survived the Mars fit cuts have $f_s < 50\ (^\circ)^{-1}$. This type of model will guide selection of scan parameters for the 2008 season of observations after time constants of the 215 GHz and 280 GHz arrays are characterized. There is a delicate balance that we are continuing to explore between scanning fast enough to combat detector $1/f$ noise and excessive filtering of small angular scale signals by the detector time constants.

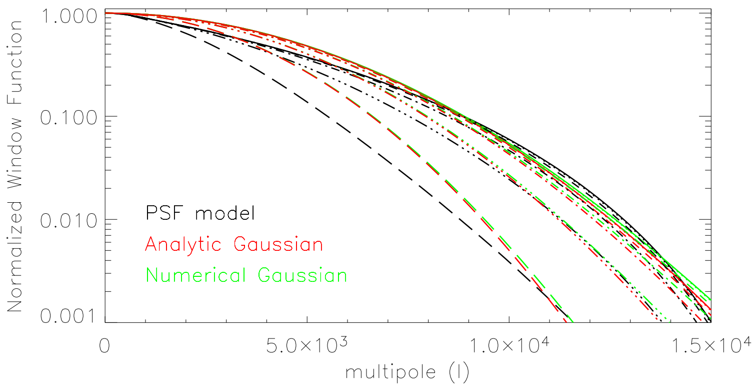

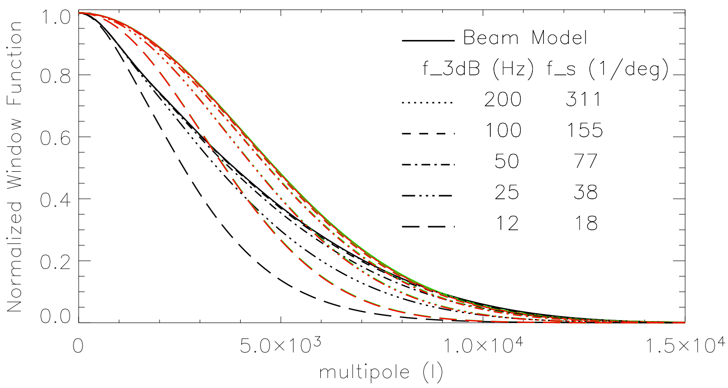

Figure 6.8: Beam window function predictions. The window functions are calculated for the bidirectional PSF models (black) at different frequencies in Figure 6.3 as well as assuming Gaussian beams (green and red). *Top*: In the logarithmic plot, the difference between the numerical (green) and analytic (red) solutions for the Gaussian beams becomes apparent near $l \approx 10,000$, which is an indication of the precision of the calculation. *Bottom*: The linear plot clearly shows the differences between the PSF based beam model and the pure Gaussian model. Preliminary evidence indicates that our beams are closer to the PSF model. The legend shows the line styles that correspond to the f_{3dB} and equivalent f_s values that were used for this analysis, which are the same for both top and bottom plots.

6.4 Efficiency Analysis

The amplitudes of the fits to the point source measurements allow estimation of the efficiency of the detectors themselves.[2] Using the optical loading prediction, the Airy disk PSF model presented in Section 2.6, and information about the planet, we can predict the loading from a planet on a given bolometer. The amplitude of the PSF is given by equation (2.5). Equation (2.4) can be converted into the total power from the planet by substituting the solid angle subtended by the planet, Ω_p, for the total solid angle, Ω. Since all the planets we measure are hot enough to be in the Raleigh-Jeans (RJ) regime, we can to first order use the $\delta P_{bb}/\delta T_{RJ}$ conversion in Table 2.4. We also use the RJ central frequency from Table 2.3 for the effective wavelength, λ, in the calculation. In addition to the instrumental efficiencies considered in Section 2.6, we must also take into account: the optical depth of the atmosphere, τ_{atm}, the airmass that the source is viewed through, $A = \sec(\pi/2 - \theta_{el})$ where θ_{el} is the elevation angle [71], and the PSF amplitude reduction due to the convolution of the PSF with the detector size, $\eta_{dc} = 0.855$ (Figure 2.9). Combing all these factors together, the predicted peak response of the PSF from a planet is

$$P_p = (T_p - T_{bg}) \frac{\delta P_{bb}}{\delta T_{RJ}} \frac{\Omega_p}{\Omega} \frac{\pi D^2}{4\lambda^2} \eta_{dc} e^{-A\tau_{atm}}, \tag{6.4}$$

where T_p is the planet temperature and T_{bg} is the astronomical background temperature.

The predicted power is compared with an observation of Mars on December 10, 2007. At that time, the angular diameter of Mars was $\sim$15.6″, or $\Omega_p \approx 4.49 \times 10^{-9}$ steradian. The PWV measured by the APEX collaboration was $\sim$0.63 mm, which can be converted at 148 GHz into $\tau_{atm} \approx 0.031$ [71], and the observations were made at $\theta_{el} = 38.2°$. The effective blackbody temperature of Mars at 148 GHz at the time of the observation is one of the dominant uncertainties in this calculation and is estimated to be $T_p \approx 215 \pm 15$ K, which is extrapolated from Wright's predictions of the Mars temperature at wavelengths between 10 – 350 μm [114]. We assume that the dominant background power is from the CMB, which at 148 GHz is equivalent to an RJ temperature of $T_{bg} \approx 4$ K (Figure 2.8). These values result in a predicted peak power at a detector of $P_p \approx 0.58$ pW. The value for $\delta P_{bb}/\delta T_{RJ}$

[2] All unknown efficiencies and power losses are included in this estimate. The telescope mirror efficiency is one of the unknowns; however, for the 148 GHz array with the current mirror alignment, the mirrors are expected to have $< 1\%$ loss, which is below the current uncertainty in the efficiency calculation.

includes known losses in the dewar windows and filters but assumes 100% efficiency at the detectors, so by comparing the prediction to the measured responses, we can quantify the efficiencies (Figure 6.10).

Multiplying the bidirectional Gaussian peak fit results by the DC responsivities calculated from a load curve gives the peak power measured by most of the working bolometers in the array (Figure 6.9). The reason not all of the working detectors in the array are plotted is because a number of them often fail the load curve acquisition. A remedy for this is to use bias-step measurements to calculate the responsivities as described in Section 4.3.2. There are also numerous scattered detectors with large increases in response amplitude relative to their neighbors. This is due to the applied S1 SQUID feedback for those detectors wrapping through the 14-bit digital to analog converter (DAC) range, and suddenly jumping the difference between the DAC range and an integer number of $V - \phi$ periods (Figure 4.11). Coincidentally, the amplitude of this effect is slightly less than half of the typical Mars response amplitude, so we see many of the detectors that have this problem plotted on the same scale as the good measurements (Figure 6.9). The peak amplitude of Mars exercises $\sim$5% - 10% of the DAC range. Since the detector feedback values are fairly randomly distributed throughout the DAC range, we expect to observe these jumps on roughly $\sim$5% - 10% of detectors during Mars observations. The MCE has the capability to prevent jumps such as these by automatically "flux-jumping" one S1 ϕ_0 when it approaches the limit of the DAC. This feature has already been tested and used for load curve acquisition, and we plan to implement an upgraded version of it for all data acquisition during the 2008 observation season.

The measured power across the array peaks near the array center (Figure 6.9). This is expected for all the arrays because of slightly increased illumination of the primary mirror near the center of each focal plane, resulting in a larger illumination solid angle. Likewise, the beam size is expected to be correspondingly smaller in this region, which will affect the window function calculations (Figure 6.8). In addition, the Strehl ratio varies across the focal plane at the few percent level (Figure 2.5), which will impact this method of using the peak response height to measure the detector efficiency. To achieve a percent level measurement of the efficiency from Mars measurements, these effects as well as the change

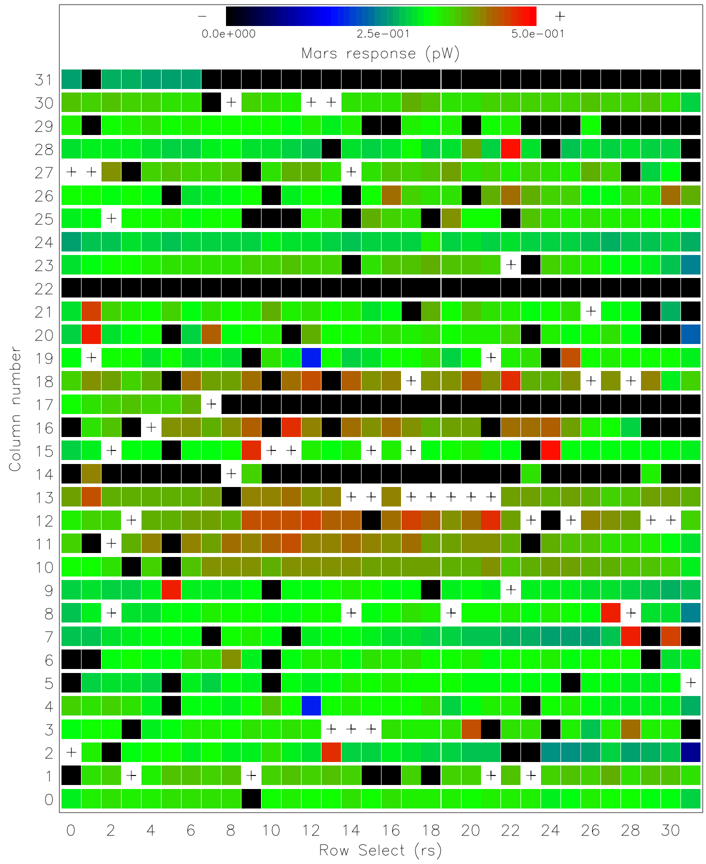

Figure 6.9: Peak responses across the array from from a Mars observation. The peak responses are extracted from two-dimensional Gaussian fits. The peaks are converted into power using DC responsivities calculated from load curves. The reason many detectors in columns 14 and 17 show no response is that they failed the load curve acquisition and thus have no responsivity data. The use of bias-step data for responsivity calculations (Section 4.3.2) will avoid these failures. Column 31 has lower saturation powers than the rest of the array, so the majority of its detectors are normal; however, this will be remedied for the 2008 season by returning it to an independent detector bias line. The scattered detectors with large responses (red and "+" signs) are caused by jumps in the time stream (see text) that have not been removed prior to this analysis. The general increase in response near the center of the array is due to slightly larger illumination solid angle than near the edges. Consistent deviations from the array trends across horizontal detector columns are similar to those observed in LN_2 load data – compare the drop in response of high row selects on columns 02 and 07 to the middle plot in Figure 5.10 – and may be related to shifts in the column alignment affecting the efficiency (Section 5.3).

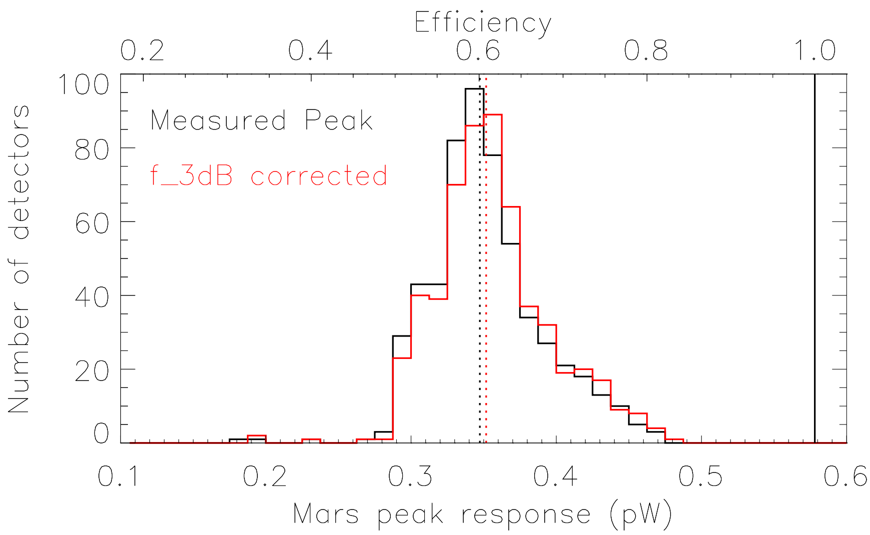

Figure 6.10: Efficiency measurement from a Mars observation. Cuts on the errors from the Gaussian fits shown in Figure 6.5 were applied to the peak response measurements in Figure 6.9. Surviving peak responses are histogrammed in black. Dividing these responses by equation (6.4) converts the powers into efficiency estimates (top axis), which have a median value of ∼60%. The Mars f_{3dB} measurements and the predicted change in peak amplitude (Section 6.2) are used to scale the responses to remove the time constant effect (red histogram). This moves the median of the efficiency distribution up to ∼61%. A few percent of the data at the high end of the distribution are likely caused by jumps in the time stream (see text) that have recently been understood, but have not been removed prior to this analysis.

in detector responsivity as a function of load power (Figure 4.13) will need to be taken into account.

After applying similar data cuts to those shown in Figure 6.5, the distribution of power measurements was studied to estimate the efficiency (Figure 6.10). The median of the distribution is ~0.35 pW, or ~60% efficiency based on the calculation above. Given the uncertainties (especially in the source temperatures of roughly ±15% and the solid angle variation across the array, which is also roughly ±15%) for the two methods of calculating the efficiency, this is surprisingly similar to the LN_2 efficiency measurements presented in Section 5.3.2. As shown in Figure 6.4, the detector time constants reduce the peak amplitude of the response. We correct for the detector time constant amplitude reduction using the time constants extrapolated from fits to the different scan directions (Figure 6.5), and find that this only increases the median efficiency to ~61% (Figure 6.10). It has not yet been determined whether this marginal increase is because the time constants are having minimal effects on the beam measurements, or whether the cuts made based on the Mars fits are simply removing a significant group of slow detectors. Studies are underway to clarify these effects.

These efficiency measurements are not as high as the theoretical predictions of ~75–80% for the detector array (Figure 2.11); however, this is not particularly surprising as discussed in Section 5.3.2. The resulting efficiency approaches the ideal achievable with the classic configuration of an absorber spaced $\lambda/4$ in front of a perfect reflector, but the classic configuration has ~30% predicted reflection which would cause a large increase in the amplitude of "ghost" images [41], while our configuration has only a few percent predicted reflection (Figure 2.11).

The consistency between calculations of the efficiency using two significantly different approaches (LN_2 lab measurements that fill the dewar aperture versus a diffraction-limited planet observation), as well as three different types of measurements of detector time constants (Section 6.2), seems to be an indication that by combining theoretical modeling and measurements we are converging on an accurate description of our experiment.

Acknowledgements

A huge number of people were responsible for getting ACT and MBAC up and running in Chile, most of whom were authors (or acknowledged) on the ACT first light paper [79] or the optical design paper [41], so for fear of forgetting one of the many critical people, I will leave it at that. The majority of the data results presented here are only possible because of the hard work of the ACT analysis team, especially (but not exclusively) T. Marriage, J. Sievers, B. Reid, S. Das, M. Nolta, R. Lupton, J. Fowler, and D. Spergel. The two-dimensional Gaussian fitting of point sources that has so often been alluded to was implemented and run by B. Reid. The plate scale and distortion analysis in Figure 6.2 was done by J. Fowler. The window function analysis was guided by L. Page. Useful discussions were had with numerous people, especially E. Switzer, D. Swetz, J. Fowler, and L. Page.

Chapter 7

Photometric Redshifts for Cross-Correlation Studies

ACT has begun surveying large areas of the sky to provide a nearly mass-selected galaxy cluster sample via the Sunyaev-Zel'dovich (SZ) effect (Section 1.3.2). Because of the lack of sensitivity of the SZ effect to redshift (Section 1.3.2), clusters or groups of galaxies detected this way need follow-up observations at other wavelengths to determine their redshifts. The large area of sky we plan to cover and the large number of expected detections makes spectroscopic follow-up of galaxies in every cluster prohibitive, so we will utilize redshifts obtained from broad-band photometry (photometric redshifts or photo-z). As broad-band photometry provides low resolution spectral information, the determination of galaxy-redshifts can be affected by relatively large errors. Photo-z errors can limit the accuracy of cosmological studies using galaxies or clusters, which highlights the importance of improving photo-z determinations. In particular, Lima and Hu estimate that the photo-z bias and scatter must be known better than 0.003 and 0.03, respectively, in order to prevent greater than 10% degradation of constraints on equation of state of dark energy from a wide field SZ cluster survey [69]. We will require photo-z not only for clusters but also for field galaxies to exploit the signal of CMB weak lensing by large scale structure [20, 27] and the kinetic-SZ effect [48]: two powerful probes of the growth of structure, which will be useful for dark energy studies.

In this chapter (which is a modified portion of our photo-z paper [78]), we present an analysis of a new approach for calculating photo-z that involves combining ultraviolet data from the space-based Galaxy Evolution Explorer (GALEX) telescope with optical data from ground-based telescopes. We begin with some photo-z background, then present the details of the source catalogs that are analyzed. After describing the data and methods used in our approach, we present a test of its performance on spectroscopic samples from the Sloan Digital Sky Survey (SDSS) stripe 82 region. The test shows that this method approaches (and in blue galaxies may improve on) the accuracy of the SDSS artificial neural network photo-z pipeline [23, 82], which uses large and sophisticated training sets. We conclude with a discussion of the results and a plan for future observations.

7.1 Photometric Redshift Background

The use of broad-band photometry to determine redshfits is not new [9, 59]. In its minimalistic approach it consists of simply finding the best fit redshift using a series of galaxy templates, which can be either chosen from stellar population models or empirically [60] as long as the set is exhaustive (i.e. fully describes the galaxy population). With the arrival of large spectrographs, it became clear that a refinement of the above technique could be achieved by using small subsets of spectroscopic redshifts as "training sets" for larger photometric samples. One can then use these training sets as inputs for empirical fits to the magnitudes versus z [19] or for artificial neural network codes to compute photo-z [23, 82, 108]. Another approach is to use prior information about galaxies, like the fact that faint galaxies tend to be farther away, as a Bayesian prior for computing the redshift likelihood from the templates [12, 39, 53]. Other recently developed techniques that go beyond simple photometry fits include using structural properties of galaxies like their size or surface brightness to obtain more accurate photo-z [113].

The above methods have their pros and cons. For example, the use of structural information of the galaxies can only help to reduce the error in the photo-z at relatively modest redshifts ($z < 0.25$). Methods based on training sets, because of their empirical basis, can only be reliably extended as far as the spectroscopic redshift limit. Training sets for surveys such as the dark energy survey (DES) and the Large Synoptic Survey Telescope (LSST) survey will need of the order of hundred of thousands of spectroscopic redshifts [81, 24].

To use Bayesian prior-based methods, one needs to construct and test different priors for different redshift ranges and surveys, which also requires spectroscopic redshifts to accurately generate the prior distributions.

Given the need to obtain relatively accurate photo-z for the large SZ survey areas (ACT may eventually cover a few thousand deg^2), we have explored an alternative approach. The goal of this approach is to optimize photo-z accuracy while minimizing external assumptions (priors) and additional data acquisition.

Our approach, presented in detail below, consists of obtaining moderate depth observations (Figure 7.2) with the Galaxy Evolution Explorer (GALEX) combined with optical data in the *griz* filter bands (shown in Figure 7.3). This data combination has been previously tried on shallower observations and using empirical approaches with spectroscopic training sets for photo-z determination [8, 19, 112]. Adding the two GALEX broad bands at central wavelengths of ∼1500 Å and ∼2300 Å to *griz* photometry, improves photo-z determinations, while requiring minimal assumptions about external priors, for the following reason. The 4000 Å break, which is the most commonly used spectral feature for optical photo-z determination, is greatly reduced for blue galaxies, making it more difficult to use as a redshift indicator. This problem is particularly acute at $z > 0.5$, where most galaxies are younger and have high star formation rates [47]. The 912 Å Lyman-limit, on the other hand, is exhibited by all galaxies (Figure 7.3). Since the GALEX filters sample closer to the Lyman-limit, they help to pin down the galaxy type and redshift, especially for blue galaxies with no substantial 4000 Å break.

7.2 Source sample

Our GALEX observations comprise a Legacy program awarded in cycle 3, with the goal of mapping ∼100 deg^2 of the SDSS stripe 82 with 3 ks exposure time per pointing in both the F_{UV} and N_{UV} filters (see Figure 7.3 for filter plots). The SDSS stripe 82 has been observed by ACT and of course offers a sample of SDSS spectroscopic redshifts to test the photo-z performance. We took advantage of the fact that the stripe 82 survey area includes a number of the GALEX Medium Imaging Survey (MIS) fields, which already had many > 1.5 ks observations and therefore needed only partial additional observations to reach our 3 ks target. In total we will collect ~210 ks of integration time — merely 2.4 days of observations.

At the time this analysis was completed, only about half of the planned observations had been made. The stripe 82 data set used for this analysis is comprised of the 56 GALEX fields (Figure 7.1 shows the ~55 deg^2 of coverage, although some field edges lie outside the SDSS stripe 82 region) to N_{UV} depths between 2 ks and 6.5 ks (Figure 7.2). Of those fields, 41 are publicly available MIS data, and the other 15 are from our guest investigator proposal. These data allowing us to probe deeper magnitudes and a more complete sample than has been possible with previous photo-z studies that used GALEX data [8, 19, 112].

As noted below (and by previous photo-z analysis teams [53]), the absence of the u band significantly degrades the performance of the photo-z estimation. We show that the addition of UV observations from GALEX is preferable to the addition of u.

7.3 Method

With the addition of the two GALEX bands, our methodology to obtain photo-z is fairly simple. We use the six galaxy templates in Figure 7.3 and perform a maximum likelihood analysis to find the best fitting model to the observed photometry. We do not use any prior information, or more accurately we use flat redshift and template priors. The six templates used are based on the four Coleman, Wu, and Weedman templates [22] ('El', 'Sbc', 'Scd', and 'Im' templates in Figure 7.3), with the addition of two Kinney et al. starburst types [58] ('SB3' and 'SB2' templates in Figure 7.3).

7.3.1 Magnitudes

Accurate absolute photometry is critical for obtaining accurate photo-z. Because of the differences in the point spread functions (PSF) of different instruments and between bands, simple aperture photometry is not appropriate for this study. The SDSS PSF widths are

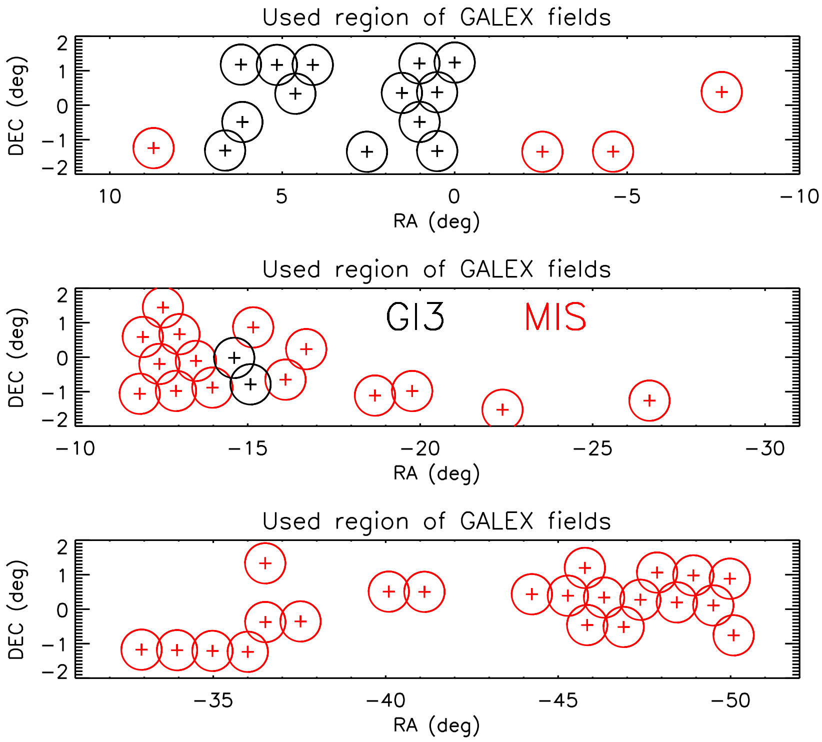

Figure 7.1: GALEX fields on the stripe 82 region. Each plot shows a different RA range. Observations have only been completed on 15 of our guest investigator (GI3) fields (black circles) at this time. There are 41 public GALEX Medium Imaging Survey (MIS) fields with > 2 ks NUV observation time that were also used for this analysis (red circles). The data from a single field is shown in Figure 7.4.

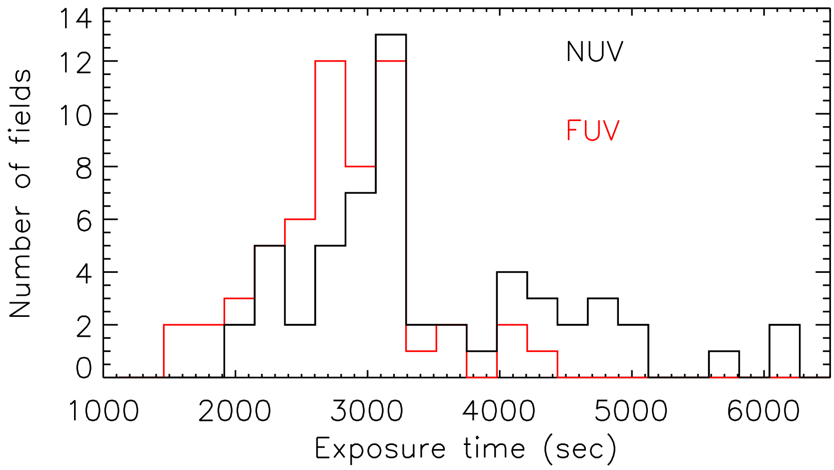

Figure 7.2: Distribution of exposure times for the GALEX fields used in this analysis for N_{UV} (black) and F_{UV} (red). Fields were only used with N_{UV} exposure > 2 ks, and 35 of the 56 fields have N_{UV} exposure > 3 ks.

approximately $1.5''$ and vary with sky brightness [2], while GALEX PSF widths vary across the field between roughly $4''$ and $7''$ [76]. Our approach is to use AB magnitude[1] measures that are as close as possible to the total flux emitted by the galaxy in each band.

As part of the standard GALEX pipeline for each field,[2] SExtractor is run on both the F_{UV} and N_{UV} images to extract multi-pixel sources that are detected above the noise threshold in background-subtracted images [15]. We use the N_{UV} and F_{UV} *mag_auto* outputs of SExtractor, which optimizes elliptical apertures for each source to integrate the total flux. The F_{UV} bandwidth and transmission are both roughly a factor of two smaller than the N_{UV} (Figure 7.3), causing it to have substantially lower sensitivity. Because of this, far fewer sources are independently detected in the F_{UV} band (Figure 7.5).

For the SDSS data we use *C-model* magnitude measurements, which consist of fitting models to the profile of the galaxy composed of an exponential disc and a deVaucouleurs profile. These fits are integrated to three and seven times the characteristic radius, at which point the function is truncated and smoothly brought to zero by four and eight times the respective radius. The two fits are weighted based on the quality of the fit and combined

[1]AB magnitudes are defined based on the flux density, f, measured in ergs per second per square centimeter per hertz as: $AB = -2.5\log_{10} f - 48.60$.

[2]galex.stsci.edu/GR2/?page=ddfaq#2

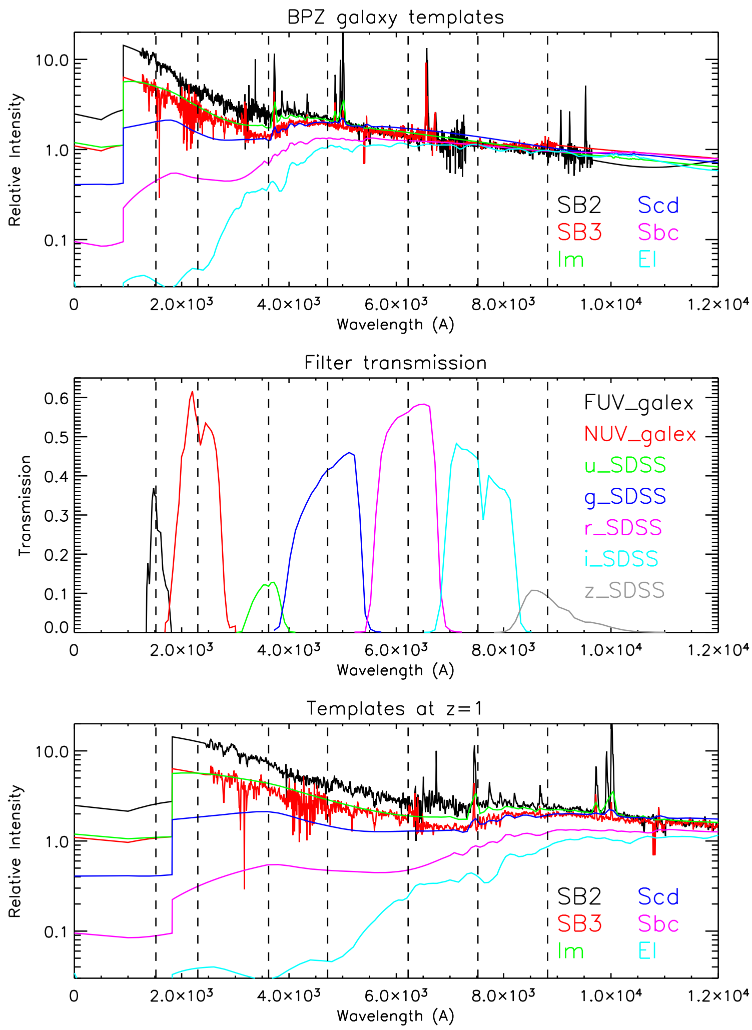

Figure 7.3: The top panel shows the six galaxy templates (distinguished by their colors in the legend) that are used to find the maximum likelihood solution for the photometric redshifts (Section 7.3.3). The vertical dashed lines show the central frequencies of the GALEX and SDSS bandpasses. The middle panel shows the two GALEX bands as well as the five SDSS bands. The bottom panel shows the templates redshifted to $z = 1$ (by simply multiplying the wavelengths by a factor of 2). As the different galaxy types are redshifted, a redshift-brightness degeneracy arises in the optical bands (especially when only considering $griz$) for the galaxies with blue spectra (SB2, SB3, and Im templates). The addition of the GALEX bands breaks this degeneracy by sampling out to the Lyman-limit. Note that by $z = 1$ the Lyman-limit has shifted out of the F_{UV} band, but it does not reach the central frequency of the more sensitive N_{UV} band until $z \approx 1.5$.

to obtain the best fitting profile.[3] This measurement provides the best estimate of the total photometry for each SDSS band.[4] Magnitude corrections of -0.04 and +0.02 are then applied to the u and z bands respectively to convert from SDSS magnitudes into AB magnitudes.[5] All reported magnitudes are in the AB system. In Section 7.4 we assess the performance of our photo-z analysis on those SDSS galaxies with spectroscopic redshifts that have redshift confidence calculated to be > 0.9. SDSS objects are also excluded using the "blended," "nodeblend," and "saturated" error flags. The vast majority of the SDSS spectroscopic measurements have $r < 20$ magnitude (as shown in Figure 7.6), so we have limited our current analysis to this magnitude regime.

7.3.2 Catalog matching

The GALEX and optical catalogs are merged as follows: we initially assign optical sources to a GALEX field pointing if they fall within $35.1'$ of the GALEX field center. This cuts the noisiest region of the GALEX fields (Figure 7.4), while maintaining complete sky coverage between neighboring fields (i.e. leaving no gaps between neighbors as shown in Figure 7.1).

Within every GALEX field, each optical source is matched to the nearest GALEX object with a N_{UV} detection within a $4''$ radius; this is a relatively conservative matching radius [6]. After all sources in the field are assigned, the combined catalog is searched to test whether any two optical sources are assigned to the same GALEX object. When there are overlapping assignments, the closest source to the GALEX position is selected and the other is removed from the catalog.[6] Objects that do not have a GALEX detection or overlapping assignments are kept in the catalog. We characterize the distributions of GALEX F_{UV} and N_{UV} magnitudes in each field using histograms with 0.1 magnitude bins. The magnitude limit used for other sources in the same field during photo-z analysis is set to be the highest magnitude where the number of galaxies exceeds half of the number at the peak magnitude

[3] www.sdss.org/dr5/algorithms/photometry.html

[4] SDSS *model* magnitudes were also tested. We found that *model* magnitudes provide a better relative calibration when comparing only SDSS bands (especially after adding the "ubercalibration" corrections [83]), but the *C-model* magnitudes provide a better absolute calibration for comparing with other instruments, such as GALEX.

[5] www.sdss.org/dr6/algorithms/fluxcal.html#sdss2ab

[6] Removing sources with overlapping assignments was also explored and had negligible impact on the results presented here.

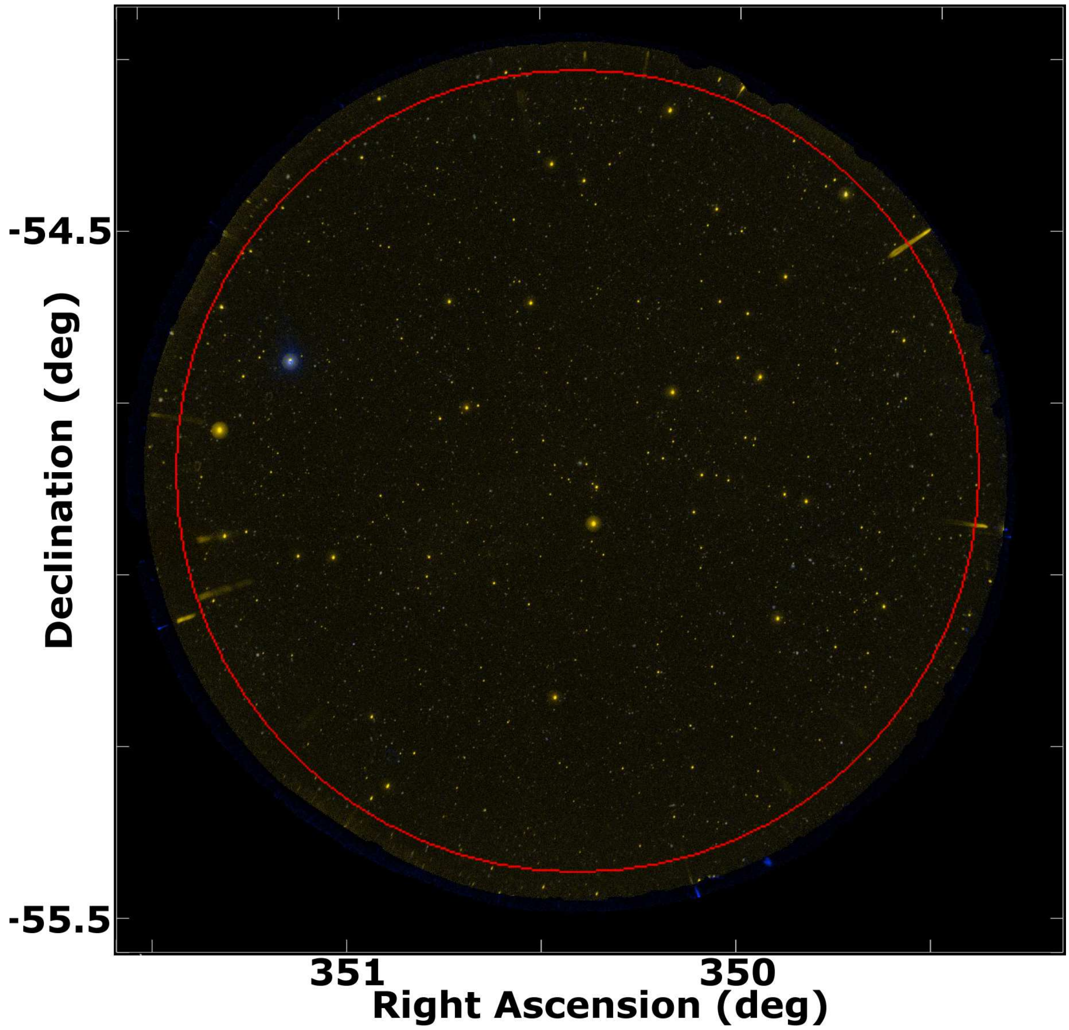

Figure 7.4: GALEX field image. The N_{UV} image is shown as yellow, while the F_{UV} image is shown as blue. The red circle is the maximum allowed matching radius of $35.1'$, which removes the noisiest regime (with the most spurious signals) near the field edges while maintaining complete coverage of the sky as shown in Figure 7.1. (Image courtesy of the GALEX analysis team.)

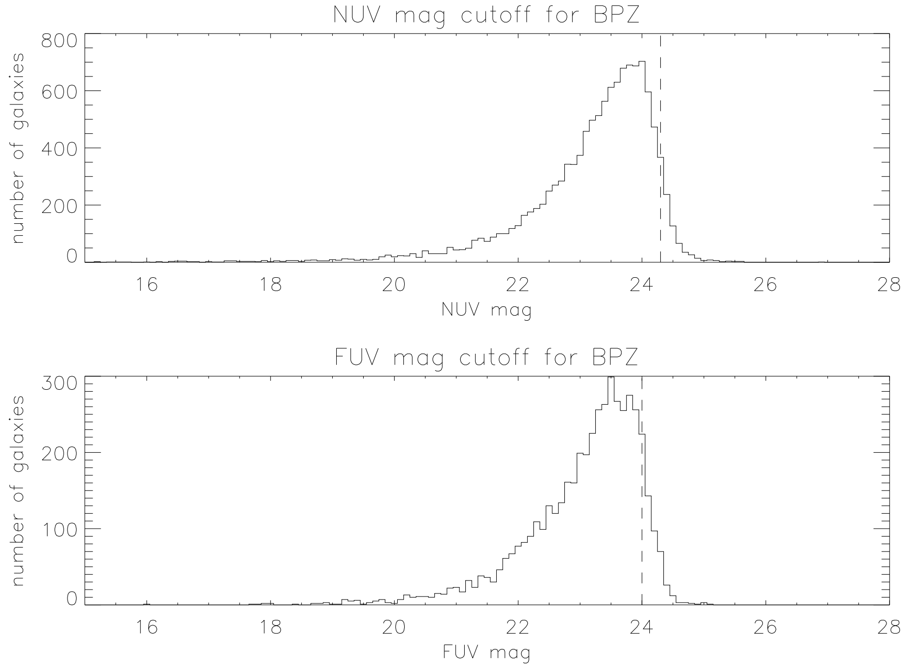

Figure 7.5: GALEX magnitude distributions for a single field. The top plot is N_{UV} and the bottom is F_{UV}. The magnitude limits for each field are automatically set to the highest magnitude bin that has more than half the number of counts of the peak bin (vertical dashed lines). In this field the magnitude limits are at $N_{UV} = 24.3$ and $F_{UV} = 24.0$. Note the much larger number of detections per field in N_{UV}. This particular field has 2.5 ks exposure time in both F_{UV} and N_{UV}. It is located at right ascension 2.54° and declination -1.35° (Figure 7.1).

bin (Figure 7.5). Objects with magnitudes higher than this limit (as well as objects with no N_{UV} detection) are labeled as non-detections, and this magnitude limit is used for the non-detections in the photo-z calculation (Section 7.3.3).

In 56 GALEX fields in stripe 82, ~3000 SDSS objects with spectroscopic redshifts were found that meet the above criteria. Of these objects, 75% were found to have N_{UV} detections within the 4″ matching radius, and only two pairs of objects were matched to the same GALEX object.

7.3.3 Photo-z analysis

The merged catalogs are analyzed using the maximum-likelihood (ML) approach with no prior. We use the code BPZ[7] [12] to compute the photo-z. The observed magnitudes are matched to the predicted spectral energy distributions through each bandpass from the templates in Figure 7.3. The photo-z computation is set to have a precision of $\delta z = 0.01$. The only limit imposed in the ML calculation is a sharp prior $z < 1.5$; further, we exclude from the sample objects with photo-$z > 1$. This is motivated by the fact that, given the optical and UV depth, we do not expect to detect galaxies at $z > 1$. As explained below, this cut excludes less than a few percent of the sample.

To quantify the accuracy of different photo-z analyses, we define the redshift error as

$$dz \equiv \frac{(z_{ph} - z_{sp})}{(1 + z_{sp})}, \tag{7.1}$$

where z_{ph} is the photo-z and z_{sp} is the spectroscopic z. The mean and standard deviation, σ_z, of dz (i.e. the photo-z bias and error) are calculated for all galaxies with $z < 1$ (as objects with photo-$z > 1$ are excluded from the sample, they are also removed from the mean and error calculations). In the SDSS results presented, the $z > 1$ failures are less than 1% of the galaxies in the catalog. A final cut is made on objects with $N_{UV} - g > 1$ as this color is typical of QSO's rather than galaxies. This cut removes less than 1% of the SDSS catalog.

The stripe 82 analysis is done on different combinations of the seven bands (five optical and two UV bands). This allows us to study the impact of including different bands on photo-z accuracy. Our photo-z (z_ML) are then compared to the most recent results (z_ANN) of the SDSS artificial neural network photo-z pipeline[8] (henceforth ANNz [82]), which was developed using a large spectroscopic training and validation set (Figure 7.7).

7.4 Results

The addition of GALEX data to the optical measurements alleviates the redshift-brightness degeneracy and greatly improves the photo-z estimation. In Figure 7.7, the upper-left panel

[7] Code version bpz.1.94e; acs.pha.jhu.edu/~txitxo/bpzdoc.html
[8] astro.uchicago.edu/sdss/dr6/photoz2.html

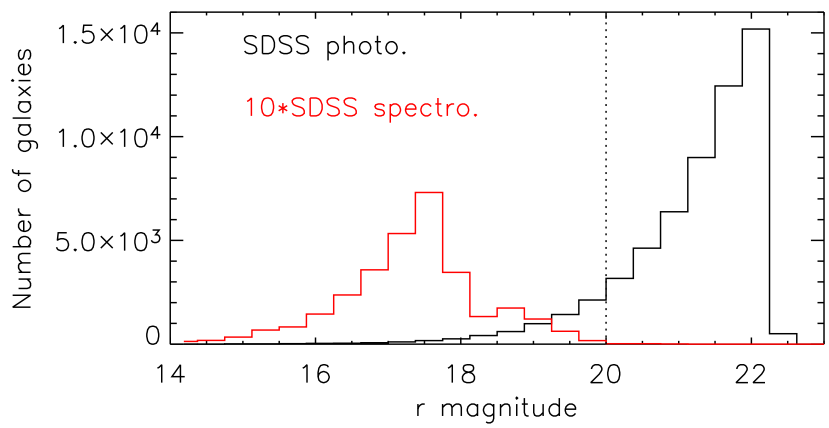

Figure 7.6: The r magnitude distributions for the SDSS photometric sample from a 7 deg^2 region (black), and the SDSS spectroscopic sample that we use for the comparisons in Figure 7.7 multiplied by a factor of ten (red). The dotted line is a cut imposed because it is beyond the depth of our current GALEX observations (Figure 7.9) and we have not yet tested our method against spectroscopic measurements with $r > 20$.

shows the ML recovered photo-z when using only $griz$ data. As expected, the number of catastrophic failures is high, resulting in a large standard deviation $\sigma_z = 0.17(1 + z)$. Addition of the u data (upper-right panel) reduces the number of catastrophic failures and halves the standard deviation ($\sigma_z = 0.08(1 + z)$). Including the GALEX data (middle panels) reduces the standard deviation by another factor of two ($\sigma_z = 0.04(1 + z)$) and removes nearly all catastrophic failures. Note that the addition of u data has negligible effect on the error when the GALEX bands are added. The bottom-left panel shows the comparison with ANNz. The standard deviation for GALEX + $griz$ is somewhat ($\sim$50%) larger than for ANNz; however, ANNz is being compared to its own training and validation set, which makes the comparison a bit unfair. We find that simply adding the GALEX moderate exposures to $griz$ imaging and using ML analysis techniques with six galaxy templates provides photo-z approaching the accuracy of ANNz on its own training and validation set.

We explore the performance of the photo-z in more detail in Figures 7.8, 7.9 and 7.10 to investigate the dependence on redshift, magnitude, and color, respectively. In Figure 7.8 we show how the mean and error in dz evolve as a function of redshift. Adding the GALEX data

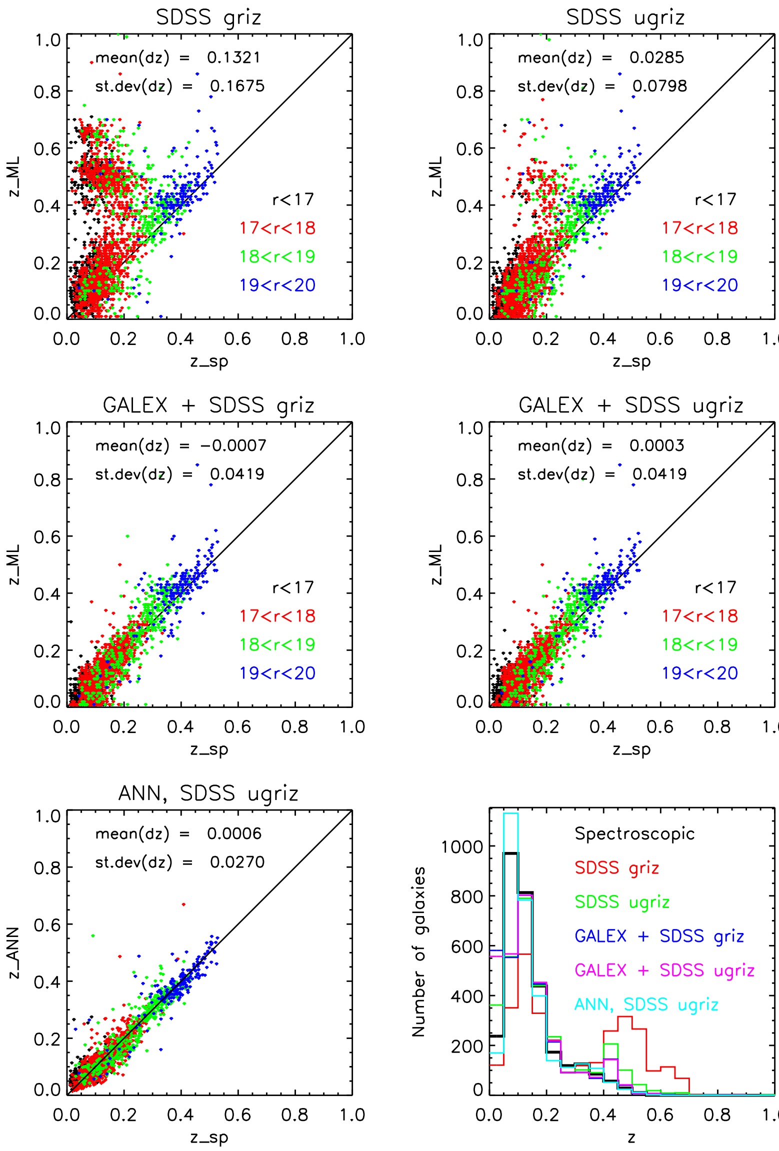

Figure 7.7: Comparison of photo-z redshift estimates (z_ML and z_ANNz) with SDSS spectroscopic measurements (z_sp). The colors on the five similar plots are different r magnitude ranges as defined in the legends. The top panels show photo-z estimates using only the optical $griz$ (left) and $ugriz$ (right) data. Adding the u-band data significantly improves the estimates, but in both analyses large groups of outliers exist in the $0.4 <$ photo-$z < 0.6$ range. By adding the GALEX data (middle panels), this group of outliers is removed, and the photo-z predictions fall much closer to the spectroscopic measurements. In the lower left panel, we show the SDSS ANNz predictions for comparison. The ANNz technique does result in less scatter than adding the GALEX data; however, ANNz is being compared to its own training and validation set. The lower right panel compares the redshift distributions from the five photo-z analyses (colors) with the spectroscopic measurements (black).

significantly reduces the photo-z bias and error over the optical bands alone at $z < 0.3$, beyond which the proportion of galaxies with GALEX detections falls off at the current GALEX observation depths (Figure 7.8, bottom panel). Still, the performance approaches the level of ANNz until $z > 0.45$. In Figure 7.9 we show the photo-z bias and error as a function of the source r magnitude. Both remain nearly flat until $r > 19$, which is where the fraction of sources detected by GALEX falls to less than 50%. These plots clearly indicate that with deeper GALEX exposures, we can expect to improve our results for fainter objects and higher redshifts. In Figure 7.10 the photo-z performance as a function of galaxy color is examined. The error is equivalent to or possibly even better than ANNz for $g - r < 0.6$ and is only slightly larger up to $g - r \approx 2$. When compared to the other ML methods without GALEX photometry, the addition of GALEX bands returns significantly more accurate photo-z for colors as red as $g - r = 1.6$.

We note that there is a significant slope in the mean of $g - r$ for the GALEX + $griz$ data as a function of redshift, as shown in the top panel of Figure 7.10. We explore the effect of using a linear fit to this slope to correct the BPZ photo-z determinations (dashed black lines in Figure 7.8, 7.9 and 7.10). We find that applying this simple a posteriori correction reduces the standard deviation of our results as a function of z (Figure 7.8) and r (Figure 7.9). This correction brings the standard deviations even closer to the ANNz level. In particular σ_z for the entire sample (as reported in Figure 7.7) is reduced by 14% with this correction. Because the cause of the slope in the $g - r$ mean has not been fully understood, we do not include this correction in our other analyses. We also consider removal of the excess of galaxies in the lowest BPZ redshift bin ($z < 0.02$). Cutting these galaxies only results in a $\sim$1% reduction of the standard deviation, which indicates that despite the excess number in the lowest z bin, nearly all are relatively low-redshift galaxies (Fig 7.7, middle and lower-right panels). We are continuing to explore the cause of this excess.

The use of a Bayesian prior developed for the SDSS data set is also explored. For analysis of the optical data alone, the addition of the prior causes a decrease in the number of catastrophic outliers, which reduces the standard deviation for the $griz$ data by $\sim$50% and for the $ugriz$ data by $\sim$25% compared to the values in Figure 7.7. The prior yields little improvement in the standard deviation of the optical + GALEX data, which only

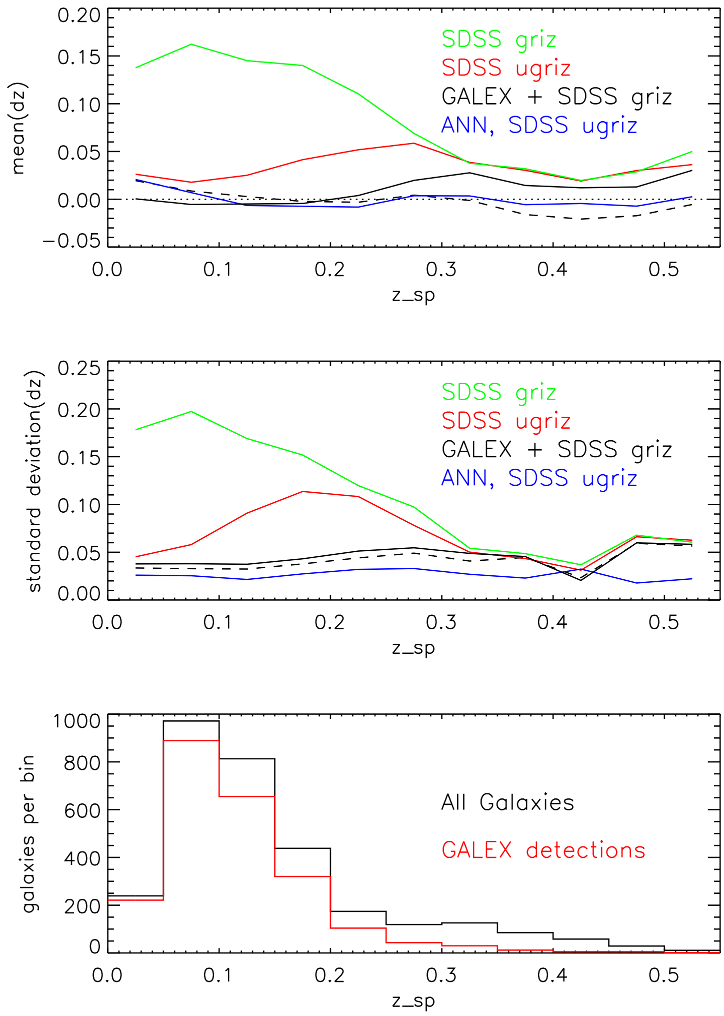

Figure 7.8: Photo-z errors versus spectroscopic redshift, z_sp. The mean (top) and standard deviation (middle) of dz are shown as a function of redshift. We compare the photo-z results using the SDSS *griz* data (green), as well as the SDSS *ugriz* data (red), the GALEX + *griz* data (black), and the SDSS ANNz results (blue). The GALEX + *griz* data approaches the standard deviation of the ANNz results without the use of priors or training sets. Also shown are the GALEX + *griz* results after applying the simple $g - r$ correction factor discussed in the caption to Figure 7.10 (black - dashed). In the bottom panel, the total number of sources in each z bin is shown (black) as well as the total number of sources with a GALEX detection (red).

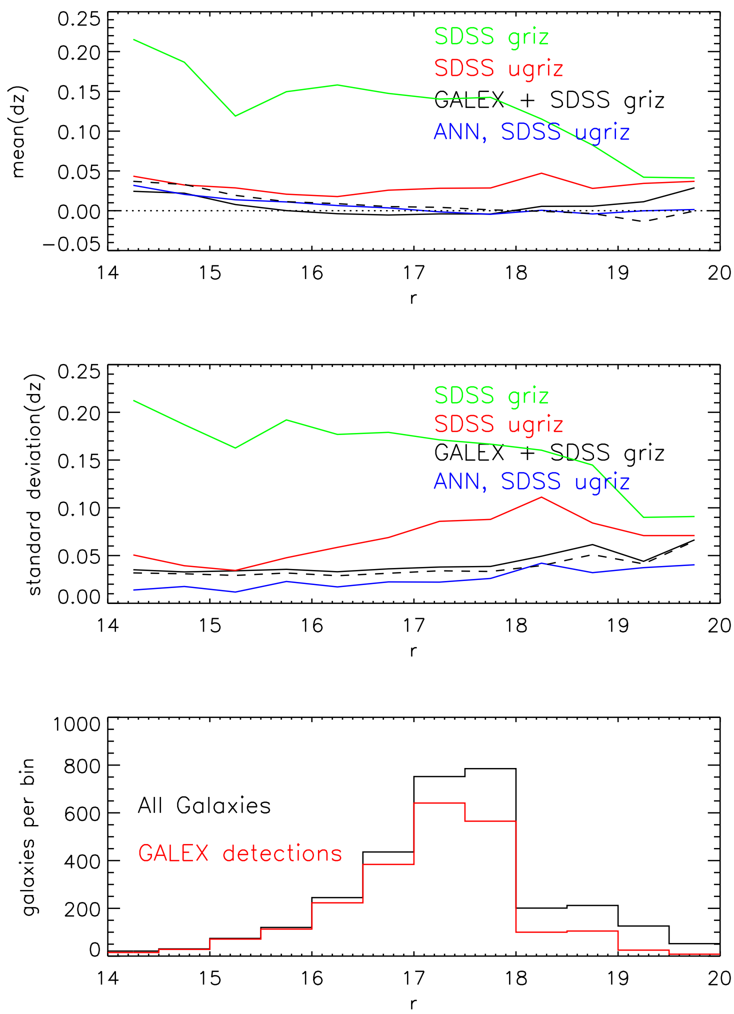

Figure 7.9: Photo-z errors versus source r magnitude. The mean (top) and standard deviation (middle) of dz are shown in different r bins. (Colors are the same as Figure 7.8 and 7.10.) The GALEX + $griz$ data approaches the standard deviation of the ANNz results without the use of priors or training sets. Also shown are the GALEX + $griz$ results after applying the simple $g - r$ correction factor discussed in Figure 7.10 (black - dashed). At the bottom, the total number of sources in each r bin is shown (black) as well as the total number of sources with a GALEX detection (red).

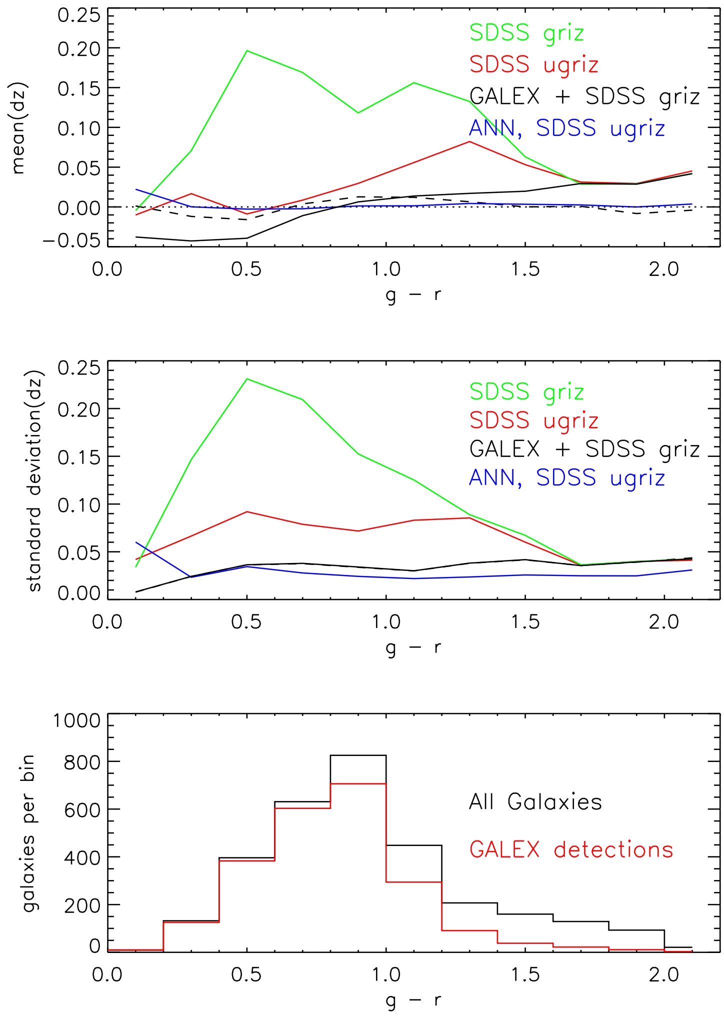

Figure 7.10: Photo-z errors versus color, $g-r$. The mean (top) and standard deviation (middle) of dz are shown in different $g-r$ bins. (Colors are the same as Figure 7.8 and 7.9.) For the low $g-r$ bins, or blue galaxies, the standard deviation of the GALEX + $griz$ results are a huge improvement over the SDSS only data and are essentially equivalent to (or better than) the ANNz results without the use of priors or training sets. A significant bias is observed in the mean of dz for the GALEX + $griz$ results. By fitting a line to the bias, and applying a z correction as a function of $g-r$, we linearize the response in $g-r$ (black - dashed); more interestingly, we also significantly reduce the standard deviation of the results versus spectroscopic z (Figure 7.8) and r magnitude (Figure 7.9). At the bottom, the total number of sources in each $g-r$ bin is shown (black) as well as the total number of sources with a GALEX detection (red).

drops by ~5% (less than the linear $g-r$ correction above), while the bias remains constant for GALEX + *ugriz* and increases for GALEX + *griz*.

7.5 Conclusions

In order to obtain accurate photo-z as efficiently as possible for the areas surveyed by ACT and other SZ experiments, we have obtained moderate depth GALEX photometry. With a modest observing campaign, and using available MIS observations, we have already covered an area of ~60 deg^2 to a mean depth of ~3 ks. At the completion of our ~210 ks of observations, we will have covered ~120 deg^2 to this depth.

Budavári et al. [19] used *ugriz* SDSS DR1 photometry together with GALEX MIS (1.4 ks exposure) F_{UV} and N_{UV} photometry to determine photo-z for about 10000 galaxies up to $z = 0.25$. They use an empirical technique which relies on a training set of about 6000 objects, and obtained photo-z errors of $\sigma_z = 0.026$ on the training set, which is similar to the ANNz performance. Here we have taken a different approach to be independent of training sets and combined deeper data sets to explore a higher redshift range.

Using the SDSS spectroscopic survey we have shown that just the addition of GALEX photometry to *griz* bands using unbiased maximum-likelihood analysis yields photo-z with an accuracy of ~$0.04(1+z)$ up to $z \approx 0.4$. Beyond this redshift, the GALEX ~$2-4$ ks exposures do not have a sufficient number of detections to provide useful constraints. Clearly, moderately deeper observations would help to bring the utility of GALEX observations closer to $z \approx 1$. Note that the current depth of $z \approx 0.4$ looks back through roughly 33% of the age of the universe and samples a volume of 15 Gpc^3. Maybe more importantly, ~20% of the clusters that will be detected by the SZ experiments (above a dark matter mass of 3×10^{14} M$_\odot$) are at $z < 0.4$. If redshift up to $z = 1$ were accessible by GALEX, 60% of the age of the universe and a volume of 153 Gpc^3 would be surveyed; 86% of the clusters that will be detected by the SZ experiments (above a dark matter mass of 3×10^{14} M$_\odot$), and 90% of the resolved ones, are at $z < 1$.

The most important aspect of the results presented here is that the photo-z accuracy of $\sigma_z = 0.04(1+z)$ at $z < 0.4$ was obtained using only a maximum-likelihood fit to six galaxy templates in BPZ. As the acquisition of training sets or priors relies on obtaining large spectroscopic data-sets, we consider the moderate GALEX exposures a very efficient way to obtain accurate photo-z over large areas.[9]

This kind of analysis can also provide a useful catalog for weak-lensing studies as photo-z redshifts remain accurate for the bluest galaxies. These determinations are commonly the most difficult to obtain because spectra of blue galaxies in the optical bands show an almost featureless power law spectra energy distribution. The photo-z catalogs obtained in this way are expected to be useful for cross-correlating galaxies with CMB maps. Possible applications of these studies include detection of the kSZ effect [48] and the lensing of the CMB by large-scale structure [20, 27], both of which can be used to constrain models of the dark energy.

Acknowledgements

R. Jimenez led the charge on this effort by writing proposals for the GALEX data until one was granted. F. Menanteau, R. Jimenez, and D. Spergel were critical in answering all my basic questions and bringing me up to speed, so that I could work on this project. L. Verde, J. Hughes, and Y.-T. Lin's input and feedback while the analysis was being completed emphasized and clarified the findings presented here. Many of the above were also critically involved in the photo-z paper [78], which includes these results as well as photo-z analyzed using other techniques. Robert Lupton and Chris Hirata contributed useful and informative conversations, and Peter Friedman helped me to get off the ground when starting out with the GALEX data. Of course, we could not have done any of this analysis without all the incredible projects with public data:

Funding for the creation and distribution of the SDSS Archive has been provided by the Alfred P. Sloan Foundation, the Participating Institutions, the National Aeronautics and Space Administration, the National Science Foundation, the US Department of Energy, the Japanese Monbukagakusho, and the Max Planck Society. The SDSS Web site

[9]Note that we just integrated $\sim$2.4 days and that, for example, a program 10 times longer could provide photo-z for about 1000 deg^2 which, is estimated to be the optimal area to extract cosmological information from SZ surveys [109].

is http://www.sdss.org. The SDSS is managed by the Astrophysical Research Consortium (ARC) for the Participating Institutions. The Participating Institutions are the University of Chicago, Fermilab, the Institute for Advanced Study, the Japan Participation Group, The Johns Hopkins University, the Korean Scientist Group, Los Alamos National Laboratory, the Max Planck Institute for Astronomy (MPIA), the Max Planck Institute for Astrophysics (MPA), New Mexico State University, the University of Pittsburgh, Princeton University, the United States Naval Observatory, and the University of Washington.

The Galaxy Evolution Explorer (GALEX, www.galex.caltech.edu) is a NASA Small Explorer. The mission was developed in cooperation with the Centre National d'Etudes Spatiales of France and the Korean Ministry of Science and Technology.

Chapter 8

Conclusions

The state of cosmology today is a remarkable one. In less than a century we have emerged from a field dominated by speculation to a highly quantitative and precise description of our universe motivated by empirical measurements. The ΛCDM standard model of cosmology is constructed based on theoretical modeling derived from a number of fields of physics, and the predictions match current observations with extraordinary precision. Yet, there are a number of critical open questions remaining in this model, including: what is the nature of the dark energy that dominates our universe?

In this dissertation, I have described how we can use observations with the Atacama Cosmology Telescope to probe dark energy. This science goal is one of the primary motivations that drove the development of the ACT project. The bulk of this dissertation comprises the design, development, testing, deployment, and preliminary observations from ACT, including: the optical design, the TES bolometer technology used to measure CMB radiation, the SQUID multiplexing readout system and its implementation, the successful integration of the largest bolometer array ever used for CMB observations, and data from the deployment of the array on ACT. All of this shows that the novel technologies used in this experiment have been successfully integrated for observations, and we have begun measuring the primordial cosmic microwave background radiation.

Data reduction from the 2007 season of observations is underway, and we have confirmed detections of the thermal Sunyaev-Zel'dovich (tSZ) effect from known clusters with high signal-to-noise. Complete understanding and calibration of the data will require taking into account many of the effects discussed in this dissertation. Two of the primary results that we will extract from this data are: a measurement of the CMB angular power spectrum at high multipoles to constrain the spectral index of inflation, and an unbiased tSZ selected cluster catalog, which will allow us to constrain dark energy. Figure 8.1 shows predictions for the error bars on the power spectrum based on the (somewhat pessimistic) noise measurements made in the laboratory of $\sim$1.4 mK sec$^{1/2}$ (Section 5.5) and the $\sim$300 hours of successful observations that were made covering a 120 deg^2 region during the (short) 2007 season of observations. Noise projections are also compared for mapping either 120 deg^2 or 1000 deg^2 regions with 1500 hours of observations during the 2008 season. The tSZ cluster catalog that we develop from these observations will be combined with redshift data (such as the data and analysis presented in Chapter 7) to probe dark energy through both the evolution of structure and the expansion history of the universe. This combination of data will be a powerful tool for improving our understanding of the universe.

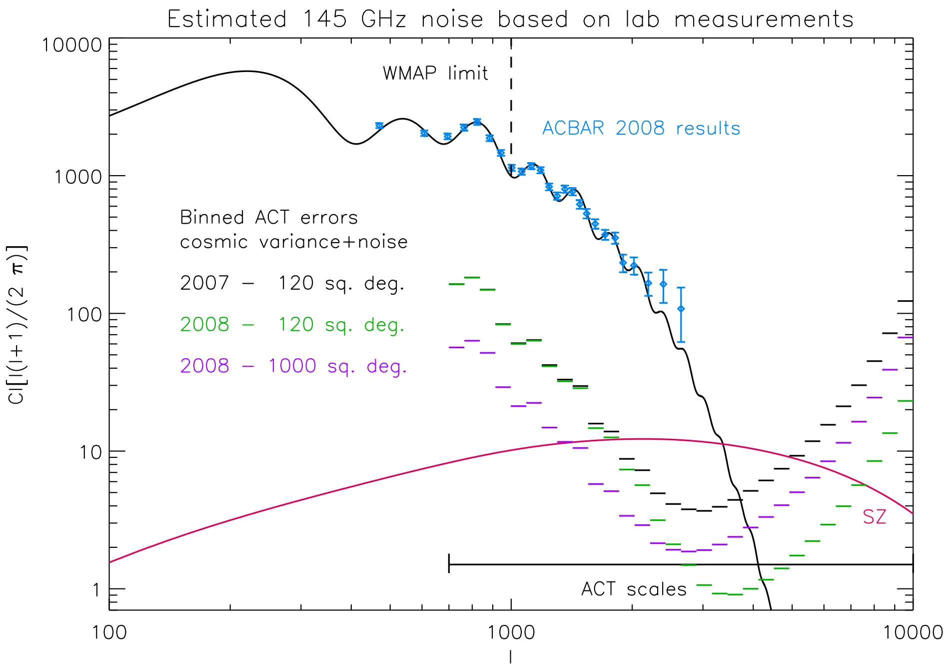

Figure 8.1: CMB angular power spectrum noise predictions. The power spectrum shown (black) is the best fit model to the WMAP three-year measurements [98]. The 2008 results from the ACBAR experiment are currently the highest multipole measurements of the temperature power spectrum (blue points) [90]. The estimated SZ power spectrum (red, courtesy of C. Hernandez-Monteagudo) is also plotted. Estimated error levels for ACT are shown (in logarithmic bins) for the best subset of measurements made with the 145 GHz array during the (short) 2007 season of observations (horizontal black lines). These error levels assume a 1.4 mK sec$^{1/2}$ noise level (Section 5.5) on 800 detectors after 300 hours of observations over a 120 deg^2 region. Also shown are estimated error levels for the 145 GHz array after a season of 1500 hours of observations covering either a 120 deg^2 region (green) or a 1000 deg^2 region (purple). The rise in the error levels at low l is due to cosmic variance limitations because of the size of the region sampled on the sky, which is why both 120 deg^2 regions have the same noise at low l despite the difference in integration time. Note that all three frequencies will be operational for the 2008 season, but only the 145 GHz estimate is shown here. (Figure made in collaboration with L. Verde.)

Appendix A

Focal Plane Orientation

The three separate optical paths in the MBAC receiver and the (awkward) detector array notation of vertical "rows", R 00 through R 31, and horizontal "columns" complicate visualization of the image of the sky in the receiver. To help build intuition for the focal surfaces, we have modified some of the figures presented in Chapter 2 with an optical view of one of our potential sources of data contamination in Figure A.1. In this figure, we have mirrored the orientation of Figures 2.5 and 2.6, so that we are viewing the image at the MBAC dewar window as though we were sitting inside the dewar and looking out at the sky. The image of the sky at the MBAC dewar windows is symmetric with the sky itself because the windows are at the second image of the sky in the Gregorian system. The detector arrays, on the other hand, are at the third image of the sky, which means that each set of reimaging optics inverts the local portion of the sky in both x and y coordinates before projecting it onto the array. Similar to the image at the MBAC dewar window, we show the image of the detector arrays as though we were looking through the back of the array and out at the sky. This is the same orientation that is shown in the "array plots", such as Figures 2.10 and 5.12. If we simply imagine that the three detector arrays were rotated 180° before installation, we can effectively plot each array in terms of sky coordinates (Figure A.1).

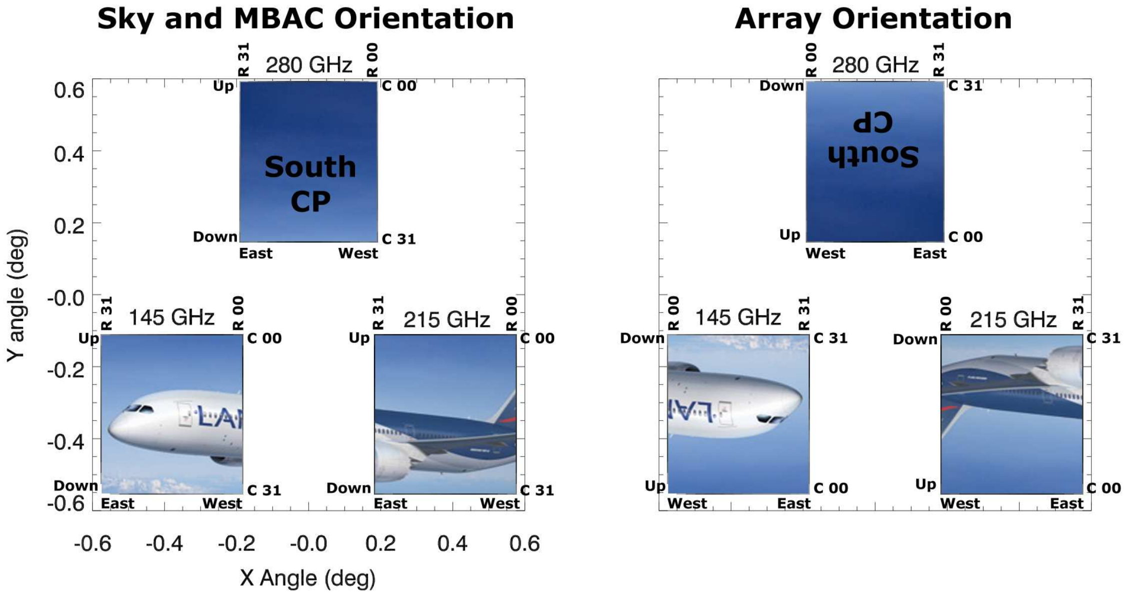

Figure A.1: Focal plane orientation on the sky, the MBAC windows, and the detector arrays. *Top*: This is a representation of an image of the sky as well as the image at the Gregorian focus, which is also roughly the MBAC windows, as viewed from inside the MBAC receiver looking out towards the secondary mirror. The image at the MBAC windows is symmetric with the sky because it is the second image of the sky in the Gregorian system. *Bottom*: The detector arrays, on the other hand, are at the third image of the sky, which means that the reimaging optics invert the three images in both x and y coordinates before projecting them onto the arrays. Here we see that the images of the LAN Chile airplane have been rotated in a way that could be quite bad for the passengers if it actually happened. In addition to the image rotations, each field has been labeled with the (awkward) detector array notation of vertical "rows", R 00 through R 31, and horizontal "columns", C 00 through C 31. We also labeled the sky image with the sensible (assuming the telescope is looking south) east and west directions as well as up and down. These directions are inverted at the arrays in the same way that the images are. Note that the axis labels have been removed from the array projections, because it no longer makes sense to label all three fields with the same angular scale.

Appendix B

TDM Cryogenic Integration

The readout system for Time-Domain Multiplexing (TDM) extends between the room temperature electronics and multiple cryogenic stages, the coldest of which are below one degree Kelvin. TDM integration requires careful consideration of cable materials and properties as well as circuit board design. Figure B.1 shows the readout cables and circuit boards that integrate TDM for one of our bolometer arrays in MBAC.

One set of cables extends between the 300 K Multi-Channel Electronics (MCE) into the vacuum chamber and is terminated at 40 K.[1] (The cables were fabricated by Tekdata [103].) These cables are ∼2.3 m long and are hermetically sealed into a common vacuum feedthrough and are comprised of twisted pairs of 0.004” diameter copper wires. Between 40 K and 4 K a set of 1 m long cables with a similar design is used, but these are made of constantan instead of copper to minimize the thermal conductivity between the 40 K and 4 K stages in the MBAC receiver.

At 4 K a pair of circuit boards was designed to provide mounts for the Series Array (SA) SQUID modules (Figure 3.4) as well as heat sinking and termination and series resistances for the readout cable lines. (The circuit boards were designed at Princeton, fabricated by Advanced Circuits [5] and assembled at Princeton as well as Tekdata [103].) These four layer circuit boards have two layers of copper that fill all gaps between circuit board vias to maximize the thermalization of all lines. The copper layers are connected to the four

[1] All of the cables and circuit boards maintain isolated grounds (or independent signal and return lines) for all signals. The grounds are made common inside the MCE.

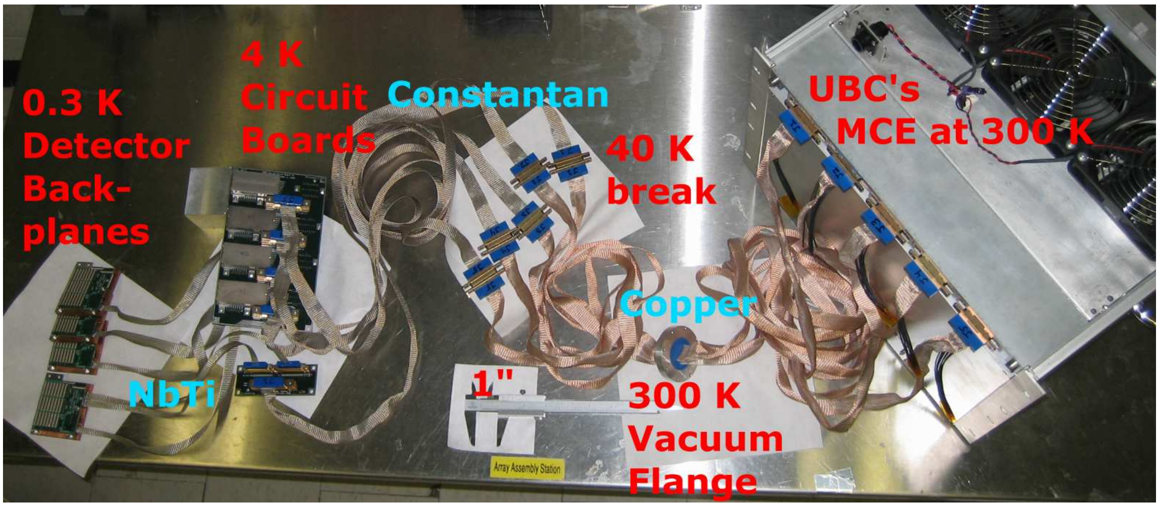

Figure B.1: Cryogenic readout system for Time-Domain Multiplexing. The cables shown extend between the Multi-Channel Electronics (MCE) [37] at ambient pressure and room temperature to the detector array backplanes, which are under vacuum and operated at 0.3 K. The first set of cables connecting to the MCE are made from 0.004" diameter copper wires, which pass through a hermetically sealed vacuum flange. These are terminated at 40 K at which point the cable material is switched to 0.004" diameter constantan wires, which have lower thermal conductivity. These connect to a pair of circuit boards at 4 K, which hold the Series Array SQUID modules and provide heat sinking for the cables. A final set of cables, which are made of 0.002" diameter Niobium Titanium (NbTi) wires, extends between the 4 K circuit boards and the 0.3 K detector backplanes, where the cables are soldered directly into the circuit boards. The final connections between these backplanes and the detector columns (Figure 3.13) are made using the single sided flexible circuitry shown in Figure 5.5.

mounting holes on each of the boards, so that by simply mounting the boards well on the 4 K stage thermalization of all lines is achieved. Between these 4 K circuit boards and the 0.3 K stage, the cables are comprised of twisted pairs of 0.002" diameter wires made of a niobium titanium (NbTi) alloy. The NbTi is wrapped in a thin layer of copper nickel cladding, which helps to thermalize the wires and ensure that they fall below the $\sim$9 K superconducting temperature. As discussed in Section 3.2, it is critical that the stage 2 (S2) SQUID connections to the SA SQUIDs have low inductance and resistance. We have measured the total inductance of the $\sim$40 cm NbTi cables to be 140 ± 30 nH [77]. We reduce this inductance by roughly a factor of two by connecting two twisted pairs of NbTi in parallel between the S2 SQUIDs and the SA SQUID inputs.

The 0.3 K end of the NbTi cables is soldered into one of the four detector backplane circuit boards for each detector array. These detector backplanes are eight layer circuit boards, which have three layers of nearly continuous copper and otherwise similar heat sinking designs to the 4 K circuit boards described above. To accomplish the series biasing of S1 SQUIDs that is utilized in TDM readout (Section 3.2), flexible circuitry is used to connect between the otherwise isolated backplanes (Figure 5.5). This is the same flexible circuitry and zero-insertion force (ZIF) connectors used to connect between the backplanes and the detector columns (Figures 3.13 and 5.5).

References

[1] 3M Corporate Headquarters. 3M Center, St. Paul, MN 55144.

[2] K. Abazajian, et al., for the SDSS Collaboration. The first data release of the Sloan Digital Sky Survey. *Astronomical Journal*, 126:2081–6, 2003.

[3] A. M. Aboobaker. *A New Millimeter-wave Camera for CMB Observations.* PhD thesis, Princeton University, Department of Physics, 2006.

[4] P. A. R. Ade, G. Pisano, C. Tucker, and S. Weaver. A review of metal mesh filters. *Proc. SPIE Millimeter and Submillimeter Detectors and Instrumentation for Astronomy III*, 6275:62750U, 2006.

[5] Advanced Circuits. 21101 E. 32nd Parkway, Aurora, Colorado 80011.

[6] M. A. Agüeros, Z. Ivezic, K. R. Covey, M. Obric, L. Hao, L. M. Walkowicz, A. A. West, D. E. Vanden Berk, R. H. Lupton, G. R. Knapp, J. E. Gunn, G. T. Richards, J. Bochanski Jr., A. Brooks, M. Claire, D. Haggard, N. Kaib, A. Kimball, S. M. Gogarten, A. Seth, and M. Solontoi. The ultraviolet, optical, and infrared properties of Sloan Digital Sky Survey sources detected by GALEX. *Astrophysical Journal*, 130:1022–36, 2005.

[7] AMEC Dynamic Structures Ltd. (Now Empire Dynamic Structures Ltd.). 1515 Kingsway Ave., Port Coquitlam, BC V3C 1S2, Canada.

[8] N. M. Ball, R. J. Brunner, A. D. Myers, N. E. Strand, S. L. Alberts, D. Tcheng, and X. Llora. Robust machine learning applied to astronomical data sets. II. Quan-

tifying photometric redshifts for quasars using instance-based learning. *Astrophysical Journal*, 663:774–780, 2007.

[9] W. A. Baum. *Problems of Extra-Galactic Research*, 15:390, 1962.

[10] D. J. Benford, J. A. Chervenak, K. D. Irwin, and H. S. Moseley. Ultralow-background large-format bolometer arrays. *Proc. SPIE IR Space Telescopes and Instruments*, 4850:944–953, 2003.

[11] D. J. Benford, G. M. Voellmer, J. A. Chervenak, K. D. Irwin, H. S. Moseley, R. A. Shafer, J. G. Staguhn, and G. J. Stacey. Design and fabrication of two-dimensional superconducting bolometer arrays. *Proc. SPIE IR Space Telescopes and Instruments*, 4855:552B, 2003.

[12] N. Benítez. Bayesian photometric redshift estimation. *Astrophysical Journal*, 536:571–83, 2000.

[13] C. L. Bennett, M. Halpern, G. Hinshaw, N. Jarosik, A. Kogut, M. Limon, S. S. Meyer, L. Page, D. N. Spergel, G. S. Tucker, E. Wollack, E. L. Wright, C. Barnes, M. R. Greason, R. S. Hill, E. Komatsu, M. R. Nolta, N. Odegard, H. V. Peiris, L. Verde, and J. L. Weiland. First year WMAP observations: Preliminary maps and basic results. *Astrophysical Jornal Supplement Series*, 148:1–27, 2003. astro-ph/0302207.

[14] B.A. Benson, S.E. Church, P.A.R. Ade, J.J. Bock, K.M. Ganga, J.R. Hinderks, P.D. Mauskopf, B. Philhour, M.C. Runyan, and K.L. Thompson. Peculiar velocity limits from measurements of the spectrum of the Sunyaev-Zeldovich effect in six clusters of galaxies. *Astrophysical Journal*, 592:674–691, 2003. astro-ph/0303510v1.

[15] E. Bertin and S. Arnouts. Sextractor: Software for source extraction. *Astronomy and Astrophysics Supplement*, 117:393, 1996.

[16] S. Bhattacharya and A. Kosowsky. Dark energy constraints from galaxy cluster peculiar velocities. *Physical Review D.* preprint, arXiv:0712.0034v1 [astro-ph].

[17] M. Born and E. Wolf. *Principles of Optics.* Cambridge University Press, Cambridge, UK, 1999. 7th ed.

[18] K. Brown and A. Prata. A design procedure for classical offset dual reflector antennas with circular apertures. *IEEE Trans. on Antennas and Propagation*, 42(8):1145–53, 1994.

[19] T. Budavári, A. S. Szalay, S. Charlot, M. Seibert, T. K. Wyder, S. Arnouts, T. A. Barlow, L. Bianchi, Y. I. Byun, J. Donas, K. Forster, P. G. Friedman, T. M. Heckman, P. N. Jelinsky, Y. W. Lee, B. F. Madore, R. F. Malina, D. C. Martin, B. Milliard, P. Morrissey, S. G. Neff, R. M. Rich, D. Schiminovich, O. H. W. Siegmund, T. Small, M. A. Treyer, and B. Welsh. The ultraviolet luminosity function of GALEX galaxies at photometric redshifts between 0.07 and 0.25. *Astrophysical Journal Letters*, 61:L31, 2005.

[20] C. Carbone, V. Springel, C. Baccigalupi, M. Bartelmann, and S. Matarrese. Simulated all-sky maps of the weak gravitational lensing distortion of the CMB. *ArXiv Astroph. e-prints*, astro-ph/0711:2655, 2007.

[21] J. A. Chervenak, K. D. Irwin, E. N. Grossman, J. M. Martinis, C. D. Reintsema, and M. E. Huber. Superconducting multiplexer for arrays of transition edge sensors. *Applied Physics Letters*, 74(26):4043–5, 1999.

[22] G. D. Coleman, C.-C. Wu, and D. W. Weedman. *Astrophysical Journal Supplement*, 43:393, 1980.

[23] A. A. Collister and O. Lahav. ANNz: Estimating photometric redshifts using artificial neural networks. *Publications of the Astronomical Society of the Pacific*, 116:345, 2004.

[24] A. J. Connolly, A. S. Szalay, Mark Dickinson, M. U. SubbaRao, and R. J. Brunner. The evolution of the global star formation history as measured from the hubble deep field. *Astrophysical Journal Letters*, 486:L11, 1997.

[25] Cosmic Microwave Background Task Force. Cosmic Microwave Background Task Force final report. 2005.

[26] Dark Energy Task Force. Dark Energy Task Force final report. 2006.

[27] S. Das and P. Bode. A large sky simulation of the gravitational lensing of the cosmic microwave background. *ArXiv Astroph. e-prints*, astro-ph/0711:3793, 2007.

[28] P. A. de Korte, J. Beyer, S. Deiker, G. C. Hilton, K. D. Irwin, M. MacIntosh, S. W. Nam, C. D. Reintsema, L. R. Vale, and M. E. Huber. Time-division superconducting quantum interference device multiplexer for transition-edge sensors. *Review of Scientific Instruments*, 74(8):3807–3815, 2003.

[29] M. J. Devlin, S. R. Dicker, J. Klein, and M. P. Supanich. A high capacity completely closed-cycle 250 mk ^{3}He refrigerator system based on a pulse tube cooler. *Cryogenics*, 44:611–616, 2004.

[30] S. Dicker and M. Devlin. Millimeter wave reimaging optics for the 100 m green bank telescope. *Applied Optics*, 44:5855–8, 2005.

[31] S. Dodelson. *Modern Cosmology.* Academic Press, San Diego, California USA, 2003.

[32] R. Doriese, 2007. private communication.

[33] C. Dragone. A first-order treatment of aberrations in cassegrainian and gregorian antennas. *IEEE Trans. on Antennas and Propagation*, 30:331–339, 1982.

[34] C. Dragone. First-order correction of aberrations in cassegrainian and gregorian antennas. *IEEE Trans. on Antennas and Propagation*, 31(5):764–75, 1983.

[35] Emerson and Cuming. Billerica, Massachusetts, 01821.

[36] T. Essinger-Hileman. Fabrication of a tuned coupling layer for the Millimeter Bolometer Array Camera of the Atacama Cosmology Telescope. Princeton University Physics Department Experimental Project, October 2007.

[37] M. Halpern et al. Read-out electronics for time-domain multiplexed bolometers for millimetric and sub-millimetric astronomy. *Journal of Low Temperature Physics*, 2007, preprint.

[38] Faro Technologies Inc. 125 Technology Park, Lake Mary, Florida 32746.

[39] R. Feldmann, C. M. Carollo, C. Porciani, S. J. Lilly, P. Capak, Y. Taniguchi, O. Le Fvre, A. Renzini, N. Scoville, M. Ajiki, H. Aussel, T. Contini, H. McCracken, B. Mobasher, T. Murayama, D. Sanders, S. Sasaki, C. Scarlata, M. Scodeggio, Y. Shioya, J. Silverman, M. Takahashi, D. Thompson and G. Zamorani. The zurich extragalactic bayesian redshift analyzer and its first application: COSMOS. *Monthly Notices of the Royal Astronomical Society*, 372:565, 2006.

[40] Forcier Machine Design. 123 Marshall Ave., Petaluma, California 94952.

[41] J. W. Fowler, M. D. Niemack, S. R. Dicker, A. M. Aboobaker, P. A. R. Ade, E. S. Battistelli, M. J. Devlin, R. P. Fisher, M. Halpern, P. C. Hargrave, A. D. Hincks, M. Kaul, J. Klein, J. M. Lau, M. Limon, T. A. Marriage, P. D. Mauskopf, L. Page, S. T. Staggs, D. S. Swetz, E. R. Switzer, R. J. Thornton, and C. E. Tucker. Optical design of the Atacama Cosmology Telescope and Millimeter Bolometric Array Camera. *Applied Optics*, 45:3746, 2007.

[42] T. A. Fulton, L. N. Dunkleberger, and R. C. Dynes. Quantum interference properties of double josephson junctions. *Physical Review B*, 6(3):855–75, 1972.

[43] M. Galeazzi and D. McCammon. Microcalorimeter and bolometer model. *Journal of Applied Physics*, 93(8):4856–69, 2003.

[44] A. Goobar and S. Perlmutter. Feasibility of measuring the cosmological constant lambda and mass density omega using type ia supernovae. *Astrophysical Journal*, 450:14, 1995.

[45] M. Griffin, J. Bock, and W. Gear. Relative performance of filled and feedhorn-coupled focal-plane architectures. *Applied Optics*, 41(31):6543–6554, 2002. astro-ph/0205264.

[46] S. Hanany and D. Marrone. Comparison of designs of off-axis gregorian telescopes for millimeter-wave large focal-plane arrays. *Applied Optics*, 41(22):4666–70, 2002.

[47] A. Heavens, B. Panter, R. Jimenez, and J. Dunlop. The star-formation history of the universe from the stellar populations of nearby galaxies. *Nature*, 428:625, 2004.

[48] C. Hernandez-Monteagudo, L. Verde, R. Jimenez, and D. N. Spergel. Correlation properties of the kinematic sunyaev-zel'dovich effect and implications for dark energy. *Astrophysical Journal*, 643:598, 2006.

[49] H. F. C. Hoevers. Thermal physics of transition edge sensor arrays. *Nuclear Instruments and Methods in Physics Research A*, 559:702–5, 2006.

[50] W. Holland, M. MacIntosh, A. Fairley, D. Kelly, D. Montgomery, D. Gostick, E. Atad-Ettedgui, M. Ellis, I. Robson, M. Hollister, A. Woodcraft, P. Ade, I. Walker, K. Irwin, G. Hilton, W. Duncan, C. Reintsema, A. Walton, W. Parkes, C. Dunare, M. Fich, J. Kycia, M. Halpern, D. Scott, A. Gibb, J. Molnar, E. Chapin, D. Bintley, S. Craig, T. Chylek, T. Jenness, F. Economou, and G. Davis. Scuba-2: a 10,000 pixel submillimeter camera for the james clerk maxwell telescope. *Proceedings of Millimeter and Submillimeter Detectors and Instrumentation, SPIE*, pages arXiv:astro–ph/0606338v1, 2006.

[51] P. Horowitz and W. Hill. *The Art of Electronics.* Cambridge University Press, Cambridge, UK, 1989. 2nd ed.

[52] K. M. Huffenberger and U. Seljak. Prospects for ACT: simulations,power spectrum, and non-gaussian analysis. *New Astronomy*, 10, 2005. astro-ph/0408066.

[53] O. Ilbert, S. Arnouts, H.J. McCracken, M. Bolzonella, E. Bertin, O. Le Fevre, Y. Mellier, G. Zamorani, R. Pello, A. Iovino, L. Tresse, D. Bottini, B. Garilli, V. Le Brun, D. Maccagni, J.P. Picat, R. Scaramella, M. Scodeggio, G. Vettolani, A. Zanichelli, C. Adami, S. Bardelli, A. Cappi, S. Charlot, P. Ciliegi, T. Contini, O. Cucciati, S. Foucaud, P. Franzetti, I. Gavignaud, L. Guzzo, B. Marano, C. Marinoni, A. Mazure, B. Meneux, R. Merighi, S. Paltani, A. Pollo, L. Pozzetti, M. Radovic, E. Zucca, M. Bondi, A. Bongiorno, G. Busarello, S. De La Torre, L. Gregorini, F. Lamareille, G. Mathez, P. Merluzzi, V. Ripepi, D. Rizzo, and D. Vergani. Accurate photometric redshifts for the CFHT legacy survey calibrated using the VIMOS VLT deep survey. *Astronomy and Astrophysics*, 439:845–862, 2005, astro-ph/0603217.

[54] K. Irwin and G. Hilton. *Transition-Edge Sensors*. Springer-Verlag, Berlin, Germany, 2005. Chapter in Cryogenic Particle Detection.

[55] K. D. Irwin, 2004. Private communication regarding the Mux05c design.

[56] K. D. Irwin and M. E. Huber. Squid operational amplifier. *IEEE Transactions on Applied Superconductivity*, 11(1):1265–70, 2001.

[57] W. C. Jones, P. A. R. Ade, J. J. Bock, J. R. Bond, J. Borrill, A. Boscaleri, P. Cabella, C. R. Contaldi, B. P. Crill, P. de Bernardis, G. De Gasperis, A. de Oliveira-Costa, G. De Troia, G. di Stefano, E. Hivon, A. H. Jaffe, T. S. Kisner, A. E. Lange, C. J. MacTavish, S. Masi, P. D. Mauskopf, A. Melchiorri, T. E. Montroy, P. Natoli, C. B. Netterfield, E. Pascale, F. Piacentini, D. Pogosyan, G. Polenta, S. Prunet, S. Ricciardi, G. Romeo, J. E. Ruhl, P. Santini, M. Tegmark, M. Veneziani, and N. Vittorio. A Measurement of the angular power spectrum of the CMB temperature anisotropy from the 2003 flight of BOOMERANG. *Astrophysical Journal*, 647:823–832, 2006. astro-ph/0507494.

[58] A. L. Kinney, D. Calzetti, R. C. Bohlin, K. McQuade, T. Storchi-Bergmann and H. R. Schmitt. *Astrophysical Journal*, 467:38, 1996.

[59] D. C. Koo. *Astronomical Journal*, 90:418, 1985.

[60] D. C. Koo. *Astronomical Society of the Pacific Conference Series*, 191:3, 1999.

[61] A. Kosowsky. The Atacama Cosmology Telescope. *New Astronomy Review*, 47:939–943, 2003.

[62] KUKA Robotics Corporation. 2250 Key Drive, Clinton Township, Michigan, 48036.

[63] Lake Shore Cryotronics Inc. 575 McCorkle Blvd., Westerville, Ohio 43082.

[64] J. W. Lamb. Miscellaneous data on materials for millimetre and submillimetre optics. *Int. J. Infrared Millimeter Waves*, 17(12):1997–2232, 1996.

[65] J. Lau, M. Benna, M. Devlin, S. Dicker, and L. Page. Experimental tests and modeling of the optimal orifice size for a closed cycle he sorption refrigerator. *Cryogenics*, 46:809–814, 2006.

[66] J. Lau, J. Fowler, T. Marriage, L. Page, J. Leong, E. Wishnow, R. Henry, E. Wollack, M. Halpern, D. Marsden, and G. Marsden. A millimeter-wave antireflection coating for cryogenic silicon lenses. *Applied Optics*, 45:3746–51, 2006. astro-ph/0701091.

[67] J. M. Lau. *CCAM: A Novel Millimeter-Wave Instrument Using a Close-Packed TES Bolometer Array*. PhD thesis, Princeton University, Department of Physics, 2007.

[68] A. T. Lee, P. L. Richards, S. W. Nam, B. Cabrera, and K. D. Irwin. A superconducting bolometer with strong electrothermal feedback. *Appl. Phys. Lett.*, 69(12):1801–3, 1996.

[69] M. Lima and W. Hu. Photometric redshift requirements for self-calibration of cluster dark energy studies. *Physical Review D*, 76:123013, 2007.

[70] M. A. Lindeman. *Microcalorimetry and the Transition-Edge Sensor*. PhD thesis, University of California at Davis, Department of Physics, 2000.

[71] T. A. Marriage. *Detectors for the Atacama Cosmology Telescope*. PhD thesis, Princeton University, Department of Physics, 2006.

[72] T. A. Marriage, J. A Chervenak, and R. B. Doriese. Testing and assembly of the detectors for the Millimeter Bolometer Array Camera on ACT. *Nuclear Instruments and Methods in Physics Research A*, 559:551–3, 2006.

[73] J. C. Mather, D. J. Fixsen, R. A. Shafer, C. Mosier, and D. T. Wilkinson. Calibrator design for the cobe1 far infrared absolute spectrophotometer (firas). *Astrophysical Journal*, 512:511–20, 1999.

[74] P. A. Mazzali, F. K. Ropke, S. Benetti, and W. Hillebrandt. A common explosion mechanism for type 1a supernovae. *Science*, 315:825–8, 2007.

[75] Y. Mizuguchi, M. Akagawa, and H. Yokoi. Offset gregorian antenna. *Electronics and communications in Japan*, 61:58–66, 1978.

[76] P. Morrissey, D. Schiminovich, T. A. Barlow, D. C. Martin, B. Blakkolb, T. Conrow, B. Cooke, K. Erickson, J. Fanson, P. G. Friedman, R. Grange, P. N. Jelinsky, S. Lee, D. Liu, A. Mazer, R. McLean, B. Milliard, D. Randall, W. Schmitigal, A. Sen, O. H. W. Siegmund, F. Surber, A. Vaughan, M. Viton, B. Y. Welsh, L. Bianchi, YI. Byun, J. Donas, K. Forster, T. M. Heckman, YW. Lee, B. F. Madore, R. F. Malina, S. G. Neff, R. M. Rich, T. Small, A. S. Szalay, and T. K. Wyder. The on-orbit performance of the Galaxy Evolution Explorer. *Astrophysical Journal Letters*, 619:L7, 2005.

[77] M. D. Niemack. Measuring two-millimeter radiation with a prototype multiplexed TES receiver for ACT. *Proc. SPIE Millimeter and Submillimeter Detectors for Astronomy III*, 6275:2750B, 2006.

[78] M. D. Niemack, R. Jimenez, L. Verde, F. Menanteau, D. Spergel, J. Hughes, and Y. Lin. Improved photometric redshifts using GALEX observations for the next generation of sz cluster surveys. *Astrophysical Journal*, 2008. in preparation.

[79] M. D. Niemack, Y. Zhao, E. Wollack, R. Thornton, E. R. Switzer, D. S. Swetz, S. T. Staggs, L. Page, O. Stryzak, H. Moseley, T. A. Marriage, M. Limon, J. M. Lau, J. Klein, M. Kaul, N. Jarosik, K. D. Irwin, A. D. Hincks, G. C. Hilton, M. Halpern, J. W. Fowler, R. P. Fisher, R. Dünner, W. B. Doriese, S. R. Dicker, M. J. Devlin, J. Chervenak, B. Burger, E. S. Battistelli, J. Appel, M. Amiri, C. Allen, and A. M. Aboobaker. A kilopixel array of tes bolometers for act: Development, testing, and first light. *Journal of Low Temperature Physics*, 2008, preprint.

[80] Optical Research Associates. 3280 East Foothill Blvd., Pasadena, California, 91107.

[81] H. Oyaizu, C. Cunha, M. Lima, H. Lin, and J. Frieman. *Bulletin of the American Astronomical Society*, 38:140, 2006.

[82] H. Oyaizu, M. Lima, C. Cunha, H. Lin, J. Frieman, and E. Sheldon. Empirical photometric redshifts for SDSS DR6. *ArXiv Astroph. e-prints*, astro-ph/0708:0030, 2007. astro.uchicago.edu/sdss/dr6/photoz2.html.

[83] N. Padmanabhan, et al. An improved photometric calibration of the Sloan Digital Sky Survey imaging data. *ArXiv Astroph. e-prints*, astro-ph/0703:454v2, 2007.

[84] L. Page, C. Jackson, C. Barnes, C. Bennett, M. Halpern, G. Hinshaw, N. Jarosik, A. Kogut, M. Limon, S. S. Meyer, D. N. Spergel, G. S. Tucker, D. T. Wilkinson, E. Wollack, and E. L. Wright. The optical design and characterization of the microwave anisotropy probe. *Astrophysical Journal*, 585, 2003.

[85] L. Page, M. R. Nolta, C. Barnes, C. L. Bennett, M. Halpern, G. Hinshaw, N. Jarosik, A. Kogut, M. Limon, S. S. Meyer, H. V. Peiris, D. N. Spergel, G. S. Tucker, E. Wollack, and E. L. Wright. First-year WMAP observations: Interpretation of the TT and TE angulare power spectrum peaks. *Astrophysical Journal*, 148, 2003.

[86] V. V. Parshin, R. Heidinger, B. A. Andreev, A. V. Gusev, and V. B. Shmagin. Silicon as an advanced window material for high power gyrotrons. *Int. J. Infrared Millimeter Waves*, 16(5):863–77, 1995.

[87] P. J. E. Peebles. *Principles of Physical Cosmology.* Princeton University Press, Princeton, New Jersey USA, 1993.

[88] S. Perlmutter, G. Aldering, M. Della Valle, S. Deustua, R. S. Ellis, S. Fabbro, A. Fruchter, G. Goldhaber, D. E. Groom, I. M. Hook, A. G. Kim, M. Y. Kim, R. A. Knop, C. Lidman, R. G. McMahon, P. Nugent, R. Pain, N. Panagia, C. R. Pennypacker, P. Ruiz-Lapuente, B. Schaefer, and N. Walton. Discovery of a supernova explosion at half the age of the universe. *Nature*, 391:51–54, 1998.

[89] M. J. Rees and D. W. Sciama. Large scale density inhomogeneities in the universe. *Nature*, 217:511, 1968.

[90] C. L. Reichardt, P. A. R. Ade, J. J. Bock, J. R. Bond, J. A. Brevik, C. R. Contaldi, M. D. Daub, J. T. Dempsey, J. H. Goldstein, W. L. Holzapfel, C. L. Kuo, A. E. Lange, M. Lueker, M. Newcomb, J. B. Peterson, J. Ruhl, M. C. Runyan, and Z. Staniszewski. High resolution CMB power spectrum from the complete ACBAR data set. *ArXiv Astroph. e-prints*, astro-ph/0801:1491v2, 2008.

[91] C. D. Reintsema, J. Beyer, S. W. Nam, S. Deiker, G. C. Hilton, K. D. Irwin, J. M. Martinis, J. Ullom, L. R. Vale, and M. MacIntosh. A prototype system for SQUID

multiplexing of large-format transition-edge sensor arrays. *Review of Scientific Instruments*, 74:4500, 2003.

[92] W. Rusch, A. Prata, Y. Rahmat-Samii, and R. Shore. Derivation and application of the equivalent paraboloid for classical offset cassegrain and gregorian antennas. *IEEE Trans. on Antennas and Propagation*, 38(8):1141–9, 1990.

[93] R. K. Sachs and A. M. Wolfe. Perturbations of a cosmological model and angular variations of the microwave background. *Astrophysical Journal*, 147:73–90, 1967.

[94] D. Samtleben, S. Staggs, and B. Winstein. The cosmic microwave background for pedestrians: A review for particle and nuclear physicists. *Annual Review of Nuclear and Particle Science*, 57:245–83, 2007.

[95] D. Schroeder. *Astronomical Optics*. Academic Press, San Diego, California USA, 2000. 2nd ed.

[96] N. Sehgal, H. Trac, K. Huffenberger, and P. Bode. Microwave-sky simulations and projections for galaxy cluster detection with the atacama cosmology telescope. *Astrophysical Journal*, 664:149–162, 2007. astro-ph/0612140.

[97] Siltronic AG. 81737 München, Germany.

[98] D. N. Spergel, R. Bean, O. Dore, M. R. Nolta, C. L. Bennett, J. Dunkley, G. Hinshaw, N. Jarosik, E. Komatsu, L. Page, H. V. Peiris, L. Verde, M. Halpern, R. S. Hill, A. Kogut, M. Limon, S. S. Meyer, N. Odegard, G. S. Tucker, J. L. Weiland, E. Wollack, and E. L. Wright. Three-year WMAP observations: Implications for cosmology. *Astrophysical Jornal Supplement Series*, 170:377, 2007.

[99] R. A. Sunyaev and Ya. B. Zel'dovich. Microwave background radiation as a probe of the contemporary structure and history of the universe. *Annual Review of Astronomy and Astrophysics*, 18:537–60, 1980.

[100] D. Swetz. Instrument design and characterization of the Millimeter Bolometer Array Camera on the Atacama Cosmology Telescope. *Proceedings of Millimeter and Submillimeter Detectors and Instrumentation, SPIE*, 2008. In preparation.

[101] H. Tanaka and M. Mizusawa. Elimination of cross polarization in offset dual-reflector antennas. *Electronics Communications of Japan*, 58:71–78, 1975.

[102] M. Tegmark. CMB mapping experiments: A designer's guide. *Physical Review D*, 56:4514, 1997.

[103] Tekdata Interconnections Limited. Westport House, Federation Road, Burslem, Stoke-On-Trent, Staffordshire, ST6 4HY, United Kingdom.

[104] Michael Tinkham. *Introduction to Superconductivity.* McGraw-Hill, New York, New York USA, 1996.

[105] J. L. Tonry, B. P. Schmidt, B. Barris, P. Candia, P. Challis, A. Clocchiatti, A. L. Coil, A. V. Filippenko, P. Garnavich, C. Hogan, S. T. Holland, S. Jha, R. P. Kirshner, K. Krisciunas, B. Leibundgut, W. Li, T. Matheson, M. M. Phillips, A. G. Riess, R. Schommer, R. C. Smith, J. Sollerman, J. Spyromilio, C. W. Stubbs, and N. B. Suntzeff. Cosmological results from high-z supernovae. *Astrophysical Journal*, 594:1–24, 2003.

[106] C. E. Tucker and P. A. R. Ade. Thermal filtering for large aperture cryogenic detector arrays. *Proc. SPIE Millimeter and Submillimeter Detectors and Instrumentation for Astronomy III*, 6275:62750T, 2006.

[107] J. N. Ullom, W. B. Doriese, G. C. Hilton, J. A. Beall, S. Deiker, W. D. Duncan, L. Ferreira, K. D. Irwin, C. D. Reintsema, and L. R. Vale. Characterization and reduction of unexplained noise in superconducting transition-edge sensors. *Applied Physics Letters*, 84(21):4206, 2004.

[108] E. Vanzella, S. Cristiani, A. Fontana, M. Nonino, S. Arnouts, E. Giallongo, A. Grazian, G. Fasano, P. Popesso, P. Saracco, and S. Zaggia. Photometric redshifts with the multilayer perceptron neural network: Application to the HDF-S and SDSS. *Astrophysical Journal*, 423:761, 2004.

[109] L. Verde, 2008. private communication.

[110] L. Verde and D. Spergel. Dark energy and cosmic microwave background bispectrum. *Physical Review D*, 65:043007, 2002. astro-ph/0108179v2.

[111] X. Wang, M. Tegmark, B. Jain, and M. Zaldarriaga. The last stand before MAP: cosmological parameters from lensing, CMB and galaxy clustering. *Physical Review D*, 68:123001, 2003.

[112] M. J. Way and A. N. Srivastava. Novel methods for predicting photometric redshifts from broadband photometry using virtual sensors. *Astrophysical Journal*, 647:102–115, 2006.

[113] J. J. Wray and J. E. Gunn. A new technique for galaxy photometric redshifts in the Sloan Digital Sky Survey. *Astrophysical Journal*, 2007, preprint, astro-ph/0707.3443.

[114] E. L. Wright. Infrared brightness temperature of mars, 1983-2103. *arXiv:astro-ph*, page 07036401.

[115] E.L. Wright. Scanning and mapping strategies for CMB experiments. *Proc. IAS CMB Data Analysis Workshop*, pages astro–ph/9612006, 1996.

[116] M. Zeilik and S. Gregory. *Introductory Astronomy and Astrophysics*. Saunders College Publishing, Orlando, Florida USA, 1998. 4th ed.